UNIVERSITY OF SOUTHAMPTON

FACULTY OF ENGINEERING, SCIENCE & MATHEMATICS

SCHOOL OF ENGINEERING SCIENCES

national Centre for Advanced Tribology at Southampton (nCATS)

ADVANCED CONDITION MONITORING TO PREDICT ROLLING ELEMENT BEARING WEAR USING MULTIPLE IN-LINE AND OFF-LINE SENSING

BY
MARK CRAIG

THESIS SUBMITTED FOR THE DEGREE OF DOCTOR OF PHILOSOPHY

2010

Abstract

The work presented in this thesis shows correlations between condition monitoring techniques, generated during the evolution of accelerated bearing wear, by inner race indentation. Off-line debris analysis consisted of an optical particle counter, ferrography calculations of severity index, spectrometric oil analysis and imaging using the electron microscope. In-line debris detection schemes included an inductive and ferromagnetic particle counter. An electrostatic oil-line sensor was also used, which produced an additional parameter called the indicator value. The in-line multi-sensing arrangement also employed electrostatic wear-site sensors, an accelerometer, acoustic emission transducer and thermocouples. Post-test assessments involved mass loss calculations and photographic evidence of damage. The sensor data was also used in another research program which was based on advanced signal processing architectures using artificial intelligence algorithms.

Four periods of debris detection related to running-in, benign wear, the early signs of distress and wear out. During running-in, a heightened quantity of plate-like particles correlated with a severity index that increased with contact pressure. The accentuated particle levels related to shearing and deformation of the largest protuberances from the surface roughness. In the benign regime, conforming bearing elements enabled elastohydrodynamic principles to prevail, resulting in a reduced quantity of plate-like particles. Periods of distress were identified during benign wear, by changes in particle morphology, as spherical, rugged, chunky and swarf-like debris were identified. Corroborating evidence of distress was shown by a heightened particle count that increased with contact pressure. The increase in wear rate was also shown by a heightened severity index and iron particle concentration. After the early distress signatures, the particle activity returned to levels observed during benign wear, which indicated a healing process. Wear out related to propagating surface damage, in which larger plate-like, spherical and swarf-like particles were formed. During this period, the debris count, severity index and iron concentration increased with mass loss.

During running-in, the heightened debris levels correlated with increased oil-line charge and indicator values. Also at this time, increased wear site charge, acceleration, AE peak amplitude and temperature were observed, which were found to be sensitive to contact pressure. All sensing levels decreased after the running-in period, indicating benign wear. The early signs of distress, which were confirmed by the particle morphology and count, were corroborated by accentuated AE levels, which increased with contact pressure. Further support of distress was shown by increased activity using the AI algorithms which identified the locality of eventual failure. The increased particle count during wear out correlated with runaway sensor activity from all techniques which increased with mass loss.

The multi-sensor approach showed that the off-line debris analysis identified the mechanism and severity of wear using the particle morphology and count. In addition, the particle analysis provided a confident assessment of the earliest signs of distress and supported the AE peak amplitude and AI structures in diagnosing the source of accentuated wear. The debris analysis also confirmed that the in-line signatures related to periods of wear, during which time the sensing levels were sensitive to contact pressure during running-in and mass loss during wear out. The in-line techniques also provided corroborating evidence in identifying degradation of specific components. Therefore, the combined analysis provided complimentary information of the early micro degradation mechanisms as well as to the precise locality and severity of wear, which are essential for prognostic condition monitoring programmes.

Contents

List of Figures

List of Tables

Nomenclature

Symbol	Meaning	Unit
b	Half the contact width for a line contact	m
a	Half the contact width for an ellitical contact	m
a'	Half the contact width for an ellitical contact	m
P	Load per rolling element	N
W	Applied load	N
z_1	Number of rolling elements	n/a
L	Length of rolling elements	m
k_1	Ellipticity integral	n/a
e	Ellipticity parameter	n/a
R	Relative radius of curvature	m
R_1	Radius of body 1	m
R_2	Radius of body 2	m
E*	Reduced modulus	Pa
E_1	Elastic modulus of body 1	Pa
E_2	Elastic modulus of body 2	Pa
υ_1	Poissons ratio of body 1	n/a
υ_2	Poissons ratio of body 2	n/a
P_m	Mean contact pressure	Pa
P_0	Peak contact presuure	Pa
Y	Yield stress in tension	Pa or Nm^{-2}
σ_1, σ_2, σ_3	Principle stresses	Pa or Nm^{-2}
k	Yield stress in pure shear	Pa or Nm^{-2}
τ	Maximum shear stress	Pa or Nm^{-2}
z	Depth of shear stress at furst yield	m
H	Hardness of material	Pa
Hv	Vickers hardness	kgf mm^{-2}
μ	Friction coefficient	n/a
η	Dynamic viscosity of lubricating film	N s m^{-2} (cP)
U	Relative speed of surfaces / entrainment velocity	m s^{-1}
P_n	Nominal bearing pressure	Pa
λ	Lamda ratio	n/a
h_{min}	Minimum film thickness	m
σ	Composite surface roughness	m
R_{q1}	Peak to valley roughness of body 1	m
R_{q2}	Peak to valley roughness of body 2	m
ηo	Base viscosity at atmospheric pressure	N s m^{-2} (cP)

α	Pressure-viscosity coefficient	Pa^{-1}
D_1	Size of identation particle	m
β	Angle of indenter	degrees
I_f	Indentation force	N
S	Stress levels	N m-2
N_1	Number of load cycles	n/a
da_1	Change in length of fatigue crack	m
K	Stress intensity factor	$N\ m^{-2}$
C_1	Emperical constant for Paris-Erdogen equation	n/a
m	Emperical constant for Paris-Erdogen equation	n/a
C2	Bearing dynamic load rating	N
m_1	Bearing life exponent. 3 & 3.3 for balls & rollers	n/a
D	Diameter of the inner race	mm
N	Bearing rotational speed	$rev\ min^{-1}$
ω_S	Shaft frequency	Hz
ω_{od}	Outer race defect frequency	Hz
ω_{id}	Inner race defect frequency	Hz
ω_{re}	Rolling element defect frequency	Hz
D_b	Pitch circle diameter	m
d_r	Diameter of rolling elements	m
α_1	Contact angle	$Radians\ s^{-1}$
dB	Decibels	dB
℃	Temperature	℃
E(r)	Electric field acting in a radial direction	$V\ m^{-1}$
q	Charge	pC
d	Distance	m
A	Area	m^2
ε	Relative permittivity	$F\ m^{-1}$
C	Capacitance	F
V	Potential Difference	V
φMa	Work function of material a	eV
φMb	Work function of material b	eV

Abbreviation	Meaning
EHL	Elastohydrodynamic
IMechE	Institute of Mechanical Engineers
STLE	Society of Tribologists and Lubrication Engineers
ASME	American Society of Mechanical Engineers
VIM	Vacuum Induction Method
VAR	Vacuum Arc Remelting
CM	Condition Monitoring
RMS	Root-Mean-Square
AE	Acoustic Emissions
FFT	Fast Fourier Transform
PoD	Pin On Disc
Is	Severity Index
SOAP	Spectrometric Oil Analysis Program
HIAC	High Accuracy
PODS	Portable Oil Diagnostic System
NAS	National Aerospace Standard
ES	Expert Systems
NN	Neural Networks
LNF	LaserNet Fines
CCD	Charged Couple Device
CAVE	Computer Aided Vision Engineering
FMEA	Failure Mode and Effect Analysis
FTA	Fault Tree Analysis
CMMS	Computerised Maintenance Management System
HUMS	Health Usage Management System
IDMS	Ingested Distress Management System
EDMS	Engine Distress Management System
WSS	Wear Site Sensor
OLS	Oil Line Sensor
CPD	Contact Potential Difference
FZG	Institute for Machine Elements Gear Research Centre
AI	Artificial Intelligence
DERA	Defence Evaluation and Research Agency
PSD	Power Spectral Density
DAT	Digital Audio Tape
PMT	Photo Multiplier Tube
SEM	Scanning Electron Microscope

Academic Thesis: Declaration of Authorship

I,…Mark Craig……

declare that this thesis and the work presented in it are my own and has been generated by me as the result of my own original research.

Advanced condition monitoring to predict rolling element bearing wear using multiple in-line and off-line sensing

I confirm that:

1. This work was done wholly or mainly while in candidature for a research degree at this University;

2. Where any part of this thesis has previously been submitted for a degree or any other qualification at this University or any other institution, this has been clearly stated;

3. Where I have consulted the published work of others, this is always clearly attributed;

4. Where I have quoted from the work of others, the source is always given. With the exception of such quotations, this thesis is entirely my own work;

5. I have acknowledged all main sources of help;

6. Where the thesis is based on work done by myself jointly with others, I have made clear exactly what was done by others and what I have contributed myself;

7. Either none of this work has been published before submission, or parts of this work have been published as: [please list references below]:

Signed:
……
…….

Date:……
…….

Publications

Journal papers

Advanced Condition Monitoring of Tapered Roller Bearings, Part 1: M. Craig, T.J. Harvey, R.J.K. Wood, K. Masuda, M. Kawabata, H. Powrie, Tribology International (42) 11-12, 2009, 1846-1856.

Advanced Condition Monitoring of Tapered Roller Bearings, Part 2: With Integrated Data Fusion Techniques, S.L. Chen, M. Craig, L. Wang, R.J.K. Wood, R. Callan, H.E.G. Powrie, Submitted to Mechanical Systems and Signal Processing.

Conference papers

Advanced Condition Monitoring of Ball Bearings. Craig, M., Harvey, T.J., Wood, R.J.K., Masuda, K., Kawabata, M., Powrie, H.E.G, STLE, Ohio, 2008.

Tapered Roller Bearing Condition Monitoring using Multiple Sensing, M. Craig, T.J. Harvey, R.J.K. Wood, K. Masuda, M. Kawabata, H. Powrie, Submitted to WTC 4, Kyoto, 2009.

Use of Artificial Intelligence Methods for Advanced Bearing Health Diagnostics and Prognostics. Chen, S.L., Craig, M., Wood, R.J.K., Wang, L., Callan, R., Powrie, H.E.G. IEEE Aerospace Conference, Montana, 2008.

Bearing Condition Monitoring using Multiple Sensors and Integrated Data Fusion Techniques. Chen, S.L., Craig, M., Wood, R.J.K., Wang, L., Callan, R., Powrie, 9th International Conference on Vibrations in Rotating Machinery, Exeter, 2008.

Posters

Advanced Condition Monitoring of Tapered Roller Bearings, Surface Engineering of Automotive Powertrains for Environmetally Friendly Transport, IMechE London 2008.

Acknowledgements

There are a number of people who immediately spring to mind when trying to express a great deal of gratitude for their generosity and kindness over this research program.

Supervision

The most influential and dedicated team who provided fantastic support and encouragement from the very first day were Prof Robert Wood and Dr Terry Harvey. Rob is an incredible engineer, mentor and motivator who deserves immense praise for his dedication and enthusiasm in helping others in all fields of tribology. Terry is also a great inspiration who is always uncompromising in facilitating experimental set-ups and instrumentation issues with all members within the group. So to both Rob and Terry, many thanks for the wonderful experience within nCATS, and for trying to impart some of your expertise into the correct ways of engaging into complex engineering problems.

Tribotex

I would also like to thank the staff at Triobotex for their consideration and commitment throughout. Also, for their thoughtfulness in making Japan such a memorable experience at their amazing facilities, and for their incredible knowledge on all matters relating to tribology. Therefore, to Masahiko Kawabata many thanks for the opportunity to be witness of the amazing work that takes place under your stewardship. Also, appreciation must go to Yoshihiro Sasaki and Masahiro Tanaka for sharing their expertise on tribological issues.

GE Aviation

To Dr Honor Powrie and Rob Callen, the many words of encouragement were greatly appreciated, as were the use of the electrostatic sensors and instrumentation which provided this project with such novelty.

University of Southampton

There are numerous colleagues, past and present from nCATS and the School of Engineering Sciences (SES), and apologies if anyone has been left out. Praise goes to the academic staff of Dr Ling Wang, Dr Julian Wharton and Prof Martyn Hill for their constant encouragement. Also, to the technical personnel of Steve Pilcher, Dave Beckett, Chris Williams and Rob Barnes for the manufacture and repair of parts, as well as to all the team at the Engineering Design and Manufacturing Centre (EDMC).

Furthermore, without the friendship of fellow colleagues my experience would never have been so enjoyable. Therefore, to Dan, Jenny, Nick, Xiao, Prassana, Fitri, Shiva, Nazilla, Mandar, Lilly, Stephane, Jun, Ram and Azlan I am very thankful of our time together. Also, thanks to those in the bio-engineering and materials departments.

Family

The most important people who for the majority of time tend to be forgotten, are those that are the closest. Without the devotion of my family I would never have been able to complete the duration of this project and for that I am forever grateful. Their endless charity over many years has on too many occasions has gone unappreciated. There are a not enough words that describe the magnitude of their contribution and to them I will always be indebted.

Keisuke Masuda

One person who has always been there with continuous assistance and encouragement has been Keisuke. If it was not for his influence and friendship then I would never be in the position I am today.

1 Introduction to the research

This initial chapter provides an introduction to the research, which is based on the condition monitoring (CM) of rolling element bearings. Also described are the motivation and aims of the work, along with the novel techniques and processes that were deployed.

1.1 Introduction

CM strategies are employed on critical engineering components to maximise machine reliability, availability and maintainability. This is achieved by sensing technologies that monitor system performance and make confident assessments of degradation. One of the most important engineering components is rolling element bearings, and for that reason they are constantly under scrutiny. There are a number of factors that contribute to bearing distress, with the dominant failure mode relating to regions of localised stress that initiates crack growth. Eventually, crack propagation and coalescence results in material liberation from the surface which prohibits functionality. The distressed surface initiates further regions of localised stress, which acts as a positive feedback mechanism that drives further damage. If the propagating damage is not treated, the inevitable consequence will be catastrophic failure to secondary systems. The resulting damage can lead to costs of unplanned repair and loss of production.

The identification of bearing degradation is based on the detection of a range of distress signatures, making it possible to identify the locality of impending and runaway wear. These include increased acoustic emissions (AE) during crack initiation/propagation [1] and vibration during interfacial element contact [2]. Thus, CM programmes are critical in maintaining equipment under satisfactory operating conditions by detecting failure mechanisms before they develop into major faults.

The most basic CM strategy is reactive, in which a failed component is immediately replaced during breakdown. A superior scheme is preventative, which is a planned schedule of works at predetermined time periods. This will involve the replacement of components, no matter what the condition and can lead to the untimely, expensive and

unnecessary removal of healthy elements. An enhanced strategy is predictive and consists of the identification of operating signatures that defines the condition of the component. Based on the condition of the component, actions are taken to ensure optimum machine performance within predetermined thresholds. Some operating signatures include temperature and vibration analysis with data collection comprising of time and frequency analysis [3], statistical parameters [4] and sensor data fusion [5]. An enhanced approach is proactive, which is based on forecasting system integrity through a prognosis aimed at identifying the origins of degradation [6].

1.2 Motivation

The motivation behind this work is that there is a continual need to effectively monitor the evolution of bearing wear, so that the early identification of distress can provide a confident prognosis of failure. This equips service personnel with sufficient time to implement remedial action strategies based on component health rather than replacement during scheduled outages. Furthermore, research programs are continually being developed to identify accurate and cost effective solutions for monitoring bearing contact distress. One of the relatively new technologies is based on the electrostatic sensing of wear. The basic concept behind this technique is that surface degradation often leads to surface charging, oil charging and charged wear debris. Therefore, the detection of charge in the vicinity of distressed wear sites and in lubrication lines can provide valuable information relating to the degradation of tribological contacts.

1.3 Aims

The aims of this research were to identify with enhanced clarity the evolution of metal-on-metal tapered roller and ball bearing wear and to detect with confidence the earliest signs of distress. For the first time, a multi-signature strategy utilised electrostatic wear site sensors (WSS), acoustic emissions (AE), vibration acceleration and thermocouples to monitor distress at wear sites. Additional operating signatures included an electrostatic oil-line sensor (OLS) which generated an additional parameter called the indicator value, as well as inductive and ferromagnetic particle counters to monitor degradation in the oil-line. Further corroboration of wear was shown by oil samples that were taken during various stages of the test and were

analysed for sub-100 μm debris content. The off-line debris analysis also consisted of correlations between a portable oil diagnostic system (PODS), severity index calculations using ferrography, a spectrometric oil analysis program (SOAP) and particle imaging using the electron microscope.

The signal processing strategy consisted of root-mean-square (RMS) trending of the electrostatic, vibration and thermocouple data. A further approach incorporated defect frequency normalisation techniques of the vibration and electrostatic signatures, which directly supported another parallel PhD programme. This scheme consisted of developing artificial intelligence techniques to provide further corroborating evidence of the wear process.

Therefore, the amalgamation of in-line, oil-line and off-line traditional and novel sensing techniques, and artificial intelligence processes provide corroborating evidence to the evolution and locality of the earliest signs of tapered roller and ball bearing distress.

1.4 Structure

Chapter 1 provides an introduction to the theme of the research, as well as the motivation and aims of the project.

Chapter 2 is a literature review that introduces a brief history of bearings and the inception of tribology. The chapter then describes the fundamentals of bearing tribology, which encompasses loading, contact pressures, surface deformation and lubrication regimes. The final stage of the chapter describes the mechanisms of bearing wear and the different types of debris that are formed within these regimes.

Chapter 3 is a further literature review that investigates the state of the art from in-line, oil-line and off-line condition monitoring strategies that are used to monitor bearing wear. The in-line techniques include vibration and AE sensing in the time and frequency domain and thermography. Oil-line techniques include inductive and ferromagnetic sensors for the identification of wear debris. Off-line wear debris analysis is also considered with ferrography, spectrometric oil analysis programs

(SOAP) and optical particle counters. The combination of techniques and analysis are then brought together in decision making algorithms and maintenance management systems. This chapter also provides a further review of the electrostatic technique. The principles of charge detection, sensor geometries and charging mechanisms are explained, as well as the latest results generated during pin-on-disc (PoD), reciprocating, FZG gear and bearing test rigs.

Chapter 4 describes the experimental set-up that was employed during testing. The test rig comprises of the in-line, oil-line and off-line technologies which were described in chapter 3. The multi-sensor approach was incorporated to provide enhanced confidence and correlations of distress, which could not be identified during single signature activity. This chapter also explains the rationale behind the positioning of the technologies, operating conditions and signal processing techniques.

Chapter 5 shows the results obtained during accelerated and defect free tapered roller bearing tests. The signature features, trends, correlations and mechanisms of sensor activity are described for each technique. The results also incorporate the analysis generated by the artificial intelligence techniques.

Chapter 6 follows a similar theme to chapter 5, with correlations between the in-line and off-line analysis generated during ball bearing testing.

Chapter 7 correlates the findings of both the tapered roller and ball bearing tests, showing the sensor levels, trends and mechanisms of tribological activity. Considerations are also made to evaluate the effectiveness and reliability of the techniques.

Chapter 8 provides some conclusions and contributions of the work which has monitored the evolution and the earliest signs of bearing distress.

Chapter 9 lists some of the future work and additional tests that could be carried out to enhance and corroborate the results provided by this project.

2 Bearing Tribology

The literature cited in this chapter reviews the concepts that drive the current understanding of rolling element bearing tribology. This chapter forms the foundations of the experimental work conducted in this thesis which is based on improving rolling element bearing condition monitoring.

2.1 Introduction

Bearings are one of the most critical engineering components found in essential modern-day equipment such as motors, gears and turbines to provide support for rotating assemblies. However, the earliest bearing applications can be dated back to the ancient Egyptians of around 2600 BC, who used logs as rolling elements to reduce friction between the ground and surfaces of large pieces of stone during sliding to construction sites. Furthermore, it was Leonardo da Vinci, who in the 1500's was first credited with the principles behind bearing mechanics, with the introduction of ball bearings to reduce friction between stationary stages and rotating platforms. This was followed by Galileo Galilei in the 1600's who utilised a cage assembly to maintain the position of the wooden balls between the surfaces.

Some important bearing milestones include a patent award, which was presented to Philip Vaughan in 1794, who described an assembly in which the balls ran along a designated raceway. In addition, Isaac Babbit in 1839 used metal alloys, which were ideal for journal bearings due to the conforming characteristics of the surfaces under motion. Around the late 19th century a renaissance in bearing work took place. Influential figures at this time included Friedrich Fischer, of Fischers Aktien-Gesellschaft, FAG, who in 1883 invented a grinding machine which permitted high-precision hardened steel balls of uniform size to be mass produced. Further developments were made by Henry Timken, of the Timken Bearing Company, who in 1898 invented the tapered roller bearing. This was followed by Sven Wingquist, of the Swedish Ball Bearing Factory – Svenska Kullager Fabriken, SKF, who in 1907 designed a self-aligning ball bearing.

Today, ball bearings are the most popular, as they are inexpensive and have a relatively high load carrying capacity, compared to rollers which cost more, but

maintain higher loads than the ball geometries. A rolling element bearing consists of 4 elements; inner race, rolling element, cage and outer race, as shown in Figure 2.1. The inner race has a grooved track on its diameter, which the rotating balls traverse during operation. The inner race has a precision finish to produce a low surface roughness, typically around 0.01 μm, of importance which is described in the following sections. The inner raceway is usually coupled to a shaft with an interference fit and is the driven element. The outer race also has a groove on its diameter, which forms a conforming track with the inner raceway to retain the balls during motion. The outer raceway has the same high precision finish as the inner raceway and is normally fixed within a stationary housing. The balls are located between the raceways to reduce friction between the raceway surfaces during loading and have a radius which is slightly smaller than the grooved track. The idealised contact between the balls and raceway is at a single point, whilst that of a roller on a raceway is a line. The rolling elements are separated and maintained at equal distances between the raceways by cages.

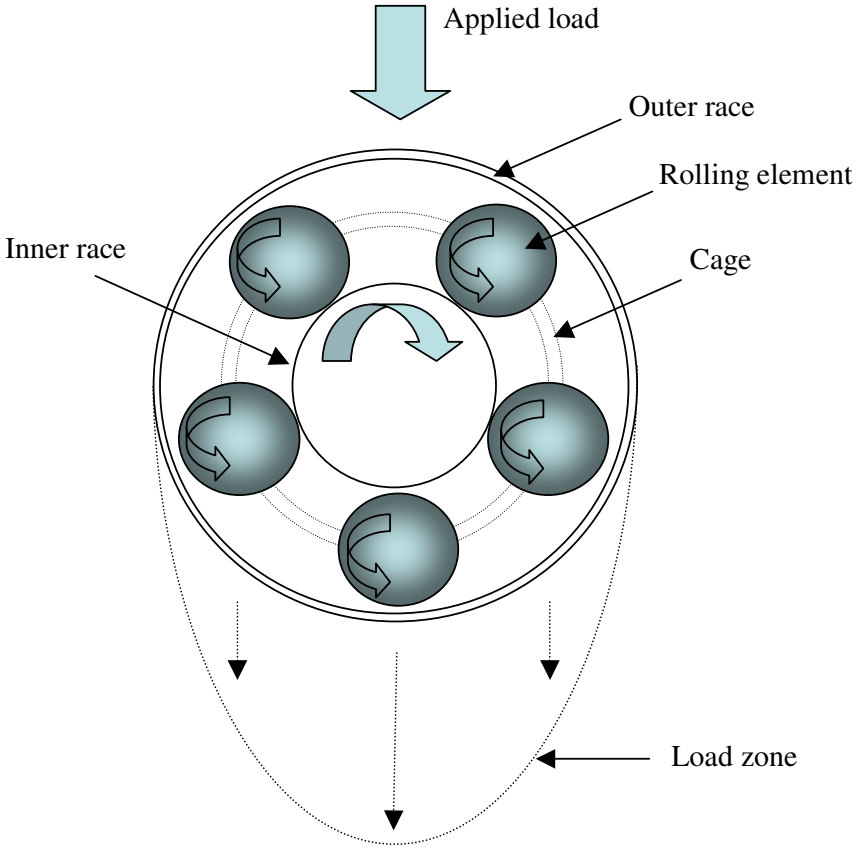

Figure 2.1 The ball bearing geometry.

The operation of a rolling element bearing is very complex, due to operational characteristics that induce repeated cyclic stresses, friction, surface deformation and wear. Therefore, in order to separate the surfaces under motion, bearings utilise a lubricating film which is developed by elastohydrodynamic (EHL) principles, discussed later in this section. The development of EHL reduces element contact, friction and wear and helps to support the appled load. Therefore, lubricant selection as well as cleanliness adds to the complexity of maintaining a trouble free operation. Further problems are associated with surface/sub-surface defects, operating temperature, speed selection and improper installation, which are described in the later sections. Thus, an unwillingness to take into account any one of these parameters will result in premature failure.

The shortcomings of friction and wear, was brought to the attention of specialists in 1964, at an Iron and Steel Works Conference organised by the Institute of Mechanical Engineers (IMechE). This meeting revealed an increase in plant and machinery failures, and resulted in the set up of a working group which called for improvements in education and research into the causes and effects of friction and wear. The first problem was to describe the interdisciplinary nature of the subject, which amongst others encapsulated the fields of physics, metallurgy and chemistry. This lead to the term “tribology”, which described the science and technology of interacting surfaces in relative motion and of related subjects and practices. In 1966 the government of the United Kingdom (UK) published the findings of the group in the renowned Jost Report [7], which estimated potential savings of £515 million per annum from the better application of tribological principles and actions. More recent findings have suggested that the economic losses from friction and wear are up to 4% of the gross national product of developed countries, about £8.5 bn for the UK in 2001, and that up to 1% of these losses can potentially be saved by the application of techniques to reduce friction and wear in machines [8].

Around this time, sensing technologies were used to monitor the health of machinery, by indicating the condition of the tribological contact. This was the inception of the modern day condition based maintenance programs which diagnose and prescribe remedial actions before machine catastrophic failures. Bearings are at the heart of these machines, where the integrity of the tribological contact is of prime significance.

The importance of bearings has been shown over the past 20 years. In the petrochemical industry, approximately 60% of all motor difficulties, such as seizures and eccentric operation, originate with bearings and 70% of all repair events show bearing problems [9]. In the U.S. air-force, 25% of machine shutdowns in aircraft carriers were due to bearing fatigue failures [10] and the Japanese Machinery Federation have reported that rolling bearing failures are consistently affect the industrial sectors [11].

Therefore, in order to identify bearing health and integrity, it is important to understand the conditions that lead to friction, distress, wear and propagating damage. This enables maintenance personnel to clarify the early warning of incipient failures and make confident assessments of the degradation processes.

2.2 Surfaces and tribology

This part of the literature review examines the bearing operating parameters such as load, lubricant viscosity and speed and their relationship with contact conditions such as contact area, pressure and deformation of the bearing surfaces.

2.2.1 Hertz theory of elastic contact

When rollers or balls interact with bearing raceways they initially contact at a single line or point. In 1881 Hertz described the dimensions of these contacts and associated contact pressures, which are described in Table 2.1. Typical mean contact pressures for bearings under field conditions range between 1.4 – 2.5 GPa [12]. However, pressures at asperity-asperity contacts have been shown to be as high as 8.5 GPa using finite element methods [13].

Contact parameter	Roller bearings – line contact	Ball bearings – elliptical contact
a = radius of contact a' = semi axis of contact b = radius of line contact	$b = \sqrt{\frac{4PR}{\pi E^*}}$	$a = \sqrt[3]{\frac{3k_1^{\,2} ePR}{4E^*}}$ $a' = \frac{a}{k_1}$
Load per rolling element, P Applied load, W Number of rolling elements, z_1 Length of roller, L	$P = \frac{5W}{z_1 L \mathrm{Cos}\theta}$	$P = \frac{5W}{z_1}$
Elliptical integral, k_1		$k_1 = 1.0339\left(\frac{R_2}{R_1}\right)^{0.636}$
Ellipticity parameter, e		$e = 1.0003 + \frac{0.5968R_1}{R_2}$
Relative radius of curvature, R (R_1 and R_2 relate to opposing surfaces 1 and 2)	$\frac{1}{R} = \frac{1}{R_1} + \frac{1}{R_2}$	
Reduced modulus, E^* (E_1 and E_2 relate to opposing surfaces 1 and 2)	$\frac{1}{E^*} = \frac{1-\upsilon_1^2}{E_1} + \frac{1-\upsilon_2^2}{E_2}$	
Mean contact pressure, P_m Max contact pressure, P_0	$P_m = \frac{P}{2b} = \frac{\pi P_0}{4}$	$P_m = \frac{P}{\pi aa'} = \frac{2P_0}{3}$

Table 2.1 Idealised contact size and pressures of line and elliptical contacts [1] [14].

2.2.2 Surface stress and the onset of yield

Under loading conditions below the yield point of the bearing raceway, elastic surface distortion takes place. However, during increased loading, there is a specific point in which the sub-surface material starts to deform plastically. In order to identify this first yield point, the Tresca maximum shear stress criterion can be adopted. If a sample yields in tension at a stress, Y, then the principal stresses are $\sigma_1 = Y$ and $\sigma_2 = \sigma_3 = 0$. Therefore, the maximum shear stress is equal to half the difference between the principal stresses which is $\frac{Y}{2}$. Thus, the Tresca criterion suggests that in pure shear the material will yield at a shear stress of magnitude equal to $k = \frac{Y}{2}$ [15].

[1] Assuming both contacting surfaces are smooth and frictionless.

Furthermore, expressions for the magnitude and depth of maximum shear stress with respect to the maximum Hertzian contact pressure are described in Table 2.2.

	Roller bearings	Ball bearings
Maximum shear stress	$\tau_{max} = 0.3P_0$	$\tau_{max} = 0.31P_0$
Depth of shear stress at first yield	$z = 0.79b$	$z = 0.4a$
Maximum contact pressure at first yield	$(P_0)_y = 3.3k = 1.67Y$	$(P_0)_y = 3.2k = 1.6Y$

Table 2.2 Load and pressure threshold for sub-surface plastic deformation according to the Tresca criterion[2] [14].

If the surface distortion is initially elastic, then the peak contact pressure is below the critical values of maximum shear and uniaxial tensile yield stresses of around 3.3k and 1.67Y. Above this threshold, sub-surface plastic deformation takes place, which is initially contained by an elastic region. The locality of the localised sub-surface stress field is shown in Figure 2.2.

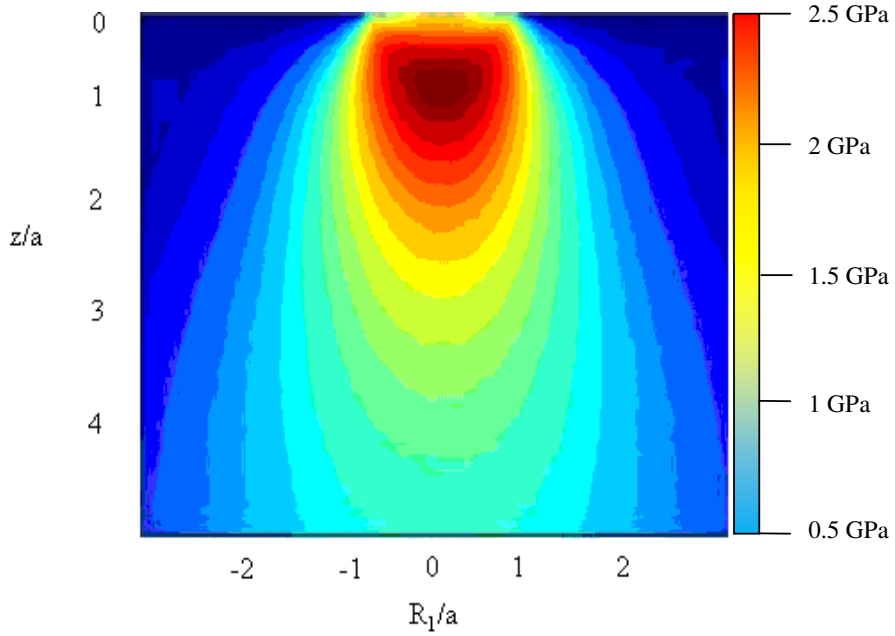

Figure 2.2 The sub-surface stress field associated with elastic deformation at the material surface [14].

[2] Assuming steel contacts and Poisson's ratio of 0.3.

As the load is further increased, the plastic region propagates to the surface, at which point full plasticity is observed. This occurs when the maximum shear stress and uniaxial tensile yield stresses are around 6.6k and 3.3Y, which is essentially the material hardness H. Empirically, from indentation tests the material hardness may be related to the yield stress by the relationship of $H \approx 2.7Y$, or when P_m>0.4H [14]. In most applications, bearing steels have typical hardness values between 700 – 800 Hv with the rolling elements up to 10% higher than the tracks [16], equating to a P_m of around 3 GPa for first yield.

2.2.3 Friction and slip

Further surface deformation mechanisms are observed during the rolling element passage on the raceway, from frictional resistance between one element moving across another. At the rolling element-inner race interface, the raceway surface material is elastically distorted to accommodate the rolling element. This causes differential movement between the roller and raceway with frictional energy dissipation during resistance, known as Reynolds slip. A further source of slip is identified in elliptical contacts and is known as Heathcote slip, which occurs to accommodate the differences in distance travelled between different points on the ball surface. Slip in the contact region has a detrimental effect on the bearing surface layers by initiating damage during sliding, with friction generated during adhesive and deformation forces, which will lead to surface initiated failures. Additional sources of sliding include contact between the cage and the other bearing elements.

2.2.4 Elastic shakedown and ratchetting

Repeated rolling and sliding in the Hertzian contact also stresses the surface material cyclically [17]. If the contact pressure is below the elastic limit, during the passing of the loaded elements, elastic surface behaviour is observed. From the Tresca criterion this is when P_0<1.67Y. However, if plastic flow is observed after the initial passing of a loaded element, residual stresses and strain hardening may develop on the raceway surface layer. After continual load passes, the accumulation of residual stresses may suppress further plastic flow which allows the following passes to be carried elastically. This is known as elastic shakedown, and occurs when 3.3k<P_0<4k. However, if the surface is loaded above the elastic shakedown limit there may be

plasticity without the accumulation of plastic strain, which is known as plastic shakedown. Above the plastic shakedown threshold the material accumulates a net strain during each cycle with surface deformation in the rolling direction, which can be observed when a ball rolling/sliding on a flat surface produces a conforming track. This is known as ratchetting [18].

2.3 Lubrication regimes

The previous section identified a number of surface deformation mechanisms during the bearing operation. Therefore, in order to separate the bearing surfaces under motion, a lubricant is entrained between the elements to form a protective film which reduces interfacial contact, friction and wear. The following section identifies the lubrication regimes and their relationship with the coefficient of friction. The coefficient of friction is then described as a function of the Sommerfeld parameter (S), i.e. load (W), speed (U) and lubricant viscosity (η). These parameters are plotted on a single graph which is known as the Stribeck curve, shown in Figure 2.3.

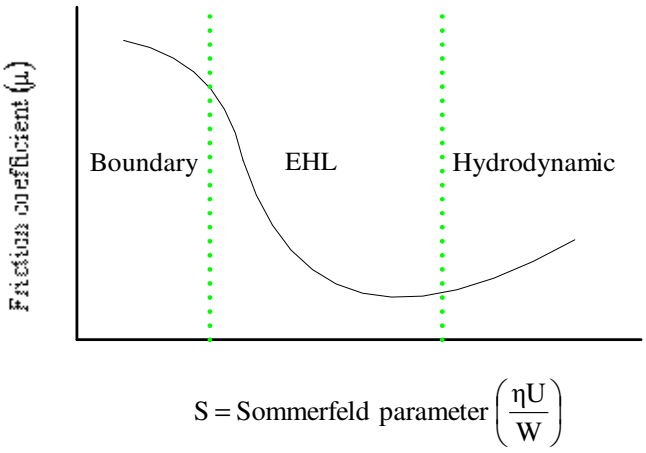

Figure 2.3 The Stribeck curve [19].

If the surface speed is increased, the lubricating film is developed hydrodynamically between the contacting surfaces. This would suggest a reduction in friction coefficient within this regime, however, an increasing trend is observed. The increasing friction coefficient trace is generated by the increased shearing action of the lubricating film at higher speeds. An increase in load leads to an increase in film viscosity during a squeeze film effect as well as elastic deformation of the surfaces. The surfaces are then elastohydrodynamically separated and yields in a reduction in friction

coefficient. Under further increasing loads the surfaces can no longer be separated by the viscous forces of the lubricating film. The increase in friction coefficient is generated by the shearing of the asperities and plastic deformation at the contact interface of the bearing elements.

2.3.1 Lambda ratio

We have seen from the Stribeck curve that the friction co-efficient (μ) depends on whether the shearing action occurs within the lubricant or at the material surface. The lambda ratio (λ) is a further expression used to identify the lubricating condition of the surfaces under motion. This parameter identifies the ratio of minimum film thickness (h_{min}) to composite surface roughness (σ) of the opposing surfaces R_{q1} and R_{q2}, as shown in Equation 2.1 and Figure 2.4. Typical composite roughness dimensions of bearing elements is around 0.2 μm [20].

$$\lambda = \frac{h_{min}}{\sigma} = \frac{h_{min}}{\sqrt{\left(R_{q_1}^{\ 2} + R_{q_2}^{\ 2}\right)}} \qquad (2.1)$$

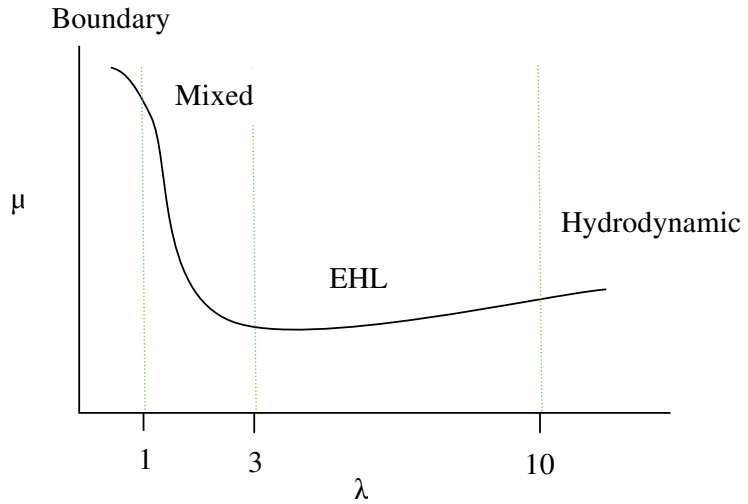

Figure 2.4 The co-efficient of friction as a function of the lamda ratio [19].

For λ greater than 10, a thick lubricating film provides surface separation under hydrodynamic conditions, producing a μ value between 0.06 – 0.08. For λ between 3 and 10, EHL conditions prevail. Considering 1<λ<3, mixed conditions initiate surface interaction at the summit of the asperities with possible fracture and plastic deformation of the asperity tips, producing a μ value in the range 0.1 – 0.2. For λ<1,

boundary conditions initiate severe contact between opposing surfaces, which results in high μ values between 0.2 – 0.3 [19].

2.3.2 Elastohydrodynamic lubrication (EHL)

In loaded bearing contacts, typical mean contact pressures range between 0.5 – 3 GPa, meaning that the contacting surfaces operate under EHL, which leads to changes in lubricant viscosity. Using hydrocarbon lubricants, the fluid viscosity at higher pressures can be as much as 10^8 times ambient conditions, so a change to a solid phase occurs in the contact [21]. The piezo-viscous lubricant behaviour can be modelled by using the Barus relationship [22], shown in Equation 2.2. Using this relationship η_o is the base viscosity at atmospheric pressure and α is the pressure-viscosity coefficient. Lubricants with high pressure-viscosity coefficients rapidly increase in viscosity, which enables the film thickness to remain relatively unchanged with increasing load. The pressure-viscosity coefficient for a mineral base oil is around $2*10^{-8}$ Pa^{-1}.

$$\eta = \eta_o \exp(\alpha P) \qquad (2.2)$$

The increased fluid viscosity enables the bearing load to be supported by the lubricating film and aids in the separation of the surface under motion, as shown by the Sommerfeld parameter. In addition to the increased lubricant viscosity, considerable elastic surface deformation increases the contact area, effectively alleviating the contact pressure, which enables an increase in the load carrying capacity of the contact. Elastic deformation of steel surfaces can be several orders of magnitude larger than the film thickness [21].

A schematic representation of the pressure distribution in an idealised rolling contact with smooth surfaces is shown in Figure 2.5. Under EHL conditions, the pressure slowly builds at the inlet and increases to maximum in the centre of the contact. Around this central region, surface elastic deformation is more significant. The pressure then begins to fall, but rapidly rises to a significant peak, and then falls to ambient pressure, due to constriction at the outlet. At high contact pressures, the EHL pressure distribution is similar to an elliptical profile generated according to Hertzian

conditions because elastic deformation dominates. However, at higher speeds the hydrodynamic effects dominate and the pressure peak is displaced towards the centre of the contact [23, 24].

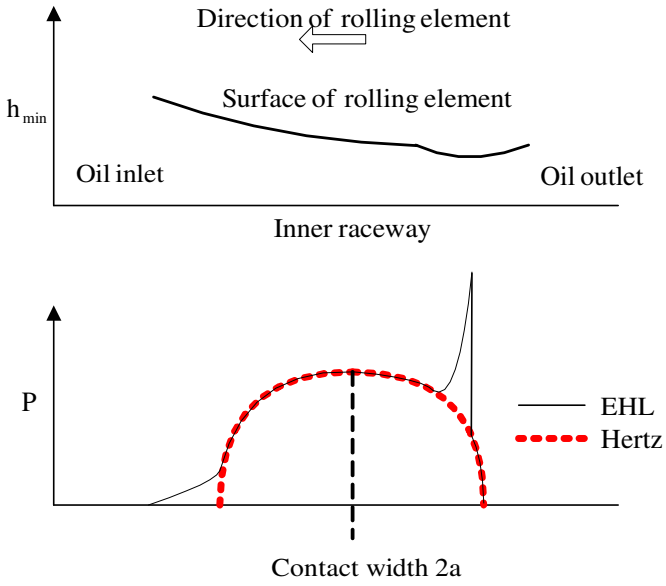

Figure 2.5 Two dimensional representation of the EHL and Hertzian contact pressure distribution [25].

Film thickness calculations have been derived by Dowson and Higginson [26] for both roller and ball bearing contacts, as shown in Equations (2.3 – 2.4). Typical film thicknesses of rolling elements are around 0.025 – 2.5 µm [19].

$$\text{Roller bearing}: \frac{h_{min}}{R} = 2.65\left(2\alpha E^{*}\right)^{0.54}\left(\frac{U\eta}{2E^{*}R}\right)^{0.7}\left(\frac{W}{2E^{*}RL}\right)^{-0.13} \qquad (2.3)$$

$$\text{Ball bearing}: \frac{h_{min}}{R} = 1.79\left(2\alpha E^{*}\right)^{0.49}\left(\frac{U\eta}{2E^{*}R}\right)^{0.68}\left(\frac{W}{2E^{*}R^{2}}\right)^{-0.067} \qquad (2.4)$$

The entrainment velocity (U), has the most significant affect on film formation due to hydrodynamic effects. The entrainment velocity, also known as the rolling velocity, is calculated as the average speeds of the surfaces under motion, where $U = ½(U_1+U_2)$. In addition, since the bearing elements rotate at different speeds there is some contribution of sliding, defined as the magnitude of the change in surface speeds,

which is $|U_1 - U_2|$. This leads to a further parameter, that indentifies the contribution of sliding to rolling (slide:roll ratio), shown in Equation (2.5).

$$S_{ROLL} = \frac{\text{Sliding velocity}}{2 * \text{Rolling velocity}} = \frac{U_1 - U_2}{U_1 + U_2} \qquad (2.5)$$

After the entrainment velocity, the pressure-viscosity effects of the lubricating film are of more significance, compared to the loading contribution, indicated by the low power laws.

2.3.3 Micro-EHL

By considering a further reduction in λ ratio, the surfaces are pushed closer together and the viscous fluid becomes trapped between the valleys of the asperities. This pressurised fluid enables the bearing load to be supported, however there is likely to be localised stress between asperities, with plastic deformation at the surface protrusions. This may result in smoothing of the surface roughness which can enhance lubricant entrainment between the elements which further enhances the load carrying capacity of the contact.

2.3.4 Boundary lubrication

Further reductions in λ ratio may initiate severe surface contact. In this case the thin lubricating film cannot separate the opposing surfaces and there is significant interaction between the asperities of the opposing elements. Element interaction results in localised stress concentrations at the surface roughness with shearing and deformation of the surface protrusions. Boundary lubrication is also experienced during start-up or shut-down of rotating machinery as a result of a low Sommerfeld parameter. Therefore, during this period contact between the opposing element roughness is observed. This results in high friction indicated by the Stribeck curve and yields in an increased wear rate, shown by the bath-tub curve which is highlighted in section 2.5.

An important consideration of boundary lubrication is the influence of lubricant formulations, i.e. base oils and additives. Anti-wear additives are employed to form

surface reactive layers that can control or reduce wear under boundary lubrication, which can prolong the life of bearing contacts [27]. The operation of the tribo-layer enables the contacting surfaces to slide over one another at the peaks of the asperity interface. However, there may be some penetration of the tribo-layer, but the contact between the bulk materials may be significantly less, compared to opposing surfaces without the tribo-layer [28-31].

2.4 Wear mechanisms

As a consequence of interfacial contact between the bearing elements, there are a number of wear mechanisms. These include abrasion, adhesion and fatigue, and are discussed in the following sections.

2.4.1 Abrasion

In section 2.3 it was shown that surface contact is suppressed by the formation of thin lubricating films. A further consideration of surface deformation involves the entrainment of contaminants/debris in the Hertzian contact. The wear debris may be generated during asperity deformation mechanisms that were described during machine start-up in the previous section. Therefore, bearing surfaces are susceptible to particle entrainment throughout the bearing life cycle. Particles that are larger than the oil film can cause damage to the surfaces. Harder debris than the contact surfaces may cause wear, compared to softer particles which may cause indentation [32]. The damaged surface acts as a region of localised stress which may lead to a fatigue initiation site, described in 2.4.3.2. Therefore, it is important to reduce particle ingression in lubricated systems. This can be achieved to some extent by filtration devices such as magnetic plugs and mesh filters. However, problems with magnetic plugs arise when non-magnetic surfaces, i.e. silicon nitride are employed, as the plug technology becomes redundant. Also, a problem with mesh filtration is the capture efficiency, which is recognised as the beta value and increased pressure drop as the mesh becomes blocked. Nevertheless, filtration is an essential part of all lubricated systems by reducing particle content in the oil-line. This has been shown by Nilsson *et al* [33], with observations of reduced bearing wear and particle generation by a factor of 10, when incorporating a 3 µm mesh filter during a 1 hour operation.

Abrasive wear is separated into categories of two and three body abrasion. Two body grooving abrasive wear occurs when a hard protuberance on one surface moves across another surface, displaces material, leaving grooves in the direction of motion [34], as shown in Figure 2.6. The hard protuberance may be an ingested contaminant, protuberance from a partner surface or debris with possible work hardening allowing penetration into the softer counterface.

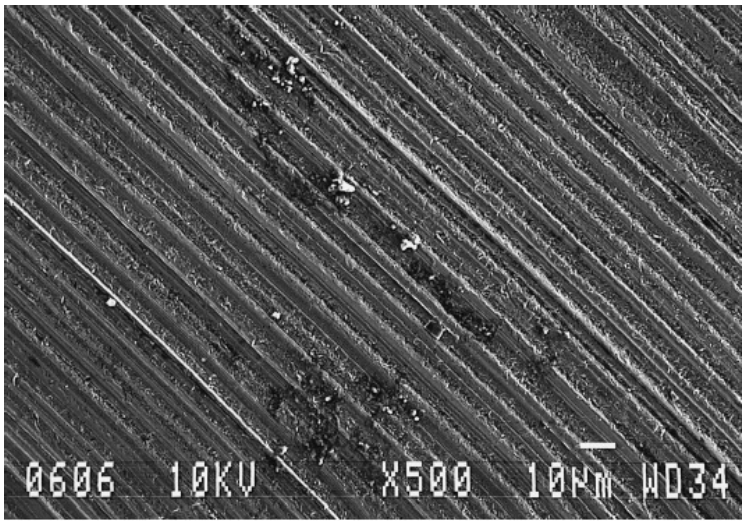

Figure 2.6 A SEM image of a worn surface of a quenched and tempered tool steel produced by microscale abrasion at a normal load of 0.25 N with a 0.0009 volume fraction (0.003 g cm^{-3}) 3 µm diamond slurry [35].

Kayaba *et al* [36] observed variations in two body (sliding or grooving) wear and described the process by using *in-situ* point scratch tests inside an electron microscope:

When the protuberance penetrates the counterface, the material in front of the protrusion is deformed and forms a curled microchip, similar in appearance to swarf generated during lathe machining. The particle type is known as cutting debris, shown in Figure 2.7 (a).

Ploughing forms a groove during sliding with high ridges on both sides. During ploughing no wear debris is formed during a single slide. However, when debris is fractured from the ploughed ridges the wear mechanisms is known as cleavage, shown in Figure 2.7 (b).

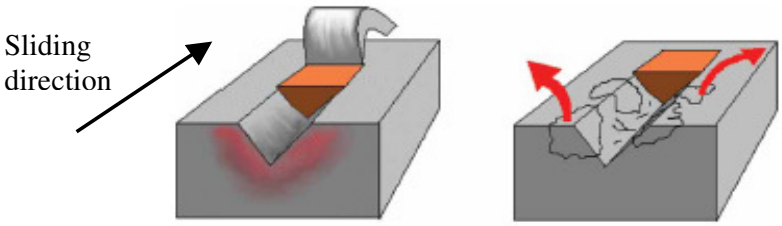

(a) *(b)*

Figure 2.7 Two body abrasive wear showing debris formation during (a) cutting and (b) cleavage mechanisms.

2.4.2 Three body abrasion

Three body rolling abrasion is initiated by wear debris or contaminants entrained between the bearing elements. The particles/contaminants roll between the opposing surfaces generating multiple indents with no directionality, as shown in Figure 2.8. The indented surface may lead to a stress concentration with possible strain hardening and fracture of the surface. This can lead to a fatigue initiation site which is a more damaging mechanism than grooving wear.

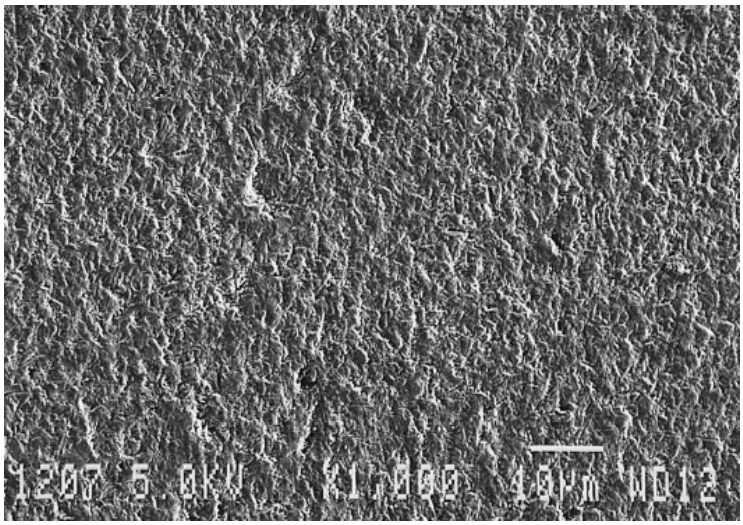

Figure 2.8 *SEM image of a worn surface of a quenched an tempered tool steel produced by microscale abrasion at a normal load of 0.25 N with a 0.237 volume fraction (1 g cm^{-3}) F1200 SiC slurry [35].*

Williams and Hyncica [37] propose a model which identifies indentation/pitting using an idealised particle as an indenter within the geometry of the minimum film thickness, as shown in Figure 2.9. When $\frac{D_1}{h_{min}} < 1$, the indenter makes occasional

impacts with the surface, with the possible generation of surface indentations induced on the surfaces.

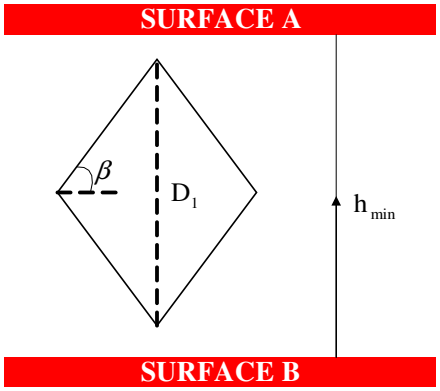

Figure 2.9 A single abrasive particle described by parameters β, D_1 and h_{min}.

Equation 2.6 describes the relationship between the indenter angle β and the ratio of minimum film thickness $\frac{D_1}{h_{min}}$. The indenter will roll freely between the surfaces to a point where $\frac{D_1}{h_{min}} \approx 1.74$, which corresponds to a β angle of 55˚. Above this angle the indenter will become lodged in a surface, causing cutting or grooving wear and can decrease bearing life by 80 – 90 % [38].

$$\frac{D_1}{h_{min}} = \mathrm{Sec}\beta \qquad (2.6)$$

Considering $\frac{D_1}{h_{min}} > 1.74$, and surfaces of equal hardness, a sequence of events described in Figure 2.10, shows the initiation of grooving. From (a-c) the indenter rotates freely between the surfaces until (d), where the indentation forces, which is the product of surface hardness and penetration area, become colinear. As this occurs, there is no impetus to continue rolling the indenter, so the particle remains stationary, causing grooving with debris removal.

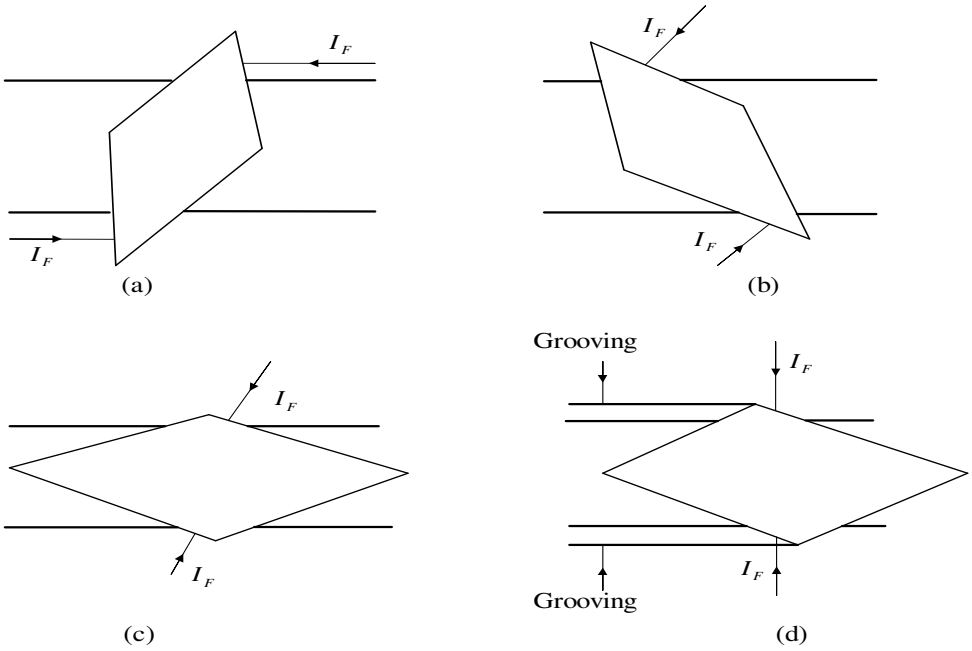

Figure 2.10 Indenter entrainment in the contact zone when $\frac{D_1}{h_{min}} > 1$ *initially causing particle rotation until equilibrium is reached and grooving takes place.*

Although abrasive wear is not the dominant failure mode of rolling element bearings, this process is still of major importance as defects, i.e. dents and scratches, on a bearing surface act as stress raisers which accelerate the dominant bearing failure mode which is fatigue.

2.4.3 Rolling contact fatigue (RCF)

RCF is directly related to the effects of stress concentrations that lead to crack initiation and propagation. As the stress (S) levels increase the number of cycles (N_1) to failure decreases, and *vice versa*, which is identified through S – N_1 curves. From sections 2.2 and 2.5 the areas of localised stress are within the sub-surface and at the material surface. The following section describes the factors that contribute to stress concentrations, crack initiation, propagation and debris liberation from the surface, which are the characteristics of RCF.

2.4.4 Sub-surface initiated RCF

If the bearing surfaces are smooth, lubricated with high λ ratios and loaded below the elastic limit, then the stress field is that due to Hertzian conditions [39]. Further sub-

surface localised stress raisers include material defects such as oxide inclusions and regions of residual stress due to heat treatments in the steel making process. An increased size and number of inclusions accelerate fatigue at decreasing stress levels [40]. However, inclusion size and number are continually being reduced due to improvements in the vacuum procedures employed during manufacturing.

High-purity steels for rolling element bearings are produced using the vacuum induction method (VIM) and vacuum arc remelting (VAR). The VIM uses steel in which the alloys are added in a melting furnace inside a vacuum chamber. The VAR method employs an electrode which is melted by an electric arc in the vacuum chamber. Both methods are then combined and referred to as VIM-VAR. In the combined method, the steel from VIM is successively remelted using VAR [41]. Bearing steels produced in this way observe a reduced number of non-metallic inclusions and therefore a reduction in initiation sites.

However, should there be a region of localised stress, there are changes in material microstructure, such as hardness, residual stress and phase transformations. Phase transformation can be identified after acid etching, which look white compared to the surrounding matrix. Accumulating plastic strain within the region of localised stress eventually leads to crack initiation. Cracks within the region of localised stress propagate under mode 2 (shear) loading due to continued cyclic stresses towards the contact surface, and eventually portions of the undermined material are liberated from the surface.

2.4.5 Surface initiated RCF

Surface originated failures are initiated at regions of localised stress, such as asperities, dents or micro-pores [42]. Surface indentation is the primary cause of surface originated failure, and debris-induced surface failure has been recognised as the predominant failure mode in rolling element bearings [43]. From the abrasive process shown in section 2.4.1 and 2.4.2, indentation may be caused by particles that become entrained in the Hertzian contact, which indent or scratch the surface and act as stress raisers. Failure initiated at any surface defect is recognised as a point surface origin. Figure 2.11 shows the passage of a rolling element on a defective bearing

raceway. As the rolling element passes the defect, mode 1 (tensile) loading gives rise to localised plastic shear deformation with crack propagation extending into the virgin metal. Crack propagation may be further accelerated in the presence of a lubricant, where increased fluid pressure between the crack faces forces the cracks to open. A further mechanism includes fluid entrapment during closure of the crack mouth which causes pressure at the crack tip [39]. Both fluid pressurisation and entrapment are generated during mode 1 loading. The cracks are driven at a shallow angle of approximately 30° by Hertzian stresses into the bulk material in the direction of the rolling element to a level corresponding to the maximum shear stress.

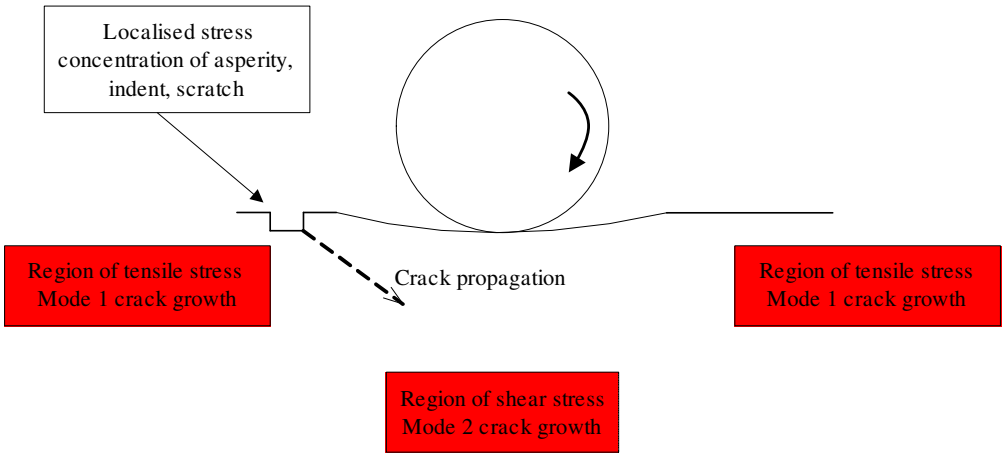

Figure 2.11 Surface fatigue crack propagation during the passage of rolling elements.

The crack growth rate is described as a function of the stress intensity factor range ΔK, which is a measure of stress intensity, strain or deformation ahead around the crack tip, indicated by the Paris-Erdogen equation [44], shown in Equation (2.7).

$$\frac{da_1}{dN} = C_1 \Delta K^m \qquad (2.7)$$

where $\frac{da_1}{dN}$ is the change in the length of the fatigue crack, a_1, per load cycles, N. The terms C_1 and m are empirical constants which are functions of the materials properties, microstructure, environment and temperature. In time the crack will lead toward the surface causing surface material to break away to form a pit. The manifestations of point surface origin failures are shown in Figure 2.12.

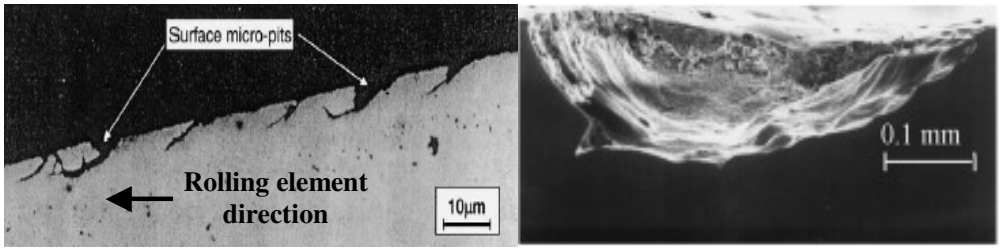

(a) *(b)*

Figure 2.12 (a) Surface crack propagation [45] and (b) a surface pit [46].

The joining of multiple pits to an area of 6.5 mm^2 [47] is known as spallation[3], which results in large, deep pits with sharp edges, steep sides and flat bases [48]. The surface spall propagates in the direction of the rolling element in a V-shape from the propagation site, which has the appearance of a "seashell" as shown in Figure 2.13.

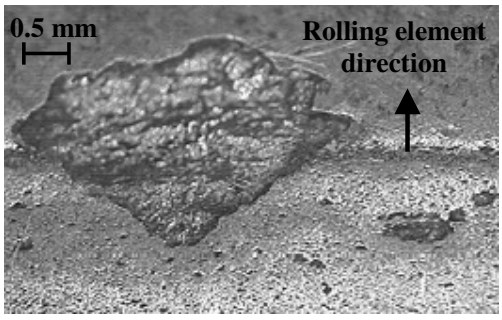

Figure 2.13 Characteristic seashell shaped surface spall [49].

When a surface spall is generated, changes in surface topography lead to further increases in contact stress which constitutes a positive feedback mechanism that drives further damage [39]. The creation of new cracks and the propagation of existing cracks causes continued and rapid deterioration with spall propagation in the direction of the rolling element. The generation of spalls does not always undermine component function. However, during continued damage, passing of the rolling elements on a roughened wear site generates increased heat and vibratory load, which may cause the internal clearances of the bearing elements to reduce, which may lead to seizure [50].

[3] 6.5mm^2 is the fatigue spall size criteria used in the laboratories at The Timken Bearing Company, since a large spalled area resulting in gross deformation makes it difficult to determine the cause of failure.

2.4.6 Bearing life prediction

In bearing lifetime tests, there is a wide scatter of results due to the stochastic nature of fatigue, because of differences in material composition and defects such as sub-surface inclusions. Early life models were derived by Weibull [51] who postulated that the probability of crack initiation, which lead to component fracture, was related to initiation sites within the volume of the stressed material. Thus, for increased stress, the greater the working volume of material and the more likely there would be a crack initiation site [52]. The Lundberg-Palmgren (LP) model followed [53], which was also based on the assumption that fatigue cracking initiates at stress raisers below the rolling contact surfaces [54]. Thus, the greater the volume of stressed material, the greater the likelihood of fatigue failure. Both the Weibull and LP models are shown in Appendix A, which are reviewed in [55]. The Weibull and LP models lead to the bearing life rating equation. The Timken Bearing Company life rating equation, L_{10}, is shown in Equation (2.8) and identifies the life that 90% of apparently identical bearings tested under the same conditions will complete or exceed in hours. In this equation C_2 is the bearing dynamic load rating, W the applied bearing load and m1 is the load life exponent which is 3 for balls and 3.33 for rollers. From this equation we see the significance of applied load and speed since doubling the applied load reduces life to one tenth and doubling the speed reduces life by one half.

$$L_{10} = \left(\frac{C_2}{W}\right)^{m1} * \frac{1.5 * 10^6}{N} \qquad (2.8)$$

Further bearing life rating calculations include adjustment factors to make more accurate predictions of life. Adjustment factors include reliability levels, material cleanliness values and lubricant-life factors [56]. These parameters are obtained from a number of tables, mainly published through the Society of Tribologists and Lubrication Engineers (STLE) and American Society of Mechanical Engineers (ASME) [57, 58].

Further considerations of bearing life and the severity of operating conditions include the DN number, which is calculated by the inner race diameter D (mm) multiplied by the driving speed N (rpm). The effect of increased bearing speed has already been

mentioned in section 2.3, which through hydrodynamic affects increases the lubricating film thickness in the contact, thus reducing surface friction and wear. However, increasing the speed increases the stress cycles and therefore decreases bearing life, as shown by the Timken life rating equation. Therefore, caution must be shown when justifying the bearing speed. The general idea of the DN number is that a specific application should be compared against the DN number provided by the bearing manufacturer. Typical DN numbers of tapered roller bearings are in excess of $2x10^6$ [59, 60], although applications which require continuous operation with minimal maintenance are operated at significantly lower DN levels. In addition, the DN number is used to justify lubrication selection. Lower DN numbers can be sufficiently lubricated by grease or oil baths, compared to higher DN numbers which are better lubricated by oil recirculation lines [61] to prohibit thermal run-off from the increased temperature generation.

2.4.7 Adhesion

In section 2.3 it is shown that bearing element separation by lubricating films restricts surface interaction, friction and wear. However, oil film breakdown initiates boundary conditions with high localised pressure, friction and temperature, generating adhesive junctions between opposing asperities [62]. Then, when the surfaces move tangentially, plastic deformation or asperity rupture occurs at a point where the shear strength is weakest. Fragments of material can then be transferred from one surface to the other or break away as debris. Stachowiaiak *et al* [63] describe the adhesive particle as irregular in shape with a rough boundary of relatively smooth surface which is interspersed with rough regions. The rough regions result from typical shear fracture between adhering layers.

First transition scuffing is the term used to describe initial asperity interaction, with contact between the peaks of the protuberances and the generation of flash temperatures. Localised heating can result in surface phase changes known ‘white layers’ which become visible during etching. White layers are formed under a number of mechanisms, including martensitic transformations, plastic deformation and thermomechanical processing [64-66]. These layers have an increase in micro-

hardness which increases the wear resistance, however the presence of microcracks during formation can lead to rapid crack propagation and delamination of the surface.

Second transition scuffing is the term used to describe the onset of adhesive wear in lubricated contacts during oil film breakdown [67]. A scuffing mechanism is proposed by Ajayi *et al* [68] during lubricated sliding. Initially, under low contact pressures the surface material deforms elastically, except at the asperities where plastic deformation and work hardening occurs. As the contact severity increases the extent of plasticity increases. This continues to a critical point when the rate of thermal softening exceeds the rate of work hardening. Plastic deformation then becomes unstable with material transfer between opposing surfaces and increases in friction with possible seizure leading to catastrophic failure.

2.5 The evolution of wear

There are a range of operating signatures generated during the bearing life, which follow particular patterns. These are reviewed by Roylance in ref [69]. One of the most familiar trends is that of the bath-tub curve, as shown in Figure 2.14, which follows the evolution of a typical bearing wear.

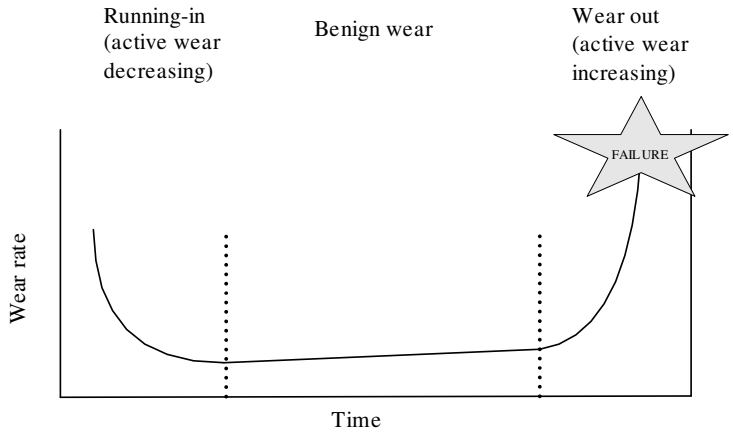

Figure 2.14 The idealised bath-tub curve.

During start-up, boundary conditions are experienced as low surface speeds prohibit the entrainment of the lubricating fluid. Then as a stable speed is maintained, entrainment of the lubricating film enables the bearing load to supported by a

combination of hydrodynamic and fluid viscosity effects. However, with thin film development there is likely to be interaction between the largest asperity peaks.

Also, under light bearing loads, the contact does not create sufficient rolling friction between the rolling elements and raceway. Therefore, the rolling elements slide along the raceway. However, under increased loading the rolling friction between the elements and raceway is increased, enabling the elements to roll between along the raceway.

The increased contact pressure results in plastic flow and fracture of the irregularities over the surface depressions [70]. Therefore, during this initial running-in period the wear rate may be quite high. As long as the Sommerfeld parameter is maintained, continual removal of the largest asperity peaks yields in a gradual reduction in wear rate and signifies a transition from running-in to benign wear, indicated by the steady state. The steady state is attained through mechanical work, which breaks down the structure of the surface material, resulting in a thin layer of short range crystalline order, known as the shear mixed layer [71]. This layer exhibits super ductility and its ability to flow when subjected to stress results in smoothing of the surface roughness which allows the bearing surfaces to conform. Smoothing of the surface roughness has a positive effect on bearing functionality, as the bearing surfaces become completely separated by the lubricating film. An increase in the λ ratio allows a normal bearing operation to prevail since the contact stresses are reduced due to the load carrying capacity of the oil-film. From the manifestations of the wear mechanisms described in section 2.5, the final stages of the remaining bearing life are identified by the transition from the steady state to the wear out period. The wear out period is identified by an increasing wear rate, which is detected by an increase in the quantity of debris. From previous work [72-74], in order to identify the earliest signs of failure an increasing quantity of sub 20 μm debris is critical, as shown in Figure 2.15.

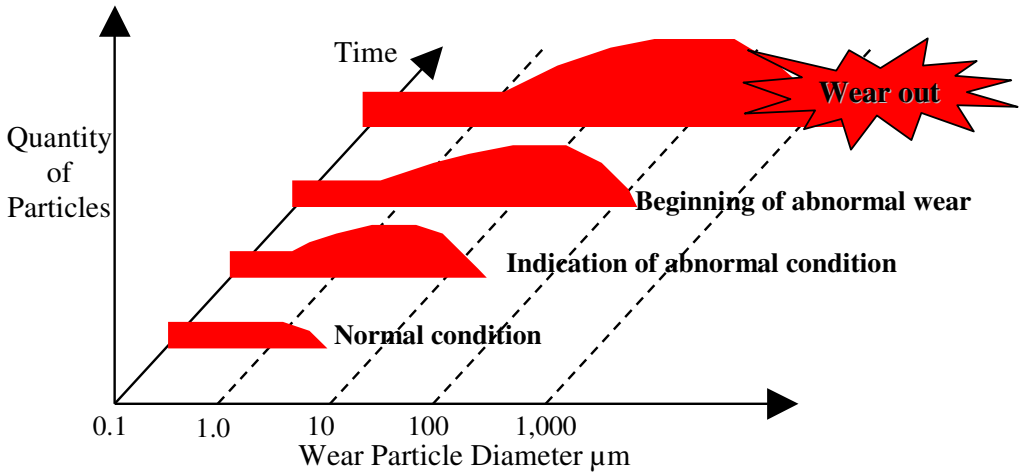

Figure 2.15 The identification of abnormal bearing wear using particle size and quantity [73].

2.6 Wear debris formation

Wearing mechanisms produce distinct particle types. Therefore, identification of particle size, shape, morphology and composition can be used identify the severity of wear, rate, mechanism and source of distress [75-81].

The following section identifies the conditions that lead to the formation of wear debris and their morphology which is used to indicate the mechanism of wear. These particle types are shown in Table 2.3.

Particle type	Description	Example
Rubbing	20 µm or smaller chord dimension and approx 1 µm thick. Results from exfoliation of a surface roughness and flaking of material from the mixed shear layer. Mostly benign wear. [3]	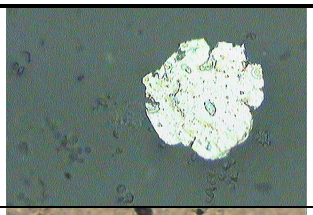
Cutting	The debris formation resembles swarf-like chips from an abrasive cutting tool action and is an indicator of contamination or component misalignment [82].	
Laminar	Around 1 µm thick, 20-50 µm chord dimension generated by the passage of debris through a rolling contact [83]. Uneven edge with holes in the surface.	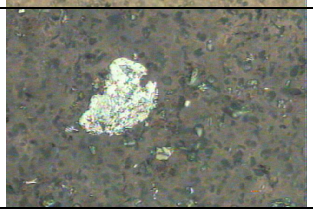
Fatigue	20-50 µm chord width, several µm thick, plate-like morphology, smooth and irregular profile. Further particles are chunky and indicate macro wear levels.	
Spheres	Usually ferrous, 1 to >10 µm diameter. Generated by rolling contact fatigue condition when micro-cracks occur. Further spheres are formed by the melting and rapid cooling of micro-portions of metal from flash temperatures. The molten material detaches and under hydrostatic pressure the spherical morphology is formed [84-86], with diameters as large a 10 µm.	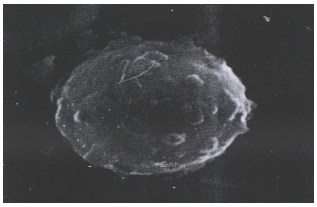
Severe sliding	Large >50 µm and several microns thick. Generated during scuffing from poor lubrication, excessive speed and load [83, 87]. Particles have striation marks from sliding with the partner surface.	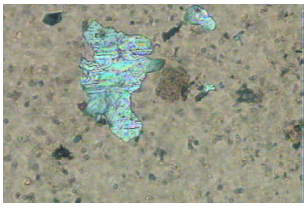

Table 2.3 No micron bars are provided in this reference [72], however the major dimension of the rubbing, cutting and severe sliding particle is 20 µm. The laminar and fatigue particle is 50 µm. The spherical particle is 10 µm.

2.7 Summary

The previous sections identify a number of operating variables including load and speed and material characteristics, such as surface roughness and yield stress. These parameters are used to justify the bearing operation in an EHL regime. The operating conditions are identified by the Hertzian contact stresses, film thickness, Sommerfeld parameter and λ calculations, which acknowledge integrity within the contact. However, during a normal bearing operation, there are a number of tribological activities, such as plastic deformation and debris formation. These activities modify the surface and sub-surface material characteristics, and these changes feed back into the contact to produce a new set of material characteristics and therefore operating conditions. Therefore, the contact is continually modified during the bearing life cycle, as shown in Figure 2.16.

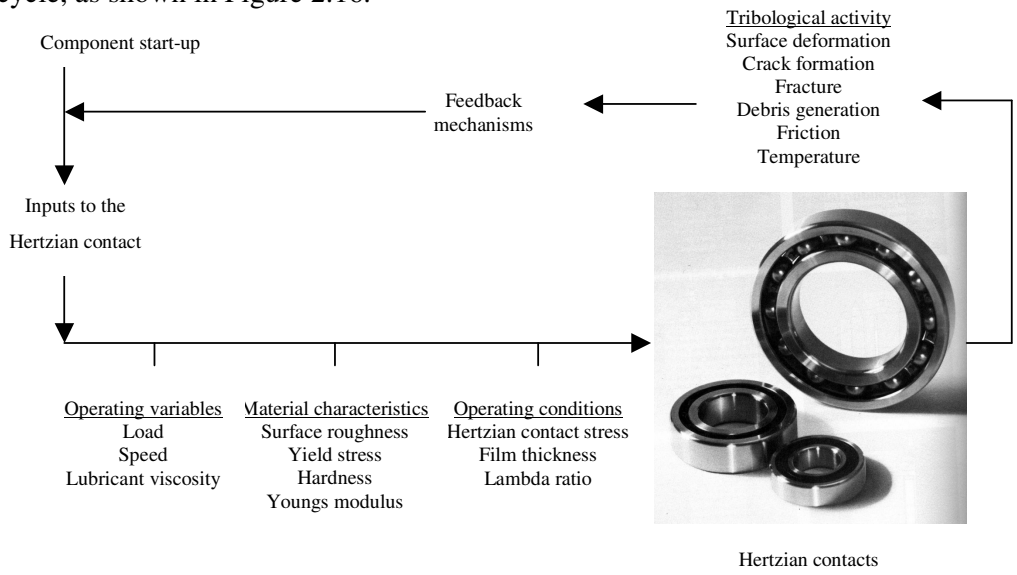

Figure 2.16 Input and output characteristics at the Hertzian contact.

Due to the difficulties in being able to monitor real time changes in material characteristics during the bearing operation, a true indication of the operating conditions is difficult to achieve. Therefore, in order to identify real time changes to the surface and sub-surface material, CM programs are introduced. This enables service personnel to make confident assessments of bearing modifications and therefore contact integrity. The use of the various CM programs is the focus of the next chapter.

3 Bearing Condition Monitoring Strategies

CM is the examination of critical engineering components such as rolling element bearings to detect the early signs of degradation before the development of major faults. This is of key importance in all bearing operations since defective elements will reduce operational efficiency and if remedial actions are not put in place, catastrophic failures to secondary equipment can occur. The purpose of this literature review is to recognise the current understanding of the important CM techniques that are being employed to identify tribological activity at rolling element bearing contacts. This chapter also introduces the current state of the art in bearing CM technologies that are being developed to identify and enhance anomalous features associated with the early signs of distress.

3.1 Introduction

Bearing CM strategies are deployed to identify operational characteristics that define the condition of the component. This involves the strategic positioning of sensors in the vicinity of the tribological contact. Some of these techniques include vibration and temperature monitoring, which are described in section 3.2. Further programmes rely on the detection of debris at remote locations from the degradation site. The detection capabilities of these techniques are also described in section 3.2. The wear debris programmes are divided into categories that include in-line, on-line and off-line particle detection and are employed based on the level of sensitivity required by the detection strategy. These processes are illustrated in Figure 3.1.

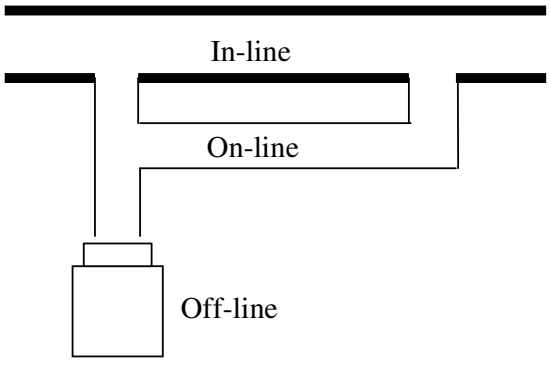

Figure 3.1 In-line, on-line and off-line debris detection.

In-line wear debris detection techniques analyse the total volume of oil that is passed through the bearings of interest. In-line systems are located downstream from the bearings and upstream of filtration devices that are situated before pumping apparatus. The advantage of the in-line techniques is that an examination of the entire oil flow is carried out, as opposed to portions of the oil flow that may be directed to other locations within the system. The disadvantage of in-line debris detection is the sensitivity of the techniques, which decreases with increasing pipe diameter and flow rate. On-line debris detection draws off a portion of the oil-flow which is then returned back into the system. The advantage of this type of analysis is that the sensing technique can be implemented to the majority of systems, without the need for adaption during the design stages, which is the case for in-line devices. However, that fact that only a portion of the oil is sampled dramatically reduces the debris detection capability of the analysis. Off-line analysis involves the removal of an oil sample which can be analysed using a varied range of technologies that have superior detection capabilities compared to the in-line/on-line strategies. However, the main drawback from off-line analysis is that a time delay in obtaining the results is produced as the oil may be sent to a laboratory far afield from the machinery under scrutiny.

In order to identify with enhanced confidence the locality, mechanism and severity of bearing wear, a combination of debris and sensor analysis may be implemented. The benefit of a multi-signature programme is explained using the following scenario. Consider a vibration sensor deployed to monitor a critical bearing in an environment which includes numerous sub-systems. The identification of increased vibration activity may lead one to believe that the critical component which is under scrutiny is operating abnormally. However, it may be that the increased vibration is the manifestations of degradation from a different system. Therefore remedial action, which involves labour costs and loss of production, may lead to the untimely removal of an efficiently operating bearing. Then consider a programme which has utilised a thermocouple and vibration sensor in the vicinity of the critical component. Now the identification of increased temperature and vibration provides machinery personnel with added insurance to the locality of the distressed component, which elucidates the decision making process in remedial action plans. A further advance on the previous strategy would be addition of an in-line wear debris detector. In this case the multi-

signature programme provides enhanced assurance to the locality, mechanism and severity of degradation. Therefore, the detection of multiple distress features can provide corroborating evidence and clarity of the wear process. However, it is not just a case of adding sensors and expecting failures to be instantaneously recognised. It is an understanding of the physics of sensor excitement and reliability of the technology that must be understood, in order to optimise the identification and earliest signs of degradation.

3.2 Condition monitoring techniques

3.2.1 Vibration

Vibration analysis is probably the most widely used examination carried out to identify bearing health, due to the simplicity of operation and experience gained from a vast number of years in numerous applications. During EHL and hydrodynamic conditions, bearing surfaces are kept apart by the lubricating film. Therefore, the vibration levels are minimal and consistent. However, displaced rotors and distressed surfaces prohibit functionality, which can lead to impacts between the opposing elements. The impacts then induce vibrations to the surrounding structure. Therefore, vibration sensors located in the vicinity of distressed elements make it possible to monitor the locality and severity of component distress.

Before implementing vibration technologies to successfully monitor the bearing condition, there are some basic rules to follow. The first is the selection of the transducer (see sections 3.2.2 – 3.2.4) that is effective in identifying the fault. The selection is largely dependent on fault and bearing type. Journals are monitored for displacement events such as imbalance, which occur at low rotational frequencies that are typically around 1.5 kHz. Velocity transducers identify events in the mid-frequency range, which is up to 3.5 kHz and includes rolling elements bearing faults such as looseness. High frequency events of up to 20 kHz are monitored using accelerometer pick-ups, and have been employed to identify the excitation of structures coupled to the rotating assemblies.

Some further issues relating to vibration sensing are concerned with the locality of the sensor relative to the contact zone. In some cases it may not be feasible to locate the sensor close to the bearing contact area because of a lack of space in the vicinity of the bearing. This can also lead to interference from machinery in close proximity to the sensor or vibration attenuation as the distance form the sensor increases. The following section provides further details on the operation of the different types of vibration sensor.

3.2.2 Displacement

Shaft/journal displacement can be monitored by non-contact proximity probes. This technique utilises eddy current technology to monitor power losses, from changes in the magnetic field in the vicinity of the probe tip, generated by conductors (shafts/journals). The change in magnetic field is then calibrated to shaft distance relative to the probe tip, from which displacement can be monitored [88]. On less critical equipment a single probe may be sufficient to monitor radial displacement, however on more important machines, two probe outputs, shifted by 90°, are installed to monitor horizontal and vertical displacement. The probe outputs are then coupled to an oscilloscope, and when combined with a keyphasor signal, rotor position and migration through the bearing can be identified by the generation of an orbit. Orbit eccentricity, phase measurements and vibration levels are then used to indicate displacement problems such as misalignment and unbalance. The advantage of the displacement pick-up is that they have an accurate low frequency response up to 1.5 kHz [89].

3.2.3 Velocity

Velocity is the first derivative of displacement and is the rate of displacement change, or the speed of vibration. Some velocity pick-ups use a suspended magnetic core surrounded by a coil of wire. Core motion in the mid frequency range between 3 – 3.5 kHz produces a voltage proportional to velocity, which is utilised to identify major mechanical and installation defects such as misalignment and looseness [90, 91]. However, these systems are unreliable in the vicinity of magnetic fields. Other velocity sensors use piezoelectric crystals that are coupled to a mass and produce an

output proportional to acceleration. The acceleration signal is then integrated to identify the velocity of vibrations.

3.2.4 Acceleration

Accelerometers monitor the rate of velocity change, using piezoelectric crystals coupled to a mass. When the crystals are displaced or squeezed, an electrical output is generated which is proportional to acceleration. The major advantage of the accelerometer is the high frequency detection capability, of up to 20 kHz, which makes it possible to identify rolling element surface defects, such as debris entrainment and surface spalls. This makes the accelerometer the sensor of choice for monitoring rolling element bearing distress.

Williams *et al* [2], used accelerometer root-mean-square (RMS) trending to monitor roller bearing wear. A normal operation was identified by a consistent acceleration trend that indicated steady state conditions. During surface failure, acceleration levels increased, decreased and then further increased. The initial increase was accredited to the appearance of spallation. The subsequent decrease was attributed to smoothing of the sharp edges of the damaged zone by continued over rolling at the contact. The further increase was identified as damage propagation. Post bearing inspection revealed that spalling had propagated to one-third of the inner raceway.

Throughout the literature, accelerated bearing failures by overloading and artificially induced defects, on full scale bearings and laboratory based tribometers have utilised accelerometers to monitor spall initiation and propagation [50, 92-94]. The consistent conclusion is that a good correlation is observed using RMS accelerometer trending to identify spall initiation and progressive wear, which is justified from post test imaging of the wear site.

3.2.5 Frequency Analysis

Further analysis looks at the frequency spectra of the time varying signal from which energy excitation at the bearing defect frequencies can be monitored. This provides a measure of the locality and severity of distress at specific bearing elements [95-101]. Conversion of the time to frequency domain can be performed with the Fast Fourier

Transform (FFT). The bearing defect frequencies may also be calculated from the bearing geometry and operating speed, shown in Equations (3.1) - (3.4) [102]. In this analysis ω_s is the shaft speed in Hertz, d_r is diameter of the rolling element in metres, D_b is the pitch diameter in metres, z_1 is the number of rolling elements and α_1 is the contact angle in rad s^{-1}.

$$\text{Outer race} = \omega_{od} = z_1\omega_c = \frac{z_1\omega_s}{2}\left(1 - \frac{d_r}{D_b}\text{Cos}\alpha_1\right) \tag{3.1}$$

$$\text{Inner race} = \omega_{id} = z_1(\omega_s - \omega_c) = \frac{z_1\omega_s}{2}\left(1 + \frac{d_r}{D_b}\text{Cos}\alpha_1\right) \tag{3.2}$$

$$\text{Rolling element} = \omega_{re} = 2\omega_b = \omega_s\left(\frac{d_r}{D_b}\right)\left(1 - \left(\frac{d_r}{D_b}\right)^2 \text{Cos}\alpha_1{}^2\right) \tag{3.3}$$

$$\text{Cage} = \omega_c = \frac{\omega_s}{2}\left(1 - \frac{d_r}{D_b}\text{Cos}\alpha_1\right) \tag{3.4}$$

3.2.6 Shock pulse method (SPM)

SPM is a further frequency technique that uses a piezo-electric accelerometer, tuned to a resonant frequency of around 32 kHz [102, 103]. Vibrations then generated during bearing distress may then be detected by the transducer. The amplitude of the shock pulse is then normalised with an initial shock pulse value of a normal bearing operation, to provide an indication of the severity of damage.

3.2.7 Acoustic emissions (AE)

AE are defined as transient elastic waves generated from a rapid release of strain energy within or on the surface of a material [104]. Sources of AE include sub-surface cracking and propagation [105], phase changes [106] and asperity contact [107]. Therefore AE technology provides a platform that may be used to monitor the early signs of tribological damage, as opposed to surafce spalls, which are the result of the final stages of bearing fatigue failure.

Transient acoustic waves originate from a single point and fill the material whilst bounded waves propagate within the boundaries of the material after impacts at the surface. Acoustic waves are made up from a wide spectrum of frequencies (broadband). Waves travelling through a medium in which the material boundary is much larger than the acoustic wavelength are known as bulk waves. There are two types of bulk waves, which are longitudinal (compressional) and shear (transverse). Longitudinal waves travel as a series of compressive and rarefactions in the direction of propagation and shear waves have motion perpendicular to the direction of propagation.

Additional waveforms include surface waves, where the maximum amplitude is at the surface and decays as the distance from the surface increases. Surface waves include Love waves, in which the direction of propagation is parallel to the surface or Rayleigh waves, where the direction of propagation is perpendicular to the surface. Since AE sensors are typically mounted on the material surface, Rayleigh waves are most commonly detected.

AE detection is by a piezo-electric transducer that converts the propagating acoustic pressure wave, in the frequency range of 25 kHz-1MHz [108, 109], into an equivalent electrical signal. These signals are categorised into burst, continuous and mixed modes [110]. Burst activity takes the form of a discrete transient, where the waveform is approximated to that of a decaying sinusoid, typically detected during the release of energy from crack initiation and propagation [111]. Continuous signals are those which result in the overlapping of multiple burst signals monitored over longer periods of time, and have been used for the identification of rubbing surfaces [112], loose parts [113], speed [114] and load changes [115] of rotating machinery. Mixed mode operation is a combination of continuous and burst, where the burst activity is superimposed amongst the continuous signal.

Sensor attachment plays a pivotal role in detecting tribological acoustic activity. A thin layer of fluid is placed between the sensor and surface to reduce attenuation, as a sensor mounted onto a surface will only contact at the asperity tips. The fluid then enables the pressure wave to be more successfully transferred between the surface and sensor. A procedure adopted in the identification of signal attenuation is the Hsu-

Nielsen source test which manufactures an acoustic wave with the breaking of a 2H pencil lead of 0.5mm diameter which is broken at predetermined locations within a system [1, 116]. These tests are a means of identifying suitable locations of sensor placement and comparing sensor performance [117].

Once detected, the AE signal is represented by various signal parameters that include RMS, amplitude, energy, counts and frequency spectra. Most of these parameters are shown in Figure 3.2.

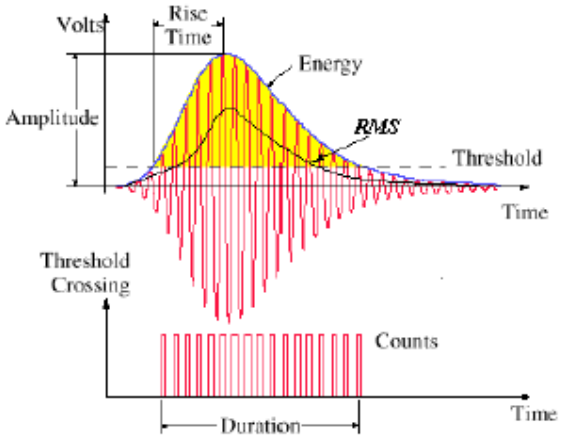

Figure 3.2 AE parameters used to identify bearing distress [118].

Hits, also known as counts and ringdown counts are related to the number of times a signal exceeds, and then returns below a threshold. A suitable threshold must be applied as a low threshold will continually monitor background noise, whilst a high threshold may not enable the acoustic wave generated during material distress to cross the threshold. The method of justifying the AE threshold is explained in the experimental section 4.1.6.

Peak amplitude describes the magnitude of an AE signal in decibels (dB). The peak amplitude measurement compares the output signal from the piezo transducer to a reference signature of 1 V excitation per micro-bar pressure. This procedure is described by the ASTM E976 standard, which employs a calibration transducer in a face to face orientation and is shown in Appendix C.

AE energy indicates the energy bounded by a signal within a specific time period. Energy measurements are taken from the area under the acoustic wave. However, it is assumed that there is no noise voltage, otherwise the integral will be infinite [119].

3.2.8 Time domain

Some of the difficulties encountered during AE sensing are similar to those experienced with accelerometers. The problems include the location of the sensor positioned at large distances away from the bearing contact, which results in signal attenuation from the contact area. Further difficulties include threshold selection and filtration, since high settings reduce the opportunities for AE detection, whilst low settings can mask the identification of AE generation during the fault. An additional problem is the linking of the tribological event with the monitored AE parameter, since a number of competing tribological events occur at the same time.

After consideration of the above problems, Yoshioka and Fujiwara [120] carried out tests out on a thrust bearing using a pin-on-disc (PoD) configuration to identify crack initiation and propagation. Crack initiation was identified using the AE counts parameter and the time to spallation was determined by increased RMS acceleration levels. These results show that the AE events were 6 minutes before the increased acceleration levels, which was thought to indicate crack propagation time. Further tribometer tests [121] involved overloading, in which the RMS parameter was found to be sensitive to contact failure, and oil starvation strategies in which the RMS parameter identified adhesive wear [122].

AE sensors have been employed to identify seeded faults on bearings, introduced to simulate defective elements. Choudbury [123] induced line defects on a bearing inner race and roller and showed that increasing the defect width produced an increase in the number of event counts and peak amplitude. Al-Gamdt [124] monitored smooth, point, line and large rough defects on the outer raceway of a roller bearing under various speeds and loads. Correlations were made against defect free surfaces. These results indicated that the source of AE was impacts between the defect protrusions as a smooth defect could not be distinguished between the defect free surface. The

remainder of the defects showed that as the defect size increased the RMS and peak amplitude increased.

3.2.9 Frequency domain

According to Mba and Rao [125], observations of the frequency spectrum have had little success, primarily due to the broadband frequency excitation associated with bearing distress. However, a good example of frequency association with tribological events, was shown by Price [110] using a lubricated 4 ball tribometer. Test results highlighted running-in wear, scuffing and recovery, which were corroborated with friction measurements. During running-in, low friction was observed with dominant frequency excitation around 25 kHz. During scuffing, a rapid increase in friction correlated with increased energy at the frequencies between 25 kHz – 825 kHz. During recovery, the dominant frequencies were between 25 – 100 kHz. Further interest in the frequency spectra was observed during rolling tests by the same author. At the start of the test, the main frequency activity was between 200 – 210 kHz. However, as the steady state prevailed, increased energy was detected between 180 – 230 kHz. Post-test SEM analysis of transverse sections of the surface identified the formation of surface pits approximately 1 mm in diameter and 0.5 mm deep, which were though to be the source of the increased frequency activity.

3.2.10 Thermography and thermocouples

Thermocouples provide important bearing analysis since increased temperature is an indication of interfacial surface contact and wear. Furthermore, lubricant viscosity is a function of temperature, and an increase in temperature will reduce lubricant viscosity, leading to reduced film thicknesses. The effect of thinning films can lead to increased surface interaction, friction and wear. Temperature measurements are taken by thermocouples positioned on the outer race of bearing elements and in lubrication lines. The key driver in identifying an abnormal bearing operation is the confirmation of steady-state temperatures that identify a normal operation. This enables deviation form the steady-state to be related to distress. According to Neale [126], abnormal temperature levels are around 10°C above the baseline.

A further method of monitoring temperature is through thermography, which is a non-intrusive method of identifying infrared radiation to monitor temperature readings and thermal patterns. A thermography programme periodically monitors and records temperature to provide a trend. After baseline levels have been observed by consistent temperature levels, deviation from the normal condition may be an indication of bearing faults such as misalignment, looseness and spallation [127-129].

3.2.11 In-line wear debris detection

As a consequence of bearing degradation, the wear debris becomes entrained in oil recirculation lines. Therefore, in-line wear debris detection presents a real time opportunity for the identification of bearing deterioration [130], by detecting particle quantity, size and composition. The following section provides an overview of their operation and capabilities.

3.2.12 Inductive

Inductive sensors monitor disturbances in the magnetic field of a coil by the passage of metallic debris through the coil assembly. Ferrous particles increase the inductance of the coil due to their high permeability and non-ferrous particles reduce inductance due to eddy currents induced on the particles. Thus, the phase of the output signal for ferrous and non-ferrous particles is opposite, which enables a distinction to be made between the different wear materials. For ferrous metals the amplitude of the signal is proportional to particle mass and for non-ferrous materials the amplitude is proportional to particle surface area.

Therefore, since debris detection is dependant on particle mass and area, this makes it difficult to effectively calibrate these technologies according to actual debris size. This problem was clearly demonstrated by Greenfield [131], where a steel sphere of 250 μm diameter has a mass of 0.064 mg. However, a typical fatigue flake with a major chord dimension of 250 μm and an aspect ratio of 10:10:1 has a mass of 0.012 mg and a further particle with the same chord dimension but with an aspect ratio of 10:1:1 has a mass of 0.0012 mg. Therefore, varying outputs are produced from particles which appear to be of the same size. This makes it difficult to obtain a true representation of the actual debris in the oil-line using this technique. Nevertheless,

inductive sensors continue to be used as they are easily implemented into oil scavenge lines, and provide a real time evaluation of wear. The commonly accepted sensitivity levels for inductive technologies is around 100 µm [132] for ferrous debris and around 250 µm for metallic non-ferrous debris [133]. Whittington [134] used a 16 mm diameter bore and achieved particle detection of rectangular steel flakes which were 200 µm on each side, whilst Miller *et al* [135] used a 12.7 mm diameter bore sensor on the Pratt and Whitney F119 engine to achieve detection of 125 µm spherical particles.

Further problems associated with inductive debris sensing include events during the onset and propagation of spallation. During these periods, the debris is removed from the wear site as a concentration of debris as opposed to individual particles. Therefore, the magnitude of the inductance change at any instant is likely to be the contribution of a number of particles in the coil assembly at that particular time. This concept has been exploited by Chambers *et al* [136] who introduced an electromagnet prior to the inductive coil to trap a concentration of debris. The electromagnet was activated for 30 seconds, and once deactivated the build up of debris are propelled through the coil arrangement. The magnitude of the inductance change provided an indication of a collective particle mass which provided a positive indication of machine wear. Additional problems relate to the detection efficiency, which is inversely related to bore size, therefore making inductive sensing unsuitable for large scale bearing applications that require large diameter scavenge lines.

3.2.13 Ferromagnetic

Ferromagnetic systems incorporate a permanent magnet in the scavenge line for the attraction of ferrous debris. Upon capture and accumulation, the change in magnetic flux is converted to an electric output signal which is associated with wear debris production [137].

Metallic lubricant borne debris detection by the inductive and ferromagnetic sensors rely on the magnetic properties of particles to identify wear. However, ceramic materials are replacing metallic elements due to improved material properties such as hardness, elevated operating temperatures, wear resistance and weight reduction,

when compared to conventional bearing steels [138]. These ceramic bearing materials, mainly silicon nitride, have no magnetic properties so inductive and ferromagnetic technologies are redundant when applied to these materials.

3.2.14 Off-line debris condition monitoring

In the previous section it was showm that the advantage of inductive technologies is the real-time identification of wear. However, it is also shown that the disadvantage is sensor sensitivity, which is around 100 µm. Therefore, one of the most widely carried out condition monitoring strategies is off-line debris analysis, due to the range of analysis that can be carried out on the oil sample. The off-line analysis provides enhanced sensitivity to the particle range of interest, which is sub 50 µm, if the earliest indication of the abnormal condition is to be identified. Further motivation behind the oil analysis programme is that the severity, rate, mechanism and source of wear can be identified though particle size, quantity, morphology and composition. In addition, the debris is a direct product of wear, as opposed to secondary signatures such as vibration and temperature, which are a consequence of wear. However, the disadvantage is that the samples may be shipped to far afield laboratories, therefore producing a time delay for results. The various laboratory based tools are described in the following sections.

3.2.15 Debris capture for off-line analysis

Techniques used for the capture of wear debris for off-line analysis are magnetic plugs, filters, drain points and pumps. A consideration of the analysis is the sampling time. Justification of the sample time comes from accentuated in-line sensor activity, indicating possible distress, and a time when the oil sample must be taken. The in-line activity is then used with the off-line analysis for corroborating evidence of wear. However, as for identifying the abnormal condition using the in-line techniques, off-line analysis also requires identification of the normal condition, for comparison and trending. Sampling times can also be justified using the bearing life rating calculation. If bearing life calculations or previous experience indicates a life of 10000 hours, then clearly sampling every 24 hours will yield in an expensive programme, and a less frequent analysis would be sufficient. Therefore, a combination of factors

incorporating expectations of bearing life, cost and criticality of the equipment determines the sampling frequency.

3.2.16 Ferrography

Ferrography is an off-line debris technique that was developed in the 1970's to find a cost effective method of determining the condition of the lubricant from jet engines [139]. This method separates ferrous wear debris according to size and non-magnetic contaminants such as sand or dust. The ferrograph, shown in Figure 3.3, is obtained by pumping the debris contaminated oil sample over a glass slide which is set at an incline. Beneath the glass slide a permanent magnet develops a high gradient magnetic field that runs the length of the ferrogram. Large particles are deposited at the entry region of the ferrogram and smaller particles further down the slide. The slide is then analysed under a microscope to identify particle concentration, size and morphology, to indicate the severity and mechanism of wear. Quantitative data is determined through a single parameter known as the severity index, I_s, which identifies the square of the optical density difference between the fractional area covered by the large (AL) and small (AS) particles. In this research, large particles are $> 15\ \mu m$ and small particles are $< 5\ \mu m$ [140, 141]. These particle sizes are also related to ISO 4406 which identifies 5 µm and 15 µm as the key sizes in evaluating contamination; 5 µm indicating non wear products such as silt and 15 µm related to wear effects [142]. Justification of this technique comes from the fact that during abnormal wear the ratio of large to small particles increases dramatically [143-147]. Derivation of the severity index is shown from Equations $(3.5-3.7)$.

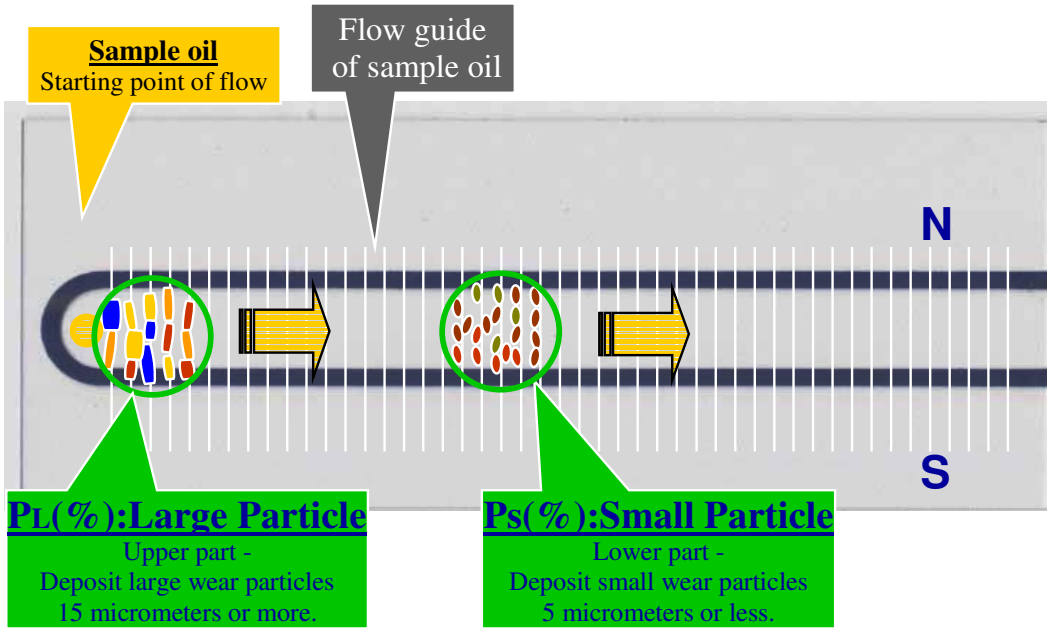

Figure 3.3 The identification of large and small particles during ferrography.

$$\text{Total wear} = \frac{\text{AL} + \text{AS}}{\text{Oil sample}\,(\text{ml})} \tag{3.5}$$

$$\text{Abnormal wear} = \frac{\text{AL} - \text{AS}}{\text{Oil sample}\,(\text{ml})} \tag{3.6}$$

$$\text{I}_\text{S} = \frac{(\text{AL} + \text{AS})(\text{AL} - \text{AS})}{\text{Oil sample}\,(\text{ml})} = \frac{(\text{AL}^2 - \text{AS}^2)}{\text{Oil sample}\,(\text{ml})} \tag{3.7}$$

3.2.17 Spectrometric oil analysis programme (SOAP)

Spectrometers have been used for the identification of wear metals in lubricating oils for approximately 50 years [148], in army oil analysis programmes (AOAP) and the naval/air forces in joint oil analysis programmes (JOAP). A common type of spectrometer uses the inductive coupled plasma (ICP) technique [149]. The ICP operation delivers a contaminated oil sample in spray form to a plasma. The debris in the sample is excited and emits light at a specific wavelength which is indicative of the contaminant element [150].

The advantage of SOAP is that both magnetic and non-magnetic elements are characterised. This enables the identification of the wear source, i.e. iron from bearing raceways, aluminium from reciprocating engines or copper from valves. However, the limitation of SOAP is that it is not sensitive to particles which are greater then 8 μm [151]. The wear elements are measured in parts per million (ppm) of the oil sample. Akagaki and Kato [152] identified abnormal journal bearing wear from increases in I_s and iron using SOAP. Further work by Jones *et al* [153] showed the I_s to be more sensitive than SOAP, as most of the iron element concentration were barely within the detection limits of the spectrograph. However, high levels of iron were detected during an advanced stage of degradation.

3.2.18 Optical Techniques

Additional off-line debris systems utilise optical techniques, such as the high accuracy (HIAC) portable oil diagnostic system (PODS) [154]. This device operates on the light extinction method, where the passage of debris through a light source casts a shadow on a photo-detector. The shadowed area for each particle is then converted to an electrical signal which is representative of size. The debris is then counted in bins according to National Aerospace Standard (NAS) 1638. The bin sizes range between 5 – 15 μm, 15 – 25 μm, 25 – 50 μm, 50 – 100 μm and particles greater than 100 μm to concentrations of 90000 particles per ml.

Odahara *et al* [154] used the PODS and I_s to monitor journal bearing wear. During benign wear, consistent debris counts were observed from all sub 100 μm bin sizes by the PODS which correlated with I_s values close to zero. The steady-state trends indicated a normal operation. However, during abnormal wear, a rapid increase in the detection of 5 – 50 μm debris was detected by the PODS which correlated with a rapid increase in the I_s to a maximum value of 70.

3.2.19 Expert systems (ES) and Neural networks (NN)

Optical techniques are incorporating decision making algorithms. These algorithms identify the severity and mechanism of wear, based on IF-THEN statements that relate to particle morphology, length, area, aspect ratio and surface texture [155-157]. Sperring and Nowell [158] and Xu *et al* [159] catalogued debris according to the wear

mechanisms of severe sliding, fatigue and cutting wear, generated from four ball, pin-on-disc and gear tribometers. The database was then used as a reference to provide an objective assessment of the wear mechanism from any tribological system.

An extension of the ES is the implementation of NN. One system that utilises the NN is Lasernet Fines (LNF) [160]. LNF is an off-line optical particle monitoring device developed at the American Naval Research Laboratory. This approach also operates on the light extinction method, which transmits a light pulse through a flow cell of approximately 90 µm. The thin glass flow cell was adapted to eliminate particles overlapping, as the large particle image would indicate a severe wear condition. Using magnifying optics, debris images are captured by a charged coupled device (CCD) video camera and stored in computer memory. Each image is then analysed to identify individual debris features such as size, morphology and striations. The debris features are then used as inputs to the NN, to classify the particles according to wear regimes of cutting, fatigue, severe sliding and non-metallic debris. A further wear particle classifier was developed by Roylance *et al* [161, 162], known as a computer-aided vision engineering (CAVE) system. The CAVE system identified the particle outline and curvature parameters, which were again processed in a NN to classify the wear mechanism.

NN have also been employed to monitor bearing surface integrity, in which multiple sensor features, mainly using vibration data sets, are used as inputs to the algorithms [163-165]. Li *et al* [166] used simulated vibration bearing defect frequency data to identify bearing inner and outer race faults. The same author then used vibration data generated from full scale bearing tests and utilised signal averaging, shaft, inner and outer race defect frequencies, which again identified inner and outer race faults [167].

3.3 Condition monitoring programmes

Further decision making programmes are employed to elucidate a range of tribological failures in any system. One such procedure is the failure modes and effect analysis (FMEA) [168, 169]. The FMEA ranks the severity, occurrence and detection capabilities of individual failures, which increases in significance between 1 – 10. The product of these assessments then produces a risk priority number (RPN), which

highlights the failures that need more attention than others. Further methods of structuring failures include root cause analysis (RCA), in which contributing factors to a fault leads to the root cause of the problem [170]. Similar investigations include fault tree analysis (FTA), in which a path from the failure to the cause of the fault is produced via a decision tree which is based on AND/OR decisions [171]. These structures were the precursors of the modern day computerised management systems (CMMS), which enhance, clarify and corroborate failure detection.

3.3.1 Health usage and management systems (HUMS)

The combination of in-line, oil-line, off-line analysis, decision making algorithms and condition monitoring programmes are utilised collectively to justify, corroborate and enhance failures across a multitude of machine contacts. These techniques can be found in HUMS, which resulted from monitoring needs in response to increases in transport helicopter accident rates [172]. A HUMS programme incorporates in-line health assessments by the measurement of operating parameters that include time, cycles, load, oil consumption, temperature and vibration, from engines, gearboxes and rolling element bearings [173]. The in-line information is then used by ground maintenance personnel, where abnormal sensing features, such as those that exceed predetermined thresholds, are used to initiate off-line analysis such as wear debris and oil inspections. The onboard and off-line assessments are also used by ground personnel, where further advanced processing includes NN, ES, sensor fusion, and feature extraction. The corroboration of in-line, off-line and advanced architectures are then used to enhance servicing, repair, overhaul, safety and air worthiness issues [174].

In addition, to the range of evolving condition monitoring practices and processing strategies, there is a constant drive for improvements in sensor technology to reduce size, weight, power consumption with increased sensitivity. One such technology that resulted from these needs was electrostatic charge sensing.

3.4 Electrostatic condition monitoring

Over the past 10 years a relatively new condition monitoring technique has been under development which is based on electrostatic charge. This technique was

originally employed for the detection of debris in the gas path of jet engines and gas turbines [175, 176]. A healthy engine has a charge level that varies with operating conditions, which identifies the normal condition. However, debris ingested at the intake has an associated charge which may dominate the baseline levels. The discrimination of accentuated charge from the normal levels is then related to foreign object ingestion and is the basis of the Ingested Debris Monitoring System (IDMS). Additionally, an Engine Distress Monitoring System (EDMS), identifies charge associated with debris present in the exhaust path, produced by deterioration and engine faults [177]. A combination of IDMS and EDMS has then been applied to identify consequential damage caused by debris ingestion, blade rubs and combustor degradation [178].

This has lead to development work which has sought to adapt electrostatic sensing as a technique to monitor tribological activity in dry and lubricated tribo-contacts. The following sections describe the concepts and contributing factors of charge generation and detection. Of particular interest is the viability and capability of the technique, compared to technologies that are currently being used to identify bearing wear. This may provide machine service personnel with a viable alternative or complimentary scheme in monitoring the earliest signs of bearing distress. The following section provides an overview of the development of electrostatic sensing over the past decade.

3.4.1 Principles of electrostatics

The most basic charged object is that of a point charge, which can be thought of as idealised spherical debris with electric field lines *E* acting radially and uniformly in all directions. If the debris is enclosed within the centre of a hollow sphere, then the electric field lines that terminate on the internal spherical surface wall can be expressed by Equation (3.8) [179]. The net charge of the spherical debris is *q* and *d* is the distance from the charged source.

$$\mathrm{E}(\mathrm{r}) = \frac{\mathrm{q}}{4\pi \mathrm{d}^2} \qquad (3.8)$$

Now consider charge emanating from the spherical debris with an area A. If the spherical debris was enclosed within a Faraday cup there would be an induced charge onto the sensing surface Q_A of the cup. The masking of charge is affected by the relative permittivity of the surrounding medium ε, as shown in Equation (3.9).

$$\frac{Q_A}{\varepsilon} \approx AE \qquad (3.9)$$

Combining Equation (3.8) and (3.9), provides an indication of the induced charge on the Faraday cup from the idealised debris, as shown in Equation (3.10).

$$Q_A \approx \frac{qA}{d^2} \qquad (3.10)$$

During electrostatic sensing, the Faraday cup can be thought of as the sensing medium from which charged wear debris can be detected after entrainment in the oil-line. The electrostatic oil-line sensors (OLS) are constructed of non-intrusive inductive ring elements, which enclose the lubricant borne debris. The sensor is covered by an insulating material, which is then earthed, as shown in Figure 3.4. During detection, baseline charge levels are associated with the oil flow. However, the passage of charged debris through the bore of the sensor, may dominate the baseline levels of the oil, which can then be associated with particle generation. The mechanisms of charge formation are described in the following sections.

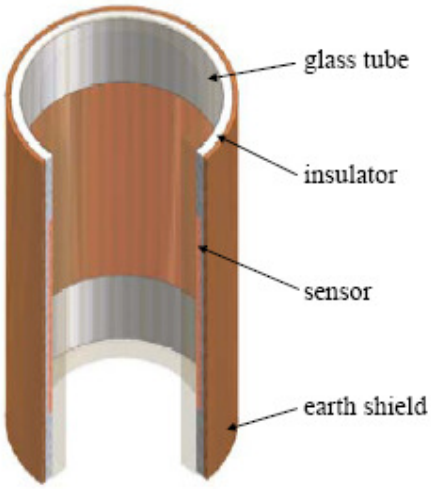

Figure 3.4 Construction of the electrostatic OLS.

A further method of charge detection is by a sensing face positioned close to potential wear sites. The wear site sensors (WSS) are passive inductive technologies that detect changes in charge in the vicinity of the sensing face. Construction of the sensor consists of a WSS face that is held in an insulating material and then enclosed in an earthed body, as shown in Figure 3.5. The sensing face acts like a capacitor of capacitance C which can be related to charge by Equation (3.11). Charge detection is controlled by the strength of the charged source, the sensing area and the distance from the sensing face.

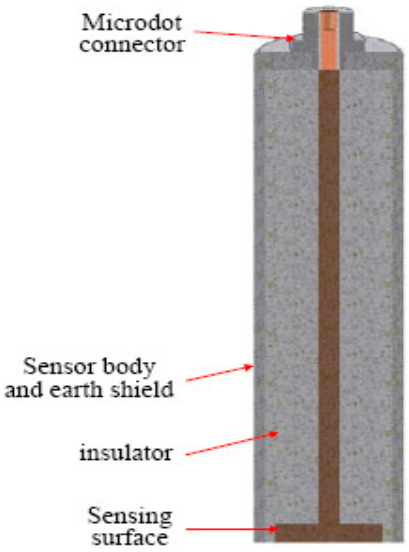

Figure 3.5 Construction of the electrostatic WSS.

$$C = \frac{q}{V} = \varepsilon \frac{A}{d} \qquad (3.11)$$

Re-arranging Equation (3.11) to give charge in (2.12):

$$q = \frac{\varepsilon V A}{d} \qquad (3.12)$$

The potential difference *V* between the sensor and wearing surface will be proportional to the charge on that wearing surface. Therefore, the induced charge on the wearing surface can be approximated through Equation (3.13).

$$Q_A \approx \frac{qA}{d} \qquad (3.13)$$

3.4.2 Electrostatic sensing

The sequence of events that lead to charge detection are shown in Figure 3.6. If we consider an isolated positive point charge +Q passing a sensor face, free electrons are attracted to the sensor surface, whilst the positive ions are repelled into the bulk material. This process is known as polarisation. If the sensor is earthed via a charge amplifier, free electrons from earth equalise the positive ions in the bulk material. The charge amplifier then converts the electron movement from earth to a measureable voltage. The measured voltage is then recorded and manipulated on computer based platforms.

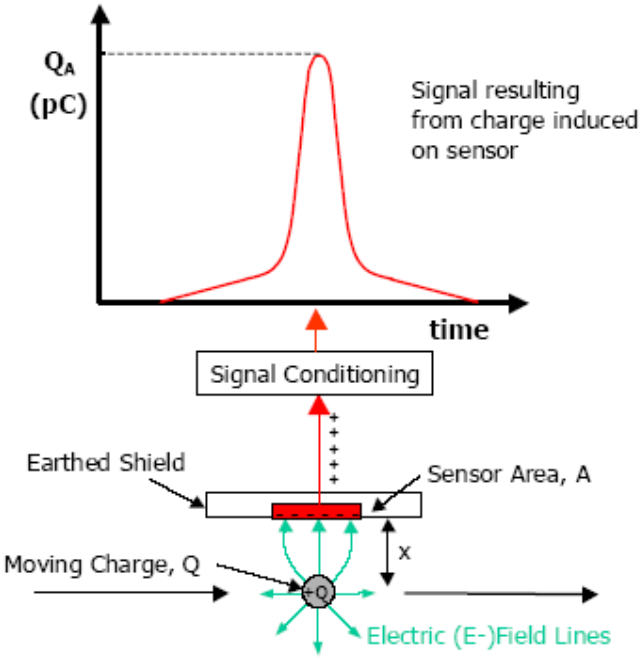

Figure 3.6 Charged source with electric field lines terminating on sensor face.

3.4.3 Charging mechanisms

WSS and OLS have been used to identify impending and progressive wear in dry and lubricated contacts. On-going research at the University of Southampton has identified 4 key areas in the generation of charge and transportation. These are shown in Figure 3.7.

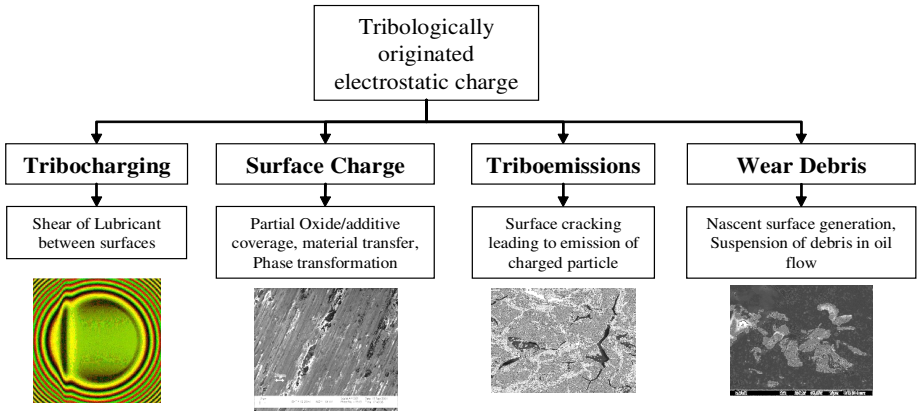

Figure 3.7 Charging mechanisms at the tribo-contact.

3.4.4 Tribocharging

Tribocharging is the term used to describe the charging of a low conductivity fluid, by its relative motion over a surface. The theories behind this process relate to double layer stripping and differential rate theory, which are reviewed by Parsons in [180]. Double layer stripping is based on the fact that at the solid-liquid interface an electrical double layer is formed. Under sufficient motion of the fluid, shearing of the double layer results in the stripping of free charge from the double layer, which becomes entrained in the fluid. This process is shown in Figure 3.8. Differential rate theory suggests that charge is created by the differential rate of diffusion of charged species to and from the interface or absorption/desorption of the charged species.

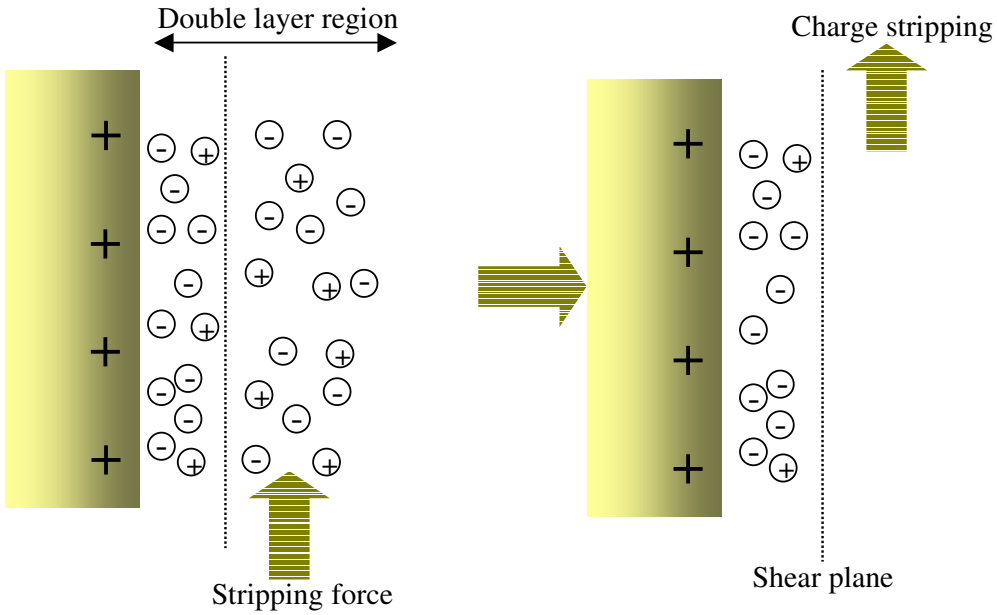

Figure 3.8 Double layer stripping effects during tribocharging.

Further factors effecting tribocharging relate to oil quality, which has been investigated by Harvey *et al* [181]. Using a spinning disc configuration it was shown that the electrostatic charging current increased with increasing temperature, and then decreased at higher temperatures. The increasing charge trend suggested an increase in charge mobility during a reduction in fluid viscosity which produces greater shearing at the double layer interface. At even higher temperatures, greater ionic mixing was thought to initiate charge recombination, and hence a reduction in

charging current. This test also showed charging effects relating to the surface roughness. These results showed an increase in charging current with an increasing surface roughness, which was thought to be due to an increased surface area that initiated charge removal from the double layer during microturbulence. Further considerations of charge detection include contaminant ingression such as debris, sand or soot, which modifies the charge levels according to the ingested product [182].

3.4.5 Surface charge

Surface charge describes the imbalance of charge on a surface. A mechanism of surface charge and the generation of contact potential differences (CPD), is observed during the bringing together of different materials. The driver of CPD is charge migration and is dependant on the work function of different materials, which is the ability of a material to give up electrons. When different materials contact, in order to achieve thermodynamic equilibrium, charge transfer occurs from the sample with the lower work function (φM_b), to the sample with the higher work function (φM_a), as shown in Figure 3.9 [183]. Charge transfer between the respective surfaces results in the formation of CPD. The CPD (eV_{CPD}) to work function relationship is defined in Equation (3.14).

$$eV_{CPD} = \varphi M_a - \varphi M_b \qquad (3.14)$$

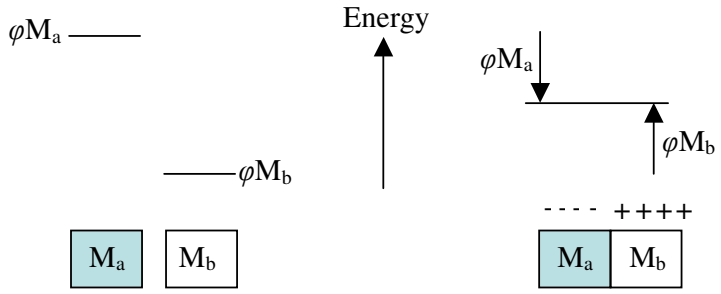

Figure 3.9 Schematic diagram of the CPD theory [183].

To monitor the CPD between dissimilar materials using the electrostatic WSS, a pin-on-disc tribometer was adapted by Morris *et al* [133]. Aluminium and copper inserts

were placed in a bearing steel disc whilst an electrostatic WSS was placed over the insert radius during disc rotation. As the aluminium sample passed the WSS, significant positive peaks were identified above the baseline levels of the bearing steel disc. For the copper sample, the WSS produced negative peaks during passage at the WSS.

Further tests have correlated the detection of charge during PoD testing with surface degradation mechanisms. In these cases, the CPD was established between the modified surface during distress and parent surface. The modified regions include plastic deformation, exposure of nascent surfaces, oxide stripping and phase changes [184, 185]. The distressed surfaces were confirmed using post test analysis, such as the electron microscope and hardness testing.

Therefore, electrostatic WSS's positioned at bearing degradation sites may provide evidence of the wearing mechanisms. Charge may be detected during the running-in period, from asperity deformation and the production of discrete areas of nascent surface, which generate a CPD between the distressed and original material. Furthermore, during benign wear, steady-state charge would be expected during full film lubrication as minimal surface wear is observed. Accentuated charge would be expected during wear out, from the generation of CPD between an area of spallation and the original surface. A further source of wear site charge may include the passing of debris in the field of view of the sensing face, as explained in the next section.

3.4.6 Debris generation

Consider the surface degradation mechanisms such as plastic deformation and phase changes with the generation of CPD on a parent surface. If we then consider the liberation of debris from that surface, then this can result in the generation of a charged particle. The charged debris may then be detected in the vicinity of the wearing site by the WSS or at remote locations from the degrading contact by the OLS, as shown in Figure 3.10. Further charge contributions may be obtained during liberation from the parent surface which requires the breaking of multiple atomic bonds, which may also modify the charged state of the particle and surface. In addition, the charged particle may be influenced during passage through a region of

localised charge i.e. an electrical double layer present at solid-liquid interfaces or discharge to earthed surfaces such as tribological surface pairs or lubrication pipe-work.

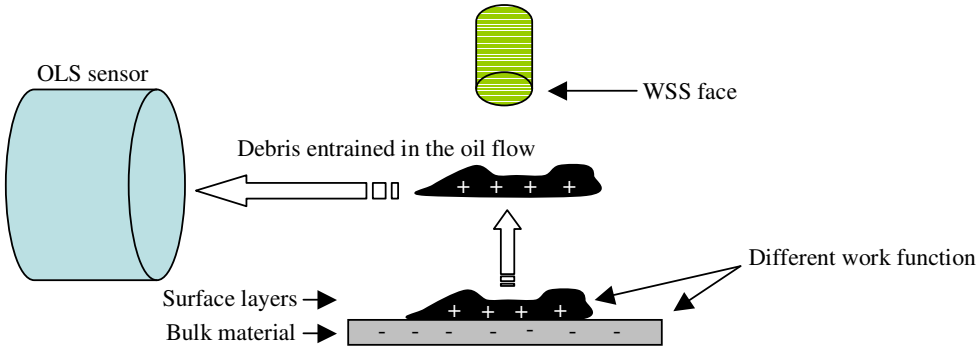

Figure 3.10 The removal of an area of different work function with the formation of charged debris for detection by the WSS and OLS.

3.4.7 Triboemissions

Triboemissions relate to the detection of particles such as exo-electrons [186], which are low energy electrons emitted from freshly exposed surfaces [187], i.e. abrasion or fatigue [188]. Charge production during surface deformation has been confirmed in scratch tests by Nakayama *et al* [189]. Results revealed the emission of burst charge and photons from semiconductors and insulators, of intensity which increased with load and speed. Nakayama [190] conducted further scratch tests in hydrocarbon liquids which showed that in semiconductors and insulators positive and negative charges were emitted, whilst in metals only negatively charged particles were emitted.

3.5 Multi-sensor condition monitoring incorporating electrostatics

Research within the national Centre for Advanced Tribology at the University of Southampton (nCATS), has employed electrostatic sensing to monitor the health of dry and lubricated tribo-contacts. In conjunction with electrostatic analysis, a multi-sensing approach has been adopted to provide greater confidence in making a diagnosis of the damage mechanisms, as well as justifying with greater clarity the possible sources of charge generation.

3.5.1 Lab based tribometers

Dry sliding tests by Morris *et al* [191] using a PoD tribometer, correlated wear site charge with the coefficient of friction and wear rate. During the running in period, high charge correlated with a high wear rate, which decreased during the transition into the steady state. During the steady state, perturbations in charge, correlated with fluctuations in friction coefficient and wear rate, which was related to an oxidation-delamination-reoxidation process [192]. The increasing charge signal was thought to be the generation of a nascent surface and charge recovery related to reoxidation of the contact.

Further dry sliding tests using the PoD were conducted by Sun *et al* [193], which correlated charge, the friction coefficient and AE (RMS) to surface distress. During running in, charge, friction and AE continually decreased from a high level. This was related to plastic deformation and fracture of the asperities with smoothing of the surface roughness, enabling conformity between the sliding surfaces. During the steady state, increased charge activity correlated with positive perturbations in friction and AE. The heightened sensor activity was consistent with metal-metal contact. As the test progressed, positive perturbations in charge correlated with negative perturbations in friction and AE. During this time, the sensor activity was associated to metal-metal and oxide-oxide interaction during reoxidation in the contact.

Tasbaz *et al* [194] investigated charge detection at lubricated unidirectional and bidirectional sliding contacts using the PoD and Plint TE 77 tribometer. Scuffing conditions were induced on the PoD by oil starvation, and on the Plint rig by overloading. On both rigs, a primary WSS was employed at the contact region to identify charge generation, whilst secondary sensors were positioned at remote locations to investigate charge transportation. Results from the PoD showed that the primary WSS detected bipolar perturbations in charge, which was associated with the formation of white layers during first transition scuffing. The secondary sensor detected weaker charge signals which were out of phase from the primary charge sensor, indicating charge transportation from the wearing site. The Plint TE 77 results also identified bipolar perturbations in charge from the primary sensor which again correlated with detection of white layers. However, there was no charge activity from

the secondary sensor, which may have been the effects of discharge to an earthed surface.

Harvery *et al* [195] used the PoD to detect charge during debris entrainment in a lubricated sliding contact. The experimental setup consisted of a primary WSS to monitor disc wear and a secondary senor to identify debris/charge transportation from the wear track. An initial baseline test consisted of incremental loading of the contact, without seeding debris. Charge from the primary sensor increased with positive and negative features from half the full load which persisted to the end of the test. The charge activity related to surface wear. The secondary sensor detected increased charge at lower levels compared to the primary sensor, which was attributed to debris transportation. The seeded debris test consisted of entraining spherical chromium steel particles periodically throughout the test. The particle size was slightly greater than the minimum film thickness. This ensured particle/surface interaction as debris passed through the contact zone. The primary sensor showed a large increase in positive and negative charge during particle seeding, which decayed after entrainment. The secondary sensor showed perturbations in charge at the time of particle seeding which also quickly reduced to baseline levels. However, dynamic negative charge also appeared after particle entrainment, which persisted until the next instance of seeding. The charge features were related to both seeded and freshly generated debris, centrifuged from the wear track.

Powrie *et al* [196] utilised an FZG gear rig which incorporated both the WSS and OLS. Incremental loads were applied every 15 minutes with the charge activity monitored by 3 WSS's, positioned above, beside and below the gear mesh. After each load stage the debris was collected from a magnetic plug. The debris was inspected for 20 and 50 µm particles using in house equipment at the Defence Evaluation and Research Agency (DERA), now QinetiQ. The debris count was then compared against velocity measurements taken across the OLS, using the timing of charge peaks detected by two ring elements. The time delay was the result of debris passage through the sensor since larger debris travels slower than the oil flow, indicating a reduced velocity. Results showed that during the final load stage there was an increase in wear site charge as the distressed gear teeth passed the sensor. The WSS charge was then associated with white layer formation which was confirmed by optical

microscopy and hardness measurements. The OLS and particle count at this time showed that a reduced velocity correlated with an increase in debris count.

3.5.2 Bearing test rigs

Harvey *et al* [197] used absolute charge levels from 3 WSS's and an OLS, to monitor accelerated tapered roller bearing wear, by inner race indention and overloading. As well as charge measurements, other instrumentation included an accelerometer, thermocouples, inductive and ferromagnetic debris counters. For the first 50 hours, steady-state conditions from all techniques indicated benign wear. At 50 hours, an increased wear site charge at the defective bearing correlated with minor debris detection from the ferromagnetic unit and an increased oil temperature. The cause of distress at this time could not be confirmed, although it was postulated that these events could be some form of damage initiation. The next period of activity was around 62 hours, with increasing vibration levels which showed a very good correlation with increasing oil temperature and debris detection by the ferromagnetic sensor. This was then followed by increases in OLS charge, charge from WSS 2 which was normalised to the inner race defect frequency and debris detection by the inductive particle count. The test was then stopped after 68 hours as the collective sensor activity indicated failure. Post-test bearing inspection confirmed considerable inner race spallation which was initiated at the inner race defect. Therefore, the WSS identified the exact locality of component failure and the OLS monitored damage propagation charged debris transportation in the scavenge line. These results also show that electrostatic sensing may be employed as a complimentary or viable alternative to the traditional bearing CM practices.

3.6 Summary

Figure 3.11 shows the adaption of the in-line and off-line traditional sensing techniques to identify tribological damage during bearing service life. Initially, bearings experience running-in, where an increased surface roughness may yield in a low λ ratio, with tribological activity observed during asperity deformation and fracture. Therefore, during this period one may expect increased vibration from impacts between opposing asperities, AE during asperity fracture and debris generation with increased temperature during frictional heating in the Hertzian

contact. However, removal of the surface roughness increases the λ ratio and enhances EHL. Hydrodynamic entrainment and viscosity effects of the lubricating film reduce tribological activity within the contact area as the surfaces become completely separated by the lubricating film. Therefore, following running-in, consistent sensor signatures including vibration, AE, temperature and debris is expected, which is consistent with trending characterised by the bath-tub curve and indicates benign wear. However, fatigue failure is the result of cyclic stresses that drive crack propagation and coalescence with debris liberation from the parent surface that can prohibit surface functionality. Therefore, the detection of accentuated distress indicators such as AE and debris provides an opportunity to identify the early stages of tribological damage. Furthermore, the employment of a multi-signature strategy provides personnel with sufficient analysis for corroborative purposes in making proactive assessments of distress. In addition, in order to maximise the distinction between the normal and abnormal condition, a number of data processing strategies are employed. These include time and/or frequency analysis [3], statistical parameters [4] and sensor data fusion [5]. The final stages of the useful bearing life are identified by runaway sensor activity from all sensing technologies which indicates the wear out period and a time which remedial actions are required before catastrophic failures to secondary systems occur.

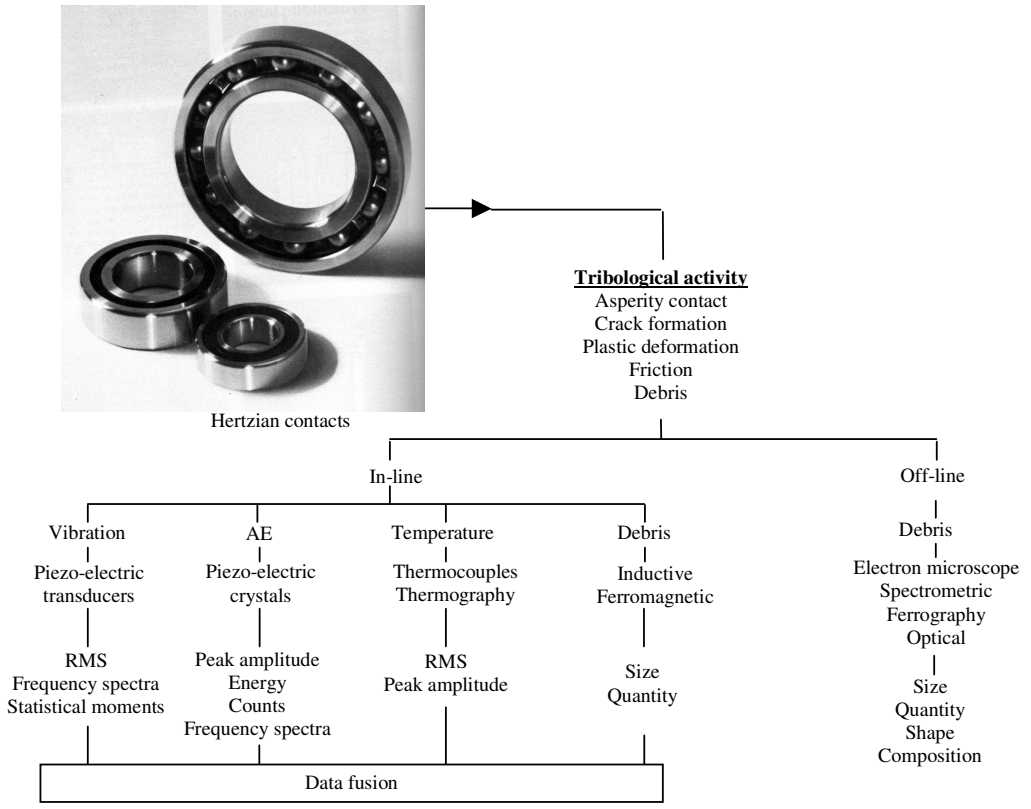

Figure 3.11 Distress signatures generated during tribological activity.

A relatively new technique is under development for the detection of distressed surfaces at wear sites and remote locations from the degradation area. This technology is based on charge measurements using electrostatic WSS and OLS. From laboratory based tribometer tests, the WSS has been shown to identify surface phase transformations, deformation and fracture, which yields in the generation of CPD between the original and modified surfaces. The OLS has shown a good correlation with velocity measurements based on the timing of charge peaks and 20 – 50 µm debris. Full scale bearing tests have shown a good correlation with RMS charge levels and debris greater than 100 µm.

However, in these tests there was no correlation with sub 20 µm, which has been shown in Figure 2.15 to be critical in identifying the earliest signs of distress. Correlations with debris within this particle range may be shown by a number of techniques that include the PODS and SOAP. A comparison of the current

understanding of the electrostatic sensitivity to debris and the range of available debris CM techniques is shown in Figure 3.12.

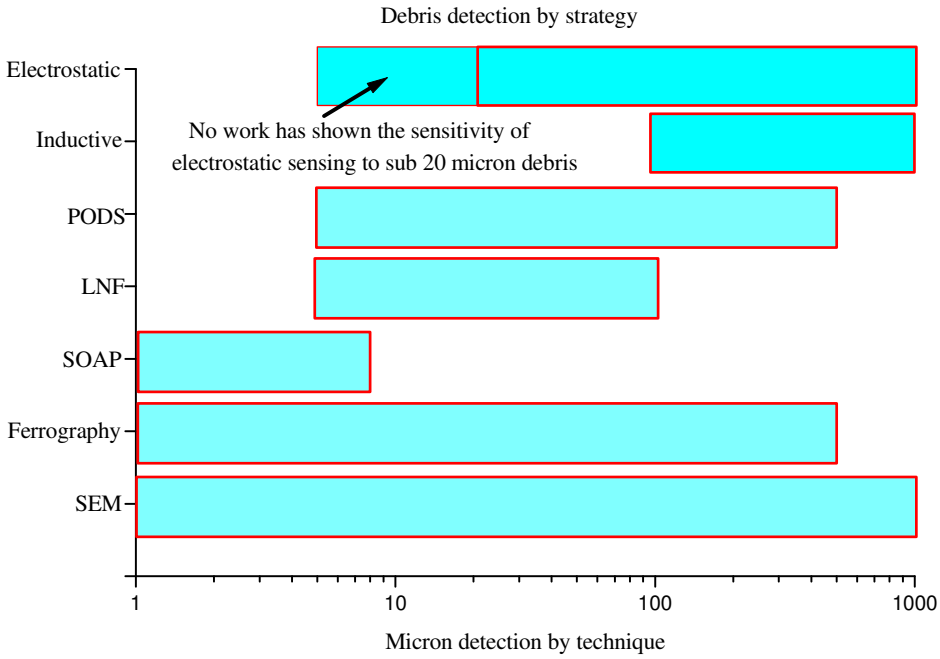

Figure 3.12 Sensitivity of debris detection techniques.

Therefore, there is a body of work that can further identify the detection capabilities of electrostatic sensing and their sensitivity to bearing failure. This includes the amalgamation of novel and traditional CM practices for corroborative purposes, and includes correlations between electrostatic WSS, AE, vibration and thermocouples which provide an instantaneous evaluation of distress at the wear site. In addition, correlations between the electrostatic OLS, inductive and ferromagnetic particle counters would provide further support of wear and enhanced confidence of degradation in the oil-line. Furthermore, correlations between off-line analysis, such as the PODS, ferrography, SOAP and particle imaging with the electron microscope would provide further confirmation to the evolution of bearing distress. A further enhancement of the distress signatures may be obtained with the use of advanced processing algorithms such as those involving AI and NN.

Thus, the collective distress signatures at the wear site, oil-line, off-line and advanced processing architectures presents a novel means of identifying a comprehensive

evaluation of distress and provides enhanced confidence in evaluating the earliest signs of bearing degradation. This work is the focus of the next chapter.

4 Experimental Procedures

This chapter describes the methodology that was adopted in the experimental investigations to identify the distress signatures at the wear site, oil-line, off-line and advanced processing architectures to monitor the evolution and the earliest signs of bearing distress. The test program utilised a test rig to monitor accelerated tapered roller and ball bearing wear of metal-metal contacts, by overloading and inner race indentation. The inner race indent was induced to act as a stress raiser which enabled the anticipation of failure at the specific bearing element. The sensing strategy is shown in Figure 4.1 with further details of all the techniques described in the later sections. In this project, the intelligent processing algorithm work was carried out by Nick Chen a post-graduate researcher within the national Centre of Advanced Tribology (nCATS) at the University of Southampton [198-200].

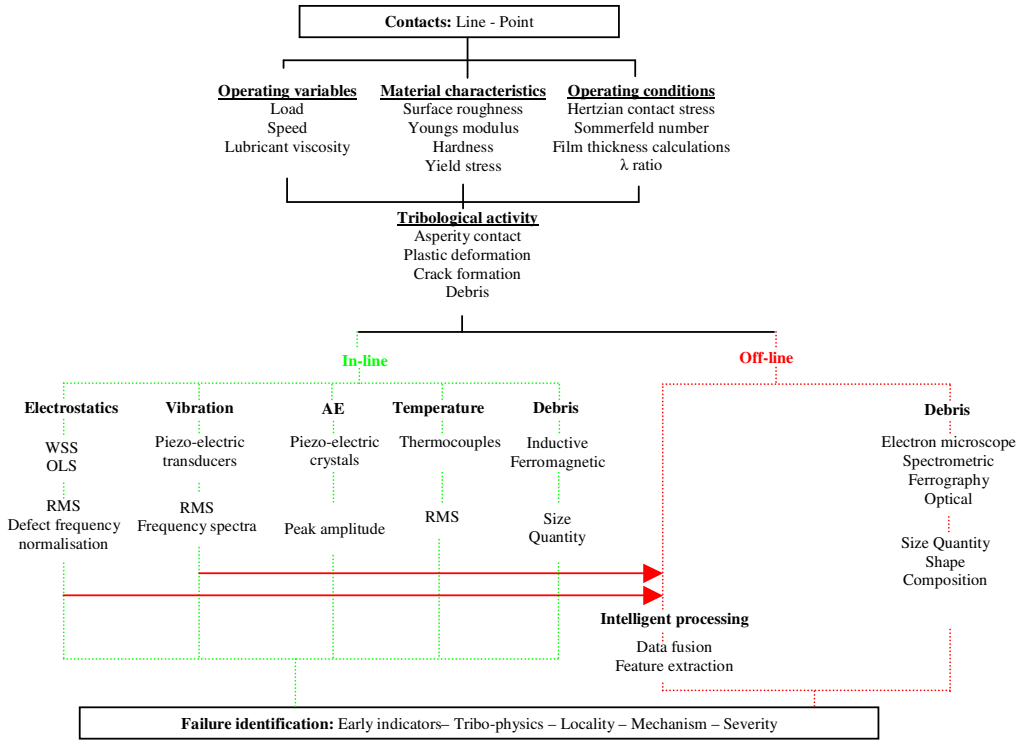

Figure 4.1 Sensing techniques utilised during bearing testing.

4.1 Bearing test rig

The bearing test rig is an exclusive design by the Timken Bearing Company which is used for lifetime testing. Therefore, these test rigs are not commonly found in experimental laboratories, which reduces the availability of the test procedure. The rig was acquired by Smiths Aerospace (currently GE aviation), for development work on the electrostatic WSS's and OLS, which were compared against the signatures generated by vibration accelerometers. The rig was then donated to the Surface Engineering and Tribology Group (currently nCATS), with further corroborative investigations planned between the two parties. This work saw the development of the data acquisition software (RMS and defect frequency analysis) with additional correlations identified between signatures generated by inductive and ferromagnetic particle counters and thermocouples. The culmination of this work is shown by Harvey *et al* [197]. This research shows the further development of the electrostatic technologies, where modifications include the refinement of the positioning of the accelerometer onto the stork of WSS 2. Further changes include the addition of thermocouples which are positioned on the outer race of the test bearings. Additional modifications include the employment of AE sensing, in which the sensor is embedded in the test housing. Other changes include the addition of a drain point, from which oil samples are taken for off-line debris analysis. Furthermore, the test housing has been modified to accommodate ball bearings. The operation and rationale behind the positioning of these techniques are described in the following sections.

The rig has a test chamber which accommodates 4 bearings which are driven by a dc motor. In all tests, the bearings are numbered in sequential order from 1 – 4, from the drive end. In all cases the support bearings are numbered 1 and 4, and are always tapered rollers, model LM67010/LM67048. The test bearings are centrally located between the support bearings and are numbered 2 and 3. During tapered roller bearing tests, the bearings are LM67010/LM67048 and during ball bearing testing the model is MM206K. A loading system incorporates a hydraulic mechanism to apply a radial load to a sealed piston assembly that presses against the centre test housing which accommodates the test bearings. The loading system has two components: a manual hydraulic pump used to apply a load of 40 kN to a piston, and an accumulator which

enables stabilisation of the hydraulic pressure applied to the load piston. This ensures a constant force is applied to the bearings throughout the test. Axial load is applied by threaded bolt which initiates pressure to the test and support housings. The configuration of the bearing set-up is shown in Figure 4.2 and the bearing specifications in Table 4.1.

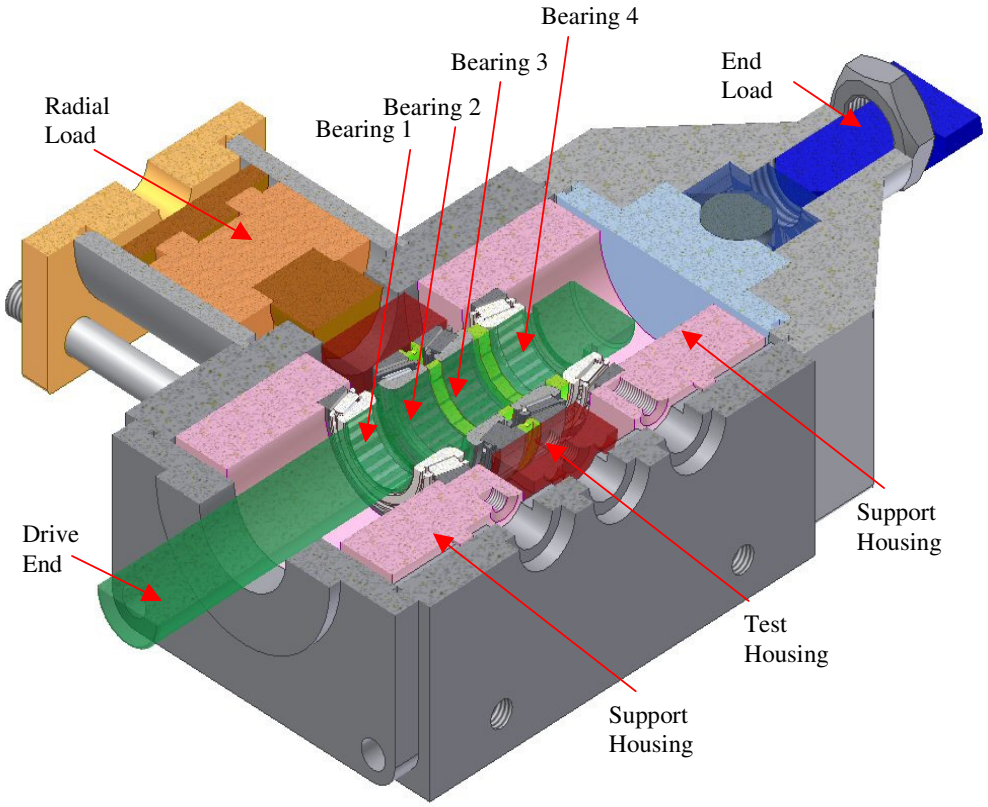

Figure 4.2 The bearing set-up in the test chamber.

	Tapered Rollers	Balls
Bearing type	LM67010/ LM67048	MM206K
Contact Angle °	13.5	0
Pitch Diameter mm	45.2	46
Inner diameter mm	31.7	30
Outer diameter mm	59.1	62
Bearing width mm	14.4	16
Mean Roller Diameter mm	6.2	9.535
Rolling elements per Row	19	9

Table 4.1 Dimensions of the test and support bearings.

A closed loop oil recirculation system is built around the bearing test chamber. The bearing chamber is operated under flooded conditions and is designed to allow lubricant borne debris to be carried from the bearing chamber, along the recirculation pipe-work, to be detected by the sensors in the oil-line and for extraction for off-line analysis. The recirculation pipe-work is connected with copper pipe and brass connectors. The flow rate is monitored by a rotameter with a range from 0 – 8 m min^{-1} and is controlled with a gate valve on a by-pass system. The pump has a 25 litre sump and a water heat exchanger to control oil temperature throughout testing. To prevent debris generated in the test chamber being constantly driven around the recirculation loop, and avoid particle entry back into the contact area, a series of measures have been put in place. These include a magnetic plug and 5 micron Pall filter. A drain point was also installed to collect oil samples during testing to monitor the evolution of wear debris. An image of the test rig is shown in Figure 4.3 which identifies the 3 key areas of monitoring degradation, the test chamber, oil recirculation line and at a drain point for off-line analysis.

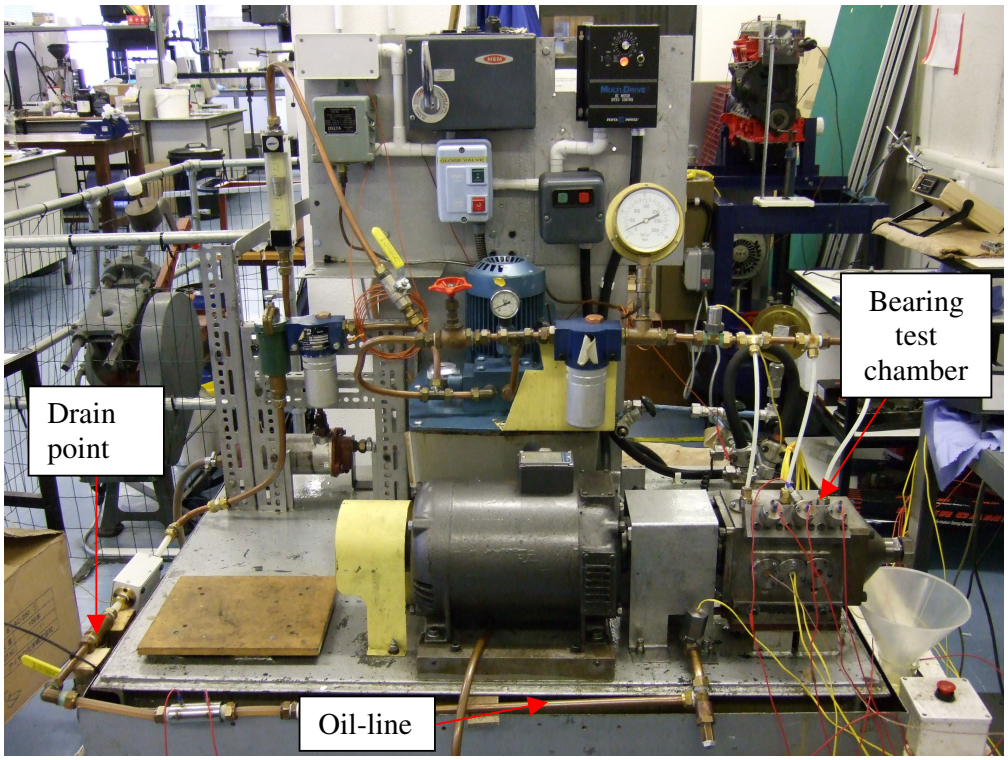

Figure 4.3 The bearing test rig highlighting the key areas available for indicating bearing failures.

4.1.1 Artificial defect

To accelerate and anticipate spallation, bearing number 2 has an artificial indent/s on the inner race. The indent was induced with a Rockwell Hardness testing machine using a "C" type diamond indenter. This applied a 150-kgf load with an included angle of 120^{o}. Each cone (inner race) was mounted on a fixture such that the diamond was perpendicular to the race way. The rolling element bearings have one indent on the inner raceway whilst the ball bearings have three indents on the inner raceway and were performed by the Timken Bearing Company, Canton, Ohio, USA before assembly. An image of the single indent surface profile is shown in Figure 4.4 for the ball bearings and the multiple inner race indents are shown in Figure 4.5 for the ball bearings.

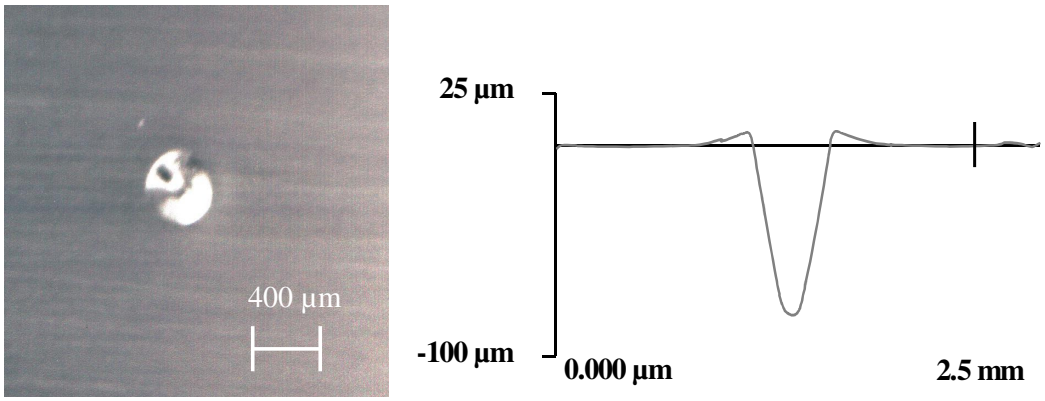

Figure 4.4 Pre-indent on inner race of bearing number 2.

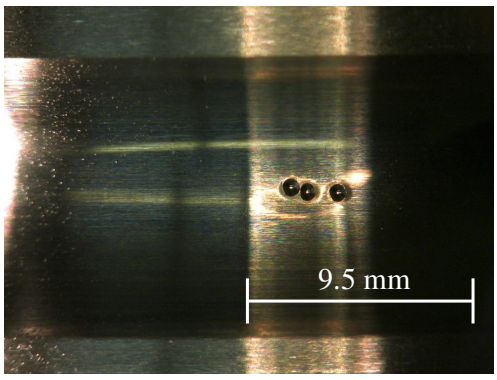

Figure 4.5 Multiple indents on the inner raceway of the ball bearings.

4.1.2 Test conditions

Before and after testing the bearings were cleaned/degreased in a solvent (petroleum ether) for 30 minutes in an ultrasonic bath. The bearings were then gravimetrically analysed with a Mettler Toledo XP 205 5-figure balance and sectioned for SEM analysis.

The lubricant used in all tests was a Shell Vitrea 32 base oil, and was selected as it contained no additives, therefore eliminating additive contribution and interaction during charge measurements. In addition, according to the oil data sheets are ideal for lubricating rolling element bearing contacts. However, it is important to realise that grease provides another form of lubrication as it is easily used and inexpensive. A constant flow rate of 4 litres min^{-1} was chosen after consultation with the bearing vendors to ensure debris removal from the bearing test chamber into the recirculation pipe work, so that the debris could be measured by the in-line sensors and collected for off-line analysis.

The load was applied in equal increments every 30 minutes for a duration of 4 hours, until the maximum contact pressures were obtained and was based on advice from the bearing vendors. The contact pressures for the tapered roller tests was 2.5 GPa and between 1.6 – 2 GPa for the ball bearing tests.

In all tests, a rotational speed of 2500 rpm (41.7 Hz) was selected in order to keep the rotational frequency away from 50 Hz, mains frequency. At 2500 rpm the DN number of the tapered roller bearings was 79250 and for the ball bearings the DN number was 75000. Therefore, as one of the test bearings (#2) was artificially indented, failure was anticipated at this region of localised stress, and since the DN numbers were low [59, 60], failure of the remaining test and support bearings was not anticipated. This enables the failure of bearing #2 to be correlated against the remainder of the test and support bearings, which were expected to operate normally. However, should the unexpected failure of bearings #1, 3 or 4 occur, the condition monitoring strategies were set-up to effectively identify the distress.

4.1.3 Sensing configuration

Figure 4.6 provides a schematic which illustrates the position the sensing techniques which are further described in the next section. The data acquisition and sampling settings for each sensing technique is shown in section 4.5.

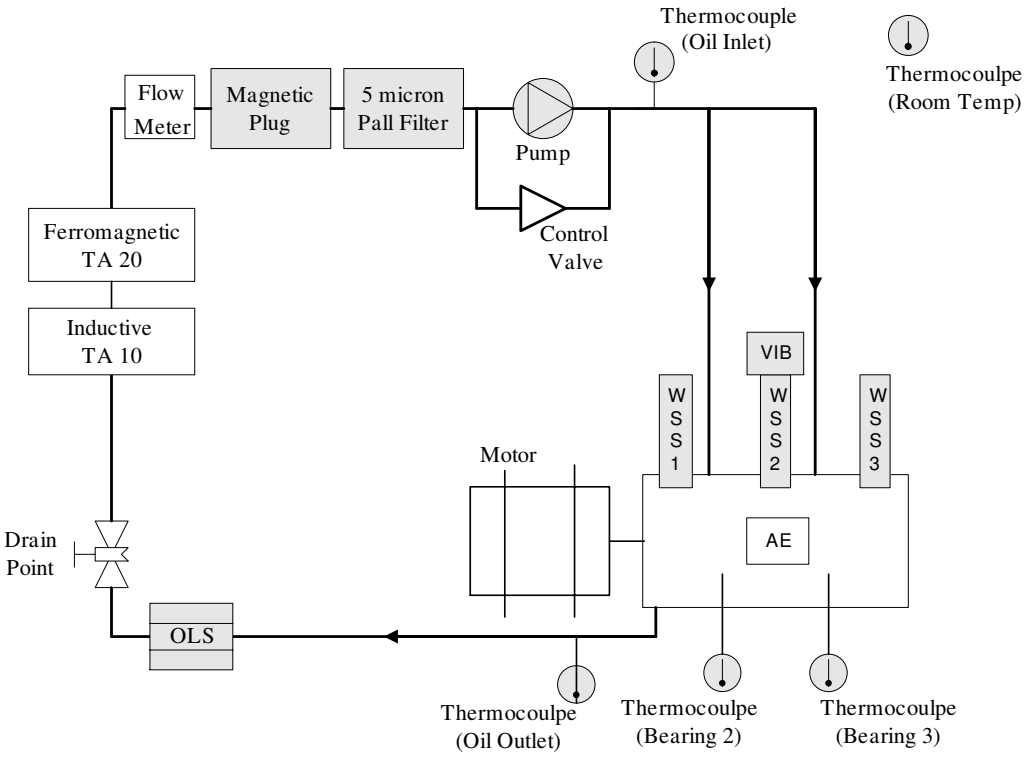

Figure 4.6 Flow diagram of the bearing test rig.

4.1.4 Electrostatic WSS

A WSS penetrates each of the support housings, therefore detecting charge from bearings 1 and 4, and are designated WSS 1 and WSS 3 respectively. WSS 2 is located between bearings 2 and 3 in the test housing. The sensing face has an area of 9.6 mm^2 and is positioned adjacent to the clearance between the cage and outer race. The locality of the sensing face for the ball bearing geometry is shown in Figure 4.7.

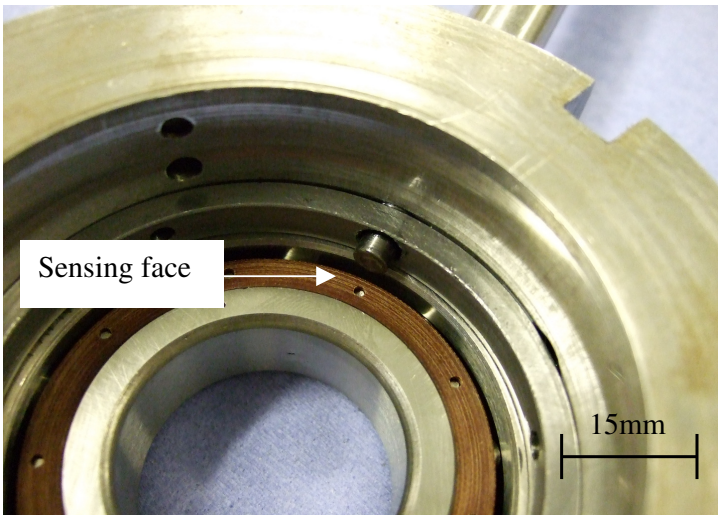

Figure 4.7 Locality of the sensing face for WSS 2.

4.1.5 Vibration acceleration

Mounted onto the stork of WSS 2 is a vibration accelerometer. The accelerometer is coupled to the test housing, since failure is anticipated from the indented test bearing. The accelerometer is a piezoelectric type model A/20/T from the DJ Birchill Company and has a sensitivity of 28.9 pC g. The positioning of the accelerometer on the stork of WSS 2 is shown in Figure 4.8. The calibration graph of the sensor is shown in Appendix B, and has a flat response up to 1 kHz and 6% deviation at 10 kHz. The flat response over the 1 kHz range is suitable for this bearing set-up, since the defect frequency of the inner-race, outer-race, rolling elements and cage are 226 Hz, 148 Hz, 96 Hz and 16 Hz respectively.

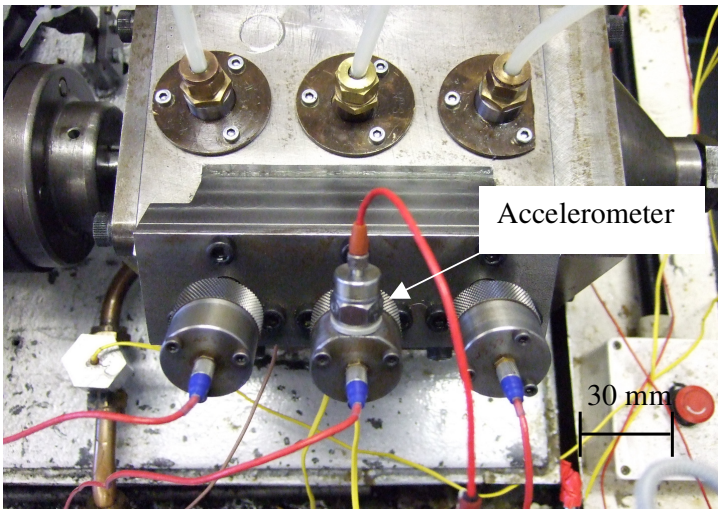

Figure 4.8 Positioning of the accelerometer onto the stork of WSS 2.

4.1.6 AE

The AE sensor was a Pancom wideband piezo-electric type. Initial testing included a Hsu-Nielsen pencil lead break (PLB) [1, 112, 116] on the sensing face to identify the effectiveness of the sensor. A peak amplitude of 92 dB was obtained which indicated that the sensor was working. The frequency response of the sensor is shown in Appendix C, which has a peak sensitivity around 550 kHz, and a relatively flat response within 25 dB of peak sensitivity between 200 – 800 MHz. The pico-Z sensor was calibrated according to ASTM E976 standards using the face to face excitation method, which is based on a 1 V signal excitation per µbar pressure. The sensor was positioned in the bearing test housing, as shown in Figure 4.9, which was then covered in silicon rubber sealant to eliminate oil ingress into the sensor, since the bearing chamber is flooded during testing. The AE sensor was coupled to AEP4 40 dB pre-amplifier which was attached to AMSY4 AE equipment, manufactured by Vallen GmbH for signal processing, using Bayonnet Neill-Concelmann (BNC) cables. The band-pass frequency range of interest was between 100 kHz – 1 MHz. The high-pass filter setting of 100 kHz was selected to remove background noise, such as the motor operation. The low-pass filter was set at 1 MHz, which enabled the clear identification of frequencies which had a relatively flat response within 25 dB of peak sensitivity and included those around the resonant frequency range of 550 kHz.

Prior to any bearing tests, further PLB tests were carried out from the test bearings i.e. the source of AE during failure to the sensor, with attenuation around 30 dB. Therefore, since the initial PLB test on the sensing face gave a signal response of 92 dB and attenuation from the source was 30 dB, this gave a preliminary indication that the threshold setting would be around 60 dB. However, this setting was observed under static conditions, and the optimum AE threshold can only be identified during the bearing operation, i.e. when the operating load and speed is maintained. Further methods of setting the optimum threshold is from observations and experience of each bearing test, which enables justification of the threshold in the preceding tests. A combination of the above threshold setting strategies was adopted in these tests, which yielded in a tapered roller bearing threshold of 75 dB and a ball bearing threshold of 50 dB. The lower threshold for the ball bearings was likely to be due to the lower Hertzian contact pressures during testing.

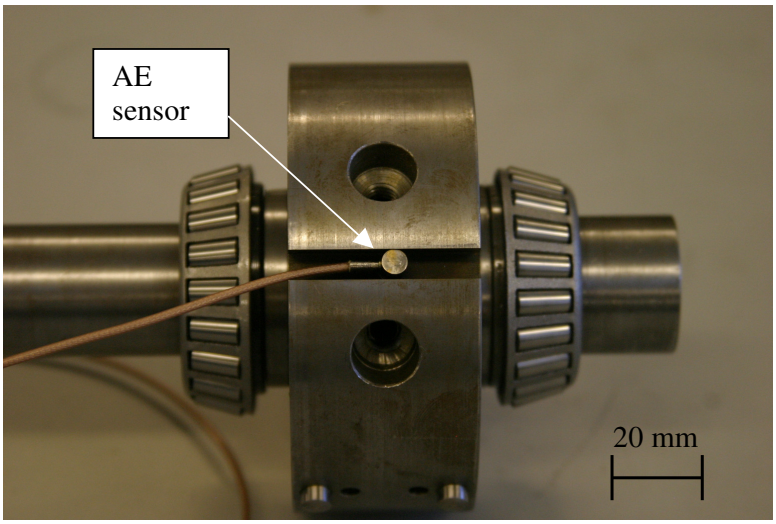

Figure 4.9 Position of the AE sensor in the test housing.

Throughout AE analysis there are a number of signal characteristics that are employed as bearing distress indicators and include counts, energy and rise time etc, which were explained in section 3.2.2. There are also a number of further processing structures and include wavelets, neural networks and fuzzy logic techniques, which are reviewed by Heng *et al* [201]. The implementation of this analysis may provide further insight into the evolution and earliest signs of bearing wear but does represent a body of work that could be adopted in a further project due to the time that would needed to be invested in the analysis. However, during the AE analysis the parameter that provided a consistent identification of the earliest signs of distress was the peak amplitude. Therefore, for this reason any further reference to AE relates to the peak amplitude.

4.1.7 Thermocouples

K-type thermocouple probes were used to monitor the outer race temperature of the test bearings, oil temperature at the inlet and outlet to the test chamber and room temperature. The thermocouples have a sensitivity of 0.1 ˚C to a maximum of 190°C.

4.1.8 OLS

The OLS consisted of 2 identical ring elements placed 30 mm apart and was located downstream from the bearing test chamber. The OLS was positioned on straight 12.7 mm diameter pipe work which was 1010 mm in length. The OLS position on the pipework was greater than 50 diameters along the pipe to reduce turbulence. The oil

flow in the pipework, based on a flow rate of 4 l min^{-1}, had a velocity of 131.6 mm s^{-1} and a Reynolds number of 52, indicating laminar conditions.

4.1.9 Inductive and ferromagnetic sensors

The inductive and ferromagnetic sensors were Macom TechAlert (TA) 10 inductive and 20 ferromagnatic particle counters, and were positioned after the OLS. The TA 10 provides debris sensitivity to a minimum of around 100 μm from a 9.2 mm diameter bore. The TA 10 is supported by the TA 20 and the operation of both these technologies is shown in section 3.5. A further reason for incorporating the ferromagnetic unit was that above the magnetic plate the unit has a glass window which provides a visual on particle collection throughout testing. Also, when the particles are collected on the sensing head, this restricts the further passage of debris in the lubrication line and back into the contact. Additionally, on completion of testing, the debris can be collected from the sensing head where a range of off-line oil analysis can be performed.

4.2 Data acquisition and sampling

The WSS, OLS and accelerometer were connected to charge amplifiers with low-noise microdot cables. The charge amps had a frequency response between 1 Hz – 10 kHz, with the high pass filter selected so that only dynamic charge was detected, thus being insensitive to static charge. Channel gains for the WSS, OLS and accelerometer were 100 mV/pC, 500 mV/pC and 50mV/pC respectively. The output voltages were then fed into an A/D card for manipulated using PC based software.

The on-line processing system, developed by General Electric (GE), formerly Smiths Aerospace Electronic Systems included RMS and bearing defect frequency calculations. The RMS values were calculated every 2 seconds at a sampling rate of 4096 Hz. The defect frequency analysis was calculated using an optical tachometer to identify the rotational speed and inputs using the bearing geometries. The bearing defect frequency calculations were shown in section 3.2.5 with a slip factor set at 5%. The 5% value was obtained after consultation with GE representatives and enabled the maximum and minimum values of the defect frequencies to be determined. The processing architecture calculated the power spectral density (psd) using Matlab.

Then from the energies bounded by the maximum and minimum defect frequencies within the psd, the average energy values were calculated. The average energy was then normalised by the WSS RMS value. The vibration bearing defect frequency and WSS defect frequency normalisation data was recorded every 30 seconds and were incorporated to identify distress at particular bearing elements. Although the frequency analysis was considered and all signatures analysed, there was no consistent information from the combination of tests which provided confidence and reliability in diagnosing distress. Therefore, in order to reduce the volume of generated data, which consists of 320 additional plots from 14 tests, these sensor outputs are not shown.

In this analysis, one does appreciate that as the sampling times were every 2 and 30 seconds, there may some information lost due to the highly processed data. Attempts have been employed to increase the sampling times by collection of the data using digital audio tape (DAT) format. However, since the tests last for around 80 hours then the amount of information for a number of technologies becomes considerable and becomes problematic for some software packages such as Microsoft Excel.

In addition, the GE algorithms utilise the OLS sensor to produce an indicator value, generated from a cross correlation function, which identifies the time-lag between the charge peaks from the outputs of OLS 1 and OLS 2. If the lag is consistent, this results in a consistent cross correlation value, which is believed to be associated with the oil flow. However, if there is slower moving debris in the oil, then the lag will be greater. This results in a greater deviation in the cross correlation value. The indicator value identifies the peak cross correlation value, which is then normalised by the product of the OLS RMS. Therefore, an increased indicator value is likely to be indicative of debris in the oil-line. The OLS and indicator value sampling is at a frequency of 4096 Hz with an RMS data point recorded every 2 seconds.

The sampling rate for the Macom TA 10 and TA 20 was every 10 minutes and the thermocouples every 1 minute, which were recorded on individual PC's. The sampling frequency of the AE peak amplitude parameter was 5 MHz with band pass frequency activity between 100 kHz – 1 MHz. The high pass filter was set at 100 kHz

to remove unwanted noise such as background motor activity. A flow diagram of the in-line sensing process is shown in Figure 4.10.

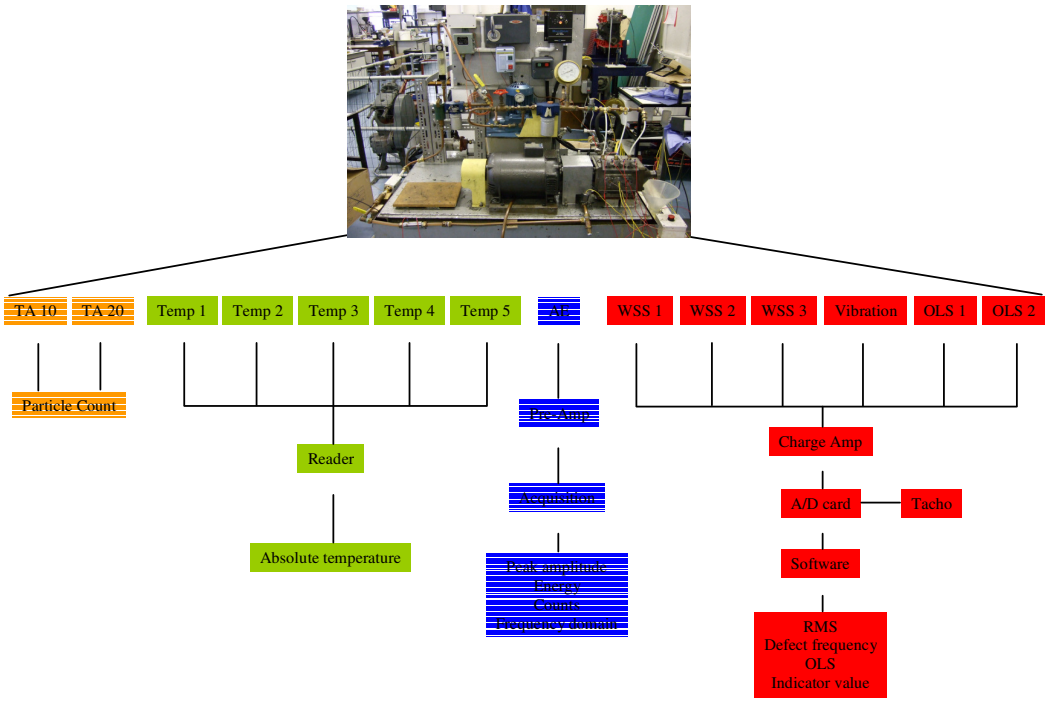

Figure 4.10 Flow diagram of the instrumentation set-up for the in-line sensors.

4.2.1 Advanced processing

As previously discussed, this work utilises the time and frequency data sets for manipulation using advanced processing architectures which are based on AI algorithms. The sensor signatures used in this process are shown in Table 4.2.

Vibration	WSS 1	WSS 2	WSS 3	OLS
RMS	RMS	RMS	RMS	RMS1
Tacho Energy	Tacho Energy	Tacho Energy	Tacho Energy	RMS2
Cage Energy	Cage Energy	Cage Energy	Cage Energy	Indicator
Roller Energy	Roller Energy	Roller Energy	Roller Energy	
Outer Race Energy	Outer Race Energy	Outer Race Energy	Outer Race Energy	
Inner Race Energy	Inner Race Energy	Inner Race Energy	Inner Race Energy	

Table 4.2 Sensor signatures used during sensor data fusion processing.

At the start of the AI procedure, the vibration and electrostatic signatures, which were shown in Table 4.2, are generated during defect free and accelerated bearing tests. The defect free signatures are used as training data and the accelerated signatures are employed as the test data. The training data was used to provide a reference from which the test data could be compared. However, caution must be shown when using a reference, as data sets which are believed to be fault-free, may contain spurious data points which relate to a degree of fault or poor integrity information. Therefore, if these data sets were to be used as the training data to develop an anomaly detection procedure, then the method will generally be flawed, as differences between the training and test data could be masked by the poor integrity information.

In order to represent the complex distributions, the data sets are characterized by a combination of Gaussians or a Gaussian mixture model (GMM). The GMM is a clustering tool which presents the data set in feature space, which have dimensions which relate to the variables of the sensing technologies as shown in Figure 4.11. In this classical case, the plot shows the generation of a normal cluster and the formation of outlier data points to the top left of the normal cluster.

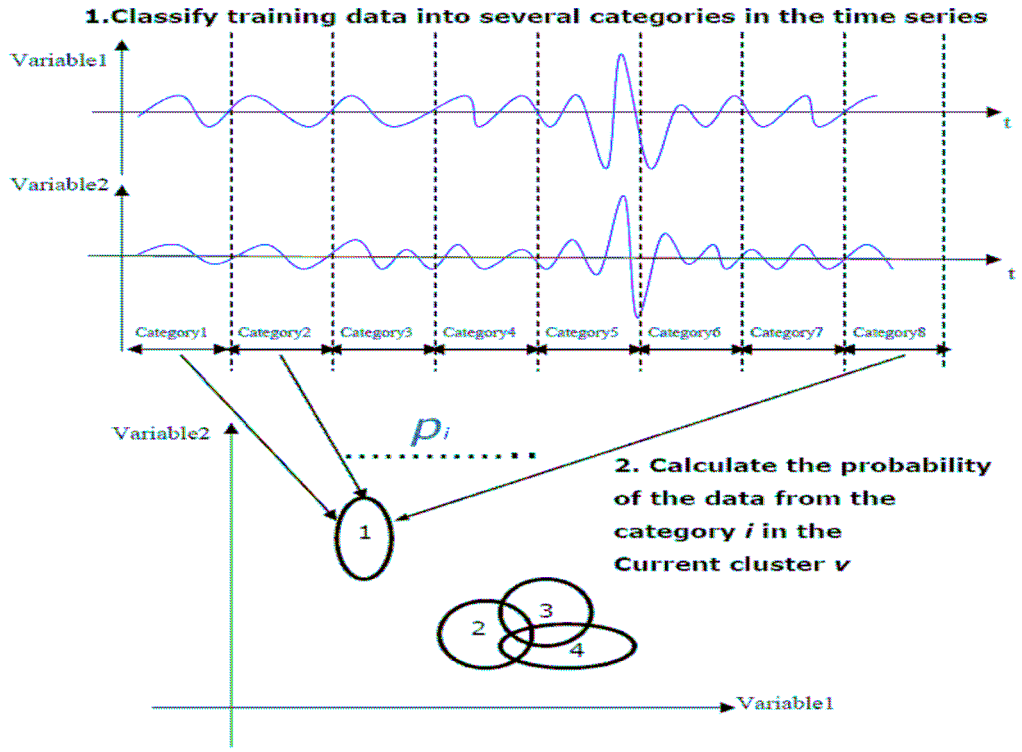

Figure 4.11 The clustering method of the GMM.

The outlying defective information is removed using the entropy statistic, which identified areas of the cluster that could be associated with the anomalies. The anomalous information is identified as the data that is distant from normal data. This process trims the GMM, enabling the model to become more sensitive to anomalies within the test data. Principle Component Analysis (PCA) is then applied to the cleansed training data. The idea behind the PCA is to reduce the dimensionality of a dataset consisting of a large number of interrelated variables, whilst maintaining the variation of the original dataset. The PCA approach uses all of the original variables to obtain a smaller set of new variables (Principle Components-PCs) that can be used to approximate the original variables. The PCA procedure is then performed on the accelerated test data and compared against the PCA from the training data, and establishes the locality and severity of the deviation between the data sets. Further comparisons are made between the data sets using Hotellings T-squared statistic. Hotelling's T-squared statistic provides a measure of the difference between the mean values of the two data sets. Additional variable contribution values include a Log-likelihood score, which measures how well an established GMM fits the test data. Another parameter is the Mahalanobis distance, which measures the similarity between the test sample and known Gaussian mixture. A methodology of the workflow is shown in Figure 4.12, whilst the procedures are described in greater detail in [202].

4.3 Software checking before testing

Before any testing was carried out, the authenticity of the in-line signatures monitored by the GE processing architecture were compared to the signals recorded by a Racal Heim DATaRec-A80 digital-audio-tape (DAT) recorder. Sampling was recrded at a frequency of 2.5 kHz. The method of artificially inducing charge on the electrostatic sensors was by passing a metallic object in the field of view of the sensing face and by manually agitating the accelerometer. The results are shown in Figures 4.12 and 4.13. Both sets of signatures show a good correlation, with the signals from the GE software having a lower amplitude, which is due to the RMS processing of the software. The identification of a good correlation between both data sets is a solid foundation which provides confidence in the further use of the processing algorithm.

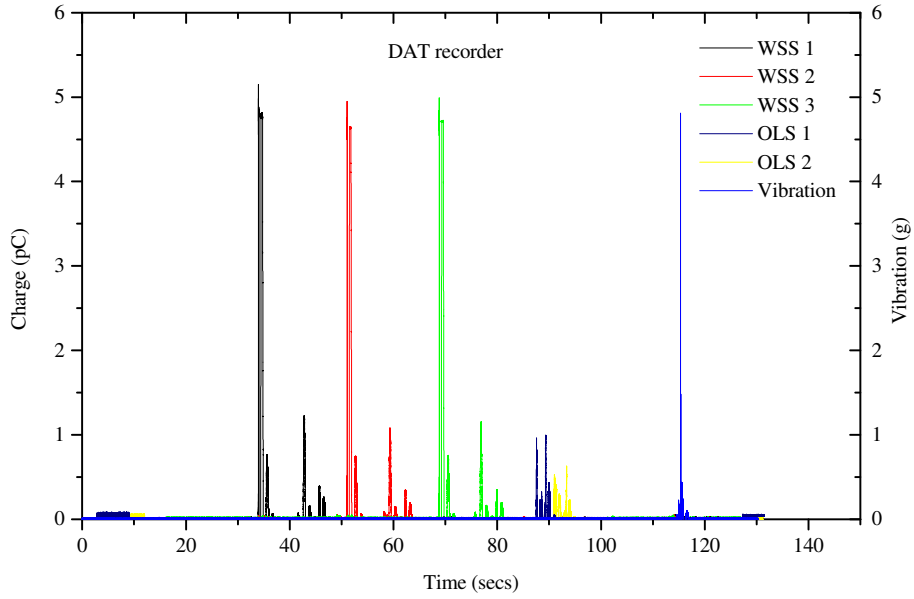

Figure 4.12 Raw signatures from the DAT recorder.

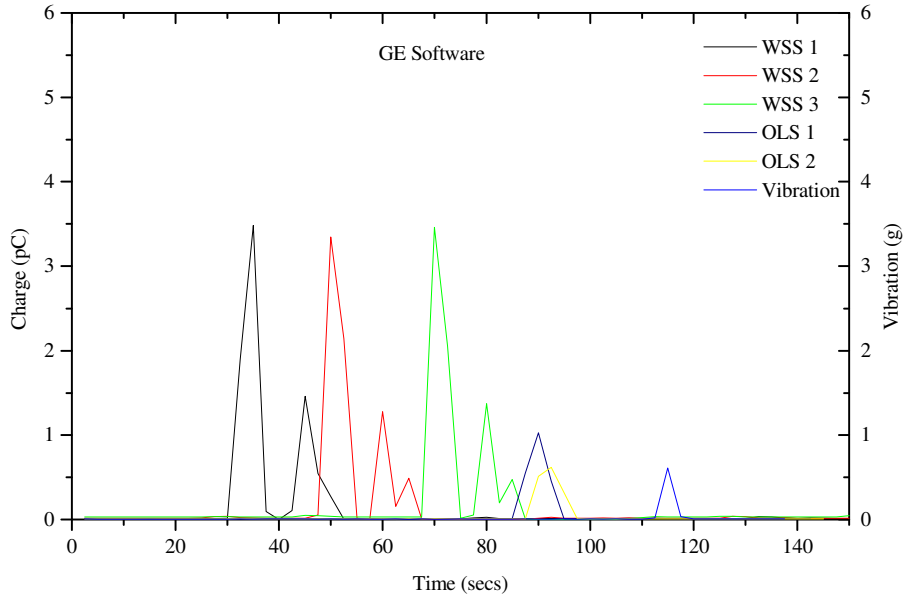

Figure 4.13 Raw data from the Smiths software.

4.4 Off-line wear debris analysis

The combination of off-line wear debris technologies were employed for the first time to monitor the evolution and earliest signs of bearing wear. Oil samples taken at a drain point which was a ball valve type. The drain was positioned after the OLS and before the inductive and ferromagnetic sensors so that turbulence generated whilst

opening the drain would not affect the charge reading by the OLS. At the start of every test, the oil used in any previous tests was removed. After the used oil was removed, 5 litres of new oil was added to the sump and pushed around the recirculation line. This oil was also removed and was carried out to try and flush additional debris that may be retained in the system.

The process of taking an oil sample consisted of removing a volume of oil (180 ml) at the drain point, and then collecting the sample (180 ml) for analysis. This ensured that the analysed sample did not consist of debris that may have accumulated in the drain point between samples. From any test there was no more than 25 oil samples taken throughout testing, thus the removal of the oil samples had no effect on the lubricated conditions within the bearing test chamber.

The off-line techniques are described in Table 4.3 and include the PODS, which for the first time is being utilised for the identification of rolling element bearing wear. Further wear debris correlations are obtained using ferrography, SOAP and electron microscopy.

Oil (ml)	Analysis Contents	Standard	Model (Company)
0	Wear debris imagery	N/A	SEM SSX-550 (Shimadzu)
0	Wear debris imagery	N/A	BH-2 (Olympus)
20	Wear severity Index	N/A	Ferrograph Analyzer (Tribotex)
30	Particle distribution	NAS 1638	HIAC PODS (Ultra Analytics)
50	SOAP	ASTM D5185	ICP8100 (Shimadzu)

Table 4.3 Off-line analysis from the oil samples which were conducted by Tribotex at their facility in Nagoya, Japan.

4.4.1 PODS

The high accuracy (HIAC) type 2 PODS, which is described in section 3.2.5.4, was selected due to its sensitivity of debris in bin sizes from 5 – 100 µm. Before processing, the collected sample (30 ml) is placed in an ultrasonic bath for 30 seconds to disperse the wear particles throughout the oil and to remove air bubbles. This

ensures that debris has not settled in the sample and that the air bubbles are not identified as debris.

4.4.2 Ferrography

Ferrography calculations of wear volume, wear rate and severity index identify the relationship between normal small and abnormal large debris, which is described in section 3.2.5.2 In this project we identify large abnormal wear particles as > 15 µm and normal small wear particles < 5 µm [140]. These particle sizes were selected in accordance with ISO 4406 which identifies 5 µm and 15 µm as the key sizes in evaluating contamination; 5 µm indicating non wear products such as silt and 15 µm related to wear effects [72, 74].

4.4.3 SOAP

The SOAP operation is shown in section 3.2.5.3. In this project the inductive coupled plasma-optical emission spectroscopy (ICP-OES) 8100 model from the Shimadzu Company was used. The oil sample is passed into a nebuliser by a peristaltic pump and then injected into a plasma torch which is surrounded by a high frequency inductive coil. The coil excites the sample to an elevated state, and as the elements relax to a lower state they emit radiation at characteristic wavelengths. The wavelengths are representative of element content. A spectrometer is used to separate the light emitted and is detected using a photo multiplier tube (PMT). The element detection is then measured as a parts-per-million (ppm) of oil.

4.4.4 Scanning electron microscope (SEM)

The debris images from the ferrograph were captured using a SSX-550 Shimadzu SEM. Preparation included the sputtering of gold on the glass slide which was non-conductive. The glass samples were then analysed for debris content. Post test bearing analysis used the JSM 6500F SEM, at the nCATS facility. The bearings were cleaned in an ultrasonic bath with the areas of interest sectioned to allow for sample holding before being inspected.

5 Tapered Roller Bearing Testing

5.1 Introduction

This chapter details tapered roller bearing tests that were designed to monitor the evolution of wear and early signs of distress. The experimental program incorporated an in-line, oil-line and off-line multi-sensing strategy using traditional and novel CM techniques. The purpose of the multi-signature set-up was to use correlating evidence from the combined techniques so that confident assessments of distress could be made. The test conditions and techniques are shown in Table 5.1.

There were six tests conducted and three representative tests are shown in this chapter. The tests include a normal bearing operation (Test 1), outer race spallation of a support bearing (Test 3) and inner race spallation of a test bearing (Test 5). The remainder of the results are located in Appendices E, F and G, and are Tests 2, 4 and 6, which show inner race failures. These tests are located in the Appendices to reduce repetition when describing the distress mechanisms and signature activities, as similar trends and levels were identified throughout the programme. However, since similar sensing characteristics were obtained during a number of tests, this shows good repeatability in the results.

There were some modifications to the sensing arrangement during progression of the experimental program. These include the use of Macom TA 10 and TA 20 particle counters in Tests 1 – 3, which were removed in Tests 4 – 6. These changes were made as Macom saw the electrostatic products as competitors to their technologies. Therefore, the use of the Macom products was prohibited. The Macom units were replaced by a Pancom AE piezo-electric sensor. This technology was selected to provide an indication of tribological activity, i.e. crack development, impacts between defective elements or debris over-rolling in the contact, which may occur in advance of debris detection by the Macom sensors.

	Test 1	Test 2	Test 3	Test 4	Test 5	Test 6
Location of analysis in thesis	Section 5.2	Appendix E	Section 5.3	Appendix F	Section 5.4	Appendix G
Rotational speed (rpm)	2500	2500	2500	2500	2500	2500
Hertzian contact pressure (GPa)	2.5	2.5	2.5	2.5	2.5	2
Defect type	None	Inner race indentation of bearing #2	Inner race indentation of bearing #2	Inner race indentation of bearing #2	Inner race indentation of bearing #2	Inner race indentation of bearing #2
Reason for test	Identify baseline conditions	Identify failure with off-line debris analysis	Off-line debris analysis throughout the test	Analysis with the addition of AE sensing	Analysis with optimum AE threshold	Failure identification under different contact pressure
In-line techniques in the bearing test chamber	WSS, accelerometer, thermocouples	WSS, accelerometer	WSS, accelerometer, thermocouples	WSS, accelerometer, thermocouples, AE	WSS, accelerometer, thermocouples, AE	WSS, accelerometer, thermocouples, AE
Oil-line techniques	Thermocouples, OLS, Macom TA 10 and TA 20	Thermocouples, OLS, Macom TA 10 and TA 20	Thermocouples, OLS, Macom TA 10 and TA 20	Thermocouples, OLS	Thermocouples, OLS	Thermocouples, OLS
Off-line debris analysis	PODS, severity index, SOAP, electron microscope	PODS, severity index, SOAP, electron microscope	PODS, severity index, SOAP, electron microscope	PODS, severity index, SOAP, electron microscope	PODS, severity index, SOAP, electron microscope	PODS, severity index, SOAP, electron microscope
Failure detected	None, since this was defect free	Inner race failure at the indented bearing	Failure at outer race of support bearing #4	Inner race failure at the indented bearing	Inner race failure at the indented bearing	Inner race failure at the indented bearing

Table 5.1 Test conditions and sensing techniques employed during the tapered roller bearing tests.

5.2 Baseline characteristics (Test 1)

The following results show baseline conditions using the techniques that were described in Test 1, Table 5.1. The results are arranged according to the locality of distress, i.e. test chamber, oil-line and off-line.

5.2.1 Distress in the bearing test chamber

Figure 5.1 shows the sensor activity from the techniques in the test chamber. From the start of the test the WSS's detected increasing charge levels up to 1 pC. The mechanisms of charge are attributed to running-in wear, which was for the first 4 hours. Running-in is a highly dynamic process, described in section 2.5, where the interaction of the largest asperity peaks results in localised pressure at the contact interface. This results in plastic flow and rupture of the irregularities over the surface depressions [70]. Smoothing of the surface roughness enables the opposing elements to conform. Sources of charge include the generation of CPD between discrete areas of nascent and original material during deformation and debris liberation from the parent surface. Additional charging mechanisms include debris entrainment and interaction between the bearing elements [203]. These mechanisms are described in section 3.2.8.

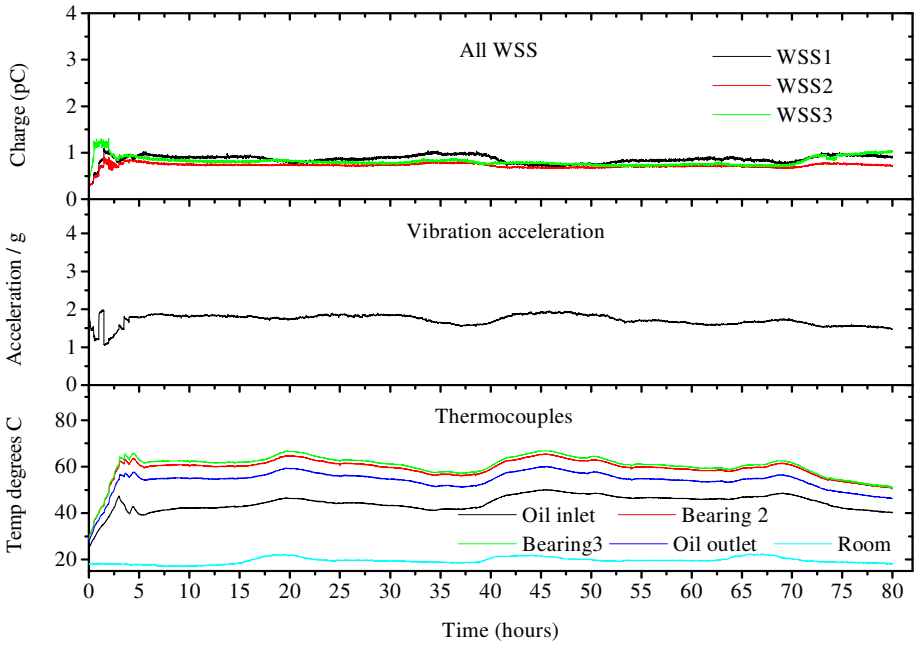

Figure 5.1 The WSS, accelerometer and thermocouple trends from Test 1 incorporating a mean Hertzian contact pressure of 2.5 GPa.

Fluctuating acceleration was detected by the vibration sensor. The dynamic vibration activity is also related to loading, which is associated with asperity deformation mechanisms and debris entrainment between the bearing elements. The tribological activity produces impulse shocks that are transmitted to the surrounding structure and sensor. The dynamic acceleration levels were between 1 – 2 g for the first 4 hours of testing, which showed a good correlation with dynamic wear site charge during running-in.

The thermocouples identified linearly increasing temperature trends which related to frictional heating in the Hertzian contact. The maximum oil inlet temperature was 50°C, bearing outer race temperatures were around 65°C and the oil outlet temperature was 60°C.

The dynamic/increasing sensor activity in the test chamber, which related to running-in, was followed by steady state charge and acceleration levels of 1 pC and 2 g respectively. The thermocouples also attained steady state levels with an oil inlet temperature of 50°C, bearing outer race temperatures around 65°C and an oil outlet temperature of 60°C. The combined steady state sensor activity indicated a transition into benign wear. This can be attributed to smoothing of the surface roughness, which has a positive effect on bearing functionality, as the surfaces become completely separated by the lubricating film. An increase in the λ ratio, which is likely to be between 3 – 10, allows EHL and benign wear conditions to prevail, as described in section 2.3.2. However, there were minor fluctuations observed from all sensors, which related to the daily room temperature cycle. The room temperature changes influence oil temperature which modifies fluid viscosity, which affects the film thickness and thus friction, resulting in the varying signature characteristics.

5.2.2 In-line wear debris detection

Heightened oil-line charge with maximum levels of 0.1 pC and a peak indicator value of 4000 were identified at the start of the test, as shown in Figure 5.2. The accentuated sensor activity is associated with running-in and related to debris entrainment in the oil-line. Debris liberation requires the breaking of multiple atomic bonds and yields a net charge on both the parent surface and detached material. The charged debris

entrained in the oil flow leads to charge detection by the OLS [204] and indicator value[1]. Further oil-charging mechanisms include charged debris generation after entrainment in the contact [203] and an increasing temperature that reduces fluid viscosity, which increases ionic mobility and leads to increased levels of tribocharging [183].

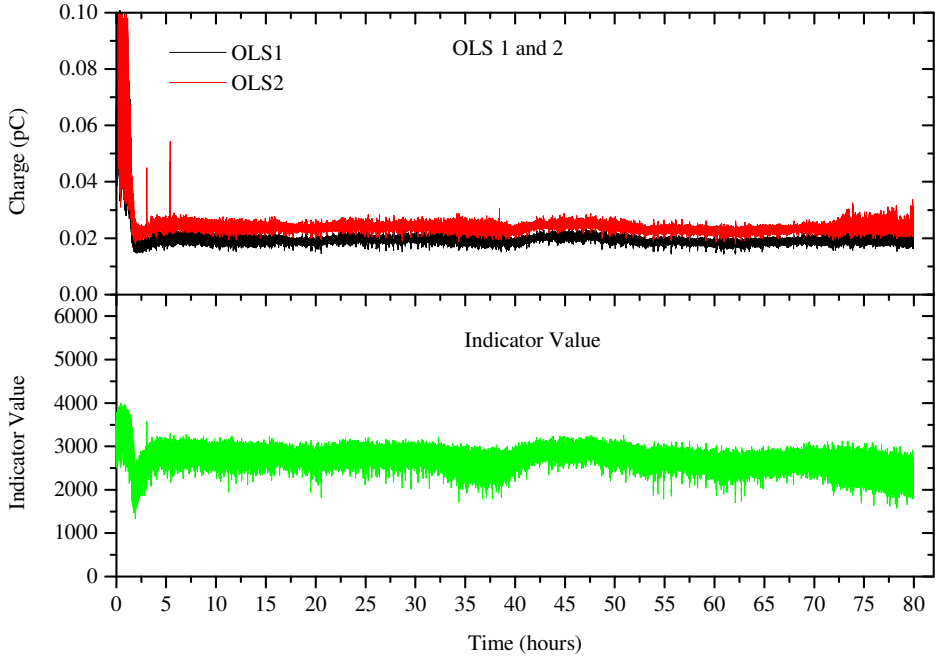

Figure 5.2 The OLS and indicator value.

After running-in there was a reduction in OLS charge, with OLS 1 and 2 indicating 0.025 and 0.02 pC respectively. There was also a reduced indicator value to 2700. The reduced sensor levels indicate a decrease in wear rate during the development of EHL and benign wear. The OLS charge and indicator levels then remained relatively stable for the remainder of the test, indicating continuation of a normal bearing condition.

There was no debris detection by the Macom TA 10 and TA 20 throughout this test, which may be due to particle levels that were below the sensitivity of the techniques. Therefore, these senor traces are not shown.

[1] The increased indicator value is due to slower moving debris than the oil flow, producing a greater time lag which is detected by the cross-correlation algorithm. This process is described in section 4.5.

5.2.3 Off-line wear debris detection

Figure 5.3 shows that at 1.5 hours, the PODS was dominated by the 5 – 15, 15 – 25 and 25 – 50 µm debris count of 5250, 300 and 100 particles respectively. At 3 hours there was a significant reduction in debris count from these bin sizes to 2700, 150 and 40 particles. In the next oil sample at 5.5 hours, the 5 – 15 µm particle count further reduced to 2500, whilst there was a slight increase in the 15 – 25 and 25 – 50 µm count to 200 and 80 particles. Further sampling at 10 hours shows reductions from these bin sizes to 1500, 90 and 70 particles which remained for the rest of the test.

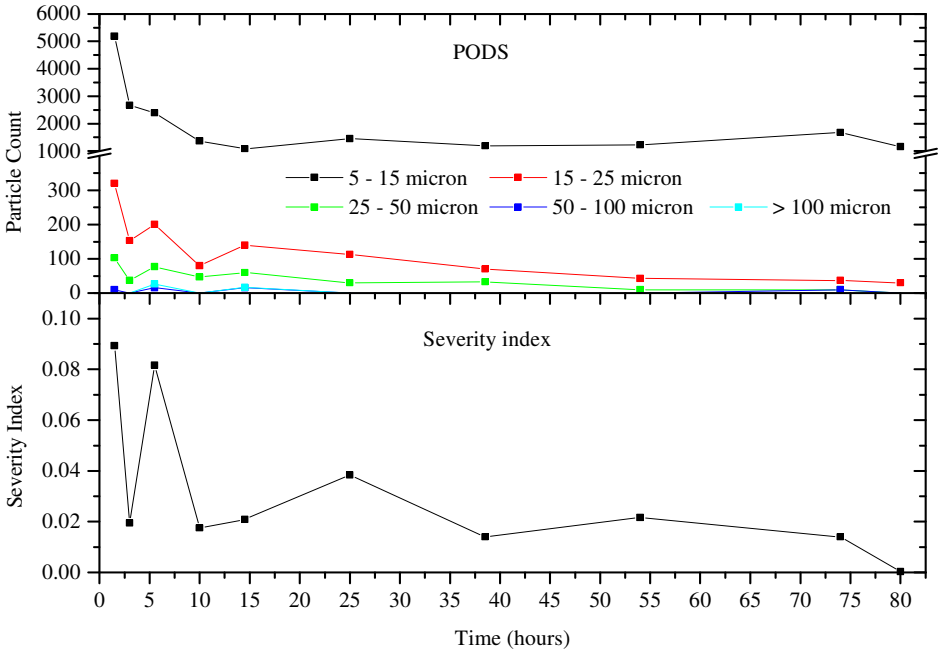

Figure 5.3 The PODS and severity index, with the sample time indicated by the box.

A good correlation is seen between the PODS, OLS charge and indicator value as the maximum debris and charge levels were observed during running-in, which then reduced and attained steady-state levels until completion of the test. A similar trend was observed by the severity index. From 1.5 – 3 hours there was a rapid decrease in value from 0.09 – 0.02. This was followed at 5.5 hours by a significant increase to 0.08, which correlated with the slight increase in 15 – 25 and 25 – 50 µm PODS particle counts. At 10 hours there was a reduced severity index to 0.02 which reminded for the duration of the test. There was no detection of iron by SOAP, as the debris levels were not within the sensitivity of the technique [153] and therefore this trend is not shown.

5.2.4 The evolution of debris

Figure 5.4 shows the evolution of debris morphology which are taken from the ferrograph slide by the SEM. The majority of particles are plate-like and are around 5 μm in size. However, there are some particles that are around 20 μm as shown in (c – d). A mechanism of plate-like debris formation includes surface crack initiation and coalescence after repeated cyclic stresses during contact loading, with particle delamination from the surface [205]. A further source of this type of particle generation emanates from asperity interaction and tangential motion of the bearing surfaces relative to each other. This results in high shear stress at the contact interface with the rupture of surface protrusions and the formation of debris that becomes over-rolled into thin plate-like particles in the Hertzian contact. These particles are also associated with the exfoliation of surface material from the shear mixed layer, as shown in Table 2.3.

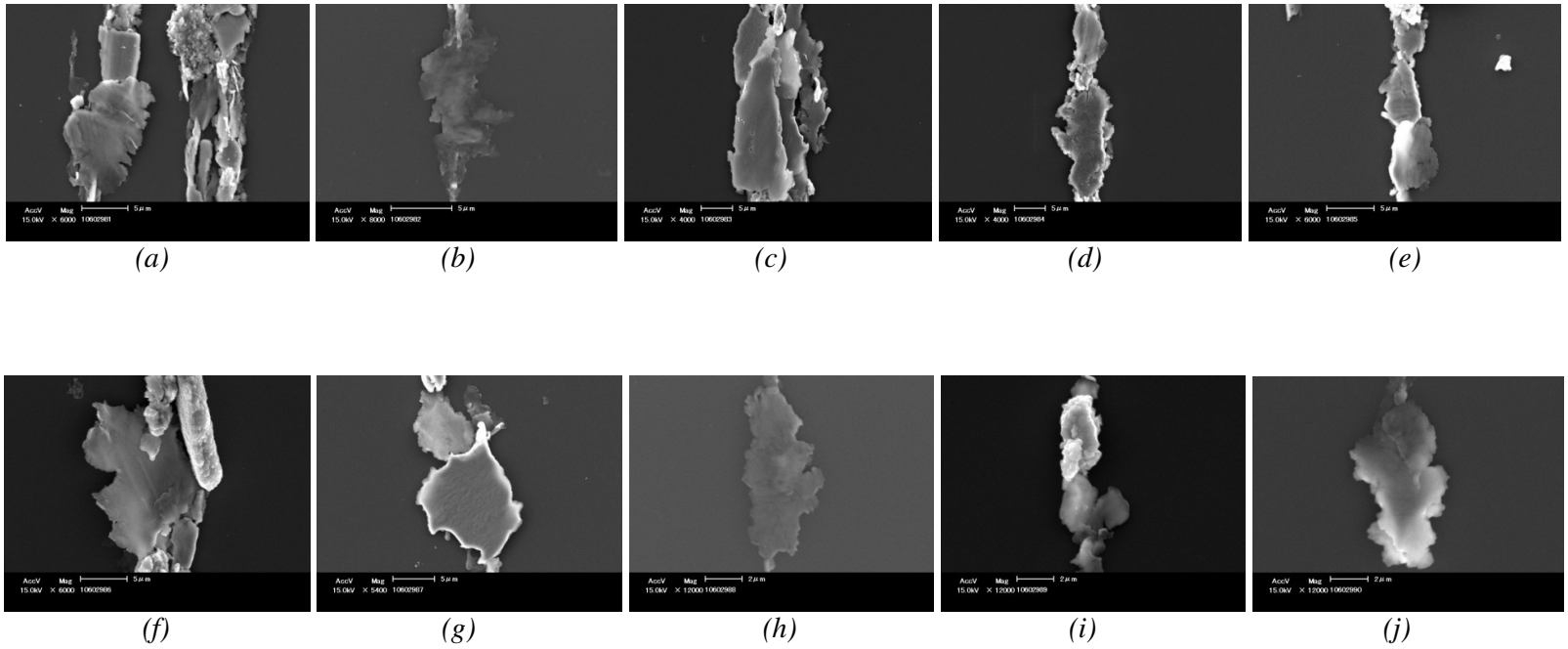

Figure 5.4 The features of the wear debris at (a) 1.5 (b) 3 (c) 5.5 (d) 10 (e) 14.5 (f) 25 (g) 38.5 (h) 54 (i) 74 and (j) 80 hours which were taken from the ferrograph slide.

Figure 5.5 shows the debris retrieved from the Macom TA 20 at the end of the test. The debris is dominated plate-like particles smaller than sub 20 μm. These debris types are consistent with the particles collected in the oil samples throughout the test. There was also a single large 50 μm particle and was likely to be formed during running-in due to the increased in-line, oil-line and off-line sensor activity at this time.

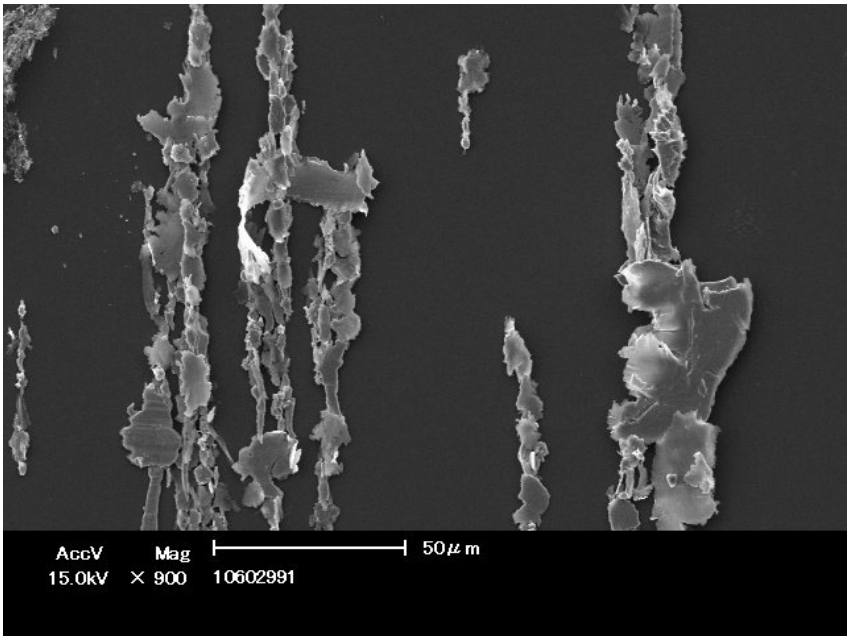

Figure 5.5 Debris retrieved from the Macom TA 20 on completion of the test.

5.2.5 Gravimetric analysis

Gravimetric analysis from Test 1, shown in Table 5.2, indicated that the greatest mass loss was observed on the cone assembly of bearing 4. This may be an indication of oil flow within the test chamber with debris entrainment around this bearing which caused the greatest levels of wear and mass loss. The mass loss to the reminder of the bearings was comparable with observations in a previous test [197].

Gravimetric analysis						
	Pre gravimetric (g)		Post test gravimetric (g)		Δ (mg)	Δ (mg)
	Cup	Cone	Cup	Cone	Cup	Cone
Bearing 1	61.1334	116.65044	61.13224	116.64409	1.16	6.35
Bearing 2	61.02045	116.51866	61.01939	116.50891	1.06	9.75
Bearing 3	61.09645	116.52825	61.09607	116.52714	0.38	1.11
Bearing 4	61.05285	117.17384	61.05252	117.15682	0.33	17.02

Table 5.2 Gravimetric analysis after a normal bearing operation from Test 1.

5.3 Failure of a support bearing (Test 3)

The following results are shown from Test 3, in which the experimental set-up is described in Table 5.1. The results are arranged in accordance with the flow of Test 1, which shows the sensor activity in the test chamber, oil-line and off-line.

5.3.1 Distress in the bearing test chamber

During the initial 7 hours, dynamic charge was detected by the WSS's as well as heightened levels of vibration and increasing thermocouple trends, as shown in Figure 5.6. These sensor levels were of similar magnitude to the observations in tests 1 and 2, which shows good repeatability in the techniques. After the running-in period, all signatures maintained steady state levels, indicating the transition into benign wear, which lasted to 53.5 hours.

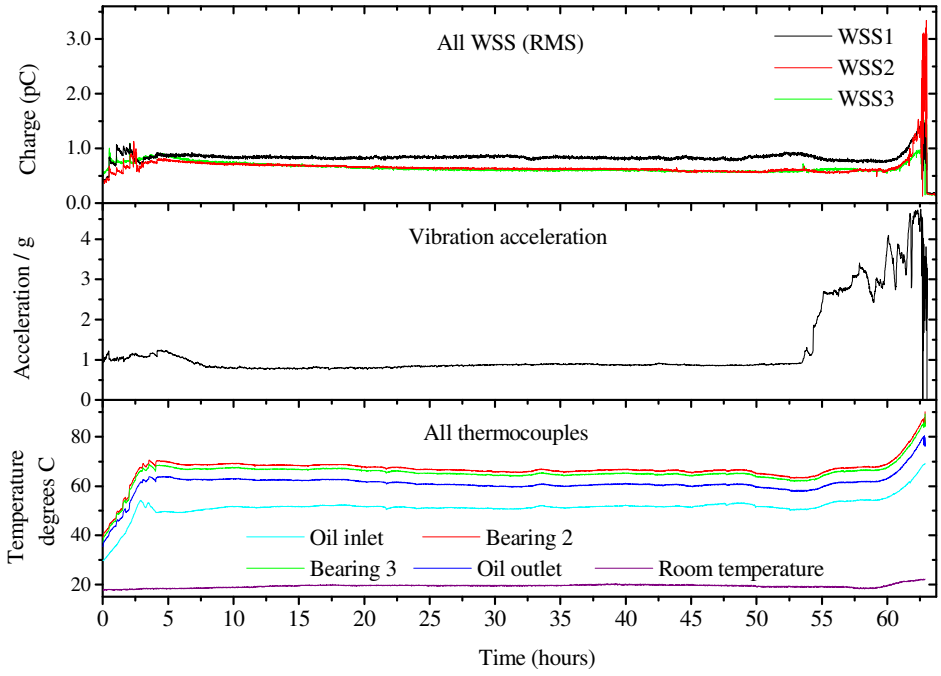

Figure 5.6 WSS, accelerometer and thermocouple trends from Test 2, incorporating a mean Hertzian contact pressure of 2.5 GPa.

In Figure 5.7, an expansion of the wear out stage shows that at 53.5 hours there was a significant perturbation in charge from WSS 3, indicating distress at bearing 4, which was accompanied by an increase in acceleration. This was followed by a relaxation in charge to the baseline level, whilst there were increasing acceleration and

thermocouple trends to a time of 55 hours. Between 55 – 60 hours, charge, acceleration and thermocouple levels remained fairly constant which were likely to indicate healing of the roughened wear site by smoothing of the sharp edges at the wear scar. This was previously shown by Williams [2] and Kotzalas and Harris [50]. From 60 hours onwards, charge, acceleration and thermocouple levels steadily increased for the remainder of the test. The maximum charge level was 1.5 pC with acceleration of 5 g. The increasing trends from these techniques indicated damage propagation, which was supported by increased thermocouple activity. The thermocouple levels were greater than 10°C above the baseline levels, which according to Neale [126], indicated an abnormal operation. The combined analysis provided substantial evidence of the wear out phase, characterised by the increasing sensing trends from the benign wear regime. The runaway sensor activity is consistent with the wear out phase identified by the bath-tub curve [69].

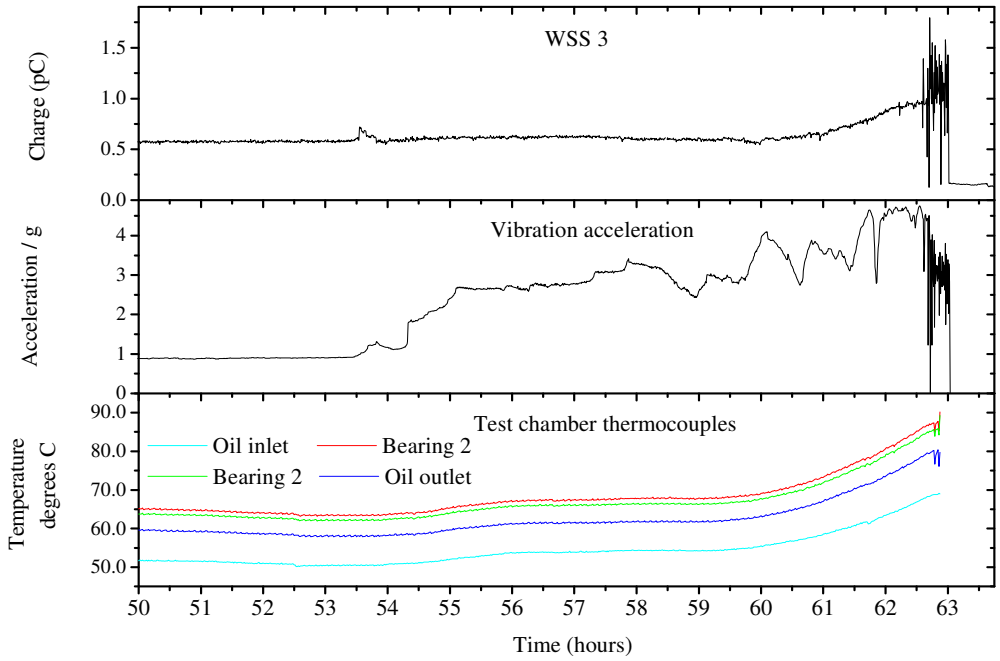

Figure 5.7 Expansion of wear site sensor 3, acceleration and thermocouples during the wear out period.

5.3.2 In-line debris detection

During running-in, which lasted until 7 hours, heightened OLS charge and indicator values were observed, as shown in Figure 5.8. The maximum sensor values were of similar magnitude with the baseline test with peak charge levels around 0.07 pC and an indicator value around 4000. The increased sensor activity related to increased

debris in the oil-line and some contribution from tribocharging. Following running-in, the OLS and indicator values decreased to steady-state values of 0.02 pC and 2000 respectively. The reducing and steady-state sensor trends indicated a transition into benign wear which lasted until 54 hours.

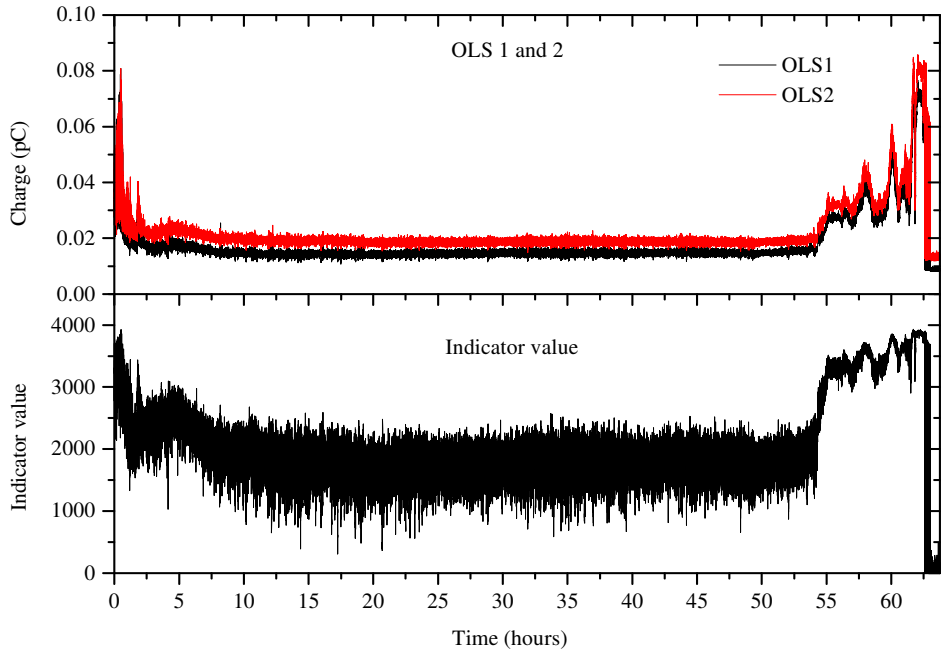

Figure 5.8 The OLS and indicator value trends.

There was a 30 minute time-lag between the increased sensor activity in the test chamber and in the oil-line. However, in a previous test by Harvey *et al* [197], the time delay between these techniques was 2.5 hours. Explanations for the differences in time-lag may be attributed to varying levels of debris production during the initiation of wear out, which are different during each bearing failure. Further reasons for the time-lag may include different charge levels of the debris, due to size, shape and surface area and times of flight for the particles to get to the bore of the sensor, since it is not clear how long the debris is retained in the test chamber before entrainment in the oil-line.

An expanded time-line of wear out phase (50 hours to the end of the test) is shown for clarity in Figure 5.9. At 54 hours, there was an increase in OLS charge and indicator value, which related to debris entrainment during spallation of support bearing 4. The OLS charge and indicator value increased until a time of 55 hours and then remained

relatively stable until 60 hours. The increased and then stable sensor behaviour is consistent with the in-line sensors in the test chamber, which was attributed to healing, or smoothing of the sharp edges of the wear scar. At 60 hours there was a significant perturbation in OLS charge that correlated with the increased sensor activity in the test chamber, which indicated further damage and debris generation. At 61.5 hours there was a rapid increase in oil-line charge which persisted to the end of the test, which was related to propagating damage. The peak oil-line charge levels were around 0.08 pC, which was of similar magnitude to maximum levels identified in the previous test [197], which confirmed runaway wear. During the wear out period, the indicator value clearly identified a distinction between the benign wear regime and the failure, with increasing values from 2000 – 4000. This was comparable to the indicator value shown Appendix E, which identified a steady-state value of 2500 during a normal operation and an increasing trend to 3500 during failure.

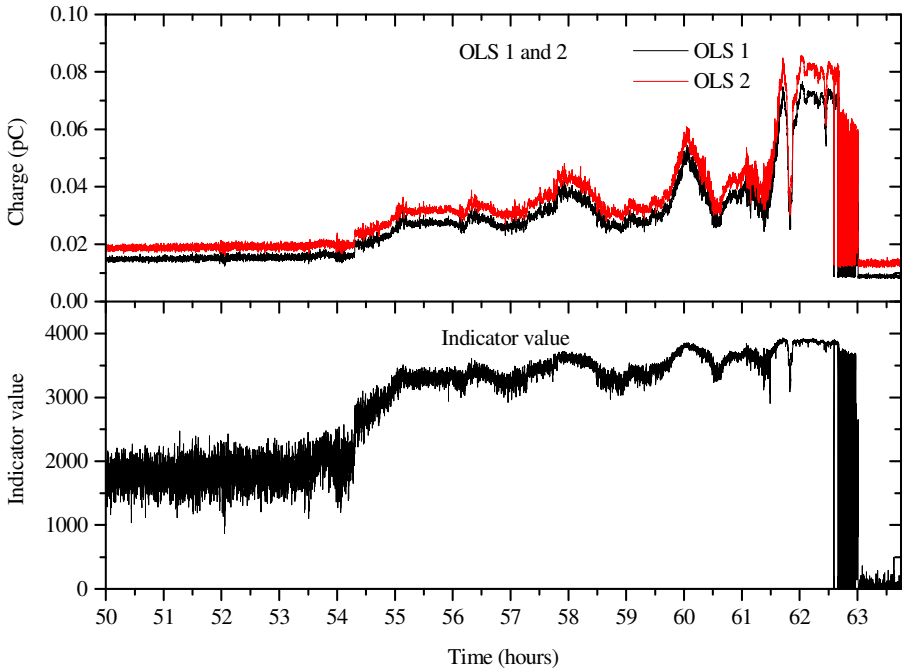

Figure 5.9 Expansion of the OLS and indicator value from 50 hours to the end of the test.

Figure 5.10 shows that from the TA 10 there were single particle counts detected by all bin sizes during the initial 3.5 hours, providing support of particle generation during running-in. There was no debris detection by the TA 20 during this time. At 43 hours there was a single sub 100 µm debris count by the TA 10. The detection of a

single sub 100 µm particle count from an individual technique does not provide any conclusive evidence of bearing damage, but may be a possible time of distress activity. However, corroborating evidence of distress is shown in the following sections by the off-line analysis, with increased 5 – 15 µm debris count by the PODS, morphology features of the wear particles and the advanced processing architectures. Further evidence of precursor activity using Macom technologies was shown in [197]. However, the bearing damage in this test was identified at 50 hours by an increased debris count of 10 particles by the Macom TA 20.

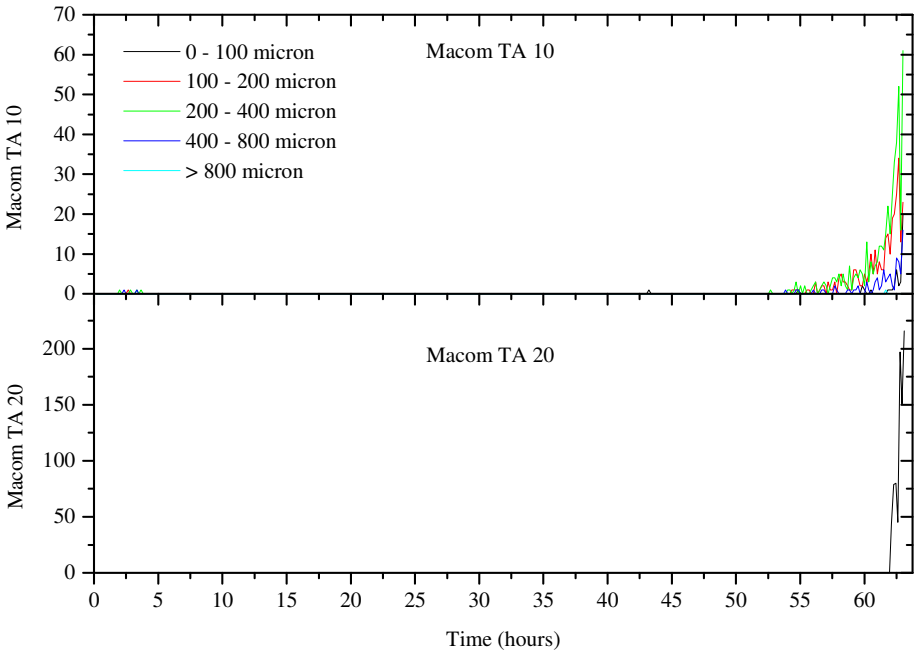

Figure 5.10 Macom TA 10 and TA 20 particle counts.

Figure 5.11 shows that at around 53 hours there was an increase from the bin sizes between 100 – 800 µm detected by the Macom TA 10, which provided support of the wear out phase. Therefore, the time of debris detection by the inductive sensor was in advance of the electrostatic technologies by 1 hour. Between 55 – 60 hours, there were minor increases in debris detection by the 100 - 800 µm bin sizes, which correlated with stable in-line sensor activity in the test chamber and in the oil-line, which was attributed to healing of the roughened contact. At 60 hours there was a significant perturbation by the 200 – 400 µm bin count which correlated with increased activity from the electrostatic oil-line sensor, which was related to a further period of damage. At 61.5 hours, there was a rapid increase in all the 100 - 800 µm

bin counts, which again showed a good correlation with the oil-line sensor, with the 100 – 400 µm bin sizes dominating. In a further test, shown in Appendix D, the 200 – 400 µm bin count also dominated during failure. The rapid increase in debris detection by the Macom TA 10 at 61.5 hours preceded rapid debris detection by the Macom TA 20, and was associated to damage propagation.

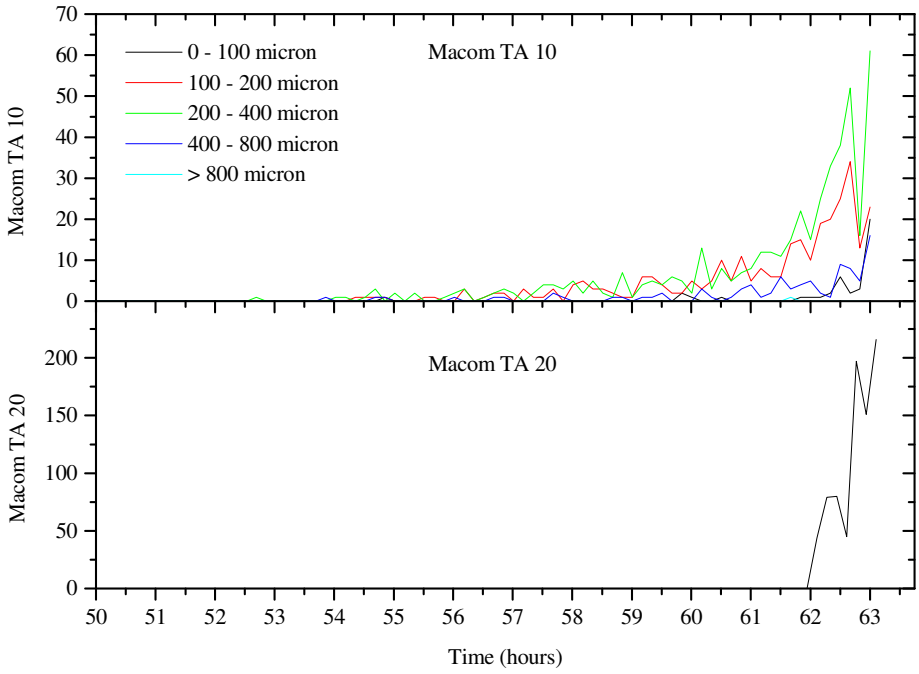

Figure 5.11 Expansion of the Macom TA 10 and TA 20 particle counts.

5.3.3 Off-line wear debris analysis

During running-in, there was heightened debris detection by the PODS, as shown in Figure 5.12. The initial sample at 2 hours was dominated by a 5 – 15 µm debris count of 7000 particles. There were also heightened 15 – 25 and 25 – 50 µm debris counts of 630 and 220 particles respectively. In the preceding samples there was a decreasing trend from the dominating 5 – 15 µm debris count, which maintained steady-state levels below 4000 particles. The 15 – 25 and 25 – 50 µm debris counts remained around 300 and 200 particles respectively. The heightened quantity of particles and the decreasing particle trends were consistent with the baseline test, which confirmed the transition from running-in to benign wear. During this period the severity index remained below 0.05 and there was no iron detection by SOAP, which was also similar to the sensor levels observed during benign wear in the baseline test. At 42

hours, there was a rapid increase in 5 – 15 and 15 – 25 µm debris count to almost 8000 and 850 particles respectively.

Correlations with the debris analysis of Tests 1 – 5, shows that the 5 – 15 µm particle range detected by the PODS consistently identified the early signs of distress. The analysis shows that baseline conditions were identified by a particle count below 4000 and a particle count greater than 4000 for abnormal wear. This provides further evidence that a 5 – 15 µm particle count of 8000 at this time was an early indicator (precursor) of the impending wear out phase. Corroborating evidence of degradation was shown by the single debris count by the Macom TA 10, which was at 43 hours. The abnormal debris activity was followed by a continual reduction in the 5 – 15 µm particle count to levels indicative of benign wear.

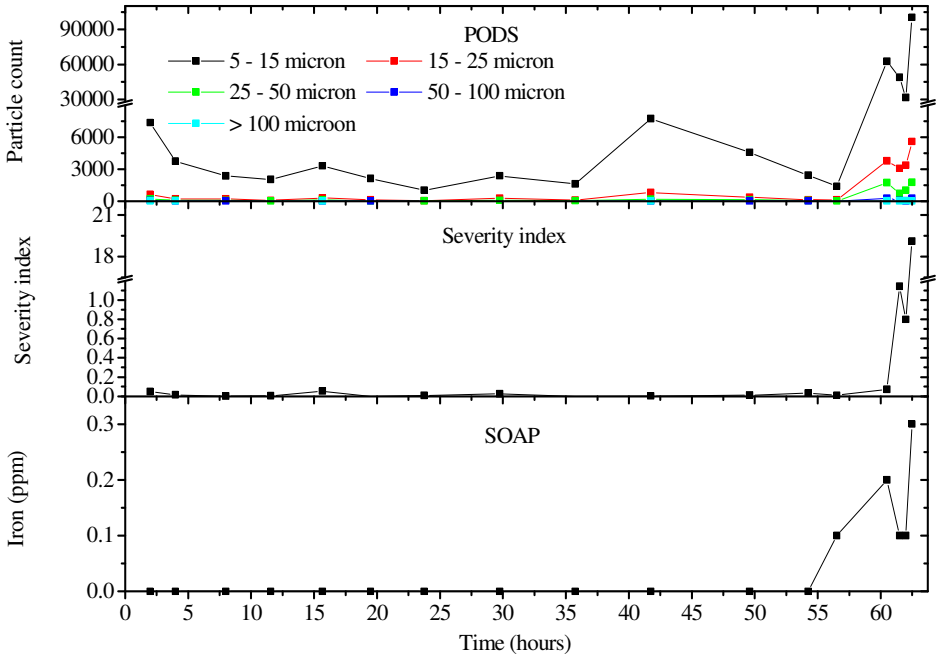

Figure 5.12 Off-line wear debris analysis detected by the PODS, severity index and SOAP.

An expansion of the wear out phase, shown in Figure 5.13, indicates an increase in iron levels to 0.1 ppm at 56.5 hours. Other tests also indicated that iron levels of 0.1 ppm or more identified abnormal wear, shown in Appendices D and E. At 60.5 hours there was a further increase in iron to 0.2 ppm, an increase in severity index to 0.1, a rapid increase in 5 – 15 µm debris to more than 60000 particles as well as increased

15 – 25 and 25 – 50 µm debris. The increased debris detection at this time correlates with the in-line and oil-line techniques, which was attributed to bearing damage. At 61.5 hours, a time when the in-line and oil-line techniques identified propagating damage, there was a rapid increase in the severity index, which was observed with reductions in 5 – 15 µm particle count and iron levels. Therefore, the increased severity index correlating with a reduced PODS and SOAP particle count suggests a shift to the generation of large debris particles. At the end of the test there was a further rapid increase in all the off-line techniques, with a 5 – 15 µm debris count of around 100000 particles, a severity index of 20 and iron levels of 0.3 ppm. The combined analysis provided further confirmation of propagating damage as the debris parameters were at the maximum levels compared to any other time of the test.

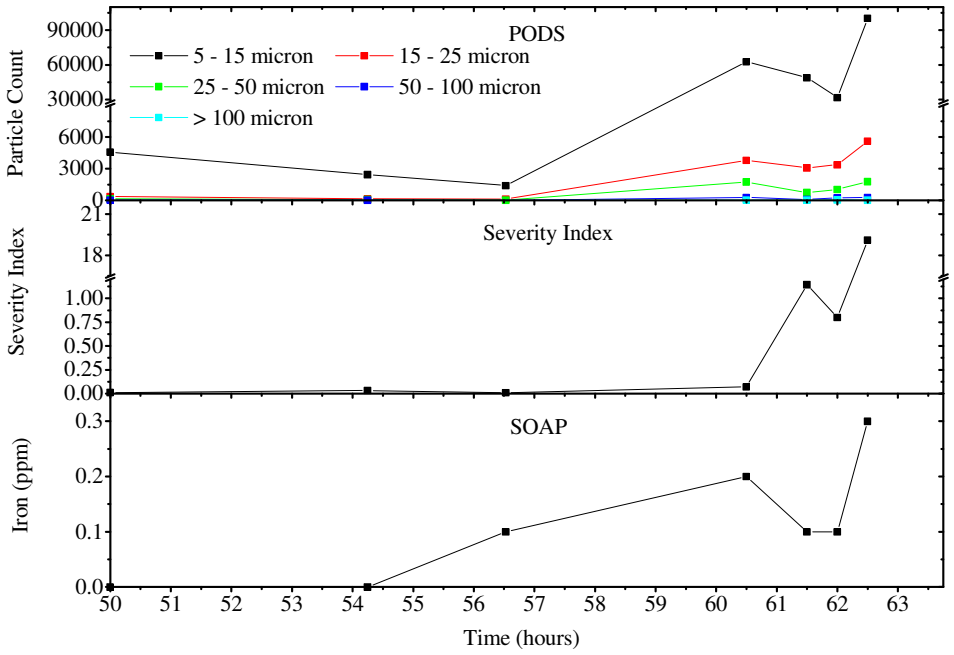

Figure 5.13 Expansion of the off-line wear debris analysis.

5.3.4 The evolution of debris

The wear particles were mainly below 20 µm in size, with the majority around 5 µm. During running-in, shown in Figure 14 (a – b), plate-like debris were around 15 µm with a smooth surface and irregular circumference. The identification of these particles was consistent with the debris that was detected in the baseline test during the running-in period. In Figure 5.14 (c - i) the plate-like debris were around 5 µm and were again consistent with the debris observed in the baseline test, which indicated

benign wear. At 42 hours, the main feature of the debris was a rough surface and jagged profile which were around 12 µm, as shown in Figure 5.14 (j). This particle was indicative of localised welding in the Hertzian contact, where the plucking out, transfer and detachment of material gives rise to the rugged particle morphology [87]. An adhesive mechanism confirms an abnormal operating condition, which was consistent with the increased particle count detected by the PODS and Macom TA 10 at this time. Further evidence of an adhesive mechanism is identified in the next couple of samples, shown in Figure 5.14 (k - l), with the detection of 3 µm spheres amongst the plate-like debris. In Figure 5.14 (m), which is at the time of initiation of the wear out phase, the 5 µm plate-like debris dominate. However, from Figure 5.14 (n – q) it is evident form that there is an increased quantity of debris when compared to all previous samples. The debris consisted of plate-like debris, some of which are as large as 25 µm, which according to Roylance [72] is typical of particles detected during fatigue failure. There were also individual 3 µm spheres, providing support of an adhesive mechanism, during boundary conditions from oil-film breakdown after roughening of the Hertzian contact. These particle types were also observed during failure of Test 2, shown in Appendix E.

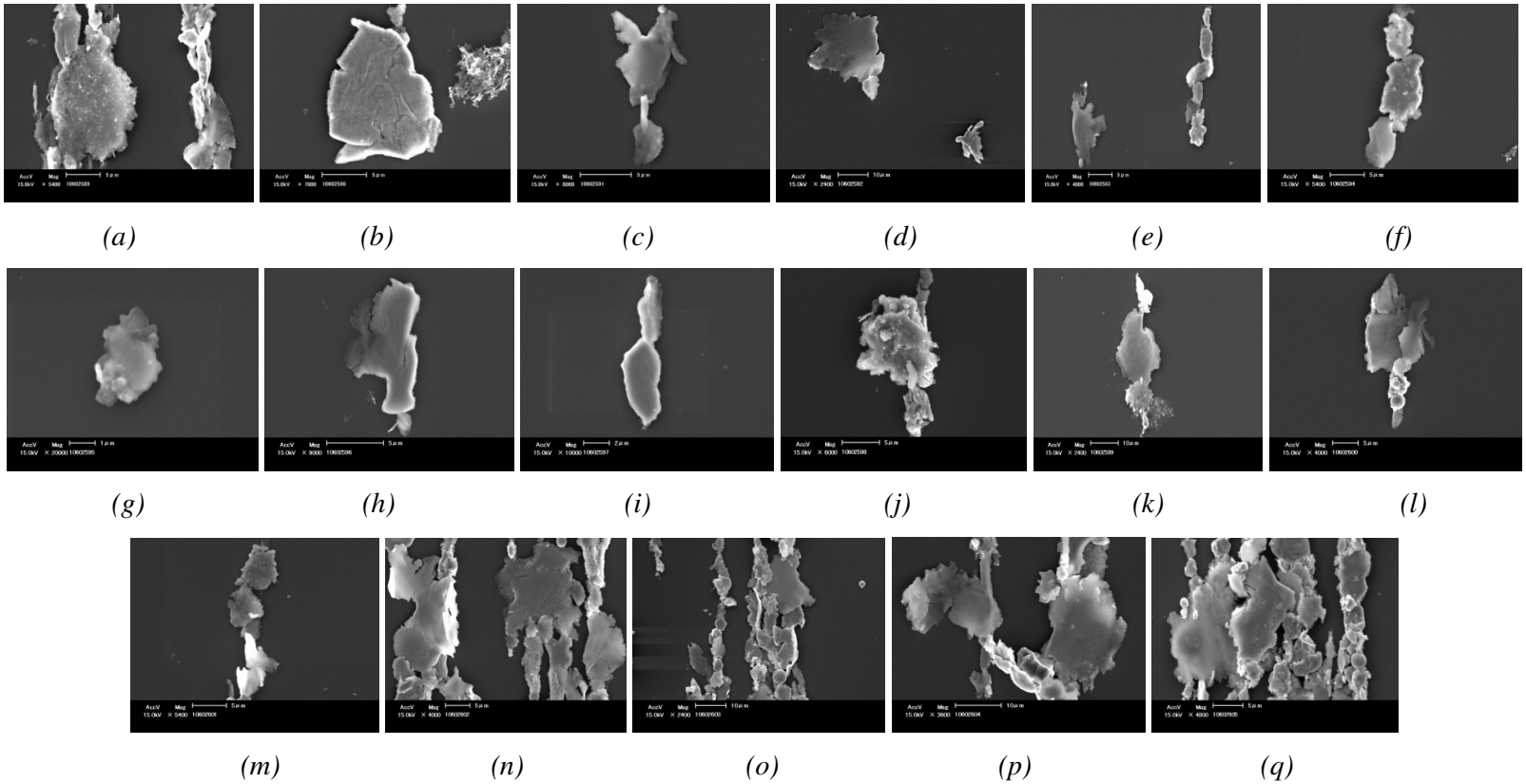

Figure 5.14 The evolution of debris morphology in which each image is taken from the debris sample of time which is indicated in Figure 5.12 by the closed box.

At the end of the test, the accumulated debris on the sensing head of the Macom TA 20 was retrieved, to provide further evidence of damage, as shown in Figure 5.15. The majority of debris had a plate-like morphology, between 5 – 15 µm with an irregularly shaped circumference. There was also evidence of some larger plate-like debris between 20 – 50 µm, and a single large single plate-like particle of approximately 150 µm. Therefore, the evolution of debris was consistent with the PODS particle count, which shows that the 5 – 15 µm particle count dominated, with reducing particle numbers as the bin size increases.

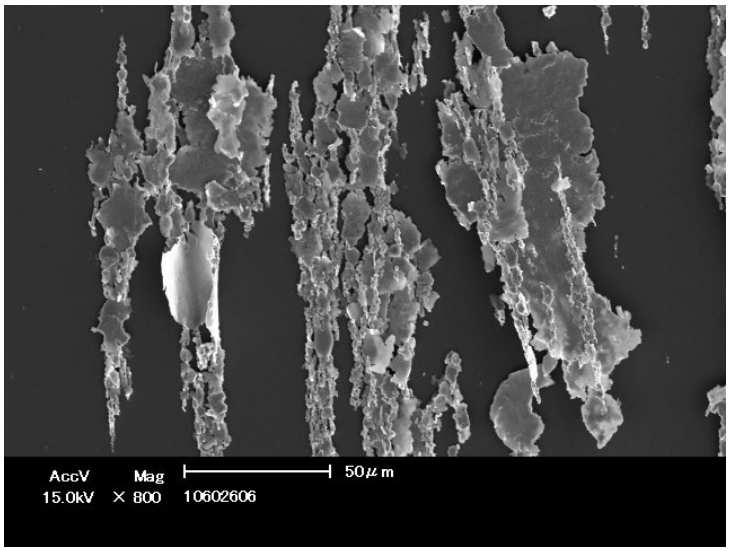

Figure 5.15 Debris accumulated on the Macom TA20.

5.3.5 Gravimetric analysis

Gravimetric analysis indicated that the highest mass loss was observed on the outer raceway (cup assembly) of bearing 4, see Table 5.3. Figure 5.16 then confirms the result of spall propagation, with the greatest damage to the outer race and some further damage to the rollers of bearing 4.

Gravimetric Analysis						
	Pre gravimetric (g)		Post gravimetric (g)		Δ (mg)	Δ (mg)
	Cup	Cone	Cup	Cone	Cup	Cone
Bearing 1	61.111	116.887	61.1108	116.879	0.2	7.93
Bearing 2	61.1432	116.72	61.1428	116.718	0.36	2.36
Bearing 3	61.1507	116.965	61.1504	116.964	0.28	0.77
Bearing 4	61.117	116.381	60.9309	116.324	186.1	57.79

Table 5.3 Gravimetric analysis.

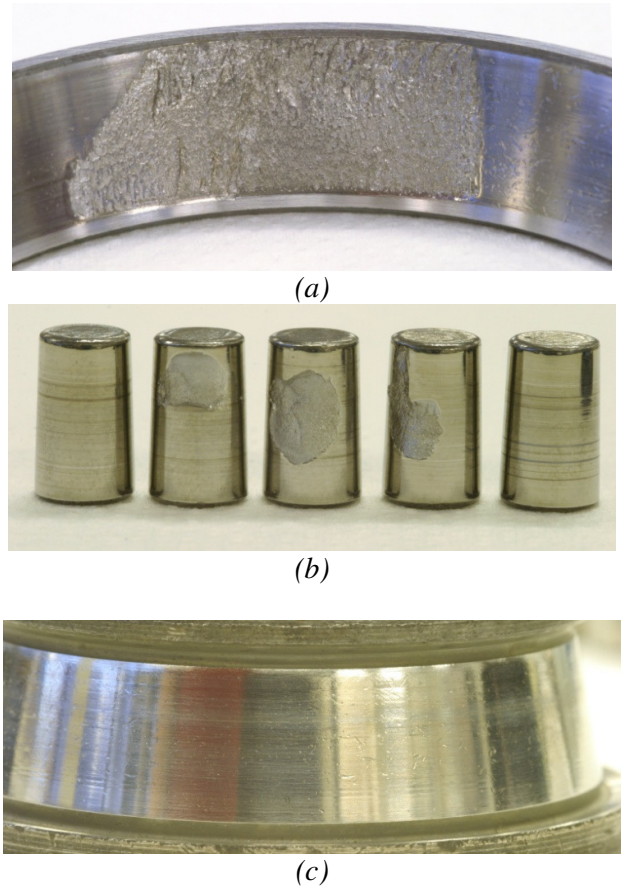

(a)

(b)

(c)

Figure 5.16 Photographic evidence of damage to bearing 4 where (a) indicates the outer race (b) rolling elements and (c) inner race.

It was originally anticipated that failure would occur on bearing 2 due to the localised stress concentration at the pre-indent. A SEM micrograph of bearing 2 is shown in Figure 5.17, which shows cracking and delamination which is associated with the initial stages of spallation. Damage was initiated on the trailing edge of the indent with respect to the direction of the rolling elements, from crack initiation due to high tensile stresses (mode 2 loading) at this location [206]. With continued bearing operation, spall propagation from this site would result in gross failure. This is corroborated by the preceding tests as the damage is shown to propagate form the indent, in the direction of the rolling elements.

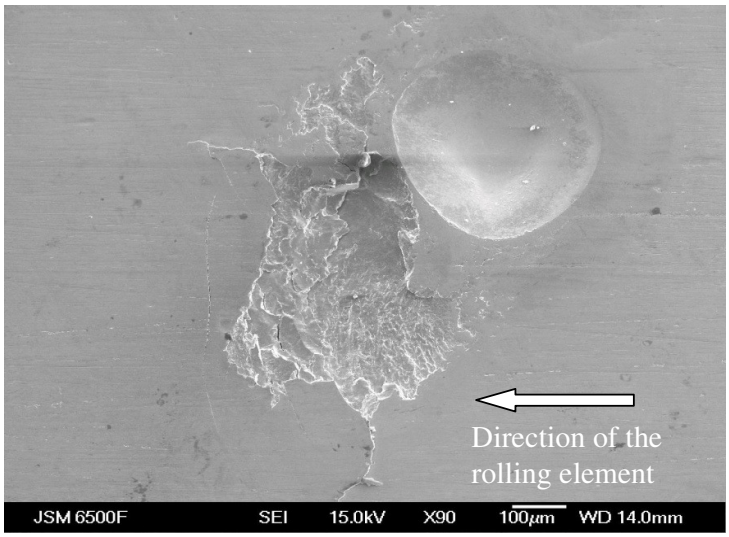

Figure 5.17 Surface initiated failure at the trailing edge of the inner race indent at bearing 2.

The other bearings exhibited indentations and striations, caused by the entrainment of wear particles between the bearing elements. A typical example of this type of damage is shown in Figure 5.18 which reveals the elements of bearing 3.

(a)

(b)

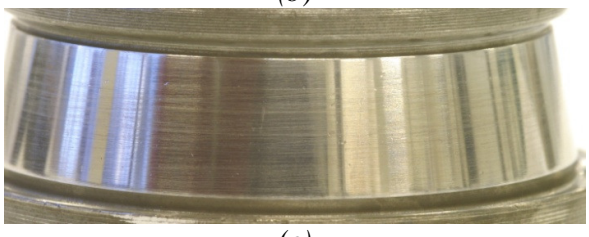

(c)

Figure 5.18 The (a) outer race, (b) rollers and (c) inner race of bearing 3.

5.3.6 Off-line advanced processing architectures

This section shows some further post test analysis performed by Nick Chien, a postgraduate researcher at the national Centre of Advanced Tribology (nCATS) University of Southampton. The methodology behind the advanced processing architectures was described in section 4.5.1 and [198-200].

The T-squared function, shown in Figure 5.19, identified the running-in period to 15 hours. This was followed by reducing trend that maintained steady-state levels which was indicative of benign wear. At around 43 hours, there was accentuated activity which coincided with the rapid increase in 5 – 15 and 15 – 25 µm debris detection by the PODS, the single particle count by the TA 10 and adhesive wear debris during SEM examination. Therefore, the accentuated T-squared function at this time provides further support of anomalous behaviour prior to failure. At 53 hours there was a further rapid increase in the T-squared function that persisted to the end of the test.

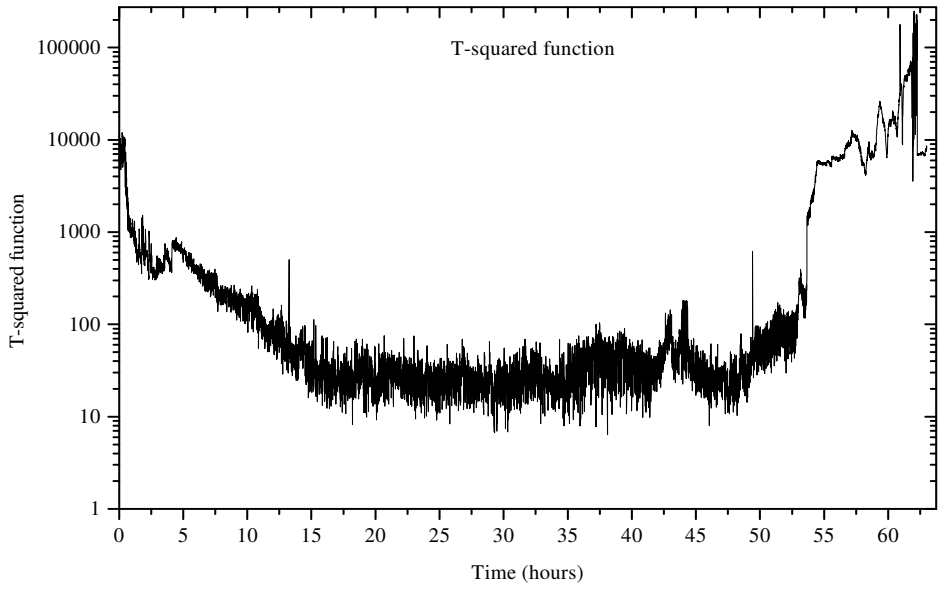

Figure 5.19 Advanced processing architectures using the T-squared function.

A further part of the analysis included the breakdown of the T-squared function to highlight the contribution of each input parameter to the signal. Figure 5.20 shows that at 43 hours the greatest contribution was obtained from WSS 3 normalised to the outer race defect frequency, which has been shown to be the locality of failure.

This suggests that a breakdown of the T-squared function could be used as a predictive tool to identify the locality of the early signs of distress. However, caution must be taken as the analysis also shows energy excitation of similar magnitude at the inner and outer raceways of bearing 1, which did not show any signs of degradation during post test analysis. In addition, accentuated signatures from any monitoring procedure need to be tested during multiple tests and over a greater range of operating conditions. This helps to identify how robust the process is and provides confidence when associating increased signal activity to post-failure investigations. Therefore, at this time, the advanced processing architecture shows promise as a predictive tool during a single accelerated test, but requires further development and testing to confirm the reliability of the technique.

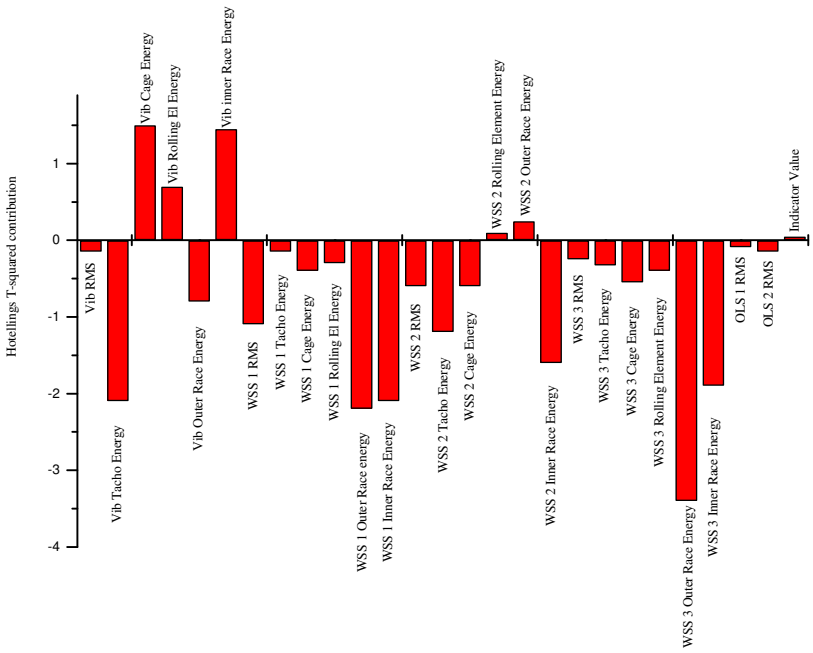

Figure 5.20 Breakdown of the T-squared function at 43 hours.

5.4 Bearing testing adapted with AE (Test 5)

This section shows the results of Test 5 using the set-up described in Table 5.1.

5.4.1 Distress in the bearing test chamber

Running-in was observed during the initial 5 hours by dynamic wear site charge with a peak amplitude of 2 pC and a reducing acceleration trend from 1 g, as shown in Figure 5.21. The maximum oil inlet temperature was 60°C, the bearing outer race temperatures were 65°C and the oil outlet temperature was 60°C. All signature levels are comparable with previous tests. Following running-in, all techniques maintained steady-state levels, indicating benign wear. Degradation was identified around 70 hours by an increasing acceleration trend to 75 hours. From 75 hours to the end of the test at 76 hours, there was a rapid increase in acceleration from 1 – 1.5 g. The increasing acceleration correlated with a rapid increase in charge from WSS 2 charge from 1.5 – 4 pC, which occurred during the final few minutes of the test. There was also a rapid increase in bearing outer race temperatures from 68 – 75°C and an oil outlet temperature from 63 – 69°C, which also occurred during the final few minutes of the test. The test was then stopped as the combined sensor activity provided evidence of distress. Dismantling the test chamber found that the bearing clearances had reduced, as it was difficult to rotate the elements with the shaft.

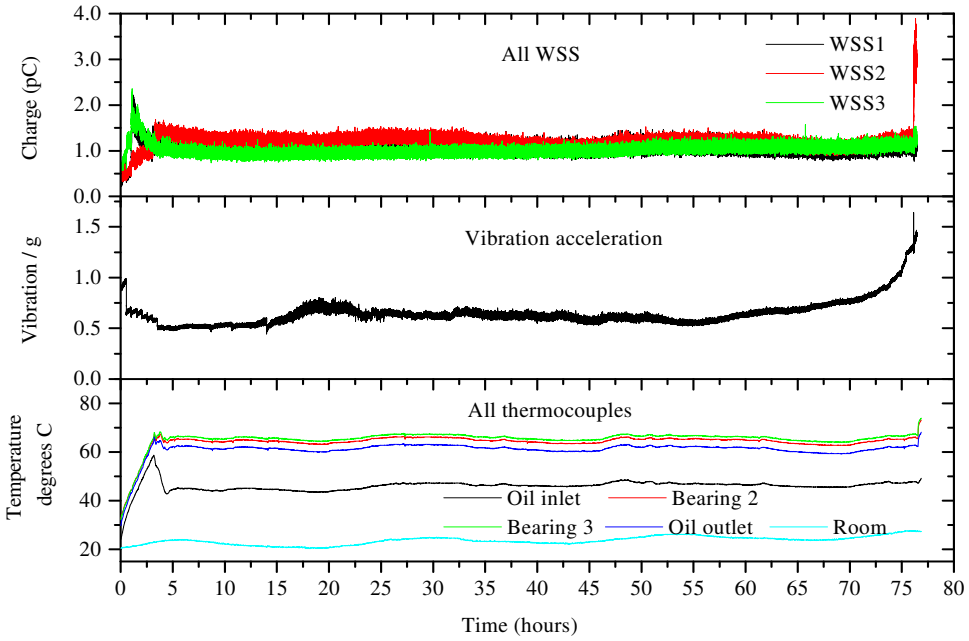

Figure 5.21 Electrostatic WSS, vibration acceleration and thermocouples from Test 5 at a Hertzian contact pressure of 2.5 GPa.

During running-in the bulk of the AE peak amplitude activity was around 77 dB, with some hits of 79 dB, as shown in Figure 5.22. The peak amplitude levels were similar to the results shown in Appendices E and F which were between 75 – 81 dB. The AE activity was thought to be related to asperity deformation mechanisms and debris entrainment in the contact. Following running-in, there was a reduction in peak amplitude that remained around 78 dB, which identified benign wear. The peak amplitude showed a good correlation with the analysis shown in Appendices E and F, which identified benign wear levels between 70 – 78 dB. The first indication of distress was at 48 hours with a single peak amplitude hit of 88 dB. This is consistent with the tests in Appendices F and G, which show that the early distress mechanisms relate to peak amplitude hits of 80 dB or more. There was a further indication of damage from 52 hours with a peak amplitude of 80 dB. At 70 hours, peak amplitude activity of 99 dB, correlated with the increasing vibration trend and provided corroborating evidence of damage. Between 75 – 76 hours, peak amplitude activity of 93 dB was comparable to the observations during damage in the tests shown in Appendices E and F, which were 86 and 95 dB respectively. The increased AE during this period correlated with the rapid increases in wear site charge, vibration and temperature, and were likely to be related to crack/debris generation, propagating damage and impacts between defective elements.

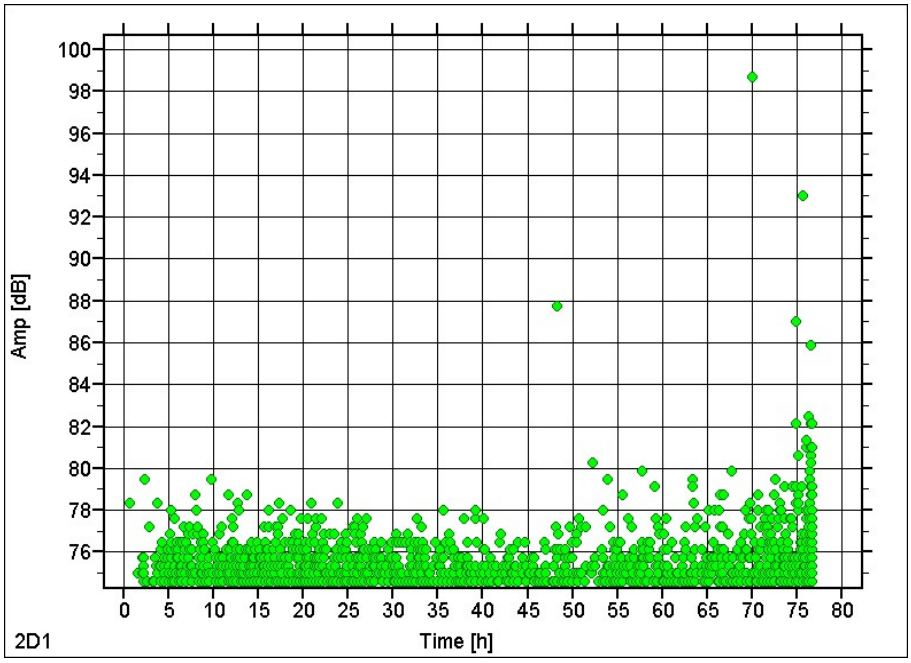

Figure 5.22 AE peak amplitude at a sampling frequency of 5 MHz.

From the frequency analysis, shown in Figure 5.23 (a – i), the dominant frequencies during the first 50 hours of testing are around 300 kHz. The frequency excitation is likely to be related to background levels of operation, which when correlated with the reminder of the techniques in the test chamber, indicate a normal bearing condition. However, in Figure 5.23 (j – o), from 50 hours to the end of the test, the dominant frequency band is between 500 – 600 kHz. The frequency change is consistent with the peak amplitude greater than 80 dB and provides corroborating evidence of distress. The mechanisms of damage probably relate to crack formation/propagation and/or impacts between rolling elements on a defective wear site. The reason why this particular frequency range has been excited during damage is probably because this is where the piezo-crystal is more sensitive, as shown in the calibration graph in Appendix B.

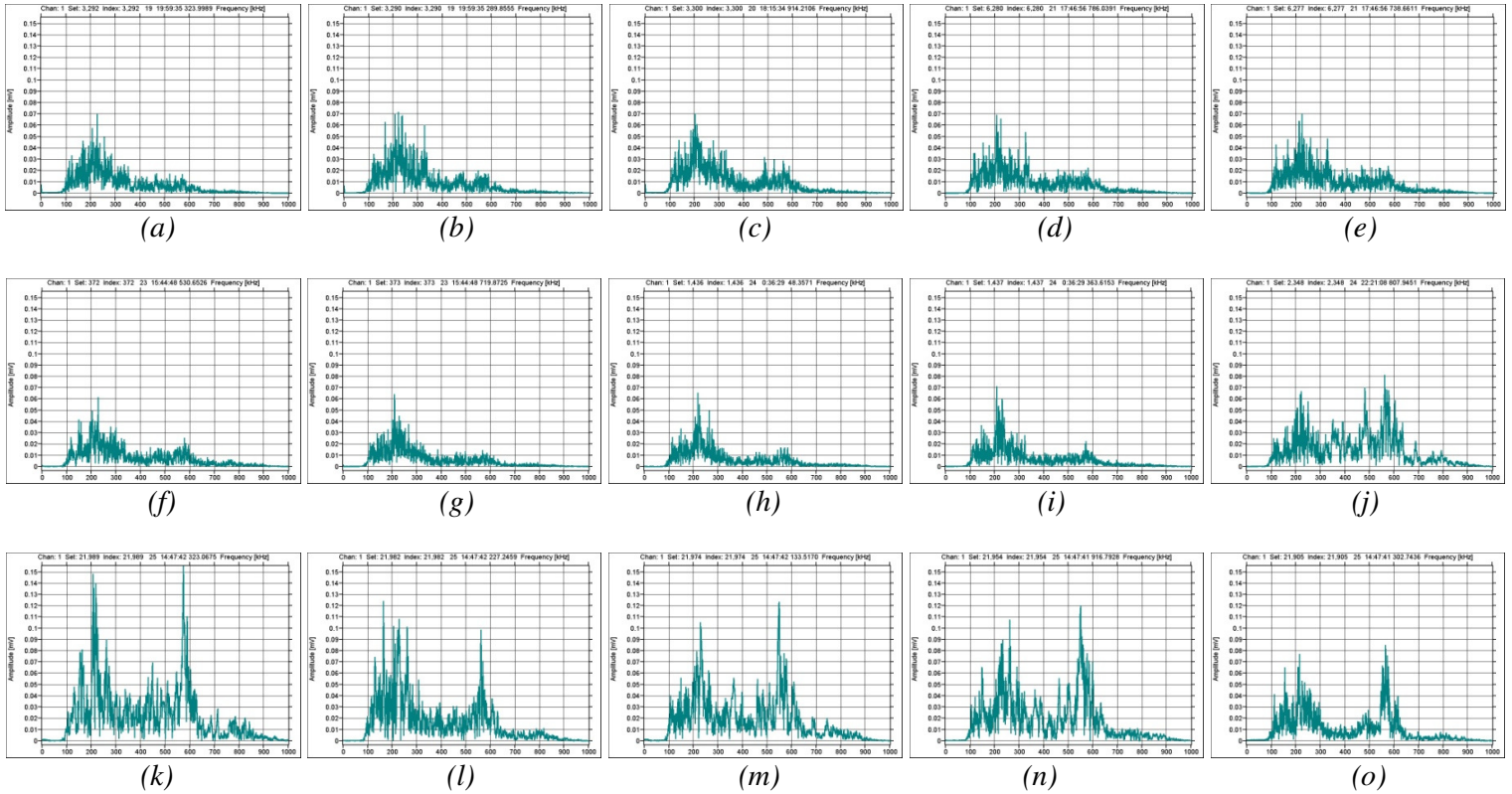

Figure 5.23 AE frequency analysis at (a) 0 – 5, (b) 5 – 10, (c) 10 – 15, (d) 15 – 25, (e) 25 – 30, (f) 30 – 35, (g) 35 – 40, (h) 40 – 45, (i) 45 – 50, (j) 50 – 55, (k) 55 – 60, (l) 60 – 65, (m) 65 – 70, (n) 70 – 75 and (o) end of test.

5.4.2 The T-squared function

Figure 5.24 shows that the T-squared function identified running-in wear for the first 15 hours of testing. At 15 hours, there was an increasing trend that does not correlate with any of the techniques in the test chamber. Also at this time, there were significant perturbations from the signature, of origin that are unknown at this time. From 22.5 – 50 hours there was a relatively stable T-squared function that was consistent with the steady-state trends from the techniques in the test chamber that confirmed benign wear. From 55 hours, a time that shows a good correlation with the AE peak amplitude activity greater than 80 dB and frequency excitation at 550 kHz, there was an increased T-squared function. The T-squared function then remained stable until 67.5 hours, which was around the same time as the increasing vibration trend. From 75 hours, there was a rapid increase in the T-squared function, which showed a good correlation with the rapid increase from all the techniques in the test chamber.

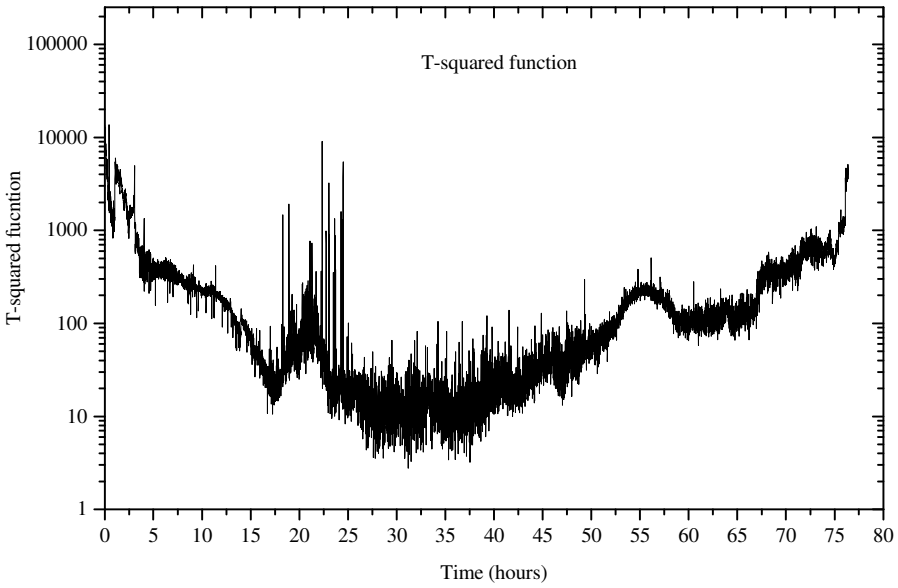

Figure 5.24 Advanced processing architectures using the T-squared function.

Figure 5.25 shows the evolution of the significant contribution values which were processed from the T-squared function. The driver behind the T-squared function during running-in is the energy at the tachometer frequency. The dominating energy at the tachometer frequency suggests a normal bearing operation, as energy excitation at any of the bearing element frequencies may be an indication of distress. At 20 hours there is an increase in energy at the cage frequency which is followed by significant

perturbations in energy at the tachometer frequency. The increased contribution values at this time suggest that there may be distress at the cage of one of the bearings and a problem with the tachometer. After 25 hours, there is a relaxation in energy at both the tachometer and cage frequencies, indicating a discontinuation of the previous activities at these locations. The next period of signal activity is at 55 hours, indicated by an increase in energy at the tachometer frequency, which precedes the heightened AE peak amplitude which is greater than 80 dB. The cause of energy excitation at the tachometer frequency is unknown. However, a possible explanation may be particle entrainment between the bearing elements, which would affect the rotational speed of the motor, due to an increase in frictional forces from the particle entrainment. From 67.5 hours, there is a further increase in energy at the cage frequency, which again may be related to debris entrainment between the elements. From this time there is runaway energy accentuation at the cage frequency, which relates to further damage, which is corroborated by the increased activity from the techniques in the test chamber.

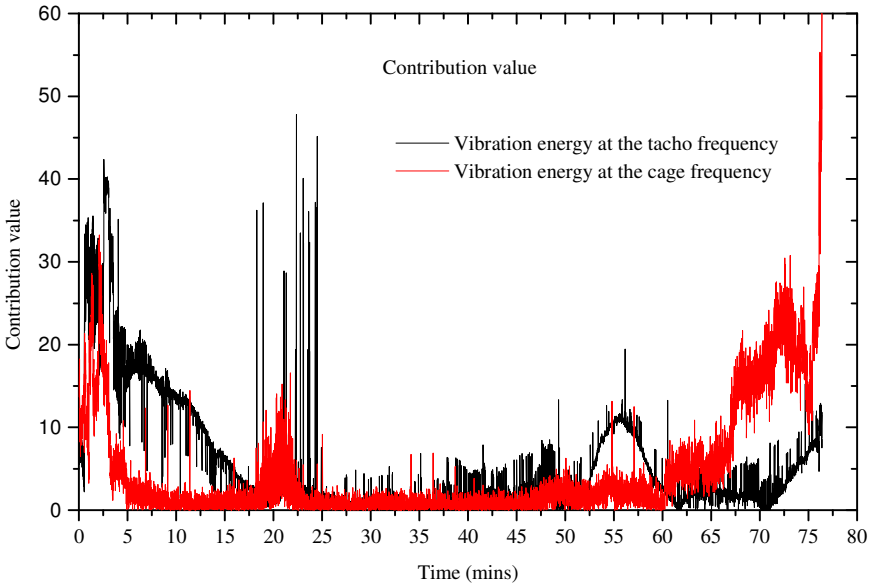

Figure 5.25 The dominating contribution values from the T-squared function.

5.4.3 In-line wear debris detection

Figure 5.26 shows the OLS and indicator value. During running-in, the peak OLS charge was 0.04 pC and the indicator value was 3500. These sensor values were typical of the sensing levels observed in the previous tests. Following running-in,

there was a reduction in OLS charge to 0.02 pC and indicator value to 1500, which maintained steady-state levels that identified benign wear, and continued for the remainder of the test. These sensor levels were similar with the previous tests, as were the reducing trend characteristics. There was no identification of the wear out period, which was shown by the other techniques in the test chamber. The possible reason for the lack of increased sensor activity during the wear out phase is the low levels of surface deterioration exhibited in this test. The minor levels of surface wear would lead to low levels of particle generation, unsuitable for detection by the oil-line technologies.

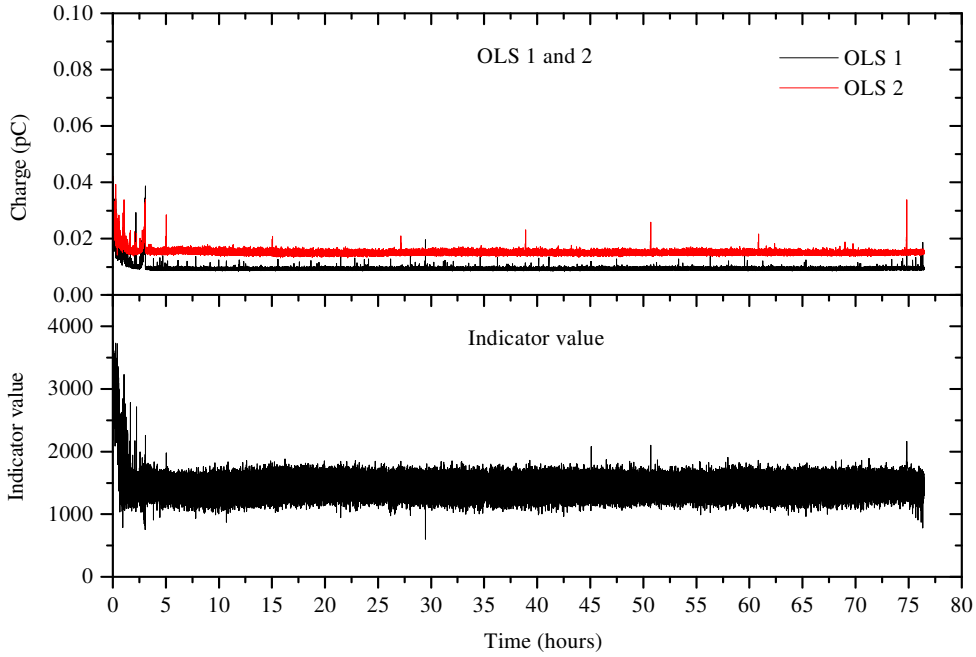

Figure 5.26 Electrostatic OLS and indicator value.

5.4.4 Off-line wear debris detection

There was a reduced number of oil samples taken for the off-line debris analysis in this test (7), compared to the previous test (17). This was to reduce the time that is needed for the post test analysis. Figure 5.27, shows that just after running-in, there was a 5 – 15 µm debris count detected by the PODS of 2500 particles. This debris count is typical of the quantity of 5 – 15 µm particles observed during the transition into benign wear, which reduces to below 4000. There was an increased severity index value at 15 hours, which was at the same time as the heightened T-squared

function. Therefore, the increased severity index provides corroborating evidence that the T-squared activity may have been particle entrainment between the elements.

A confident assessment of distress was observed at 51 hours by an increase in the severity index to 0.1. Evidence that a severity index value of 0.1 related to distress was found in the previous test during failure, and those shown in Appendices E and F. Further evidence of degradation was shown by the increased AE peak amplitude that was identified 3 hours earlier and the 550 kHz frequency excitation around the same time. In the next oil sample at 63 hours there was a rapid increase in the 5 – 15, 15 – 25 and 25 - 50 µm particle counts of 60000, 2200 and 300 respectively. Compared to the previous test, the 5 – 50 µm particle count is reduced, providing support that the lack of increased OLS charge was related to lower levels of wear. Identification of the increased particle count by the PODS was again prior to the wear out phase that was identified by the in-line and oil-line techniques. At the end of the test, the debris count was typical of benign wear conditions, indicating healing of the defect. There was no identification of iron levels by SOAP at any stage of the test, as the debris levels were below the detection capabilities of the technique, and therefore is not shown.

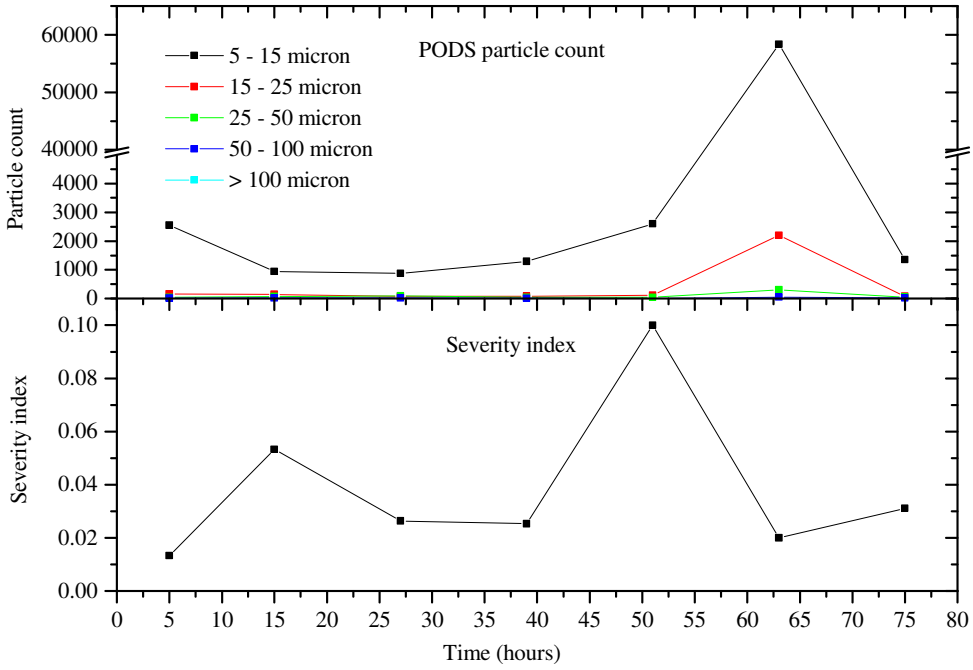

Figure 5.27 The PODS and severity index.

5.4.5 The evolution of wear debris

In 5.28 (a) plate-like debris around 10 µm were consistent with those observed around the running-in period in previous tests and was consistent with the dominating 5 -1 5 µm particle count by the PODS. Following the transition into benign wear, there was 5 µm plate-like debris with some feather-like particles [193] that were around 1 µm, as shown in Figure 5.28 (b - d). In Figure 5.28 (e), at time when an increased severity index of 0.1 identified distress, the debris consisted of agglomerated feather-like particles that were below 5 µm. The agglomerated particles were likely to be identified as larger debris during ferrographic analysis, which may have been the source of increased severity index at this time. In the next sample at 63 hours, Figure 5.28 (f) provides corroborating evidence of degradation by the identification of fatigue chunks, indicating gross material removal in a fatigue mechanism. Supporting evidence of gross surface wear is confirmed by the rapid increase in the 5 – 25 µm particle count by the PODS at this time. The final sample in Figure 5.28 (g) shows that there were plate-like debris around 5 µm and some further feather-like debris that were smaller than 1 µm.

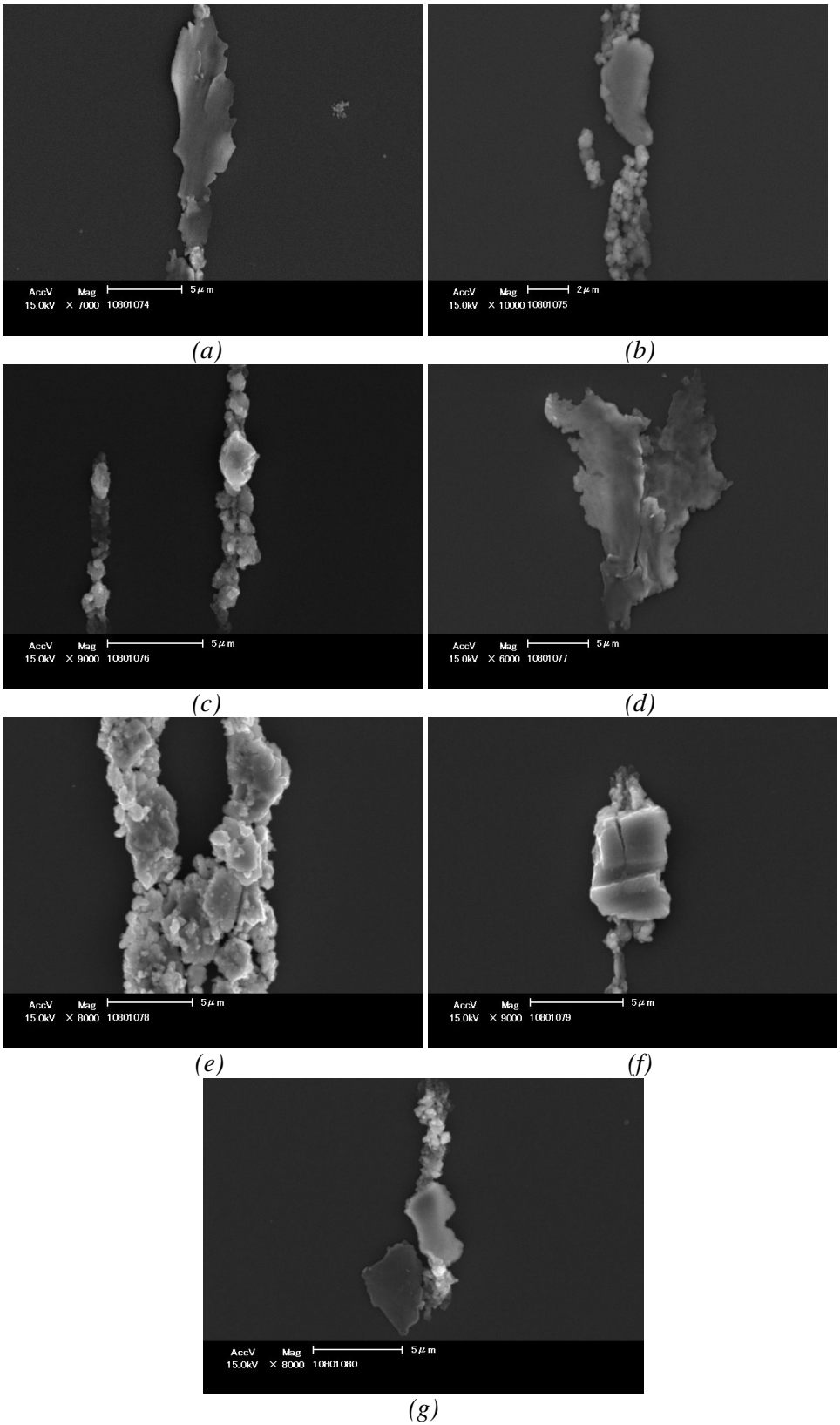

Figure 5.28 The evolution of wear debris from Test 5.

5.4.6 Gravimetric analysis

Gravimetric analysis confirmed that the greatest mass loss was observed on the cone assembly of bearing 2, as shown in Table 5.4.

Gravimetric Analysis						
	Pre gravimetric (g)		Post gravimetric (g)		Δ (mg)	Δ (mg)
	Cup	Cone	Cup	Cone	Cup	Cone
Bearing 1	61.20675	116.65536	61.2034	116.65387	3.35	1.49
Bearing 2	61.19786	116.85761	61.1949	116.83431	2.96	23.3
Bearing 3	61.20769	116.60531	61.20625	116.60303	1.44	2.28
Bearing 4	61.20627	116.59734	61.20277	116.59669	3.5	0.65

Table 5.4 Gravimetric analysis.

A SEM image of damage, shown in Figure 5.29, shows that spallation was initiated at the indent and propagated in the direction of the rolling elements. The wear scar, starting from the initiation site, has a "sea-shell" morphology, which is consistent with literature.

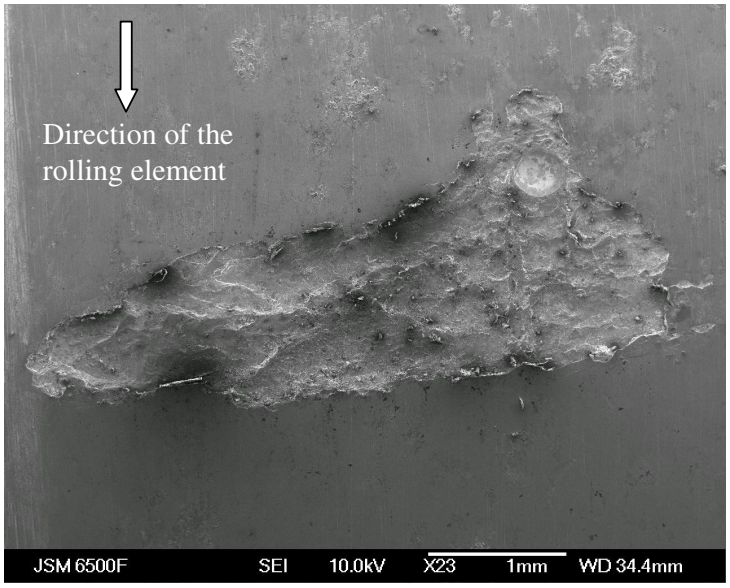

Figure 5.29 Inner race damage to test bearing 2.

5.5 Chapter summary

Six tapered roller bearing tests were conducted, which identified a normal operation, outer race failure of a support bearing and inner race failure of a test bearing. The contact pressures were 2 and 2.5 GPa. The collective techniques provided corroborating evidence of the evolution of fatigue wear and adhesive wear mechanisms. The collected signatures generated wear against time trends that are consistent with the bath-tub. The operational signatures included wear site charge, vibration acceleration, bearing outer race and oil temperatures, electrostatic oil-line charge and an indicator value. These results show that the main advantages of using these techniques are that they provide a real-time evaluation to the probable locality of runaway surface wear. The reason why these techniques indicate the probable locality of surface degradation is because they can be influenced by the external environment, which includes machinery in proximity to the sensor. However, the drawback of the above mentioned analysis is that in order to confidently link the sensor levels to wear, then the analysis can only be corroborated with the identification of debris.

The most important contribution from the debris analysis was that the particle quantity, size and shape provided an early indication of distress. These debris parameters consisted of a 5 – 15 µm particle count by the PODS which was greater than 4000, a severity index greater than 0.1, iron particle levels detected by SOAP greater than 0.1 ppm, a single sub 100 µm particle count by the inductive Macom TA 10 and particles with spherical and chunky morphologies. The combined analysis identified adhesive and fatigue mechanisms. Further early distress signatures that were corroborated by the debris analysis included an AE peak amplitude greater than 80 dB and frequency excitation at 550 kHz. The wear debris also provided supporting evidence of distress to the advanced processing architectures that was based on a T-squared function. A drawback of the debris analysis is that it is difficult to locate the precise locality of wear, since the particles can be formed from any surface prior to the drain point. However, the main drawback of the debris analysis is that the analysis is taken off-line. These results highlight the trade-off that is made between the off-line analysis that provides enhanced sensitivity, and the in-line techniques that are less sensitive.

The collective analysis is explored further and in greater depth in Chapter 7. In order to avoid repetition of the sensing characteristics the sensor activities are not described. Therefore, the focus of Chapter 7 will be to look at correlations between the tests; incorporating sensing levels, trends and cataloguing of the wear debris generated within the different periods of wear. Correlations are also shown between different bearing types, as ball bearings are tested in the next chapter.

6 Ball Bearing Testing

6.1 Introduction

This chapter shows experimental results from ball bearing tests, using the combined analysis described in chapter 4. These tests were incorporated to identify if any operating signatures from the tapered roller tests were consistent with the ball bearings and therefore transferrable to the elliptical contact geometry. The test bearings were Timken LM67010 which had 3 indents, centrally located on the inner race to accelerate spallation, as shown in section 4.1.1. The test conditions and techniques employed are shown in Table 6.1.

In Test 7, the Macom TA 10 and TA 20 were used before the units were recalled by the vendors. There was also no AE sensor as the test housing was being optimised to accommodate the ball bearing geometry. The mean Hertzian contact pressure was 2.5 GPa, which after consultation with the bearing vendors should have been 1.6 GPa. As a consequence, overloading resulted in rapid bearing failure. Due to a short test time there was no off-line debris analysis.

In Test 8, a reduced load which induced a Hertzian contact pressure of 1.6 GPa was applied. The reduced load was used after consultation with the bearing vendors, as rapid failure was observed in Test 7 due to the overloading. However, this test had to be stopped after 92 hours as the motor speed began to fluctuate. After investigation the brushes were worn and required repair. The results are shown in Appendix G.

Test 9 is a further attempt at a Hertzian contact pressure of 1.6 GPa. The initial part of the test lasted for 115 hours, after which time, the wear out phase could not be confirmed. Therefore the test was stopped, which provided two choices. These included dismantling the bearings or to restart the test. It was decided to restart the test with a slight increase in contact pressure to 1.8 GPa, to encourage failure within a more manageable time-frame.

Test 10 is a continuation of Test 9 with the slightly increased mean Hertzian contact pressure of 1.8 GPa..

	Test 7	Test 8	Test 9	Test 10
Location of analysis in thesis	Section 6.2	Appendix G	Section 6.3	Section 6.4
Rotational speed (rpm)	2500	2500	2500	2500
Hertzian contact pressure (GPa)	2.5	1.6	1.6	1.8
Defect type	Inner race indentation of test bearing # 2			
Reason for test	Identify sensor activity during failure	Identify sensor activity during failure	Repeat of test 2 with off-line debris analysis	Continuation of test 3
In-line techniques in the bearing test chamber	WSS's accelerometer thermocouples		WSS's Accelerometer Thermocouples AE	
Oil-line techniques	Thermocouples, OLS, Macom TA 10 and TA 20	Thermocouples OLS		
Off-line debris techniques	No off-line analysis as early bearing failure was detected	No off-line analysis due to motor failure during test	PODS, severity index, SOAP, electron microscope	
Failure detected	Expected inner race failure at the indented bearing	Unexpected motor failure which required repair	Not conclusive so test was stopped and restarted after weekend	Expected inner race failure at the indented bearing

Table 6.1 Test conditions and sensing techniques employed during the ball bearing tests.

6.2 Ball Bearing (Test 7)

6.2.1 Distress in the bearing test chamber

The output from the WSS's, accelerometer and thermocouples are shown in Figure 6.1 and indicate that during loading, which was to 3 hours, there were incremental increases in wear site charge which correlated with the times of applied load. The increases in charge were from 0.25 pC to maximum levels of 1 pC. The thermocouple levels showed a maximum oil inlet temperature of 45°C, the outer race temperatures were 60°C and the oil outlet temperature was 55°C. During this period the vibration level remained relatively stable at 1 g. The collective signatures were of similar magnitude as those observed during the running-in period in the tapered roller tests. The mechanisms of sensor activity probably related to asperity deformation and debris entrainment in the Hertzian contact. The first sign of degradation was when the maximum load was applied at 3 hours, by a linearly increasing vibration signature, which persisted until the end of the test, to a level of 4.5 g. Also at 3 hours, there was an increase in charge of 0.5 pC from WSS 2, followed at 3 hours 45 minutes hours by a linearly increasing trend, indicating distress at the test bearings. The vibration and wear site charging mechanisms were described in section 5.2.1 and relate to spallation. There was no increased temperature detected by the thermocouples.

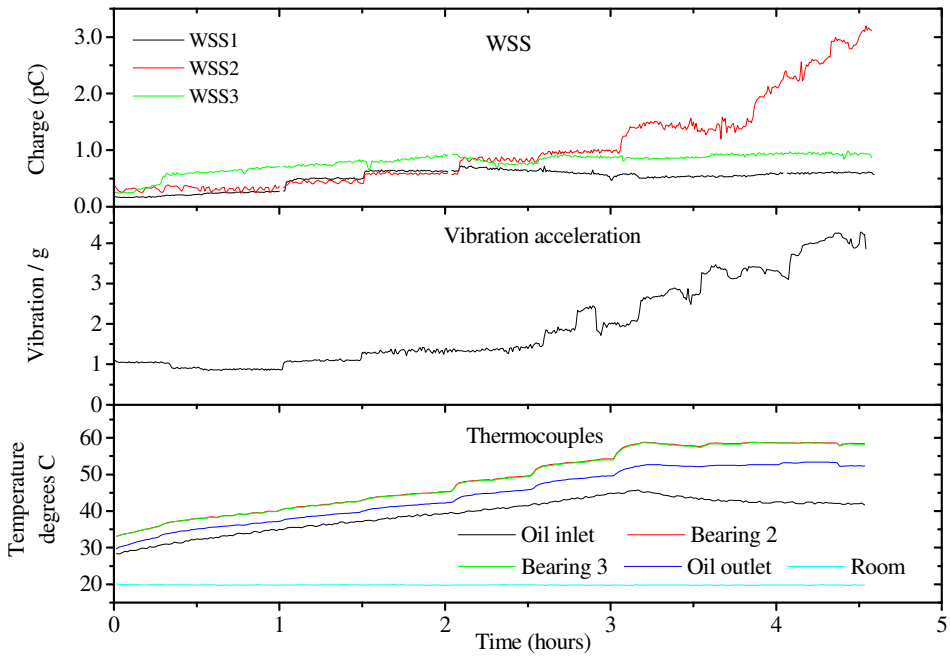

Figure 6.1 The WSS, accelerometer and thermocouple trends at a mean Hertzian contact pressure of 2.5 GPa.

6.2.2 In-line wear debris detection

Figure 6.2 shows that from the start of the test there was a decreasing OLS charge and indicator value. The OLS charge decreased from 0.05 pC and the indicator value reduced from 3500. Throughout this time, the sensor levels and trends were consistent with the signatures detected in the tapered roller tests. Further activity during this period, consisted of slight increases in charge that correlated with the times of applied load at 1, 1.5 and 2 hours. The increased charge was likely to be related to debris entrainment and oil tribocharging mechanisms. At 3 hours the OLS charge was between 0.02 – 0.03 pC and the indicator value was 3000. Compared with the tapered roller tests, these sensing levels were similar to the signatures detected during benign wear. From 2 hours 45 minutes to the end of the test, there was a continual increase in indicator value, with a maximum level of 3750 and was followed at 3.5 hours by an increasing OLS charge which was between 0.35 – 0.45 pC. The increasing OLS charge and indicator value related to debris entrainment in the oil-line and some contribution of tribocharging.

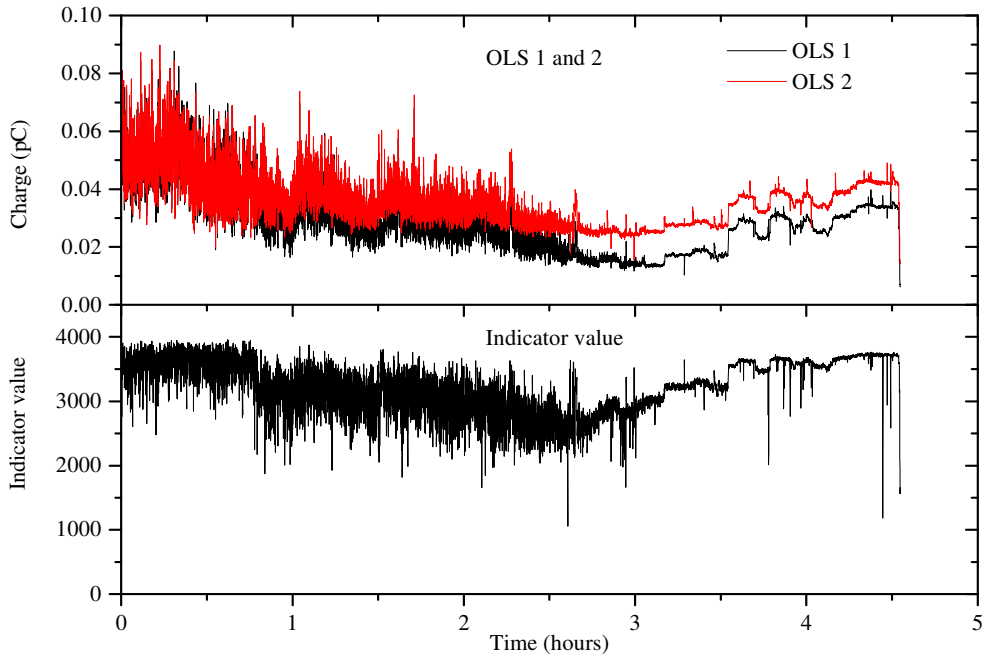

Figure 6.2 Oil-line charge and indicator value.

Figure 6.3 shows the Macom TA 10 particle counter only, as there was no debris detection by the TA 20 at any stage of the test, and is therefore not shown. The first debris was detected by a single 200 – 400 µm particle count around 1.5 hours, which

correlated with the slight increase in OLS charge during loading. There was also a single 100 – 200 µm particle around 2 hours, which again correlated with the slight increase in OLS charge. Single particle counts were also observed in the tapered roller tests and provided evidence of debris entrainment in the oil-line during running-in. At 3 hours, there was increased debris detection from the 100 – 800 µm bin sizes that provided evidence of damage that was corroborated by the increasing vibration and indicator value. At this time the 200 – 400 µm bin size detected the greatest number of particles, which was also found in the tapered roller tests. There was also heightened debris detection by the 400 – 800 and 100 – 200 µm particle sizes. The increased particle count was followed by a reduction in the above mentioned particle sizes until 4.5 hours. At this time, there was an increased debris count and the greatest quantity of particles was again detected by the 200 – 400 µm bin size, followed by the 100 – 200 and 400 – 800 µm count respectively. It is also clear that there was a significant reduction in the quantity of detected particles, compared to the degradation identified in the tapered roller tests. The low levels of debris detection are attributed to low levels of surface wear and the reduced time of damage detection.

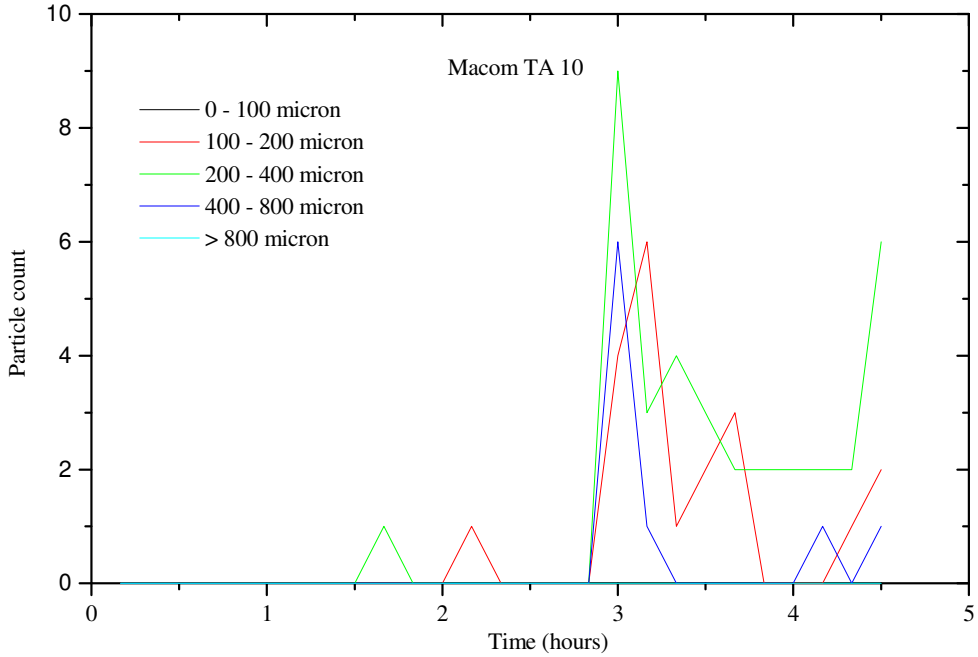

Figure 6.3 The Macom TA 10 particle counter.

6.2.3 Photographic and gravimetric analysis

Figure 6.4 shows photographic evidence of damage to bearing 2. The inner race spall had propagated to approximately 7 % of the raceway. There was no clear evidence of the indents, which were likely to the masked by the roughness of the spalled surface. There was no evidence of damage such as indents or striations to the other bearings.

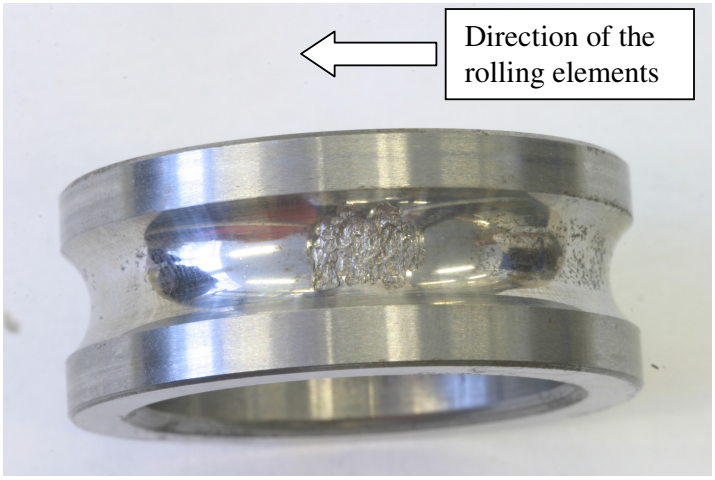

Figure 6.4 Photographic evidence of spallation at the pre-indented inner race of bearing 2.

Gravimetric analysis is shown in Table 6.2 which confirmed that the greatest mass loss was to bearing 2. There were no indents or scratches to test bearing 3, confirming that the accentuated sensor activity and debris detection was attributed to the failure of test bearing 2.

Gravimetric analysis						
	Pre gravimetric (g)		Post test gravimetric (g)		Δ (mg)	Δ (mg)
	Cup	Cone	Cup	Cone	Cup	Cone
Bearing 1	61.2271	116.6283	61.2253	116.6187	1.8	9.6
Bearing 2	194.93959		194.90139		38.2	
Bearing 3	195.21048		195.20868		1.8	
Bearing 4	61.1948	116.5385	61.1926	116.5317	2.2	6.8

Table 6.2 Gravimetric analysis of the test bearings.

6.3 Ball bearing (Test 9)

6.3.1 Distress in the bearing test chamber

Figure 6.5 shows that during running-in, which lasted to 4 hours, dynamic wear site charge levels were around 1 pC whilst vibration remained consistent at 0.4 g. There were linearly increasing thermocouple trends with a peak oil inlet temperature of 35°C, the bearing outer race temperatures were 45°C and the oil outlet temperature to 45°C. Compared with the previous test, which had an increased mean Hertzian contact pressure of 2.5 GPa, the vibration and thermocouple levels were reduced, due the reduced loading employed in this test. However, the wear site charge levels were of the same magnitude. After the running-in period, the WSS's and thermocouples attained steady state levels for the duration of the test, indicating a normal bearing condition. At around 65 hours there was a slowly increasing acceleration trend, which was later found to be around the time of increased 5 – 15 µm particle count by the PODS to almost 4000 particles and the identification of adhesive wear debris, which from the tapered roller tests indicated surface distress. However, low vibration levels of 0.9 g at the end of the test, which when compared to the tapered roller tests was indicative of a normal condition. Therefore, a confident assessment of failure could not be made and as the test ran for 115 hours, the test had to be stopped as sufficient weekend supervision could not be put in place.

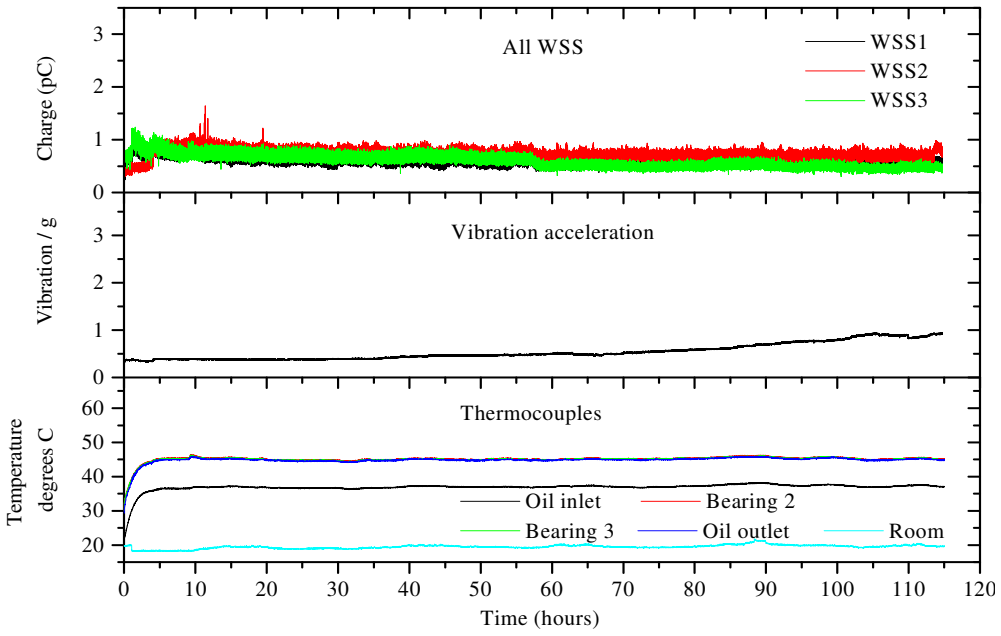

Figure 6.5 WSS, acceleration and thermocouple trends.

The AE peak amplitude analysis, shown in Figure 6.6, was divided into 3 data sets due to the amount of information that could be collected on a single directory. In Figure 6.6 (a) from 0 – 33 hours, the peak amplitude was no more than 70 dB, which was also observed from 33 – 71 hours, as shown in Figure 6.6 (b). The maximum peak amplitude levels of 70 dB indicated a normal bearing condition that was corroborated by the steady-state sensor activity in the bearing test chamber. In Figure 6.6 (c) there was a single hit of 75 dB at 77 hours, which was 10 hours after the increasing vibration trend. The single hit of 75 dB may be significant, since single peak amplitude hits were observed in the tapered roller tests, which identified distress by crack initiation/propagation and/or impacts between defective elements. However, in the tapered roller tests the peak amplitude was 80 dB or more. The differences in the magnitude of the single hits that identify distress are likely to be related to the changes in contact pressures employed during testing. There were two further periods of peak amplitude activity following the single hits of 75 dB. The first was between 82 – 90 hours by an increasing trend from 65 – 70. The second period was from 90 – 100 hours by an increase from 70 – 76 dB. However, as previously mentioned, the tapered roller tests identify a critical threshold level in excess of 80 dB. Therefore, at the end of the test, a confident assessment of failure could not be made.

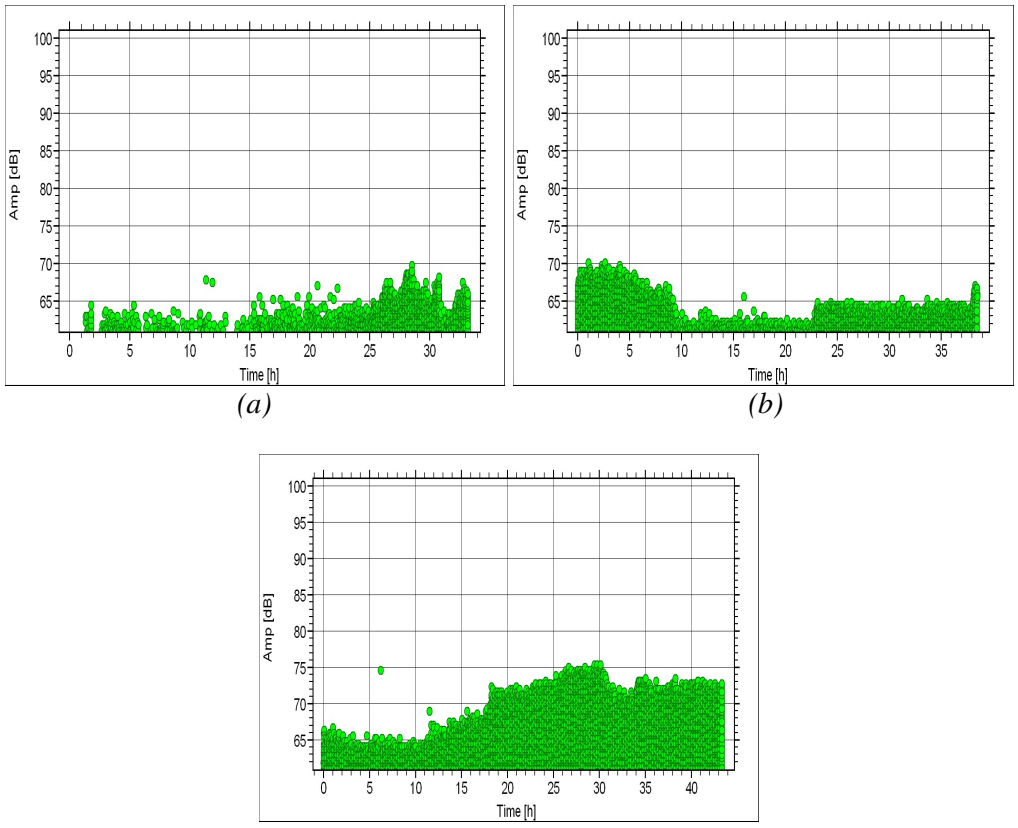

Figure 6.6 Peak amplitude from (a) 0 – 33 hours, (b) 33 – 71 and (c) 71 – 115 hours.

6.3.2 In-line wear debris detection

Figure 6.7 shows that there was no variation in the OLS charge and indicator value between 0 – 90 hours. There was also very low sensing levels, with OLS charge between 0.15 – 0.02 pC and an indicator value of 200, which slightly increased to 500 by the end of the test. These sensor levels and trends were inconsistent with any other tests, as running-in is usually identified by a decreasing OLS charge from around 0.05 pC and a reducing indicator value from 3500 or more. Also, the OLS charge and indicator value usually observe some variation in signatures during benign wear. At this stage it is not clear why the sensor values are of this magnitude and why the trends are very consistent.

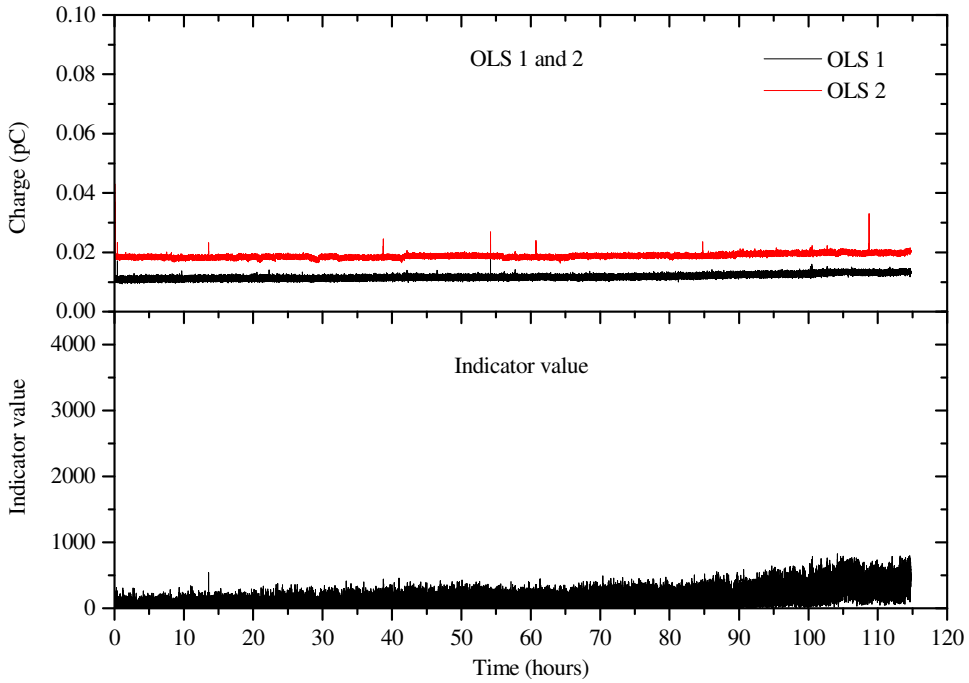

Figure 6.7 OLS and indicator value throughout Test 9.

6.3.3 Off-line wear debris detection

The off-line debris analysis in Figure 6.8, shows that during the first oil sample the PODS was dominated by a 5 – 15 µm debris count of 15000 particles. There was also a heightened 15 – 25 and 25 - 50 µm debris count of 1000 and 400 particles respectively. The debris activity from these bin counts was consistent with particle levels observed during the running-in stages of the tapered roller bearing tests. After the running-in period, there were reducing particle trends, in which the dominating 5 – 15 debris count was approximately 3000 particles. These particle levels were indicative of benign wear in the tapered roller tests. However, at 61 hours, the 5 – 15 µm debris count was 3943 particles, which is very close to the critical 4000 particle threshold, and was probably the first sign of distress. In addition, the increased PODS activity was at a similar time to the increasing vibration trend at 65 hours. Therefore, the combined sensor activity provides corroborating evidence of distress between 61 – 65 hours. After the increased PODS activity there was a reduced quantity of 5 – 15 µm debris to 3200 particles. The reduced particle count is indicative of a normal operation and suggests minor levels of surface damage around the time of 61 hours. From the severity index there was a heightened value close to 0.06 in the first oil sample that was similar to the levels observed during running-in, in the tapered roller

tests. The heightened severity index was followed by a reducing trend which remained around 0.01, showing a good correlation with the tapered roller tests, as a value below 0.06 identified benign wear. There was no detection of iron debris by SOAP, as the particle levels were not within the detection capabilities of the technique and is therefore not shown.

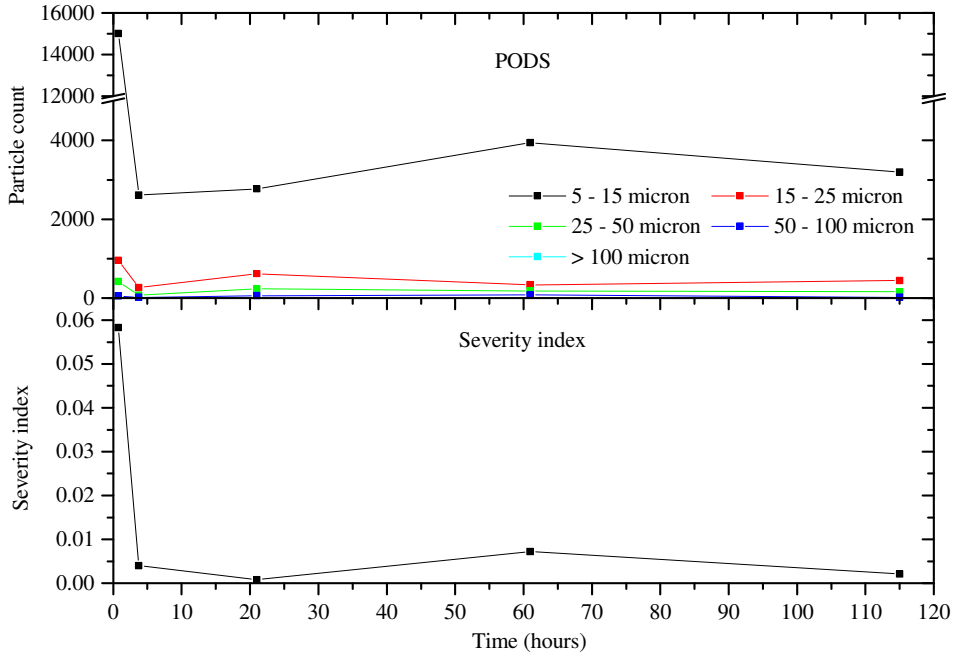

Figure 6.8 The PODS and severity index.

6.3.4 The evolution of wear debris

Figure 6.9 (a) shows that in the first oil sample, 10 µm plate-like particles were typical of the debris observed during the running-in stages of the previous tests. In Figure 6.9 (b - c) the 5 µm plate-like debris dominated which are typical of the particle types generated during benign wear. In Figure 6.9 (d), a time when the 5 – 15 µm particle count by the PODS approached the critical 4000 particle threshold, there was confirmation of an adhesive mechanism with the detection of 5 µm spheres. Therefore at 61 hours, spherical debris provides further support that the detection and a 5 – 15 µm debris count by the PODS approaching 4000 particles provided evidence of a distressed surface. In Figure 6.9 (e), 5 µm plate-like debris were confirmed, and when correlated with a reducing 5 – 15 µm particle count by the PODS to 3200 particles, provided supporting evidence of a return to a normal operating condition.

The isolated distress activity at 61 hours suggests that there was limited surface damage, followed by healing of the wearing site.

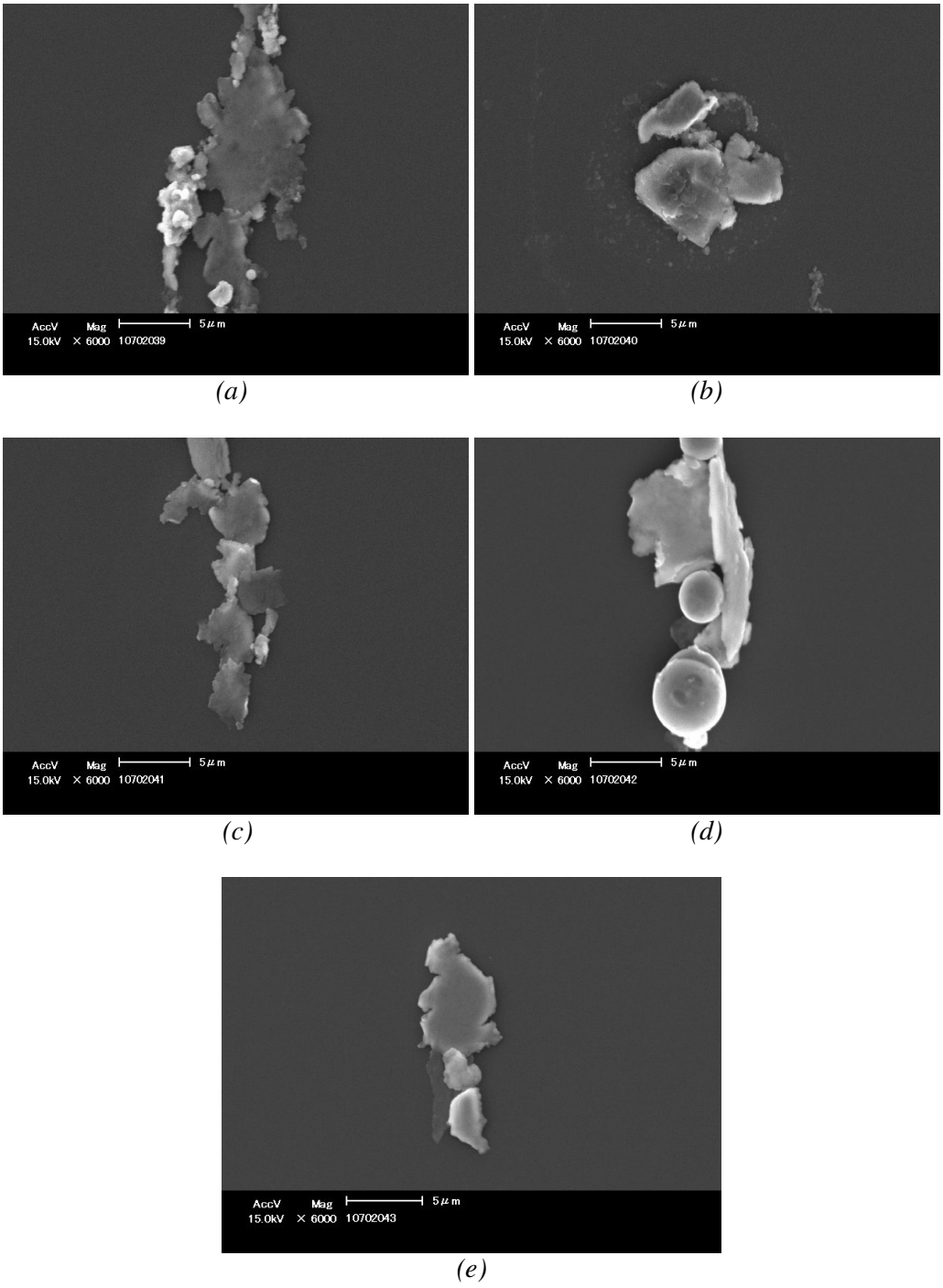

(a) *(b)*

(c) *(d)*

(e)

Figure 6.9 The evolution of debris at (a) 0.75 (b) 3.75 (c) 21 (d) 61 and (e) 115 hours.

6.4 Continuation of experiment (Test 10)

6.4.1 Distress in the bearing test chamber

During running-in, which was to a time of 6 hours, there were incremental increases in charge from WSS 2, as shown in Figure 6.10. The step changes were around 1 pC during each load stage and reached a peak value of 4 pC. Compared to the previous tests, the step changes and the peak charge level was elevated in magnitude. Typical step changes were no more than 0.5 pC and the with maximum levels around 2 pC. Therefore, the accentuated charge at the start of the test may indicate a damaged surface. During this period there was fluctuating vibration from 1.5 – 2.5 g, whilst the thermocouples showed linearly increasing trends that would be expected during loading. The peak oil inlet temperature was 40°C, bearing outer race temperatures were 45°C and the oil outlet temperature was 45°C. After the maximum load was attained at 6 hours, the charge from WSS 2 remained stable at 3.5 pC until 17.5 hours. From 17.5 hours to the end of the test, an increasing charge was typical of the trending observed during failure in previous ball and tapered roller tests, with a peak value around 5 pC. The vibration sensor showed two periods of accentuated activity. At 10 hours there was an increase in acceleration to 3.5 g which then reduced to the previous level of 2.5 g at 13 hours. From 13 hours there was a continual increase in acceleration which reached a peak value of 4.5 g at 17.5 hours, and persisted at this level for the reminder of the test. At 17.5 hours the maximum acceleration level showed a good correlation with the initiation of the increasing charge from WSS 2. The thermocouple levels remained steady until 15 hours which was 2.5 hours before the increasing charge and maximum acceleration levels and then increased by 5°C. The runaway sensor activity at the end of the test provided supporting evidence of failure.

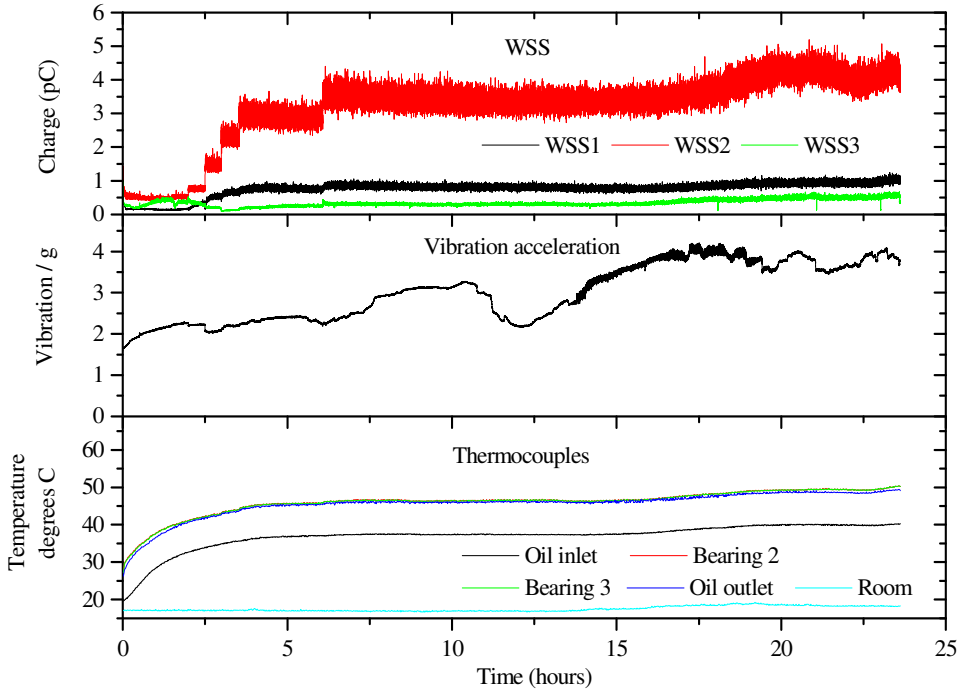

Figure 6.10 WSS, acceleration and thermocouple trends.

In Figure 6.11, the AE peak amplitude showed that during loading there was a slight increase in activity from 55 dB to 60 dB, and showed a similar fluctuating trend with the acceleration signature. Compared to the tapered roller tests, these peak amplitude levels were indicative of a normal condition. Between 8 – 11 hours, the peak amplitude was 69 dB with single hits of 74 and 79.5 dB. Single peak amplitude hits of 79.5 dB are very close to the critical 80 dB threshold that identified damage in the tapered roller bearing tests. The single peak amplitude hits of almost 80 dB showed a very good correlation with the increasing acceleration at this time. This was followed by a decrease in peak amplitude to 55 dB, which again showed a good correlation with the decreasing acceleration trend. From 13 hours to the end of the test there was an almost linear increase in peak amplitude from 70 – 88 dB that correlated with the increasing acceleration trend. However, there were multiple that were between 5 – 15 more than the general trend. Some of these hits, that were in excess of 90 dB, were also detected during the wear out phase in the tapered roller tests, and were therefore related to surface damage.

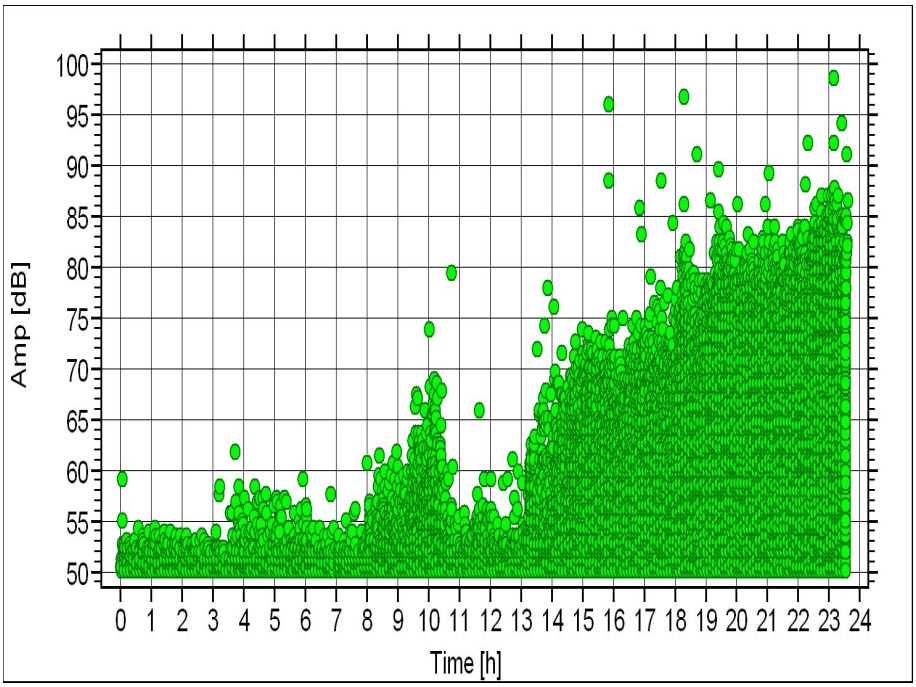

Figure 6.11 AE peak amplitude for the duration of the test.

6.4.2 In-line wear debris detection

The OLS and indicator value showed a good correlation with the acceleration and AE trends throughout the test, as shown in Figure 6.12. During running-in, fluctuating OLS charge and indicator values reached maximum levels of 0.02 – 0.03 pC and 2750 respectively. From the previous tapered roller tests, these sensing levels were indicative of a normal bearing operation. Evidence of distress was identified between 8 – 11 hours by an increase in OLS charge between 0.03 – 0.05 pC and indicator value of 3500. Corroborating evidence of damage at this time was shown by the increasing acceleration of 3.5 g and AE peak amplitude hits close to 80 dB. From 13 – 17.5 hours the OLS charge showed a linear increase with levels between 0.06 – 0.08 pC with an indicator value of 3900. These sensor levels were typical of the oil-line signatures detected during failure in the tapered roller tests that identified bearing failure.

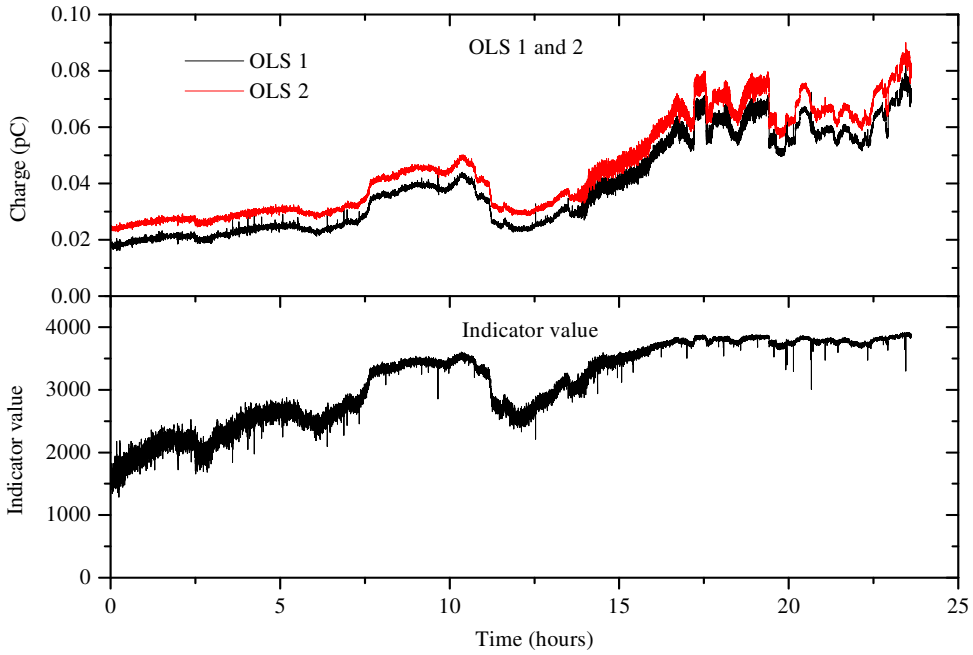

Figure 6.12 The OLS and indicator value.

6.4.3 Off-line wear debris detection

During running-in, the 5 – 15 µm particle count by the PODS was below 4000, with the 15 – 25 and 25 – 50 µm below 500 and 350 respectively, as shown in Figure 6.13. The severity index was around 0.01 and there was no iron particle levels detected by SOAP. These debris parameters were typical of the particle levels detected during a normal bearing condition in previous tests. The PODS showed two periods accentuated debris activity, at the times that provided a good correlation with the increased acceleration, AE peak amplitude, OLS and indicator value. The first period was between 7.5 – 11 hours with an increase in the 5 – 15 µm debris count to 4060 particles. The 5 – 15 µm debris count greater than 4000 provided evidence of an abnormal condition in the tapered roller tests. At this time, the severity index increased to 0.06, however, this value previously indicated a normal operation in the tapered roller tests. This was followed by a reduction in 5 – 15 µm debris count to below 4000 particles, which correlated with the decreasing acceleration, AE peak amplitude, OLS and indicator value trends. The next period of increased sensor activity was at 18 hours with a severity index of 0.07, which correlated with the increases in wear site charge, vibration, AE, OLS, indicator value and thermocouples which related to bearing degradation. Therefore, a critical severity index value of 0.07 may provide a threshold for the identification of bearing failure. The increased

severity index preceded an increase in iron detection by SOAP to 0.1 ppm and was followed by a 5 – 15 µm debris count of 5000 particles by the PODS and a severity index of 0.22. These debris parameters provided further evidence of bearing failure that was confirmed in the tapered roller tests.

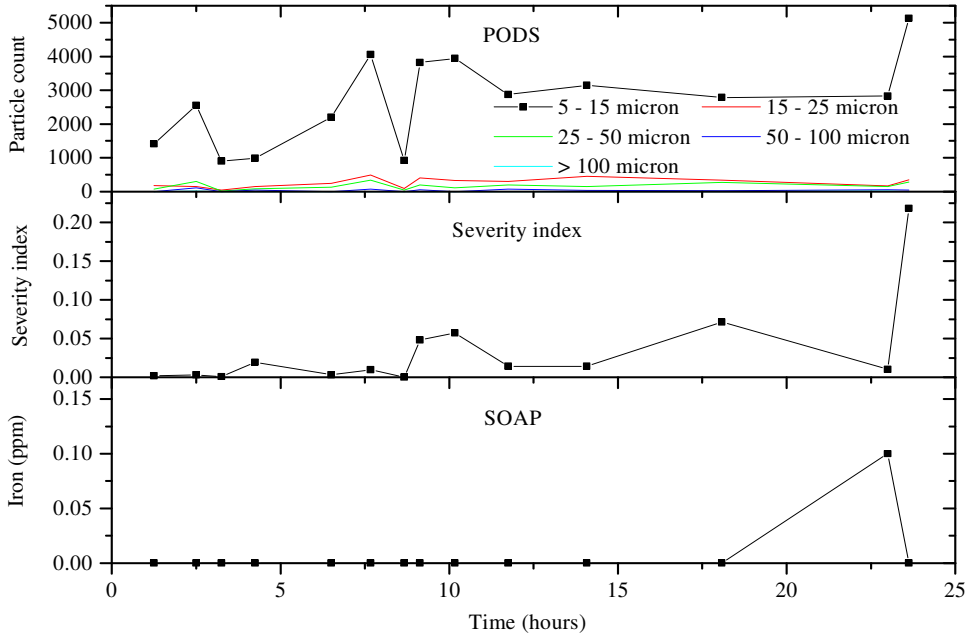

Figure 6.13 PODS, severity index and SOAP.

Figure 6.14 (a) shows a large 75 µm particle with an irregular circumference, which under EDX analysis, is composed of copper. This particle size and composition is inconsistent with all previously detected debris and is likely to be an ingested contaminant that could have been entrained during the off-line analysis. In Figure 6.14 (b - d), 20 µm plate-like particles were consistent with the debris detected during the running-in stages of the previous tests. Between 7.5 – 11 hours, Figure 6.14 (e – i) shows evidence of distress by 40 µm swarf-like debris that are similar in morphology to chips generated in a lathe cutting action, as in Figure 6.14 (h – i), and indicate an abrasive mechanism. The cutting debris were detected during the same period as the accentuated acceleration, AE peak amplitude, OLS and indicator value and 5 – 15 µm particle count by the PODS. In Figure 6.14 (j – l) the 5 µm plate-like dominated, however, during the final stages of the test, Figure 6.14 (m – n) shows 40 µm plate-like debris that are consistent with a fatigue failure mechanism. The 40 µm plate-like particles were identified at the same time as the runaway sensor activity in the test chamber and in the oil-line at the end of the test, of levels which confirmed failure.

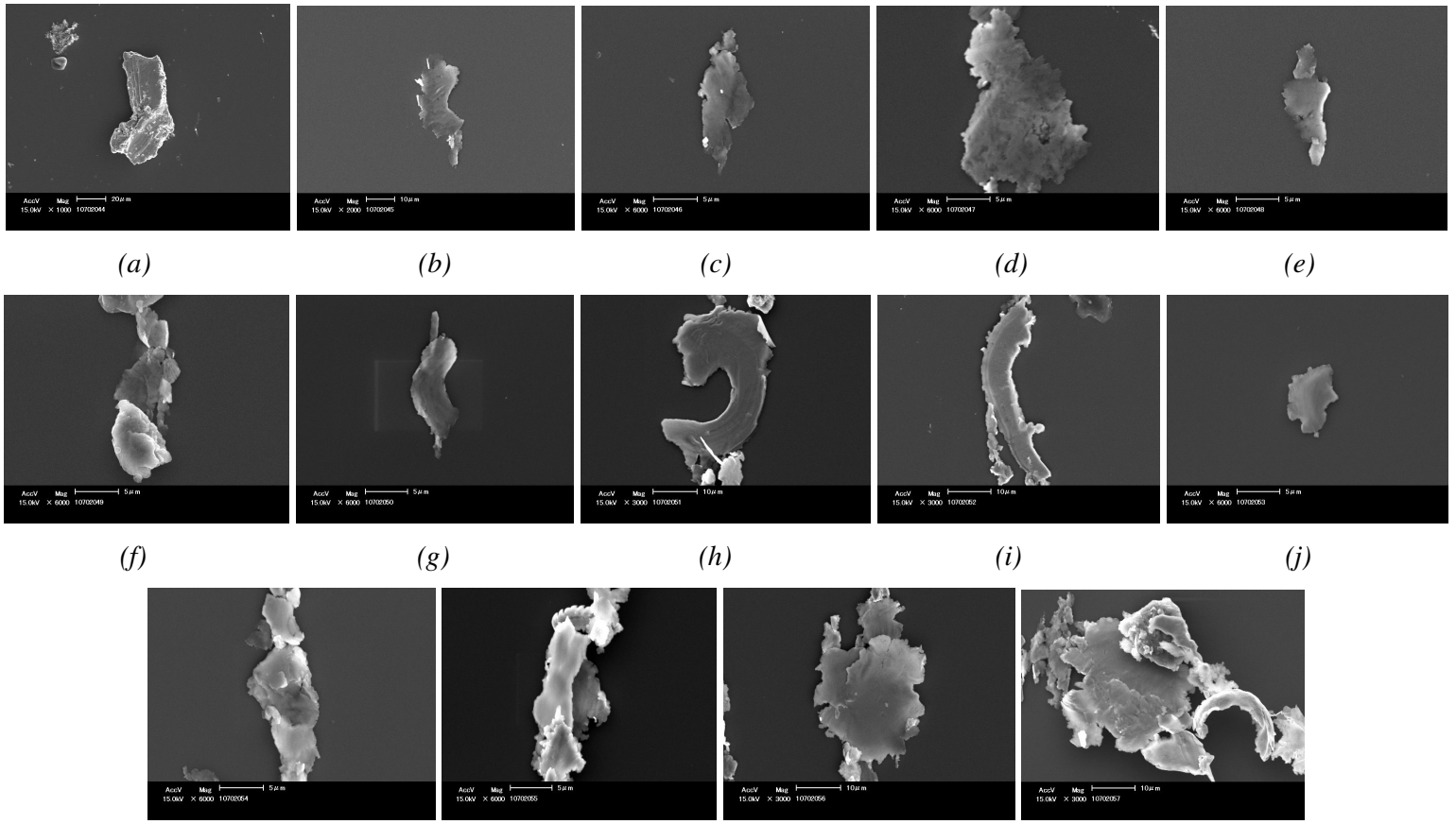

Figure 6.14 The evolution of the morphology of the wear debris, in which the time of sampling is indicated by the box in the PODS analysis.

6.4.4 Photographic and gravimetric analysis

Photographic evidence of the failure at the inner race of test bearing 2 is shown in Figure 6.15, where damage was initiated at the indents and propagated in the direction of the rolling elements. The damage had propagated to 15 % of the raceway.

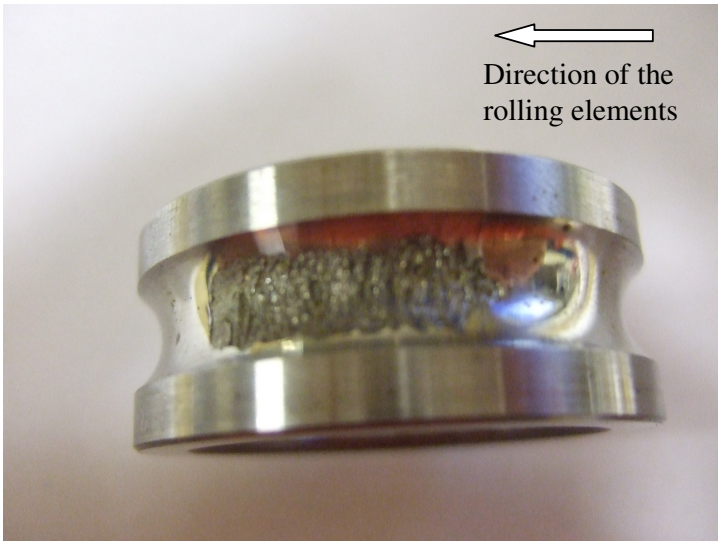

Figure 6.15 Photographic evidence of damage to bearing number 2.

Table 6.3 shows that gravimetric analysis provided further confirmation to the locality of failure as the greatest mass loss was to the pre-indented test bearing. There was insignificant mass loss to test bearing 3, indicating that the accentuated sensor activity was due to damage of bearing 2.

Gravimetric Analysis						
	Pre gravimetric (g)		Post gravimetric (g)		Δ (mg)	Δ (mg)
	Cup	Cone	Cup	Cone	Cup	Cone
Bearing 1	61.271	116.1926	61.6295	116.1895	1.5	3.1
Bearing 2	194.87958		194.80868		70.9	
Bearing 3	195.19438		195.19178		2.6	
Bearing 4	61.0728	116.3196	61.0701	116.3133	2.7	6.3

Table 6.3 Gravimetric analysis of the test bearings.

6.5 Summary

From the tapered roller tests, the most important characteristics were debris and AE activity that provided corroborating evidence of the early signs of distress. Similar results were shown in the ball bearing test at a reduced contact pressure of 1.6 GPa. The early indicators of distress were a 5 – 15 µm particle count by the PODS of almost 4000 particles and the detection of 5 µm spherical debris, which indicated an adhesive mechanism, as well as an AE peak amplitude parameter of 75 dB. These sensing levels were slightly lower than the critical values detected in the tapered roller tests, which employed a contact pressure of 2.5 GPa. The likely reason for the attenuated sensor outputs could have been the reduced loading. Nevertheless, these results again show that the debris analysis and the AE peak amplitude parameter provided corroborating evidence of the early distress mechanisms.

At a contact pressure of 1.8 GPa, the first sign of degradation was a 5 – 15 µm particle count by the PODS of more than 4000 particles and the detection of 40 µm cutting particles, indicating an abrasive mechanism. The PODS count greater than 4000 and the AE peak amplitude was greater than 80 dB, showed good consistency with the tapered roller tests. Also at this time, there was an increased vibration, OLS charge and indicator value indicating a severe form of damage. The OLS and indicator values were 0.05 pC and 3500 respectively, which were similar to the sensing levels during the wear out phase in the tapered roller tests. A further period of damage was then shown by further increases in vibration, OLS charge, indicator value, an AE peak amplitude greater than 80 dB, increased wear site charge and thermocouple activity. This was supported by a 5 – 15 µm debris count by the PODS which was greater than 4000 particles, a severity index greater than 0.1 and the detection of 40 µm plate-like particles, confirming a fatigue mechanism.

Evidence that the rapid increases in vibration, wear site charge, OLS and indicator value related to damage, was again shown during testing at a contact pressure of 2.5 GPa. In this analysis the increasing signal activity was corroborated by an increased 100 – 800 µm particle count by the inductive Macom TA 10.

7 Discussion

This chapter brings together the data from Chapters 5 and 6, which incorporates the analysis from the tapered roller and ball bearing tests. Initially, the evolution of wear debris is shown using the off-line analysis, which incorporates the SEM to capture the size and morphology of the particles. The debris images are then correlated with the particle counting techniques that involves the PODS, severity index and SOAP. The combined analysis then provides corroborating evidence of the mechanisms and severity of wear.

The evolution of the particle size, morphology and quantity are then compared against the real time signatures of inductive and ferromagnetic debris count, OLS charge and indicator value. Comparisons are also shown between the wear site charge, vibration acceleration, temperature and the AE peak amplitude parameter. The combined analysis provides a good agreement between the mechanisms and severity of wear and the dynamic sensing signatures. The dynamic signatures also present threshold limits for a traffic light alarm based system that justifies the transition from normal to abnormal wear.

7.1 The wear debris generated during running-in

Figure 7.1 shows the wear debris formed during the running-in period of both the tapered roller (Figure 7.1a – k) and ball bearing (Figure 7.1l – o) tests. The images highlight the main features of the debris collected on the ferrography slide.

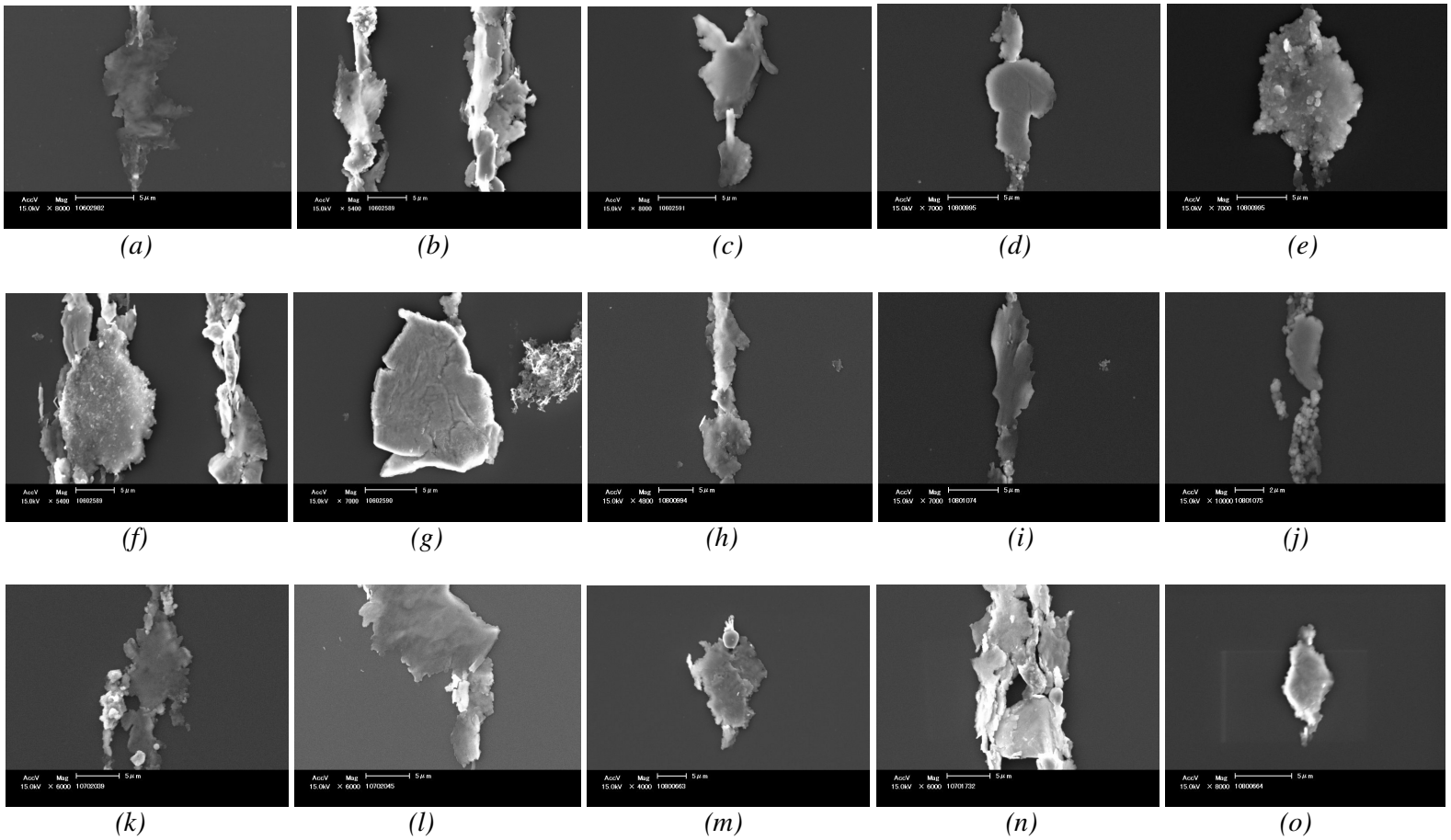

Figure 7.1 The morphology of wear debris during the running-in period. Samples (a – k) show tapered roller bearings and (l – o) ball bearings.

The particles range between 0.5 – 20 µm in size, however, the majority of debris are around 5 – 10 µm and have a plate-like morphology with an irregular edge profile. The particles have a smooth surface texture with no holes or striations, which would indicate debris entrainment in the Hertzian contact and interaction with opposing bearing elements [83]. There are a few larger particles, as in Figure 7.1(f), which are 20 µm in size, and have the same irregular edge profile and smooth surface texture as the smaller 5 – 10 µm debris. These particles are consistent with the particle type and size observed in the literature which are described as platelets or flakes [72, 205, 207].

There is no difference in the size, morphology, surface and edge characteristics of the debris generated in the tapered roller and ball bearing tests. A number of images, as in Figure 7.1(b,f,k,l and n), also show that multiple particles are clustered in close proximity to each other, which indicates a heightened wear rate, compared to the following benign wear regime. The heightened wear rate would be expected during running-in, from the removal of the largest surface protuberances, which in the case of the accelerated tests is at the inner race indent. These particles are formed during bearing start-up, from shearing of the largest surface irregularities, which enables conformity between the surfaces under motion. However, conformity between the elements will only remain if there are no changes to any bearing surface geometry and operating conditions, which involves the Sommerfeld parameters of load, rotational speed and oil viscosity. Therefore, since the load was applied in incremental steps, the running-in process would be initiated upon the application of each load stage, until the final contact pressure is attained.

7.2 Particle analysis during running-in wear

Table 7.1 shows the maximum and minimum particle levels generated during running-in. At this time, a number of tests are not included for reasons which are described in the footnote.

	The wear particle analysis during running-in wear			
	Tapered roller bearings			Ball bearings
	Test 1	Test 3	Test 4	Test 9
Location in thesis	Section 5.2	Section 5.3	Appendix F	Section 6.3
Hertzian contact pressure (GPa)	2.5	2.5	2.5	1.6
Spalled element	n/a	Outer race	Inner race	n/a
% spalled element/mass loss (mg)	n/a	15/186	10/38.4	n/a
Time within wear period (hours)	0 – 6	0 – 4	0 - 25	0 - 4
PODS (5 - 15 µm particle count)	5250 - 2600	7500 - 3900	4000	15000 - 2700
Severity Index (5µm + 15µm)	0.09 - 0.02	0.08 - 0.015	0.12	0.058 - 0.005
SOAP Fe content (ppm)	0	0	0	0
Particle range (µm)	1-20	1-15	0.5 - 5	1-10
Particle morphology	Platelets	Platelets	Platelets	Platelets

Table 7.1 Results generated from all tests during the running-in period [1].

[1] In Table 7.1, the running-in period is not included for some of the tests. In Test 2, as shown in Appendix E, there was no debris analysis taken during running-in and benign wear as this was the first accelerated test and the particle analysis during wear out was deemed to be more important. In Tests 5 and 6, shown in section 5.4 and Appendix G, the oil sample was taken slightly after the running-in period to reduce the number of oil samples, and therefore the time required to complete the analysis. In Test 7, shown in section 6.2, the contact was overloaded and the test lasted for a few hours, and so there was no oil samples taken. In Tests 8, as shown in Appendix H, failure was caused by motor failure and so the oil samples were not analysed in order to save time. In Test 10, which was a continuation of Test 9, loading was induced on a defective raceway and is therefore not a true representation of the running-in period when compared to the remainder of the tests.

The important question regarding Table 7.1, is how the running-in period has been defined. This has been achieved by monitoring the particle count during and after loading. During loading, an increased particle count, compared to the following benign wear regime is observed, as shearing of the asperities results in a heightened wear rate. The SEM at this time shows that 5 – 10 µm platelets dominate, with a few particles as large as 20 µm. Therefore, the 5 – 15 µm particle range detected by the PODS provides consistency with the debris shown during SEM analysis and indicates that the quantity of particles in this size range are the most important. The maximum 5 – 15 µm debris count in all tests has a range between 4000 – 15000 particles. A higher severity index was observed in the tapered roller tests at a contact pressure of 2.5 GPa, with values between 0.08 – 0.12, compared to the ball bearing test which employed a contact pressure of 1.6 GPa, the values were between 0.005 – 0.058. This suggests that the severity index is sensitive to bearing type and contact pressure. No iron particles were detected by SOAP in any of the tests during running-in, and can be attributed to debris levels that were below the sensitivity of the technique.

7.3 The wear debris generated during benign wear

Figure 7.2 shows the wear debris generated during benign wear. The particles generated within this regime are generally 5 μm in size, and have a plate-like morphology, smooth surface texture and irregular edge profile, and are explained further in the following section.

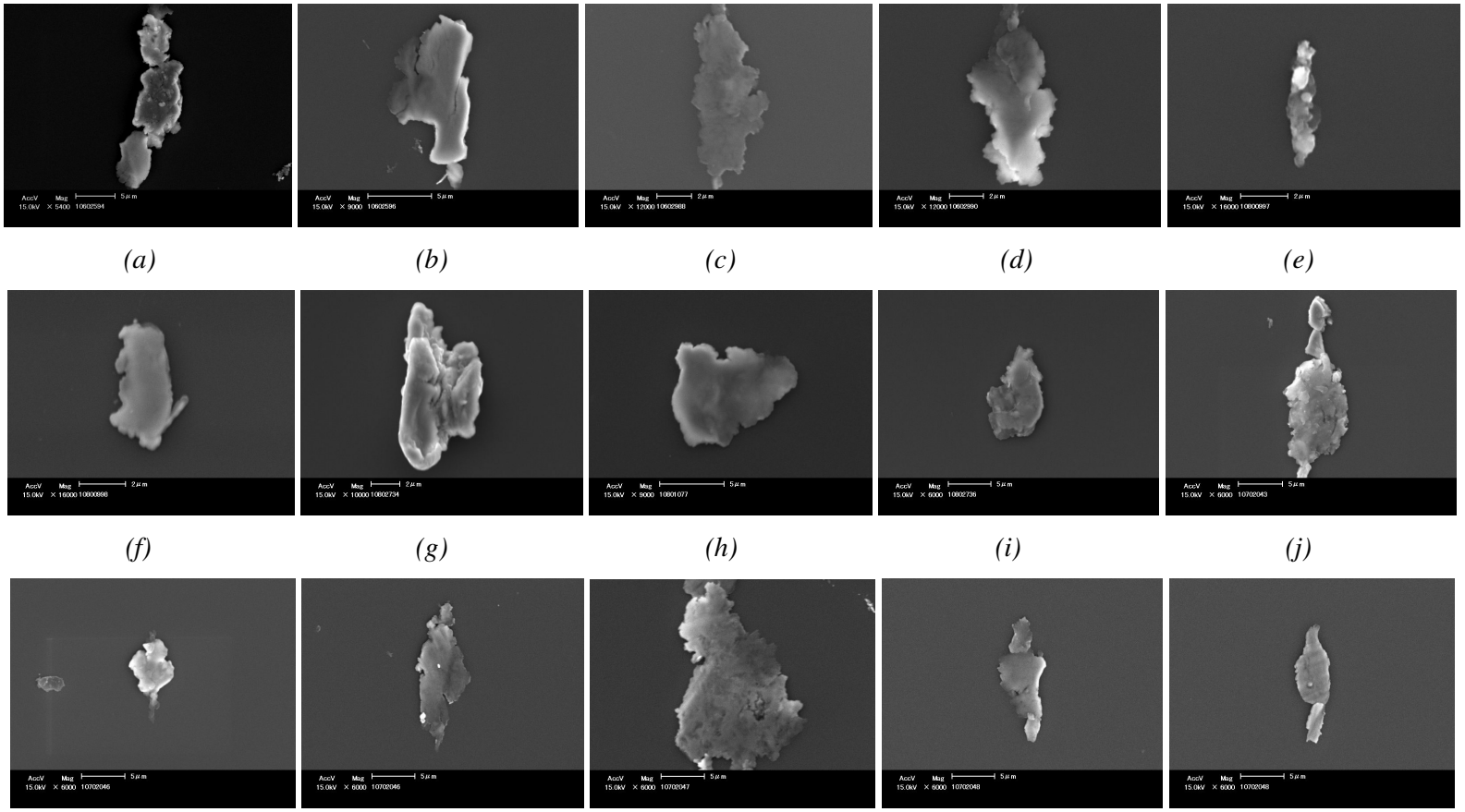

(a) *(b)* *(c)* *(d)* *(e)*

(f) *(g)* *(h)* *(i)* *(j)*

(k) *(l)* *(m)* *(n)* *(o)*

Figure 7.2 The morphology of wear debris during the steady-state. Samples (a – k) show tapered roller bearings and (l– o) ball bearings.

The wear debris generated during benign wear consists of plate-like particles which are between 3 – 20 μm in size; however, the majority of particles are around 5 μm. The importance of this particle size has been shown elsewhere, as particles less than 15 μm relate to low wear levels [87] and a large increase in the particle count indicates abnormal wear [72-74, 208]. These particles have the same plate-like morphology, irregular edge profile and smooth surface texture as those observed during running-in. The particles are isolated, compared to the running-in debris which are clustered, suggesting a reduction in wear rate. The formation of this particle type is attributed to the exfoliation of surface material from the shear mixed layer [69] and identifies a benign wear regime [87].

7.4 Abnormal debris generated during benign wear

Abnormal wear debris, collected during periods of distress within the benign wear regime are shown in Figure 7.3.

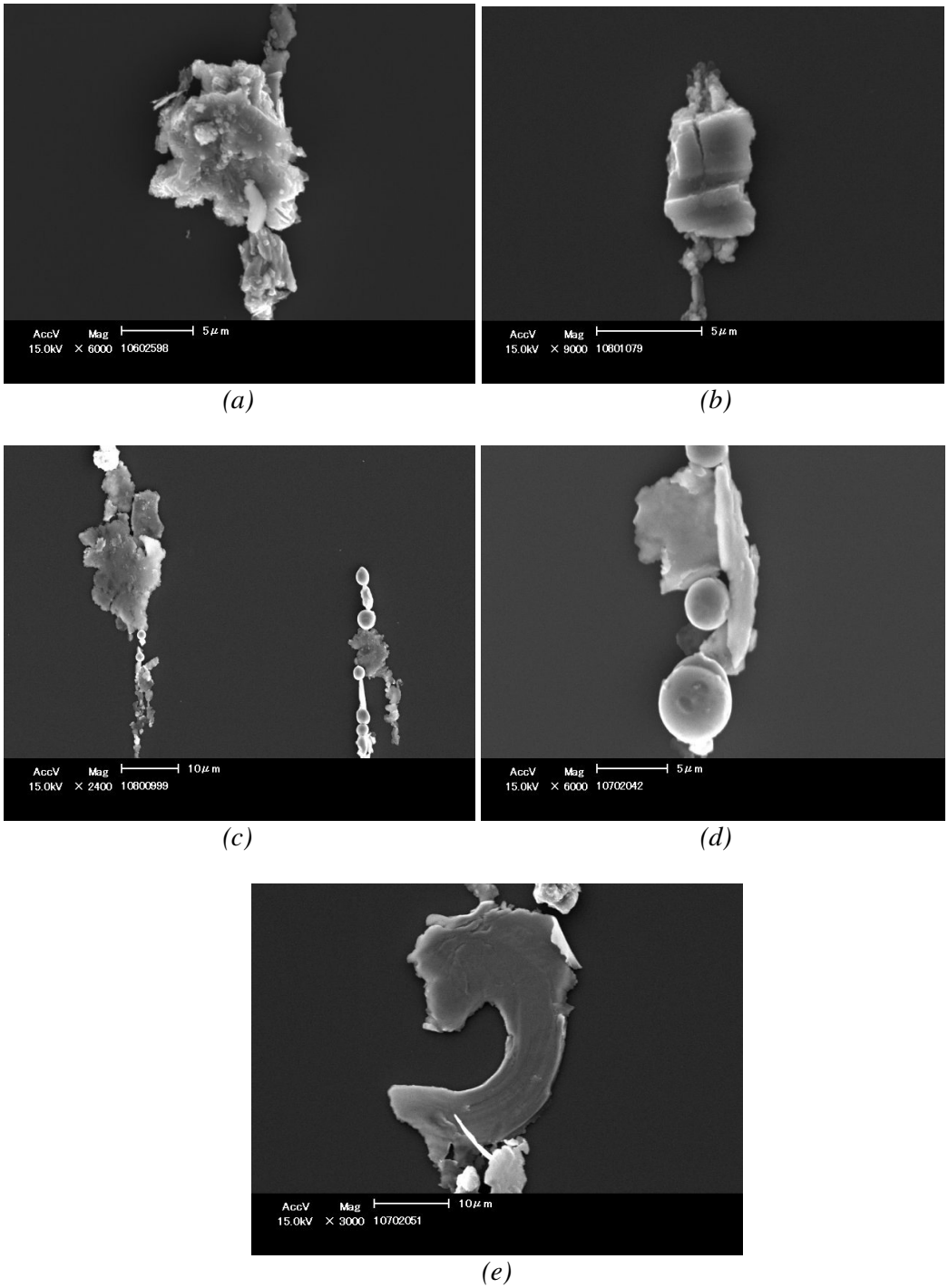

Figure 7.3 The morphology of the wear debris prior to the wear out phase. Samples (a - c) show tapered roller bearings and (d - e) ball bearings.

In Figure 7.3(a), the particle is 12 μm in size with a rugged edge profile, as opposed to platelets identified in the previous regimes. This particle is formed during the plucking out and detachment of material during an adhesive mechanism [209]. In Figure 7.3(b) the wear debris shows a chunky type particle, around 5 μm in size and has a smooth surface texture and irregular circumference. This particle is formed during a fatigue mechanism and indicates the removal of chunks of material with macro levels of wear [72]. In Figure 7.3(c,d), spherical particles around 5 μm in size identify localised welding at the contact interface between surface protuberances, with the generation of flash temperatures and the melting of micro portions of material. After detachment, the molten material solidifies into the spherical shape under hydrostatic pressure in the oil. The detection of this particle type is another indication of an adhesive mechanism [84, 85]. In Figure 7.3(e) the wear particle is curled into an elongated chip. This particle indicates abrasive wear, as a surface protuberance moves across an opposing counter-face, removing material in an action typically found during lathe cutting. These particles are known as cutting debris [72, 74].

In all cases, when the abnormal particle morphology is identified, complimentary evidence of distress is shown by an increased 5 – 15 μm particle count by the PODS, which is consistent with the size of the majority of particles observed during this period. Further evidence of distress is shown in some cases by an increased severity index and iron particle concentration detected by SOAP. These correlations are shown by the particle counting techniques in the following sections and highlight the importance of the debris analysis, as the morphology provides conclusive evidence of the failure mechanisms and the severity of wear is supported by the particle count.

The particles that identify the early signs of distress, brings about an important question. Do rolling element bearings always produce these mechanisms prior to failure, or are they exclusive to the set-up employed in these tests? Compared to the literature review, this is the first time that these particles have been identified during rolling element benign wear, suggesting that these mechanisms are exclusive to this test set-up. However, this is also the first time that corroborating evidence of bearing distress has been obtained using the PODS, severity index, SOAP and SEM. Therefore, if these technologies were implemented on different bearing systems, it is possible that similar observations could be made.

7.5 Collective particle analysis during benign wear and abnormal activity prior to the wear out phase

Table 7.2 shows the maximum and minimum particle levels generated during the steady-state and abnormal debris activity detected within this regime. The steady-state debris levels show a reduced count from running-in, whilst abnormal particle levels are indicated by an increased count compared to benign wear.

	The wear particle analysis generated during benign wear and (the early signs of distress)						
	Tapered roller bearings					Ball bearings	
	Test 1	Test 3	Test 4	Test 5	Test 6	Test 9	Test 10
Location in thesis	Section 5.2	Section 5.3	Appendix F	Section 5.4	Appendix G	Section 6.3	Section 6.4
Contact pressure (GPa)	2.5	2.5	2.5	2.5	2	1.6	1.8
Spalled element	n/a	Outer race	Inner race	Inner race	Inner race	n/a	Inner race
% spalled/mass loss (mg)	n/a	15/186	10/38.4	5/23.3	5/15.31	n/a	15/70.9
Time within period (hours)	4 - 80	4 – 53	25 - 100	4 - 70	4 - 120	4 – 115	6 - 12
PODS (5 - 15 µm count)	1000 - 2000	1400-3200 (7750)	1500-2500 (6500)	1000-3000 (60000)	2750 - 50	2700-3100 (3900)	2000-3200(4100)
Severity Index (5+15µm)	0.0005 - 0.04	0.001 - 0.055	0.001-0.01 (0.14)	0.015-0.06 (0.1)	0.065 - 0.001	0.001 – 0.01	0.001 - 0.025
SOAP Fe content (ppm)	0	0	0 (0.1)	0	0	0	0
Particle range (µm)	1 - 15	1 – 15	1 - 10	1 - 10	5 - 15	3 – 5	1 - 10
Particle morphology	Platelets	Platelets	Platelets	Platelets	Platelets	Platelets	Platelets
Particle range (µm)	n/a	10 – 12	2 - 4	4 - 6	n/a	3 – 5	30 - 40
Particle morphology	n/a	Rugged	Spheres	Chunks	n/a	Spheres	Swarf-like

Table 7.2 Results showing the wear particle analysis during the benign wear regime and abnormal debris levels detected prior to wear out [2,3].

[2] The early distress signatures are coloured in red and/or in brackets alongside the steady-state signatures.
[3] Some debris analysis was not taken during this period. In Test 2 the reason that there was no debris analysis was because this was the first accelerated test, whilst Test 7 was overloaded and lasted for a few hours and in Test 8 because failure was caused by motor failure.

7.6 Wear particle count during benign wear

In all tests, at contact pressures between 1.6 – 2.5 GPa, during the benign wear regime, the maximum 5 – 15 µm debris count was between 2000 – 3200 particles. This shows a reduced debris count, compared to the running-in period, which was identified by a maximum quantity greater than 4000 particles and up to 15000. The severity index also shows reduced levels compared to running-in, and is again shown to be sensitive to bearing type and contact pressure. In the tapered roller tests at 2.5 GPa, the maximum severity index values were between 0.01 – 0.06, and in the ball bearing tests at 1.6 GPa the severity index was between 0.001 – 0.01. Compared to the running-in period, at 2.5 GPa the severity index was between 0.08 – 0.12 and at 1.6 GPa the values were between 0.005 – 0.058. There was no iron particle levels detected by SOAP in any of the tests, which was also the case for the running-in period.

7.7 Wear particle counting levels during the early signs of distress

The most important contribution of any condition monitoring programme is to confidently identify the early signs of distress. In the tapered roller tests, at a contact pressure of 2.5 GPa, this was achieved by the maximum 5 – 15 µm debris count by the PODS which was between 6500 – 60000. Therefore, the evolution of the maximum 5 – 15 µm debris count shows a quantity greater than 4000 and up to 15000 during running-in, which reduced to 2000 - 3200 during benign wear and a quantity in excess of 6500 and up to 60000 during the early signs of distress. In addition, when the 5 – 15 µm debris count was greater than 6500, corroborating evidence of distress is shown by abnormal wear particles, which are shown in section 7.2.1. These particles were rugged, spherical and chunky, as opposed to the plate-like debris that confirmed the benign regime. Further corroborating evidence of abnormal wear was shown by the severity index, indicated by increased values that were between 0.1 – 0.14. A severity index of 0.1 is consistent with the heightened levels that identified an increased wear rate during running-in, and exceeds the maximum value of 0.06 observed during benign wear. Also, one of these tests show increased iron particle detection by SOAP of 0.1 ppm.

In the ball bearing tests, during the early signs of distress, increased 5 – 15 μm particle counts between 3900 - 4100 were identified at contact pressures of 1.8 and 1.6 GPa respectively. However, the debris count was less than 6500, which identified distress at a contact pressure of 2.5 GPa in the tapered roller tests. Therefore, the combined analysis shows a reduced particle count with bearing type and contact pressure during the early signs of distress. Corroborating evidence of abnormal wear, observed by the heightened 5 – 15 μm particle count, was shown by spherical and swarf-like particles, compared to plate-like debris identified during the benign regime. There was no heightened severity index and iron particle levels detected by SOAP, which were likely to be related to the changes in bearing type and reduced contact pressures employed in the other tests.

7.8 Wear debris generated during the wear out phase

The wear debris formed during the wear out phase are shown in Figure 7.4. The debris range is between 2 – 40 μm in size, however, the majority of particles are between 5 – 10 μm and have a plate-like morphology, irregular edge profile and smooth textured surface, which is consistent with the particle types identified in the previous regimes. This analysis again confirms that the quantity of 5 – 15 μm particles is the most important. There are a few plate-like particles that are between 30 – 40 μm in size, as shown in Figure 7.4(m), that also have an irregular edge profile and smooth textured surface. These plate-like particles that are greater than 20 μm in size are consistent with the debris identified in the literature, which relate to gross surface delamination during fatigue failure [83, 85, 87]. Also present are spherical debris, as shown in Figure 7.4(c,d,f), that are around 3 μm in size and confirm adhesive wear. Additional debris types include severe sliding particles [87], as shown in Figure 7.4(b), which are different from the plate-like particles formed during the previous regimes, by the striation marks on the surface. The striations may be formed during particle entrainment between any opposing elements, and during slip or element seizure, the opposing surface slides across the particle counter-face. Another abnormal wear particle is shown in Figure 7.4(i), which is an elongated swarf-like chip that is 3 μm wide and 40 μm in length, and is typically found in a cutting mechanism, similar to a lathe cutting action [74].

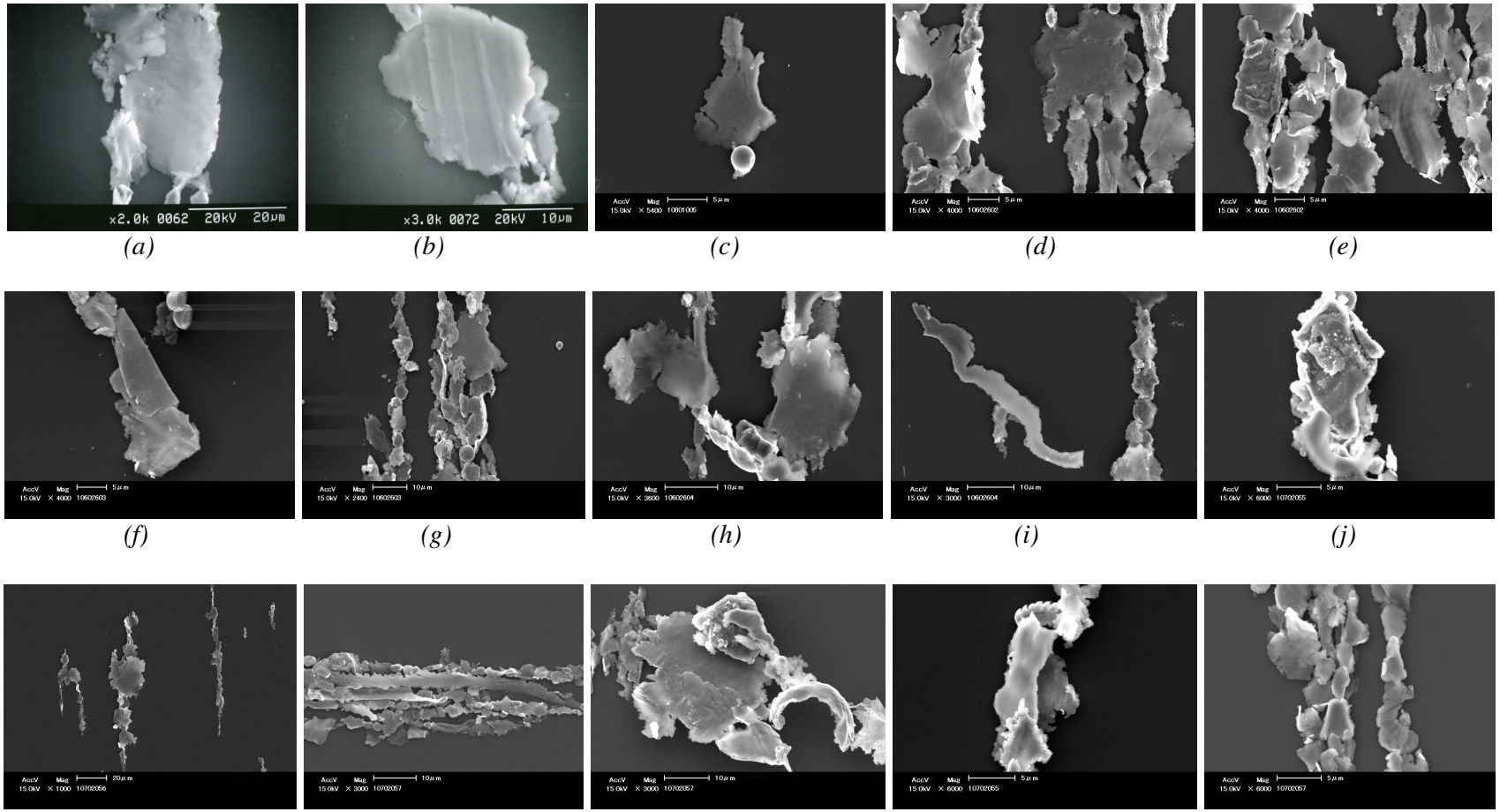

(a) *(b)* *(c)* *(d)* *(e)*

(f) *(g)* *(h)* *(i)* *(j)*

(k) *(l)* *(m)* *(n)* *(o)*

Figure 7.4 The morphology of wear debris during the wear out phase. Samples (a – k) show tapered roller bearings and (l– o) ball bearings.

As can be seen, the size and morphology of the wear particles alter significantly during wear out, indicating several mechanisms are occurring. A possible sequence of events includes gross surface wear after crack growth and spall initiation, which is shown by the increased quantity of 5 – 15 µm plate-like particles and some that have a maximum size of 40 µm. This surface degradation then disrupts element conformity, leading to adhesive and abrasive regimes.

7.9 Collective particle analysis generated during wear out

Table 7.3 shows the debris count during the wear out phase, which is identified by further increases in the quantity of particles, compared to all the other periods of wear. As would be expected, the damaged bearing element showed increased mass loss with an increased area of spallation. In the tapered roller tests, at a contact pressure of 2.5 GPa, the greatest levels of mass loss show the largest plate-like debris and the greatest diversity of mechanisms with adhesive and sliding wear confirmed by the morphology of the particles. A feature of the debris count was that the maximum quantity of 5 – 15 µm debris was between 5000 – 105000. In addition, the heightened 5 – 15 µm debris count was accompanied by abnormal wear particles, which were spherical, plate-like and had striation marks along the surface. This result is consistent with the analysis generated during the early signs of distress, which shows that during abnormal wear, an increased 5 – 15 µm debris count greater than 3200 is complimented by abnormal wear particles. There was also a very good correlation between the particle counting techniques. Thus the 5 – 15 µm particle count increased, the severity index and iron particle content detected by SOAP increased and were higher than the baseline levels, as shown in Table 7.4.

	The wear particle analysis generated during wear out			
	Tapered roller bearings			Ball bearings
	Test 2	Test 3	Test 4	Test 10
Location in thesis	Appendix E	Section 5.3	Appendix F	Section 6.4
Contact pressure (GPa)	2.5	2.5	2.5	1.8
Spalled element	Inner race	Outer race	Inner race	Inner race
% spalled/mass loss (mg)	50/459	15/186	10/38.4	15/70.9
Time within wear period (hours)	68 - 78	53 - 62	100 - 142	12 - 23
PODS (5 - 15 µm particle count)	3000 – 30000	2800 - 105000	1500 - 5000	3000 - 5100
Severity Index (5µm + 15µm)	0.0033 - 1.3	0.05 - 19	0.0008 - 0.006	0.02 - 0.22
SOAP Fe content (ppm)	0 - 0.2	0 - 0.3	0	0.1
Particle range (µm)	5 - 40	1 - 20	5 - 20	5 - 40
Particle morphology	Platelets	Platelets	Platelets	Platelets
Particle range (µm)	2 - 5	2 - 5	2 - 5	15 - 20
Particle morphology	Spheres	Spheres	Spheres	Swarf-like
Particle range (µm)	35 - 40	n/a	n/a	n/a
Particle morphology	Sliding	n/a	n/a	n/a

Table 7.3 Results showing the wear particle analysis during the wear out period [4].

[4] The debris analysis was not taken in a number of tests for the following reasons. Test 1 monitored a defect free bearing and so there was no wear out period. Test 5 and 6 did not identify the wear out period by increasing debris count. Test 7 lasted for a few hours and so there was no oil samples taken. In Test 8, failure was due to motor failure and in Test 9, the wear out period was not identified by any of the techniques.

Test	Δ 5 - 15 μm particle count	Δ Severity index	Δ SOAP
3	102200	18.95	0.3
2	27000	1.2967	0.2
4	3500	0.0052	0

Table 7.4 Changes in the particle count from the baseline levels observed in the tapered roller bearing tests.

There was insufficient debris data generated during the ball bearing tests, for reasons that are shown in the footnote of Table 7.3, to provide any correlations between the techniques. However, in the one bearing test in which the debris analysis was available, results showed that when the maximum 5 – 15 μm particle count was greater than 3200, the severity index exceeded 0.1 and the iron concentration was 0.1 ppm or more. In addition, the heightened debris count was complimented by abnormal wear particles, which in this case was swarf-like and confirmed an abrasive regime.

7.10 Summary of the evolution of wear debris with threshold levels

A summary of the evolution of wear debris is shown in Table 7.5, and confirms that plate-like particles between 5 – 15 μm dominate during all periods of wear. However, there are changes in particle quantity, maximum size and morphology during the changing periods of wear. The debris formed during running-in consists of some plate-like particles that have a maximum size of 20 μm. The plate-like particles are also observed during benign wear and have a slightly smaller maximum size which is up to 15 μm. However, the particle morphology and size changes during the early signs of distress, in accordance with the mechanisms in which they are formed. Spherical particles between 2 – 5 μm in size confirm an adhesive mechanism and chunky 5 μm particles identify fatigue wear. Rugged 12 μm particles also confirm adhesive wear and a few swarf-like chips between 30 – 40 μm identify an abrasive regime. The wear out phase also shows changes in particle morphology and size, when compared to the debris formed in the previous regimes. The plate-like particles dominate with a few particles as large as 40 μm in size. The larger plate-like particles which are 40 μm confirm gross delamination during a fatigue mechanism. Some of these platelets become entrained in the Hertzian contact, and during a sliding mechanism, striations are formed on the particle surface. This occurs when an opposing protuberance moves across the particle counter-face during abrasive wear or

during the over-rolling of other debris in the contact. Further evidence of abrasive wear is shown by some swarf-like chips that are 20 μm in length. Other particles generated during opposing element interaction are spheres that are between 2 – 5 μm in size and identify adhesive wear.

	Tapered roller bearings				Ball bearings			
	Running-in	Benign wear	Distress	Wear out	Running-in	Benign wear	Distress	Wear out
(Particle range µm) Particle type	(0.5-20) Platelets	(1-15) Platelets	(10-12) Rugged (4-6) Chunks (2-4) Spheres	(5-40) Platelets (35-40) Sliding (2-5) Spheres	(1-10) Platelets	(1-10) Platelets	(3-5) Spheres (30-40) Swarf-like	(5-40) Platelets (15-20) Swarf-like
SEM images	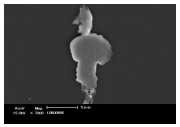	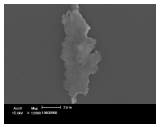	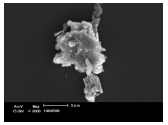 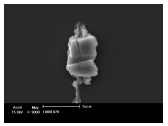 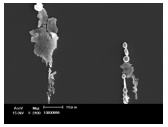	 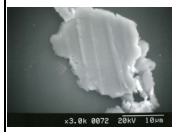 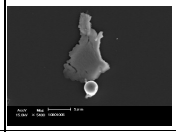	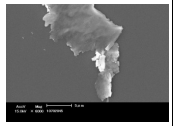	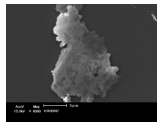	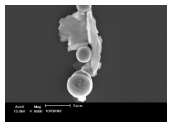 	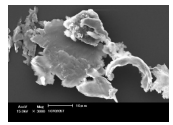
PODS (5 - 15 µm) particle range	2600 - 7500	50 - 3200	6500 - 60000	1500 - 105000	2700 - 15000	2000 - 3200	3943 - 4100	3000 - 5100
PODS (5 - 15 µm) maximum count	4000 - 7500	2000 - 3200	6500 - 60000	5000 - 105000	2700 - 15000	3100 - 3200	3900 - 4100	3000 - 5100
Severity index range	0.015 - 0.12	0.0005 - 0.065	0.1 - 0.14	0.0008 - 19	0.005 - 0.058	0.001 - 0.025	n/a	0.02 - 0.22
Severity index maximum values	0.08 - 0.12	0.01 - 0.065	0.1 - 0.14	0.006 - 19	0.005 - 0.058	0.01 - 0.025	n/a	0.02 - 0.22
SOAP Fe (ppm) concentration range	0	0	0.1	0 - 0.3	0	0	0	0.1
SOAP Fe (ppm) maximum values	0	0	0.1	0.2 - 0.3	0	0	0	0.1

Table 7.5 Summary of the evolution of the particle size, morphology and count during the evolution of bearing wear.

Also shown in Table 7.5, the changes in particle morphology and maximum size are complimented by a fluctuating quantity of debris. The majority of debris identified during SEM analysis during all periods of wear are between 5 – 15 µm in size. This is why the quantity of particles in this range, which is counted by the PODS, is most critical. During running-in, the plate-like particles correlate with a maximum 5 – 15 µm debris count between 4000 – 15000. In the benign regime, the plate-like debris correlate with a reduced quantity of 5 – 15 µm particles, which has a maximum count of 2000 – 3200. The maximum 5 – 15 µm count of 3200 particles provides evidence of a benign wear condition and justification that a particle count above this value should be identified as a potential period of abnormal wear. This is confirmed during the early signs of distress, as the abnormal particle morphology correlates with a maximum 5 – 15 µm debris count that is dependant on bearing type and contact pressure. In the tapered roller tests at 2.5 GPa, the maximum 5 – 15 µm debris count increased to 6500 – 60000 particles, and in the ball bearing test at 1.8 GPa, the maximum particle count increased to 3900 – 4100 particles.

These 5 – 15 µm debris counts provide evidence of particle limits that identify the transition from normal to abnormal wear, which can be justified by a traffic light alarm system. In the tapered roller tests, a maximum 5 – 15 µm debris count of 3200 particles identified benign wear. Therefore, a debris count less than 3200 particles, identifies the green light for normal wear. There was no particle count between 3200 – 6500 particles, therefore, a 3200 – 6500 particle count identifies the amber condition and a period of caution for possible abnormal wear. The amber condition also provides a safety margin for particle counts that exceed the green light condition, but can still be related to normal wear. An example of this is illustrated by the following scenario. A steady-state debris count of 3150 particles increases to 3250, which slightly exceeds the normal wear threshold. However, compared to the previous values, trending of the data set would indicate a nominally steady-state condition, and that a healthy component may not be in need of attention. However, a steady-state debris count of 1000 particles, which increases to 6000, results in a rapid increase in the data trend and would certainly be a cause for urgent attention. Therefore, an upper particle count must be established to identify what safety margin is acceptable. The tapered roller tests show that the minimum debris count that identified abnormal wear was 6500 particles. Therefore, a particle count greater than 6500 identifies the red

light condition, when urgency is required to anticipate the likelihood of bearing failure.

A similar procedure is employed for the ball bearing tests, in which a debris count less than 3200 identifies the green light for normal wear. The amber condition is shown between 3200 – 3900 particles and identifies a period of caution. The red light is shown by a particle count greater than 3900 particles that identifies abnormal wear.

The wear out phase was confirmed by the detection of abnormal particle morphology as well as significantly increased particle count, compared to all other periods of wear. In the tapered roller tests at 2.5 GPa, the maximum 5 – 15 μm debris count was between 5000 – 105000 particles. Therefore, in the tapered roller tests, all periods of abnormal particle formation are complimented by a maximum 5 – 15 μm debris count greater than 3200. In addition, the maximum debris count was greater than 6500 particles, which is consistent with the alarm based threshold that indicates abnormal wear. In the ball bearing test at 1.8 GPa, the maximum debris count was 5100 particles. The reduced particle count compared to the tapered roller tests relate to bearing contact geometry and contact pressure. However, the ball bearing test also shows that abnormal particle formation correlates with a maximum 5 – 15 μm count greater than 3200, and exceeds the 3900 particle threshold that confirms abnormal wear.

Another debris parameter that changes during the evolution of wear is the severity index, with values that are again dependant on bearing type and contact pressure. In the tapered roller tests, during running-in the maximum severity index values were between 0.08 – 0.12, and decreased to 0.0005 – 0.065 during benign wear. The severity index increased to 0.1 – 0.14 during the early signs of distress, and increased further with a maximum value of 19 during wear out. Therefore, the abnormal particles that confirm the mechanism of wear and the 5 – 15 μm particle count greater than 6500 also correlates with a severity index of 0.1 or more. This combined analysis provides further evidence of another traffic light alarm based system. Severity index values less than 0.065 indicates benign wear, 0.065 – 0.1 indicates a period of potential distress and values greater than 0.1 confirm abnormal wear.

In the ball bearing test, the severity index was between 0.05 and 0.058 during running-in, and decreased to between 0.01 and 0.025 during benign wear. There was no accentuated severity index value during the early signs of distress. The reduced severity index values compared to the tapered roller tests was probably due to the change in bearing type and reduced contact pressure, generating lower debris levels. However, as the particle levels increased during wear out, the severity index increased to 0.02 – 0.22. This analysis also shows the promise of another alarm system. Severity index values less than 0.025 indicates benign wear, between 0.025 – 0.05 indicates the potential period of abnormal wear and values greater than 0.05 indicates abnormal wear.

The SOAP showed that the iron concentration increased to 0.1 ppm or more during periods of abnormal wear. Therefore, the combined analysis shows a good correlation between the abnormal particle morphology, a 5 – 15 µm debris count greater than 3200, a severity index in excess of 0.065 and 0.025 and an iron concentration of greater than 0.1 ppm. This is shown in the tapered roller tests, when during the early signs of distress, a maximum iron concentration of 0.1 ppm was observed, and increased to 0.2 – 0.3 ppm during wear out. In the ball bearing test, there was no increase in iron concentration during the early signs of distress. This is consistent with the severity index, which did not identify increased activity at this time, due to changes in bearing type and reduced contact pressure. However, during wear out the iron concentration increased to 0.1 ppm, which correlated with the increased severity index which was greater than 0.1.

7.11 In-line sensor signatures generated during running-in

Table 7.6 shows the minimum and maximum sensor levels generated during running-in. Correlations are shown between the different techniques, contact pressures, mechanisms and severity of wear.

	The in-line sensor analysis during running-in wear								
	Tapered roller bearings						Ball bearings		
	Test 1	Test 2	Test 3	Test 4	Test 5	Test 6	Test 7	Test 8	Test 9
Location in thesis	Section 5.2	Appendix E	Section 5.3	Appendix F	Section 5.4	Appendix G	Section 6.2	Appendix H	Section 6.3
Hertzian contact pressure (GPa)	2.5	2.5	2.5	2.5	2.5	2	2.5	1.6	1.6
Spalled element	n/a	Inner race	Outer race	Inner race	Inner race	Inner race	Inner race	n/a	n/a
% spalled element/mass loss (mg)	n/a	50/459	15/186	10/38.4	5/23.3	5/15.31	7/38.2	n/a	n/a
Time within wear period (hours)	0 - 6	0 - 7.5	0 - 4	0 - 25	0 - 4	0 - 4	0 - 3	0 - 4	0 - 4
OLS (pC)	0.1 - 0.02	0.125-0.75 [5]	0.06 - 0.02	0.03 - 0.025	0.03 - 0.01	0.025-0.019 [6]	0.07 - 0.03	0.03 - 0.02	0.01-0.02 [7]
Indicator value	4000 - 2000	3000 - 3900	3750 - 2000	2750 - 3000	3500 - 1500	2000 - 300	3750 - 3000	3250 - 2750	300 - 0
Inductive (0 - 100 µm bin count)	0	0 - 10	0 - 1	n/a	n/a	n/a	0 - 1	n/a	n/a
Ferromagnetic (accumulative)	0	0	0	n/a	n/a	n/a	0	n/a	n/a
WSS 2 (pC)	0.3 - 0.8	0.5 - 2.1	0.5 - 1 [8]	0.25 - 1.5	0.5 - 1.75	0.25 - 1	0.25 - 1	0.5 - 1.5	0.5 - 1
Vibration (g)	1.6 - 1.9	2 - 3.5	1 – 1.1	0.5 - 0.8	0.9 - 0.5	1.1 - 0.5	1 - 2	0.75 - 1	0.4 - 0.3
Bearing outer race temperature (°C)	25 - 65	n/a	38 – 70	30 - 67	25 - 65	32.5 - 56	32.5 - 59	30 - 46	30 - 46
AE (peak amplitude - dB)	n/a	n/a	n/a	62 - 82	75 - 79	70 - 76	n/a	n/a	63 - 65

Table 7.6 Results showing the real time sensor analysis during running-in wear [9,10].

[5] In Test 2, OLS sensor was positioned on Nylon recirculation pipe-work, which increased the RMS charge measurement compared to copper pipe-work.
[6] In Test 6, the OLS and indicator values were of poor integrity as there was no variation from the steady-state throughout the test.
[7] In Test 9, the OLS and indicator values were of poor integrity as there was no variation from the steady-state throughout the test.
[8] In Test 3, the charge measurement was taken from WSS 3, which monitors single bearing (4) and is therefore not included in the analysis.
[9] Test 10 is not shown as this was a continuation of Test 9. Therefore running-in took place on defective surface which is not comparable to the remainder of the tests
[10] In all cases, n/a indicates that the sensor was not used due to the availability of the technique.

Comparing the oil-line signatures show that in the majority of tests, using copper recirculation pipe-work, the maximum OLS charge levels were between 0.02 – 0.1 pC, and correlate with maximum indicator values between 3000 – 4000. A likely source of sensor activity is the heightened particle count, confirmed by the 5 – 15 µm particle count greater than 3200 by the PODS and severity index values of 0.05 or more, which were observed in the previous sections.

However, in Tests 6 and 9, there was uncertainty about the authenticity of the indicator value (with maximum levels of 2000 and 300 respectively) as they exhibited no variation throughout testing. Therefore, these data sets were deemed to be of poor integrity, possibly due to poor sensor or instrumentation connection. The identification of poor integrity data provides justification for the implementation of the multiple sensing suite. This is due to reliability issues that relate to spurious data collection, which do not provide a true indication of component performance. Therefore, comparisons between sensors from multiple tests, provide confidence that skewed data sets should be approached with caution and that signal levels of similar magnitude can be believed.

The common feature observed for the WSS's is that for all tests the no load condition was identified by charge between 0.25 – 0.5 pC. These initial charge levels indicate a reference for a correct bearing installation and that the sensor set-up is working correctly. Further comparisons are shown between the WSS data for the tapered roller tests. For Test 1, the baseline of the defect free signature shown that the difference between the minimum and maximum charge level was 0.5 pC. However, in the tests which had an inner race defect, the difference in the minimum and maximum charge levels increased to 1.25 pC and up to 1.6 pC. This suggests that the increase in charge is related to interfacial contact between the defect protuberance and the rolling elements during loading. Further sources of wear site charge relate to the generation of contact potential differences, between original and modified surfaces during distress, which includes plastic deformation, nascent surfaces and phase changes [185, 194]. An additional source of charge includes the generation of wear debris, which requires the breaking of multiple atomic bonds, and results in charge modifications to the particle and parent surface.

In the tapered roller tests, it appears that contact pressures influence wear site charge. At the higher contact pressure of 2.5 GPa, charge is between 1.25 – 1.6 pC, compared to 0.75 pC at the lower contact pressure of 2 GPa. These results show that the wear site charge is sensitive to contact pressure, which can be associated with the amount of conforming (plastic deformation and asperity shearing) of the contacting surfaces.

A feature of the ball bearing tests is that the vibration sensor showed an increase in acceleration levels with contact pressure. Levels change from 0.25 to 1 g at 1.6 to 2.5 GPa respectively. This increase may be explained by impacts generated during the passage of the rolling elements on the inner race defect. However, there is no clear relationship between the vibration levels and contact pressure in the tapered roller tests, as at contact pressures of 2.5 and 2 GPa in Tests 5 and 6, there was a decrease in acceleration levels of 0.4 and 0.6 g respectively. A possible reason why the increased vibration with contact pressure is more prominent in the ball bearings, may be because there were three indents located on the inner race, compared to one on the tapered rollers. However, a greater range of testing would be required to validate this.

Correlations between the thermocouples in the tapered roller tests show that at the higher contact pressure of 2.5 GPa, the bearing outer race temperatures were between 65 - 70°C, whilst at 2 GPa, a reduced temperature of 56°C was observed. A similar effect is seen in the ball bearing tests. At the higher contact pressure of 2.5 GPa, the outer race temperature was 59°C, whilst at the lower contact pressure of 1.6 GPa, the outer race temperature were reduced to 46°C.

Further effects of contact pressure are shown with the AE peak amplitude parameter. In the tapered roller tests, at 2 and 2.5 GPa, the maximum peak amplitude levels were 76 dB and between 79 and 82 dB respectively. In the ball bearing tests, at 1.6 and 1.8 GPa the maximum peak amplitude was 65 dB. The combined analysis shows increased peak amplitude parameter with contact geometry and pressure, which may be related to surface deformation mechanisms such as asperity collisions between opposing elements.

7.12 In-line sensor signatures generated benign wear and abnormal wear

Table 7.7 shows the minimum and maximum sensor levels generated during the steady-state and abnormal events detected within this regime. The steady-state sensor levels show reduced levels compared to running-in and attain steady-state trends. Abnormal signatures are then identified by heightened activity generated during the benign wear regime.

	The in-line sensor analysis generated during benign wear and (the early signs of distress)								
	Tapered roller bearings						Ball bearings		
	Test 1	Test 2	Test 3	Test 4	Test 5	Test 6	Test 8	Test 9	Test 10
Location in thesis	Section 5.2	Appendix E	Section 5.3	Appendix F	Section 5.4	Appendix G	Appendix H	Section 6.3	Section 6.4
Contact pressure (GPa)	2.5	2.5	2.5	2.5	2.5	2	1.6	1.6	1.8
Spalled element	n/a	Inner race	Outer race	Inner race	Inner race	Inner race	n/a	n/a	Inner race
% spalled/mass loss (mg)	n/a	50/459	15/186	10/38.4	5/23.3	5/15.31	n/a	n/a	15/70.9
Time within period (hours)	4 - 80	7.5 - 68	4 - 53	25 - 100	4 - 70	4 - 120	4 - 90	4 - 115	6 - 12
OLS (pC)	0.02 - 0.03	0.125-0.625 [11]	0.015 - 0.025	0.019 - 0.03	0.01 - 0.02	0.01 - 0.02 [12]	0.02 - 0.03	0.01 - 0.02	0.02 – 0.03
Indicator value	2000 - 3250	1000 - 4000	1000 - 2500	2000 - 3000	1000 - 1750	500 - 2000	3250 - 2000	200 - 500	2000-3000
Inductive (<100 µm count)	1	0 - 9	1	n/a	n/a	n/a	n/a	n/a	n/a
Ferromagnetic	0	0	0	n/a	n/a	n/a	n/a	n/a	n/a
WSS (pC)	0.7 - 0.85	0.8 - 1.5	0.6 - 0.8	0.3 - 1.5	1.25 - 1.5	0.25 - 1.5	1 - 1.5	0.5 - 1	3 - 4
Vibration (g)	1.5 - 2	2 - 3	0.75 - 1	0.5 - 1	0.5 - 0.8	0.5 - 0.75	0.75 - 1.3	0.35 - 0.75	1.5 - 2.25
Outer race temp (°C)	57.5 – 67.5	n/a	65 - 70	50 - 62	60 - 68	47 - 60	40 - 45	44 - 46	44 - 46
AE (peak amplitide - dB)	n/a	n/a	n/a	65 - 78 (80)	76 - 79 (88)	72 - 77 (81)	n/a	65 - 70 (75)	55 - 70 (79)

Table 7.7 Results showing the real time sensor analysis during benign wear and abnormal events [13,14,15].

[11] The OLS and indicator value is taken using Nylon recirculation pipe-work.
[12] The OLS charge and indicator values from Tests 6 and 9 were deemed to be of poor integrity.
[13] Test 7 is not shown as the test lasted a few hours in which there was no clear evidence of benign wear.
[14] In Table 7.6, n/a indicates that the technique was not used.
[15] In all cases the signal activity during the early signs of distress are coloured red and in brackets.

7.13 Sensor analysis during the steady-state

The OLS charge and indicator value showed that with the use of copper recirculation pipe-work, maximum sensing levels of 0.02 – 0.1 pC and 2750 – 4000 during running-in, reduced to 0.02 – 0.03 pC and 1750 – 3250 during benign wear. The reduced signatures, with maximum values of 0.03 pC and 3250 correlates with the maximum 5 – 15 µm debris count of 3200 particles.

From the techniques in the test chamber, in all tests the maximum wear site charge level was 1.5 pC, except for Test 10, which was a continuation of Test 9. Correlations between the thermocouple data shows that outer race temperatures increased with contact pressure. At 1.6 – 1.8 GPa, the maximum outer race temperature was 46°C, whilst at 2 GPa this increased to 60°C. At 2.5 GPa the maximum outer race temperatures were between 62 – 70°C. AE peak amplitude also increased with contact pressure. At 1.6 – 1.8 GPa the maximum levels during benign wear were 70 dB, whilst at 2 GPa there was an increase to 77 dB and at 2.5 GPa there were further increases to 78 – 79 dB.

7.14 Sensor analysis during the early signs of distress

In the tapered roller tests at a contact pressure of 2.5 GPa, the maximum AE peak amplitude increased from 78 – 79 dB during benign wear to 80 – 88 dB during the early signs of distress. At a contact pressure of 2 GPa, the baseline level was between 72 - 77 dB with an increase in activity to 81 dB during distress. This suggests that the AE peak amplitude is sensitive to contact pressure during the early signs of distress. Corroborating evidence that the increased peak amplitude at this time related to the early signs of distress is shown by the detection of abnormal wear particles, a 5 – 15 µm debris count greater than 6500 particles, a severity index greater than 0.1 and an iron particle concentration of 0.1 ppm detected by SOAP.

In the ball bearing tests, the peak amplitude during the early signs of distress was again sensitive to contact pressure. At 1.6 and 1.8 GPa, the baseline levels were 70 dB, with heightened activity at 75 dB and 79 dB respectively during distress. The periods of increased AE peak amplitude correlate with an increased 5 – 15 µm debris count of greater than 3943 and abnormal wear particles. The heightened AE peak

amplitude and particle count in both sets of tests is believed to be related to short periods of debris generation associated with the early stages of fatigue failure. The reduced sensor activity after this initial period of wear is associated with healing of the defect zone by smoothing of the sharp edges of the defect protuberances [2].

7.15 In-line sensor signatures generated during wear out

Table 7.8 shows the minimum and maximum sensor levels generated during wear out. The signatures show runaway sensing levels that provide evidence of propagating surface wear. Assuming that the majority of wear occurred during this period, which is supported by the heightened off-line debris analysis, correlations between tests show an increased inductive and ferromagnetic particle count with mass loss. The mass loss also increases with the maximum OLS charge and indicator values. In the tapered roller tests, the lowest mass loss of 23.3 g in Test 5 gave the lowest charge and indicator values of 0.02 pC and 1750 respectively. As the mass loss increased to 38.4 g in Test 4, the charge and indicator value increased to 0.04 pC and 3500. For Test 3, a mass loss of 186 mg produced further increases in charge and indicator value to 0.085 pC and 3900 respectively. Correlations between the OLS charge, indicator value and mass loss are not provided for Test 2, as nylon recirculation pipe-work was used which produced much higher background charge levels than copper employed in the other tests. Similar observations are shown in the ball bearing tests, with Test 7 yielding the lowest mass loss (38.2 g), charge (0.045 pC) and indicator value (3750). While Test 10 produced higher mass loss (70.9 g), charge (0.09 pC) and indicator value (3900). This can be explained by the increased debris entrainment in the oil-line during damage propagation.

Correlations between tests indicate that the WSS charge levels and trends identified in Tests 4 and 6, were typical of the levels identified during benign wear (maximum levels of 1 pC), indicating that the wear out phase was not identified in these tests. In Addition, Test 3 monitored bearing 4, which was charge of one bearing compared to the measurements which monitored two bearings. However, in the reminder of the tests, the charge signatures showed increasing trends with levels that exceeded 1.5 pC, which confirmed benign wear.

	The in-line sensor analysis generated during wear out							
	Tapered roller bearings					Ball bearings		
	Test 2	Test 3	Test 4	Test 5	Test 6	Test 7	Test 8	Test 10
Location in thesis	Appendix E	Section 5.3	Appendix F	Section 5.4	Appendix G	Section 6.2	Appendix H	Section 6.4
Contact pressure (GPa)	2.5	2.5	2.5	2.5	2	2.5	1.6	1.8
Spalled element	Inner race	Outer race	Inner race	Inner race	Inner race	Inner race	n/a	Inner race
% spalled/mass loss (mg)	50/459	15/186	10/38.4	5/23.3	5/15.31	7/38.2	n/a	15/70.9
Time within wear period (hours)	68 - 78	53 - 62	100 - 142	70 – 76	120 – 165	3 - 4.5	91 - 92	12-23
OLS (pC)	0.125 - 0.6 [16]	0.015 - 0.085	0.02 - 0.04	0.01 - 0.02	0.01 - 0.025	0.015 - 0.045	0.021 - 0.03	0.02 - 0.09
Indicator value	1000 - 4000	2000 - 3900	2700 - 3500	1000 - 1750	500 - 2000	2000 - 3750	2000 - 3000	2500 - 3900
Inductive (0 - 100 µm bin count)	0 - 780	0 - 20	n/a	n/a	n/a	0 – 9 [17]	n/a	n/a
Ferromagnetic	0 - 390	0 - 220	n/a	n/a	n/a	0	n/a	n/a
WSS (pC)	0.5 - 3.5	0.6 - 1.5 [18]	0.5 - 1	1.25 - 3.9	0.25 – 1	1 - 3.25	1 - 1.5	3 - 5
Vibration (g)	3 - 22.5	0.8 - 4.5	1 - 1.9	0.75 - 1.5	0.75 - 1.25	2 - 4	1.25 - 1.4	2.2 - 4.2
Bearing outer race temperature (°C)	n/a	70 - 90	50 - 60	65 – 75	45 – 55	57.5 - 60	47 - 55	46 - 50
AE (peak amplitude - dB)	n/a	n/a	75 - 95	80 – 99	77 – 86	n/a	n/a	60 - 98

Table 7.8 Results showing the real time sensor analysis during wear out [19,20].

[16] The OLS charge is taken using Nylon recirculation pipe-work which resulted in increased oil-line charge.
[17] The particle count is taken from the 200 – 400 µm particle range as there was no 0 – 100 µm particles detected.
[18] Charge is taken from WSS 3, since failure was observed on bearing 4.
[19] Test 1 is not included as this was a defect free bearing in which wear out was not identified. Test 9 is not included as there was no wear out period.
[20] In Table 7.7, n/a indicates that this technique was recalled by Macom Technologies.

In the tapered roller bearing tests, temperature increases above the baseline levels in the benign regime were typically around 10 °C. However, in Test 3 there was an increase of 20°C which was likely to be related to the increased mass loss, causing an increased surface deformation and roughening of the contact, initiating oil-film breakdown and frictional heating. In the ball bearing tests, there were minor temperature increases (2.5 – 8°C), which were typical of the variations observed during benign wear in the tapered roller tests. This reduced temperature differences is believed to be related to bearing type, as the contact pressure and mass loss measurements were similar for the tapered roller tests.

In all tests, the AE peak amplitude showed increasing trends, with levels in excess of 80 dB and maximum values of 99 dB. In addition, increased AE levels showed a very good correlation with increasing acceleration levels, mass loss and the 5 – 15 µm particle count, as shown in Table 7.9.

Test	Δ AE (dB)	Δ acceleration (g)	Δ mass loss (g)	5 - 15 µm particle count
6	9	0.5	15.31	500
5	19	0.75	23.3	1500
4	20	0.9	38.4	5000
10	38	2	70.9	5100

Table 7.9 Correlations between the peak amplitude, acceleration, mass loss and 5 – 15 µm particle count.

7.16 The sensing signatures with threshold levels

Table 7.10 shows a summary of the minimum and maximum sensor levels. Results show that the sensor trends are consistent with the profile characterised by the bath-tub curve. These show heightened activity during running-in, reduced sensing levels during benign wear, short periods of increased signal activity during the early signs of distress and runaway signatures during wear out. The fluctuating sensor activity also shows very good correlation with the evolution of wear debris and this is the likely the source of signal activity.

The OLS charge and indicator values were of similar magnitude for both bearing types during running-in, with maximum levels of 0.1 – 0.07 pC and 4000 – 3750

respectively. These signatures then decreased with maximum values of 0.03 pC and 3250, which confirmed benign wear. Both signatures show a very good correlation with the 5 – 15 μm debris count, which indicated benign wear by a maximum particle count of 3200. Further evidence that these signal levels relate to benign wear are shown during wear out, as the signatures increase from 0.03 pC and 3250 to 0.085 – 0.09 pC and 3900. Further support that an OLS charge of 0.03 pC relates to benign wear is shown in a previous test by Harvey *et al* [197]. During the benign regime, the OLS charge was 0.03 pC, and increased to 0.095 pC during wear out. The source of increased OLS charge and indicator values in all tests were increased debris in the scavenge line, which was confirmed by the runaway particle levels.

As was the case for the particle analysis, the OLS and indicator values provide corroborating evidence of threshold limits based on the traffic light system. This system indicates the transition from benign wear, with a safety margin to allow for variation during testing and abnormal wear. OLS charge and indictor values less than 0.03 pC and 3250 respectively identify the green light for benign wear. The caution band in the amber region, allowing for variation during testing, is shown by values between 0.03 – 0.07 pC and 3250 – 3750. The upper sensing limits that indicate abnormal wear are shown by values greater than 0.07 pC and 3750.

	Tapered roller tests				Ball bearing tests			
	Running-in	Benign wear	Distress	Wear out	Running-in	Benign wear	Distress	Wear out
OLS (pC) – Range	0.01 - 0.1	0.01 – 0.03		0.01 - 0.085	0.02 - 0.07	0.01 - 0.03		0.015 - 0.09
OLS (pC) - Maximum	0.03 - 0.1	0.02 – 0.03		0.02 - 0.085	0.03 - 0.07	0.02 - 0.03		0.03 - 0.09
Indicator value - Range	1500 - 4000	1000 - 3250		1000 - 3900	2750 - 3750	2000 - 3250		2000 - 3900
Indicator value - Maximum	3000 - 4000	1750 - 3250		2000 - 3900	3250 - 3750	3000 - 3250		3000 - 3900
Inductive (0 - 100 µm bin count) - Range	0 - 10	0 - 9		0 - 780	0 - 1	0		0 - 9
Inductive (0 - 100 µm bin count) - Maximum	1 - 10	1-9		20 - 780	0 - 1	0		0 - 9
Ferromagnetic - Range	0	0		0 - 390	0	0		0
Ferromagnetic - Maximum	0	0		20 - 390	0	0		0
WSS (pC)-Range	0.25 - 2.1	0.25 - 1.5		0.25 - 3.5	0.25 - 1.5	0.5 - 1.5		1 - 5
WSS (pC) - Maximum	0.8 - 2.1	0.8 – 1.5		1.5 - 3.5	1 - 1.5	1 - 1.5		1.5 - 5
Vibration (g) – Range	0.5 - 3.5	0.5 - 3		0.75 - 22.5	0.3 - 2	0.35 - 1.3		1.25 - 4.2
Vibration (g) - Maximum	0.8 - 3.5	0.75 - 3		1.25 - 22.5	0.4 - 2	0.75 - 1.3		1.4 - 4.2
Bearing outer race temperature (°C) - Range	25 - 70	47 - 70		45 - 90	30 - 59	40 - 46		46 - 60
Bearing outer race temperature (°C) - Maximum	65 - 70	60 - 70		86 - 90	46 - 59	45 - 46		50 - 60
AE (peak amplitude - dB) - Range	62 - 82	65 - 79	80 - 88	75 - 99	63 - 65	55 - 70	75 - 79	60 - 98
AE (peak amplitude - dB) - Maximum	76 - 82	77 - 79	80 - 88	86 - 99	63 - 65	65 - 70	75 - 79	60 - 98

Table 7.10 The evolution of the in-line sensing signatures.

In all tests, a feature of the WSS during benign wear was maximum charge levels of 1.5 pC. The maximum 1.5 pC wear site charge correlates with the maximum 5 – 15 µm particle count of 3200; OLS charge and indicator values of 0.03 pC and 3250, which are thresholds that indicate a normal operation. Further support that a wear site charge of 1.5 pC identifies benign wear is shown during wear out, as the charge increased to maximum values of 3.5 – 5 pC. Additional confirmation that wear site charge of 1.5 pC relates to a normal bearing operation is again shown by Harvey *et al* [197]. These results show that during benign wear the charge was 1.5 pC and increased to 11 pC during wear out. This combined analysis provides justification of additional threshold bands that identify the transition from normal to abnormal wear. Wear site charge less than 1.5 pC identifies benign wear, levels between 1.5 – 3.5 pC identify a period of caution and charge greater than 3.5 pC confirms abnormal wear.

The source of increased wear site charge related to contact between the opposing elements during surface damage, which increased with mass loss. Correlating evidence of contact between opposing elements during surface damage was shown by runaway vibration, temperature and AE peak amplitude which also increased with mass loss. Further evidence which shows that the source of wear site charge relates to contacting surfaces can be explained by a combination of sensor activity, particle analysis and observations made during testing. In all tests, the increase in charge above the 1.5 pC threshold correlated with abnormal wear debris. These particles were plate-like with striations, spherical and swarf-like and identified abrasive and adhesive wear, which results from oil-film breakdown and contact between surfaces under motion. In further tests, the increase in charge was identified when the bearing elements were overloaded, seized and during a fluctuating motor speed when the brushes were worn. These activities also encourage oil-film breakdown and contact between opposing elements. Further support that the increase in wear site charge is associated to boundary conditions are shown in the literature, where perturbations in signal activity were linked to first transition scuffing by the confirmation of white layers [194, 196]. Also, a rapid increase in charge correlated with rapid increases in surface temperature and friction coefficient [210], which were also related to scuffing. Further rapid increases in charge were observed with perturbations in friction and was again consistent with boundary wear [193].

An important feature of the AE peak amplitude was that this parameter identified the early signs of distress, and was corroborated by the increased 5 – 15 μm debris count, severity index, SOAP and abnormal wear particles. The heightened AE peak amplitude was sensitive to bearing type and contact pressure and related to impacting between the rolling elements on the damaged region. Threshold limits that identify the integrity of the tapered roller bearings are shown by peak amplitude levels between 60 – 80 dB during benign wear, signatures of 80 – 88 dB that identify a period of caution and values greater than 88 dB which identify abnormal wear. Ball bearing thresholds are shown by peak amplitude values between 60 – 70 dB during benign wear, levels of 70 – 79 dB which identify a period of caution and levels of 80 dB or more that confirm abnormal wear.

The source of the heightened peak amplitude was likely to be related to impacts between the rolling elements and protuberances of the roughened raceway during runaway wear. Corroborating evidence of impacting elements has been shown by Al-Gamdt and Mba [20] who noted that heightened peak amplitude levels related to contact between a rolling element on a protruding wear site. Further evidence that the heightened peak amplitude related to contact between opposing elements during surface damage was observed by and Choudbury and Tandon [123]. These results show that more events were identified at higher peak amplitude values as the size of an inner race defect increased. An additional source of heightened peak amplitude activity is crack initiation and propagation which must occur during material liberation from the wear site. However, decoupling the contribution of crack growth and impacting elements to the peak amplitude parameter presents a very difficult task.

However, if impacting was detected by the AE peak amplitude in advance of the wear phase, then why was this not identified by the wear site sensor? The wear site sensor did identify the early signs of distress, but this required the application of the AI methods. This shows that the wear site charge signatures do have valuable information within the data set, which upon extraction can elucidate the early signs of distress.

The vibration acceleration signatures were not sensitive to the early signs of distress. However, this technology clearly identified the running-in process and the wear

phase, which provided corroborating evidence of tribological activity (impacting elements during oil-film breakdown) to the remainder of the in-line techniques. The acceleration signature also generated threshold bands that identified the transition from normal to abnormal wear, which related to contact geometry and pressure. In the tapered roller tests, at 2 – 2.5 GPa, acceleration levels of 0.75 – 3 g identified benign wear, increasing to 3 – 3.5 g during periods of caution, whilst levels greater than 3.5 g confirmed abnormal wear. In the ball bearing tests, which induced contact pressures of 1.6 – 1.8 GPa, benign wear was identified by levels of 0.4 – 1.3 g, periods of caution were shown with levels between 1.3 – 2 g and values greater than 2 g confirmed abnormal wear.

The thermocouples were also not sensitive to the early signs of distress, but again provided corroborating evidence of the tribology (frictional heating) at the Hertzian contact during running-in and wear out. The temperature levels also generated thresholds that were dependant on contact geometry and pressure. In the tapered roller tests at 2 – 2.5 GPa, the benign regime was identified by outer race temperatures between 60 – 70°C. In the ball bearing tests at 1.6 – 1.8 GPa, the outer race temperatures were 45 – 46°C. In both bearing types, a period of caution was shown by a temperature increase within 10°C of the benign regime, whilst a temperature increase greater than 10°C from the benign regime confirmed abnormal wear.

As the detected bearing characteristics show, the sensor outputs are dependent on the geometry of the contact and applied pressure. Further factors that influence each sensing technique include material type, operating speed, lubricant type, flow rate and locality of the sensing technology relative to the contact region. Therefore, if these technologies were applied to different machine components and process parameters, then the sensor outputs would again be dependent on that particular set-up. This shows that these machine signatures are exclusive to the process that they monitor.

8 Conclusions

This chapter identifies the conclusions to this work, which has used corroborating signatures to confidently identify the evolution and earliest signs of rolling element bearing wear. This multi-sensing suite utilised traditional and novel technologies, which incorporated an off-line debris monitoring program, in-line debris detection schemes and dynamic sensor responses that monitored degradation at the wear site.

From tapered roller and ball bearing tests, several regions of wear were identified from debris and sensing levels observed, as shown in Table 8.1. These regions conform to the bath-tub curve, initially with running-in, which was followed by benign wear and the final part of the curve which is wear-out. Additional periods of abnormal (increased) activity were observed within the later stages of benign wear and these were believed to be associated with early stages of fatigue failure.

Operating bands were also shown which define the above mentioned regions and form the basis of a traffic light alarm system. This type of practice is consistent with machinery used in industry, as experience and conclusions from multiple data sets enable benign wear regimes to be justified and associates abnormal signal levels with distress mechanisms [211-213].

These operating bands are specific to the bearing type and operating conditions to which they serve. However, the parameters are generic to the industry and will be of interest to others looking to adopt the multi-sensing strategy in condition monitoring programmes.

Tapered rollers 2 – 2.5 GPa	Running-in	Benign	Caution or distress	Wear out
SEM particle type	Plate-like	Plate-like	Plate-like/spheres/swarf/striations	Plate-like/spheres/swarf/striations
SEM particle size	< 20 µm	< 15 µm	< 50 µm/< 5µm/40 µm/30 µm	< 50 µm/< 5µm/40 µm/30 µm
Particles on ferrography slide	Clustered	Isolated	Isolated	Clustered
PODS (5 - 15 µm count)	4000 - 7500	2000 - 3200	3200 – 6500	> 6500
Severity index	0.08 - 0.12	0.04 - 0.065	0.065 - 0.1	> 0.1
SOAP (Iron ppm)	0	0	0.1	> 0.1
OLS (pC)	0.03 - 0.1	0.02 - 0.03	0.03 - 0.07	> 0.07
Indicator vlue	3000 - 4000	1750 - 3250	3250 - 3750	> 3750
WSS (pC)	0.8 - 2.1	0.8 - 1.5	1.5 - 3.5	> 3.5
Acceleration (g)	0.8 - 3.5	0.75 - 3	3 - 3.5	> 3.5
Outer race temp (°C)	65 - 70	60 - 70	70 - 80	> 80
Peak amplitude (dB)	76 - 82	60 - 80	80 - 88	> 88

Ball bearings 1.6 – 2.5 GPa	Running-in	Benign	Caution	Wear out
SEM particle type	Plate-like	Plate-like	Plate-like/spheres/swarf/striations	Plate-like/spheres/swarf/striations
SEM particle size	< 20 µm	< 15 µm	< 50 µm/< 5µm/40 µm/30 µm	< 50 µm/< 5µm/40 µm/30 µm
Particles on ferrography slide	Clustered	Isolated	Isolated	Clustered
PODS (5 - 15 µm count)	2700 - 15000	2000 - 3200	3200 - 3900	> 3900
Severity index	0.005-0.058	0.001 - 0.025	0.025 - 0.05	> 0.05
SOAP (Iron ppm)	0	0	0.1	> 0.1
OLS (pC)	0.03 - 0.07	0.02 - 0.03	0.03 - 0.07	> 0.07
Indicator vlue	3250 - 3750	3000 - 3250	3250 - 3750	> 3750
WSS (pC)	1 - 1.5	1 - 1.5	1.5 - 3.5	> 3.5
Acceleration (g)	0.4 - 2	0.4 - 1.3	1.3 - 2	> 2
Outer race temp (°C)	45 - 59	45 - 46	46 - 56	> 56
Peak amplitude (dB)	65 - 70	60 - 70	70 - 80	> 80

Table 8.1 The maximum sensing levels that identify the transition from benign to abnormal bearing wear [1].

[1] The parameters coloured in red during the period of caution have been confirmed as the early signs of fatigue failure, prior to the wear out phase.

8.1 Running-in wear

The evolution of bearing distress was monitored using off-line debris, as technologies such as the SEM and PODS confirm the actual size, morphology and quantity of particles. The off-line debris analysis provides confidence of the severity and mechanisms of wear, which are the source of dynamic signal activity from the in-line techniques. During running-in, the off-line debris parameters were sensitive to bearing type and increased with contact pressure. Heightened particle counts compared to the benign regime indicated an increased wear rate, as shown in Table 8.1. The debris had a plate-like morphology and were formed during shearing of the asperities from the surface roughness. The debris was clustered on the ferrography slide and correlated with an increased 5 – 15 µm particle count by the PODS and severity index values. The increased particle count correlated with heightened in-line signatures of OLS charge and indicator value, which related to a combination of particle entrainment in the oil-line and a tribocharging mechanism. The increased particle count was the source of heightened in-line sensor activity in the test chamber. Increased wear site charge resulted from interfacial contact between the surface roughness of opposing elements during loading, as well as the generation of contact potential differences between original and modified surface areas. This includes plastic deformation and the generation of discrete areas of nascent surface during debris formation. Increased vibration acceleration, AE peak amplitude and bearing outer race temperatures related to impacts between the surface protuberances and frictional heating in the contact.

8.2 Benign wear and periods of distress

Confirming benign wear is of prime importance in any condition monitoring programme, as sensing levels in this regime define a healthy component from which increased signatures can be associated with distress. Table 8.1 shows that after running-in, all in-line and off-line sensing parameters reduced and maintain steady-state trends. These signatures identify the green light for benign wear in a traffic light alarm system.

However, a safety margin (amber region) allows for variation during testing and a period of caution for sensing levels that may increase above the benign threshold, but may be related to benign wear. In addition, sensing levels in this region identify a

period of possible abnormal wear which can be associated to the early signs of distress. The early distress mechanisms were corroborated by off-line debris and in-line sensor analysis, which were sensitive to bearing type and contact pressure. In the tapered roller tests, the particles were spherical, rugged, chunky and elongated swarf-like chips, which identified adhesive, fatigue and abrasive wear. The abnormal particles correlated with an increased 5 – 15 µm debris count, severity index, iron concentration and AE peak amplitude levels. In the ball bearing tests, spherical and swarf-like chips identified adhesive and abrasive regimes and correlated with an increased 5 – 15 µm debris count and AE peak amplitude. The increased signatures related to short periods of particle formation with impacts between the rolling elements on the roughened wear site, and were associated with the early stages of fatigue failure. The sensor activity reduced after the early signs of distress which indicated healing at the defective region.

8.3 Wear out

A further increase in off-line debris count and in-line sensor activity, above the levels that indicated the early signs of distress, identifies the red region of the alarm system and the wear out period. The off-line debris analysis shows that plate-like particles indicate gross surface delamination, spheres indicate adhesive wear, platelets with striations of the surface and swarf-like chips identify abrasive regimes. The abnormal debris morphology correlated with a runaway 5 – 15 µm particle count, severity index and iron concentration. These particle detection schemes increased with mass loss and related to propagating surface damage. The runaway particle trends provide a distinction between wear out and the early signs of distress, which occurred within a very short time-frame during the benign regime. The increased debris count correlated with runaway sensor activity from all the in-line techniques, which also increased with mass loss. The increased OLS charge and indicator values related to debris entrainment in the scavenge line. Wear site charge, vibration and AE peak amplitude related to contact between opposing surfaces during oil-film breakdown and bearing outer race temperatures related to frictional heating in the contact.

8.4 Concluding remarks

A suite of sensing techniques, confident thresholds and purpose built algorithms (AI) enhanced the ability to confirm early stages of fatigue failure. Corroborating evidence from off-line debris and in-line sensor analysis provided a confident assessment of benign wear. This justified a baseline that enabled increased signatures to be associated with the early signs of distress. The early signs of distress were identified by off-line line debris analysis which identified the mechanisms and severity of wear. However, the off-line debris analysis required a time-delay in obtaining the results, which is detrimental to predictive programs which anticipate bearing failures. Nevertheless, the increased debris parameters provide a true indication of surface wear, which is essential for supporting the in-line techniques in diagnosing the fault. The in-line signature that indicated the early signs of distress was the AE peak amplitude parameter. The source of increased activity related to impacting elements on the defective wear site and a possible contribution from crack initiation and propagation. Therefore, the AE peak amplitude parameter provided added value compared to the other in-line technologies, by clearly identifying the early stages of fatigue failure, which is essential for prognostic health evaluations. The combined analysis also demonstrates the effectiveness of the multi-sensing suite, which provides complimentary analysis between the different techniques. This provides a robust monitoring programme that enables clear and decisive decisions to be made for remedial action strategies.

Novel technologies included electrostatic charge detection. The value of the wear site sensor was that the charge clearly identified the locality of expected and unexpected component failure. The charge measurements provided complimentary information of surface contact during oil-film breakdown to the established techniques in diagnosing the degradation mechanisms in the contact. However, using the AI methods, the wear site sensor indicated signal enhancement at the source of eventual failure. As the AI methods were off-line, this analysis also provided a complimentary diagnosis of component health and the source of impending runaway wear to the in-line techniques. The oil-line sensor monitored the evolution of wear which also provided support to the in-line techniques in diagnosing failure of upstream components.

9 Future work

There are a number of additional tests that could be carried out to enhance and corroborate the results of this project. Reasons for not completing these additional tests during this research program were time and financial restraints.

9.1 Threshold analysis

Now that a traffic light alarm system has been developed, additional test could look at the source of signal activity within the operating bands. For instance, consider the AE peak amplitude operating within the green threshold of the benign regime. As the first peak amplitude hits are identified in the amber region, which is a period of caution or distress, the test could be stopped. This would allow for bearing element inspections, for confirmation of spall initiation, enabling a more confident association to be made between the source of heightened signal activity and tribolgical events. This would be extended to the remainder of the techniques and would provide additional added value to the threshold bands.

9.2 Debris

The most significant monitoring parameter that confidently identified the earliest signs of bearing distress was the increased quantity of 5 – 15 µm debris detection by the PODS. However, this technique was used utilised as an off-line strategy, which incurred a time delay in producing the results. Therefore, in order to identify the evolution of the quantity of debris in real-time, it would be advantageous to incorporate the PODS into the oil scavenge line. This would represent further novelty to the developed test rig and could be achieved by manipulation of the downstream lubrication line. The on-line debris monitoring would then provide an instantaneous evaluation of wear particle content in the oil line which could then be correlated with the other sensing technologies.

In addition, the morphology of the debris provided evidence of the mechanisms of wear, since spherical and rugged debris confirmed an adhesive mechanism, chunky particles confirmed fatigue and elongated chips identified abrasive wear. Therefore, an in-line system that could identify the particle morphology in real time would

provide significant benefit to the industry. Thus, it is no surprise that the state of the art for particle imaging is the adaption of the Lasernet Fines system as an in-line strategy to monitor the quantity and morphology of sub 20 µm debris. Therefore, the combination of the Lasernet Fines and corroborating evidence from the techniques already in place, would provide significant value in identifying the evolution of wear.

Relationships between the debris and oil-line charge may be elucidated by a test program that would allow particle concentrations to be entrained in the oil flow. This would enable correlations to be made between a known particle size, quantity and composition with charge levels. The debris entrainment rig that could be used in this programme has been constructed, and a flow diagram is shown in Figure 9.1. However, the tests could not be carried out, due to time restrictions of the project.

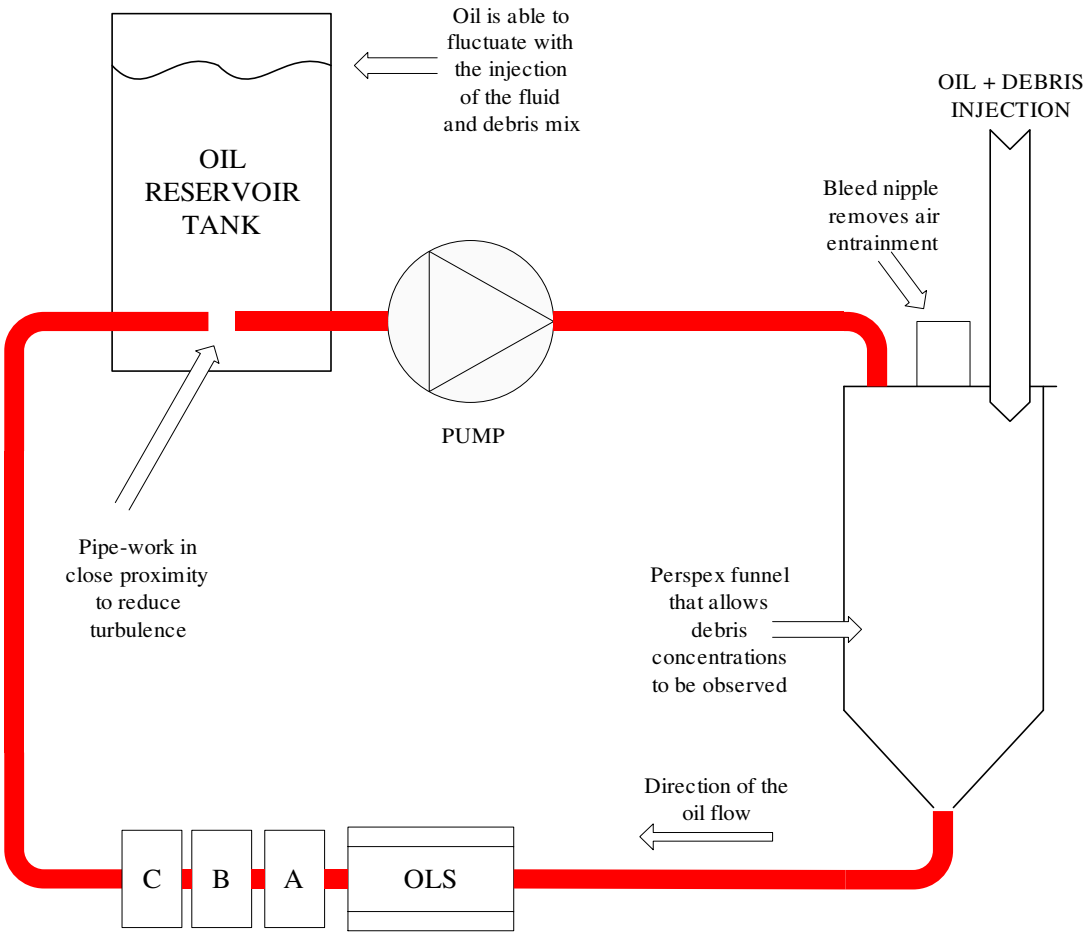

Figure 9.1 Flow test rig to enable debris size, quantity and shape to be controlled for detection by the electrostatic oil-line sensor (A, B and C other particle detection systems).

The recirculation line is constructed from 12.7 mm copper pipe-work, replicating the flow used in the bearing tests. The debris is injected into a Perspex funnel, which allows the particle concentrations to be observed, prior to detection by the OLS. The funnel has a tapered exit to eliminate dead areas that can restrict the passage of particles in the system. After the funnel exit, the OLS is located at the end of a 1 m straight pipe section, which is a distance greater than 50 times the pipe diameter, this will ensure that laminar flow can be attained. After the OLS, a range of particle detection schemes can be employed, designated A, B and C in Figure 9.1. These particle detection schemes could include the PODS, Lasernet Fines and Macom devices. Initially, the test rig would be operated by pumping just oil around the flow loop; this would allow baseline charge levels at different flow rates to be obtained. On identification of the baseline charge, a known debris concentrations can be added to the oil flow, enabling correlations with charge and the other debris detection schemes.

Further oil charging relationships could employ matrix based work with different types of lubricating oils, moisture content and acidic contaminants. Additional correlations could be observed between different OLS's constructed of a range of smaller sensing diameters, which have been postulated to enhance the sensitivity of the technique.

The final series of tests would seek to introduce seeded charged debris into the recirculation line, using the same debris size and concentrations as the uncharged debris. As of yet, a system needs to be developed that can successfully seed and charge debris at the same time. These tests will then identify the difference in charged and uncharged seeded debris, and provide a clear indication of the detection capabilities of the technique.

9.3 Sensors

Using a single AE sensor embedded into the bearing test housing, there was significant interest in the peak amplitude activity, which identified precursor events of the impending wear out phase. Therefore, with the addition of another two transducers, located into each of the bearing support housings, a location identifier could be adapted to provide greater focus on the precise locality of distress.

Additional work that could be carried out relates to the source of AE, which can be attributed to crack initiation and propagation or impacts between defective elements. One test program that could be employed would involve the use of computer tomography (CT), with analysis before and after each bearing test. The aim of the experimentation would be to investigate crack initiation sites and growth after detection of the AE parameter.

There may also be added value in modifying the geometry of the wear site sensor, so that the sensing face could be deployed at different regions within the bearing contact. This work would seek to enhance the field of view of the sensing face, which could be positioned orthogonally to the rolling elements, as opposed to the radial arrangement employed in these tests.

9.4 Bearing contacts

With additional time, further research would have utilised hybrid (metal on ceramic) and all ceramic ball bearing contacts, which have been provided by the Timken bearing company. This work would look to evaluate correlations between the sensing signatures generated by the hybrid and ceramic contacts, and identify the suitability of the novel electrostatic technologies to hybrid contact distress.

An extension of the hybrid and ceramic bearing research could also involve lab based tribometers such as pin-on-disc and twin disc rigs, so that an initial understanding of the degradation process can be identified. The findings from the tribometers may then be used for corroborative purposes with possible data transfer to full-scale bearing tests.

9.5 Signal processing

A significant feature of the results generated in this project was the incorporation of the advanced processing architectures, which were used to corroborate the earliest signs of distress. Therefore, due to the significance of these results, there will be further research within nCATS, which will investigate the artificial intelligence techniques using a multi-feature input strategy. One of the goals of the artificial intelligence program will be to incorporate the processing strategy in-line, so that a

real time indication of the locality and severity of operating conditions could be identified.

The long term goals for the test programme, is an intelligent sensing strategy that would act autonomously, and could discriminate, diagnose, alleviate and self-repair bearing faults. This could involve automatic oil replenishment, load reductions or machine stoppages, which would eliminate runaway wear and catastrophic failures. Another advance of the autonomous programme would be the development of remote monitoring, thus eliminating the need for personnel to continuously monitor the bearing performance.

Appendix A

Wallodi Weibull postulated that the fatigue lives of a group of homogeneous rolling element bearings are dispersed according to the following equation [55].

$$\ln\ln\left(\frac{1}{S_p}\right) = e\ln\left(\frac{X}{X_\beta}\right)$$

where:

S_p = Percentage of bearing population surviving
e = Weibull slope
X = Load, time or stress
β = Characteristic life or stress

The Gustaf Lundberg and Arvid Palmgren, (LP) bearing life prediction model [214].

$$\ln\left(\frac{1}{S_p}\right) = N^e \frac{\tau_o^c}{z^h} azl$$

where:

e = Weibull exponent (9/8)
τ_o = Maximum orthogonal stress in contact
c = LP stress exponent (31/3)
h = LP depth weighting exponent (7/3)

Appendix B

The Calibration graph of the accelerometer is shown in B.1, which indicates a flat response from 0 – 1 kHz and a 6 % deviation at 10 kHz.

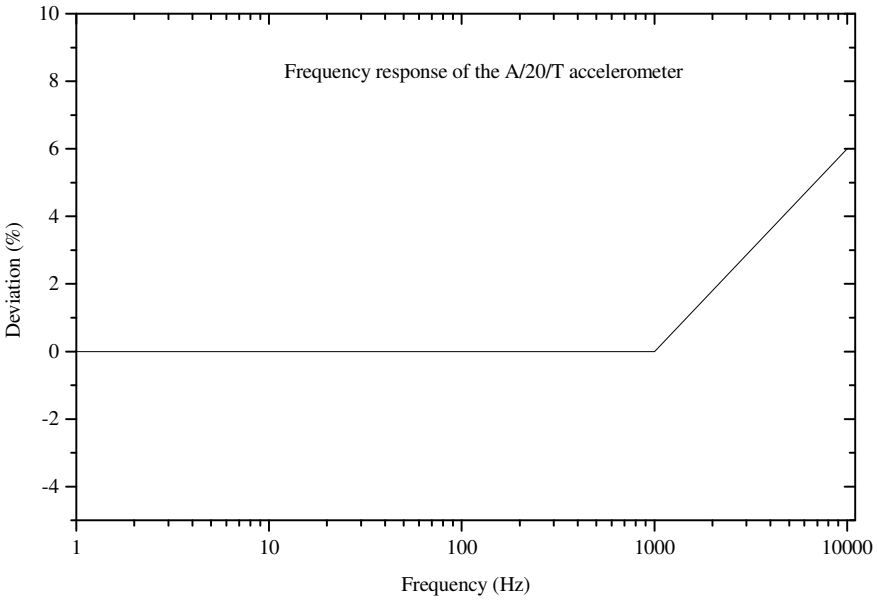

Figure B.1 Frequency characteristics of the A/20/T accelerometer.

Appendix C

Figure C.1 shows the frequency response of the Pancom AE sensor which was used during testing. The sensor is compared against a product from the Physical Acoustic Corporation (PAC). The calibration method used the ASTM E976 standard which utilised the face to face excitation method. The Pancom sensor has superior performance since there is less attenuation over the broadband frequency range.

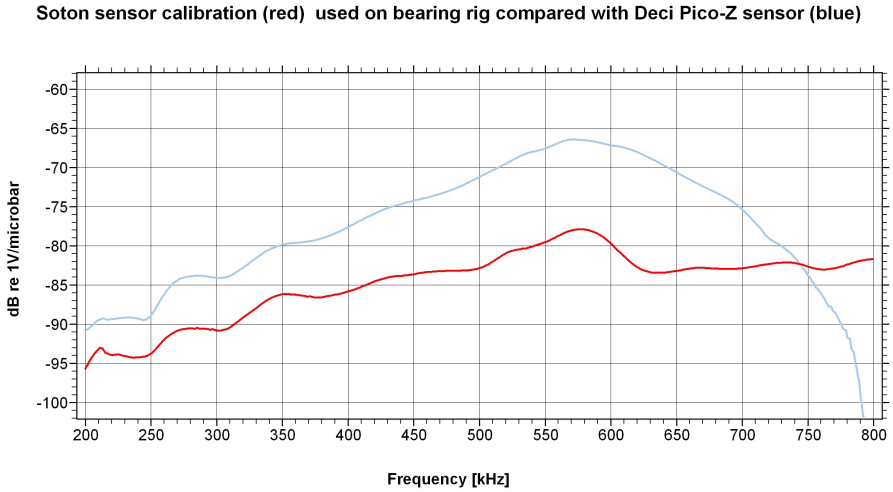

Figure C.1 Frequency response of the Pancom and PAC sensors.

Appendix D

D.1 Roller bearing Hertzian line contact pressure

Mean contact radius of roller = 3.093 mm
Length of roller = 10.73 mm
Contact angle = 13.5 °
Number of rollers = 19
Applied load = 20 kN
Outer race radius = 29.565 mm
Outer race track radius = flat =R= ∞
E of steel = $207*10^9$

$$P = \frac{5*F}{Z*\text{Roller length}*\text{Contact Angle}} = \frac{5*20*10^3}{19*10.73*10^{-3}*\text{Cos}13.5} = 504*10^3\,\text{N}$$

Relative radius of curvature $\frac{1}{R} = \frac{1}{R_1} + \frac{1}{R_2}$

$$R_x = \left(\frac{1}{R_{1x}} + \frac{1}{R_{2x}}\right)^{-1} = \left(\frac{1}{3.093} + \frac{1}{-29.565}\right)^{-1} = 3.45\,\text{mm}$$

$$R_y = \left(\frac{1}{R_{1y}} + \frac{1}{R_{2y}}\right)^{-1} = \left(\frac{1}{3.093} + \frac{1}{-\infty}\right)^{-1} = 3.093\,\text{mm}$$

$$R = \left(\frac{1}{R_x} + \frac{1}{R_y}\right)^{-1} = \left(\frac{1}{3.45} + \frac{1}{3.093}\right)^{-1} = 1.63\,\text{mm}$$

$$E^* = \left(\frac{1-\upsilon^2}{E_1} + \frac{1-\upsilon^2}{E_2}\right) = \left(\frac{1-0.3^2}{207*10^9} + \frac{1-0.3^2}{207*10^9}\right)^{-1} = 113.7*10^9$$

$$b = \sqrt{\frac{4*P*R}{\pi*E^*}} = \sqrt{\frac{4*504*10^3*1.63*10^{-3}}{\pi*113.7*10^9}} = 0.1\,\text{mm}$$

$$P_m = \frac{P}{2b} = \frac{504*10^3}{2*0.1*10^{-3}} = 2.5\,\text{GPa}$$

D.2 Ball bearing Hertzian elliptical contact pressure

For a ball bearing on a conforming raceway an elliptical contact is generated. The mean and maximum contact pressure is described below.

Number of balls = 9
Radius of ball = 4.765 mm
Outer race radius = 27.95 mm
Outer race track radius = 5.0509 mm
E of steel = $207*10^9$
Applied load 9 kN

First the relative radii and reduced modulus is identified

Relative radius of curvature $\frac{1}{R}=\frac{1}{R_1}+\frac{1}{R_2}$

$$R_x=\left(\frac{1}{R_{1x}}+\frac{1}{R_{2x}}\right)^{-1}=\left(\frac{1}{4.765}+\frac{1}{-27.95}\right)^{-1}=5.74\,\text{mm}$$

$$R_y=\left(\frac{1}{R_{1y}}+\frac{1}{R_{2y}}\right)^{-1}=\left(\frac{1}{4.765}+\frac{1}{-5.0509}\right)^{-1}=84.2\,\text{mm}$$

$$R=\left(\frac{1}{5.74}+\frac{1}{84.2}\right)^{-1}=5.37\,\text{mm}$$

$$E^*=\left(\frac{1-\upsilon^2}{E_1}+\frac{1-\upsilon^2}{E_2}\right)^{-1}=\left(\frac{1-0.3^2}{207*10^9}+\frac{1-0.3^2}{207*10^9}\right)^{-1}=113.7*10^9$$

The maximum load on a ball is from an applied load of 9 kN:

$$P=\frac{5F}{Z}=\frac{5*9*10^3}{9}=5*10^3$$

Approximations for the elliptic integral and ellipticity parameter are made:

$$k=1.0339\left(\frac{R_y}{R_x}\right)^{0.636}=1.0339\left(\frac{84.2}{5.74}\right)^{0.636}=5.73$$

$$1.0003+\frac{0.5968(R_x)}{R_y}=1.0003+\frac{0.5968(5.74)}{84.2}=1.04$$

The semi-major and semi-minor axis of the contact ellipse are identified.

$$a=\sqrt[3]{\frac{3k^2EPR}{\pi E^*}}=\sqrt[3]{\frac{3*5.73^2*1.04*5*10^3*5.37*10^{-3}}{\pi*113.7*10^9}}=1.97\,\text{mm}$$

$$b = \frac{a}{k} = \frac{1.97}{5.73} = 0.34\,\text{mm}$$

The maximum contact pressure is:

$$P_0 = \frac{3*P}{2\pi*a*b} = \frac{3*5*10^3}{2\pi*1.97*0.34*10^{-6}} = 3.56\,\text{GPa}$$

For a ball bearing on a conforming raceway an elliptical contact is generated. The mean and maximum contact pressure is described below.

Number of balls = 9
Radius of ball = 4.765 mm
Outer race radius = 27.95 mm
Outer race track radius = 5.0509 mm
E of steel = $207*10^9$
Applied load 9 kN

First the relative radii and reduced modulus is identified

Relative radius of curvature $\frac{1}{R} = \frac{1}{R_1} + \frac{1}{R_2}$

$$R_x = \left(\frac{1}{R_{1x}} + \frac{1}{R_{2x}}\right)^{-1} = \left(\frac{1}{4.765} + \frac{1}{-27.95}\right)^{-1} = 5.74\,\text{mm}$$

$$R_y = \left(\frac{1}{R_{1y}} + \frac{1}{R_{2y}}\right)^{-1} = \left(\frac{1}{4.765} + \frac{1}{-5.0509}\right)^{-1} = 84.2\,\text{mm}$$

$$R = \left(\frac{1}{5.74} + \frac{1}{84.2}\right)^{-1} = 5.37\,\text{mm}$$

$$E^* = \left(\frac{1-\upsilon^2}{E_1} + \frac{1-\upsilon^2}{E_2}\right)^{-1} = \left(\frac{1-0.3^2}{207*10^9} + \frac{1-0.3^2}{207*10^9}\right)^{-1} = 113.7*10^9$$

The maximum load on a ball is from an applied load of 9 kN:

$$P = \frac{5F}{Z} = \frac{5*9*10^3}{9} = 5*10^3$$

Approximations for the elliptic integral and ellipticity parameter are made:

$$k = 1.0339\left(\frac{R_y}{R_x}\right)^{0.636} = 1.0339\left(\frac{84.2}{5.74}\right)^{0.636} = 5.73$$

$$1.0003 + \frac{0.5968(R_x)}{R_y} = 1.0003 + \frac{0.5968(5.74)}{84.2} = 1.04$$

The semi-major and semi-minor axis of the contact ellipse are identified.

$$a = \sqrt[3]{\frac{3k^2EPR}{\pi E^*}} = \sqrt[3]{\frac{3*5.73^2*1.04*5*10^3*5.37*10^{-3}}{\pi*113.7*10^9}} = 1.97\ \text{mm}$$

$$b = \frac{a}{k} = \frac{1.97}{5.73} = 0.34\ \text{mm}$$

The maximum contact pressure is:

$$P_0 = \frac{3*P}{2\pi*a*b} = \frac{3*5*10^3}{2\pi*1.97*0.34*10^{-6}} = 3.56\ \text{GPa}$$

The mean contact pressure is:

$$P_m = \frac{2}{3}*P_0 = \frac{2}{3}*3.56\ \text{GPa} = 2.4\ \text{GPa}$$

The maximum Hertzian contact pressure is 3.56 GPa and the mean is 2.4 GPa. However, for accelerated testing using the Timken method the maximum pressure should be 2.4 GPa giving a mean pressure of 1.6 GPa. This is why rapid failure took place on the initial ball bearing test.

Appendix E

E.1 The detection of inner race failure

The aim of this initial test was to monitor accelerated tapered roller bearing failure, by inner race indentation and overloading, using a combination of in-line and off-line analysis. The in-line techniques included electrostatic WSS, vibration acceleration, thermocouples, electrostatic OLS, Macom inductive and ferromagnetic particle counters. Off-line debris analysis included PODS particle counting, ferrography calculations of severity index, SOAP and debris imaging using the electron microscope.

As this was the first test of the project, there were some modifications to the set-up which was described in chapter 4. The accelerometer was located in the position of WSS 1, which was removed due to leakage at this point. Since WSS 1 monitors charge at support bearing 1, and failure was expected at bearing 2 which was monitored by WSS 2, it was considered that this configuration would have no detrimental effects on monitoring charge in the vicinity of anticipated failure. In addition, nylon recirculation pipe-work was used instead of copper. The rationale behind this selection was to monitor oil-line charging effects for the first time using non-conductive recirculation pipe-work. A schematic of the test set-up is shown in Figure E.1.

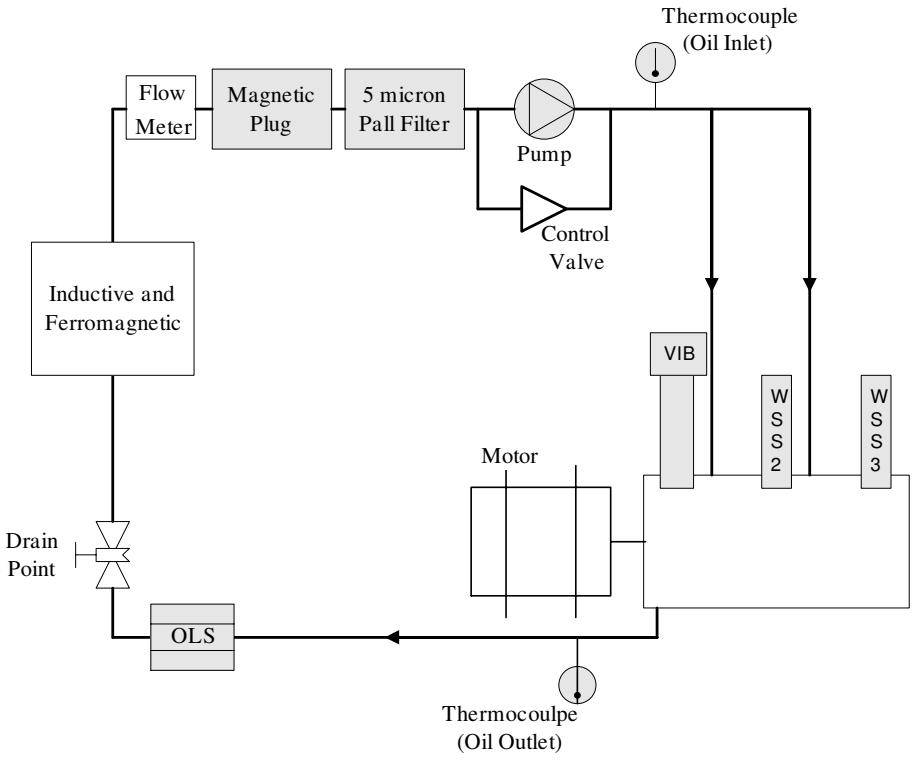

Figure E.1 The bearing set-up for test 1.

E.2 Distress in the bearing test chamber

Figure E.2 shows the trending of WSS 2 and 3, vibration acceleration and thermocouples that were positioned on the recirculation pipe-work at the inlet and outlet of the bearing test chamber.

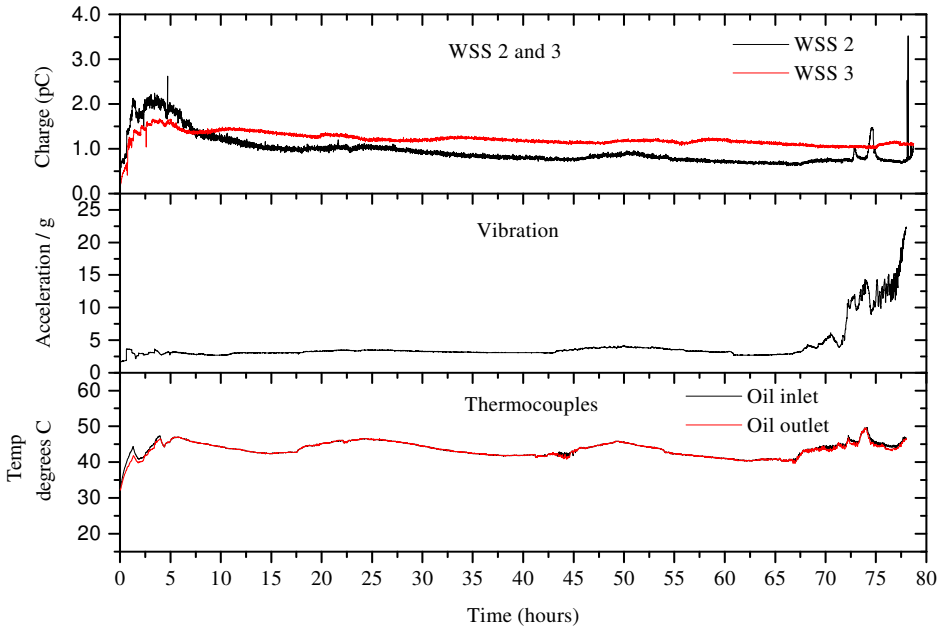

Figure E.2 WSS, accelerometer and thermocouple trends.

During the loading stages there was increased charge from the WSS's, vibration acceleration and thermocouple activity. The increased sensor activity was likely to be attributed to contact loading and running-in wear, which would be expected during testing of any new bearings. Running-in is a highly dynamic process, described in section 2.6, where the interaction of the largest asperity peaks and protuberances from raceway defects, results in localised pressure with plastic flow and rupture of the irregularities over the surface depressions [70]. Charging mechanisms at the wear site include the application of each load stage, which modifies the charge level in the vicinity of the WSS. This shows that the WSS are sensitive to load. Further charging mechanisms include increases in temperature which increases the charge mobility during fluid viscosity changes. Additional sources of charge include the generation of CPD between discrete areas of nascent and original material during deformation and debris liberation from the parent surface, as well as debris charging during interaction between the elements. These mechanisms were described in sections 3.8.3.

The vibration levels are also sensitive to load, asperity and defect deformation mechanisms, as well as debris entrainment between the bearing elements, with impulse shocks transmitted to the sensor and surrounding structure. The increasing thermocouple trends were related to frictional heating during loading of the Hertzian contact. However, the two thermocouples indicated the same temperature, which was not expected. In this set-up, a greater outlet temperature was anticipated due to the heating of oil passing through the test chamber. These errors were likely to be related to the position of the thermocouples which were located on the recirculation pipe-work. In the proceeding tests, this problem was rectified by positioning the thermocouples in the oil flow.

After the loading stages, the WSS, vibration and thermocouples attained nominally steady-state levels. The sensor activity during this period indicated a transition from running-in to benign wear, as indicated by the bath-tub curve, shown in Figure 2.13. During the transition from running-in to benign wear, smoothing of the surface roughness and defect protuberances has a positive effect on bearing functionality, as the surfaces become completely separated by the lubricating film. An increase in the λ ratio allows EHL conditions to prevail, as described in section 2.3.2. However, there were minor fluctuations observed from all sensors, which were likely to be related to the effects of room temperature variation during the transition from day to night. The room temperature variations will modify oil viscosity, resulting in minor changes in contact conditions and hence wear site charge, vibration and thermocouple activity.

The first indications of distress were around 67 hours by an increasing vibration trend that correlated with increased thermocouple activity. However, significant evidence of damage was observed at 72 hours, by a rapid increase in vibration acceleration, which showed a very good correlation with a rapid increase in charge from WSS 2, indicating failure of the test bearings, and the thermocouples. The rapid increase in acceleration was likely to be an indication of surface failure. Surface failure prohibits bearing functionality which results in the breakdown of EHL conditions, resulting in interfacial surface contact, debris liberation and entrainment between the elements, with the transmission of impulse shocks to the accelerometer. Possible mechanisms of charge at the distressed bearing surface include boundary conditions, the exposure of nascent surfaces during plastic deformation, debris removal from the wearing site and debris interaction between the elements. Further factors include tribocharging effects, where roughening of the contact increases the surface area and initiates charge removal from the double layer during microturbulence. At around 73 hours there were further rapid increases in acceleration, wear site charge and temperature which were again likely to indicate further boundary conditions.

Between 74 – 77 hours there was an increasing vibration trend that correlated with a relaxation in charge from WSS 2 and thermocouple activity. The increase in vibration was likely to indicate propagating damage and/or debris entrainment between the elements. However, correlations with a relaxation in charge and temperatures indicate that scuffing was unlikely be the dominating mechanism.

From 77 hours there was a rapid increase in acceleration that correlated with further rapid increases in charge from WSS 2 and thermocouple activity. The sensor activities persisted for the remainder of the test and were likely to indicate further damage with boundary conditions.

Therefore, from the collective sensor activity in the test chamber, the probable cause of distress was spallation at the defective test bearing, indicated by the rapid increases in charge from WSS 2. In addition, the rapid increases in charge provided an indication of boundary conditions, which was corroborated by rapid increases in acceleration and temperature.

E.3 In-line wear debris detection

The OLS and indicator value are shown in Figure E.3. During the initial 7 hours, there was an increasing oil-line charge that may be an indication of running-in. The oil-charging mechanisms include temperature increases which increases charge mobility

during fluid viscosity changes. Further charging mechanisms include debris entrainment in the oil flow after liberation from the parent surface and/or interaction between opposing elements. After the running-in period, the OLS charge levels remained relatively stable with perturbations that correlated with the temperature fluctuations during the transition from day to night. The charge fluctuations were likely to be related to charge mobility variations during fluid viscosity changes. During the wear out period, there was no conclusive evidence of accentuated oil-line charge which clearly distinguished periods of normal and abnormal wear. From previous testing [197] using copper recirculation pipe-work, baseline charge levels were 0.02 pC, with maximum levels of 0.08 pC during failure. Therefore, since the background charge levels in this test were around 0.375 pC, the accentuated charge during periods of wear may have been masked within the noise of the OLS charge signal using the nylon pipe-work. This may be a reason why there was no clear discrimination of any periods of wear activity from the indicator value.

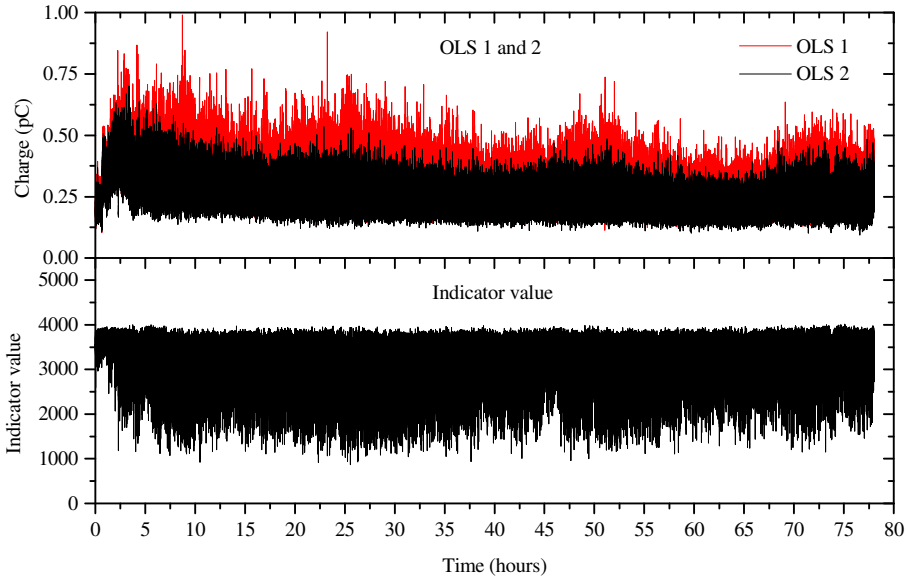

Figure E.3 The OLS and indicator value.

Figure E.4 shows the Macom TA 10 and TA 20 analysis. The time-line of debris detection by the inductive TA 10 shows that during the initial 7 hours, the dominating debris activity was from the 0 – 100 µm particle range, with single counts from the 100 – 400 µm bin sizes. It was not anticipated that this sensor provided an accurate representation of the actual debris in the oil-line due to sensitivity and calibration problems of the technique, which were described in section 3.5.1. The next period of debris detection was at 67 hours, when the dominating particle count was from the 0 – 100 µm bin size with single particle counts in the 100 – 400 µm particle range. Therefore at this time, the correlation of increasing vibration, temperature and inductive particle count provided corroborating evidence to the initiation of the wear out phase. At 72 hours there was a rapid increase in all sub 800 µm bin counts by the TA 10, with the sub 100 µm bin size dominating. The detection of increased debris at this time was very consistent with the rapid increase in wear site charge, acceleration and temperature, which were likely to indicate boundary conditions. In addition, at 73 hours there was a further rapid increase in debris detection by the TA 10 and TA 20,

which were again consistent with increased acceleration, charge and temperature, and provided further corroborating evidence of boundary conditions. From 74 – 77 hours there was steadily increasing debris detection by the TA 10 and TA 20, and was further support of progressive wear, indicated by the accelerometer at this time. From 77 hours to the end of the test, there was further rapid debris detection from the TA 10 and TA 20, which were again consistent with rapid increases in charge from WSS 2, vibration and temperature, and provided support of further damage and surface interaction.

Therefore, increased wear site charge, acceleration and temperatures show a very good correlation with periods of increased debris detection by the Macom units, which provided further corroborating evidence to the initiation of surface failure, with probable boundary conditions and propagating damage.

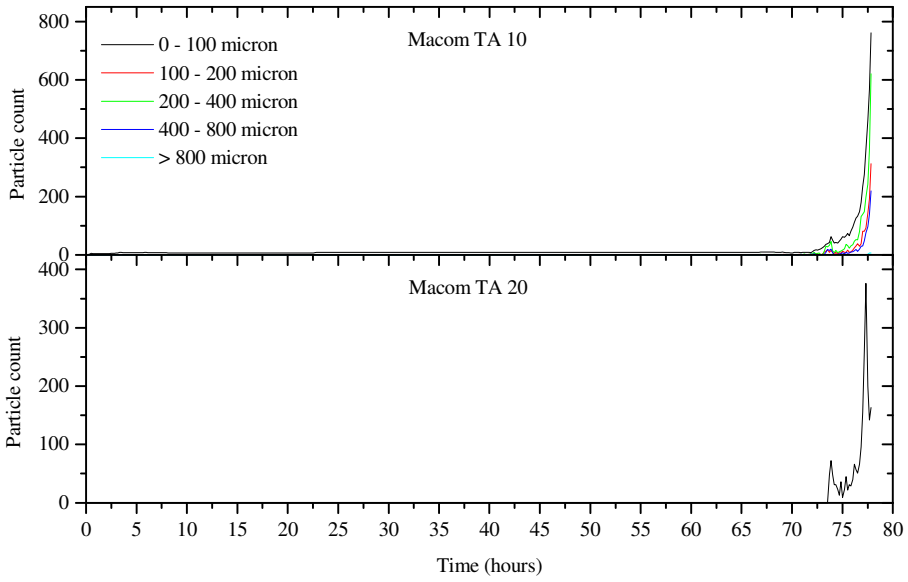

Figure E.4 Macom TA 10 and TA 20.

E.4 Off-line wear debris detection

During the final stages of the test, the increased in-line sensor activity initiated periods of oil sampling for off-line wear debris analysis. Employment of the off-line analysis provided further support of debris production, as indicated by the in-line techniques. The results from the PODS, severity index and SOAP are shown in Figure E.5.

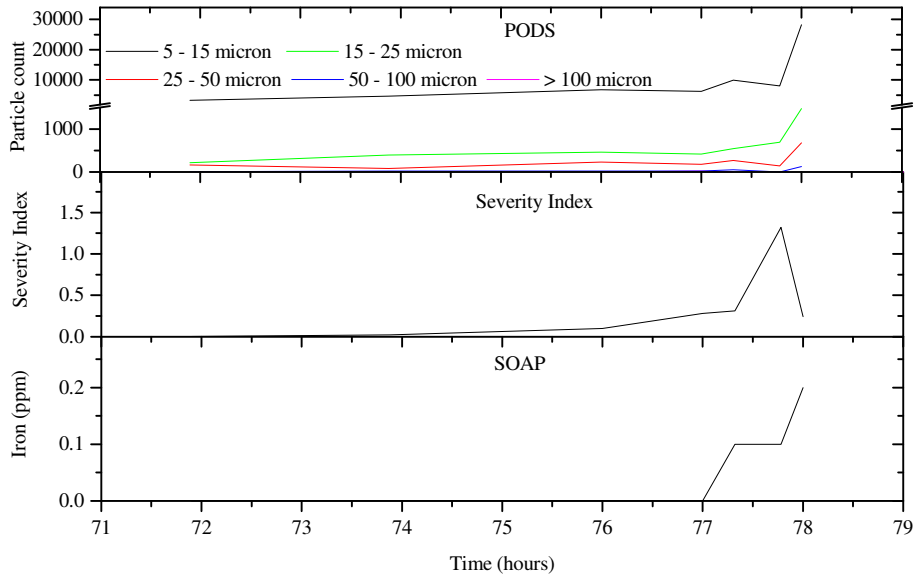

Figure E.5 Off-line PODS, severity index and SOAP.

From the PODS particle count there was a progressive increase in sub 50 µm debris between 72 – 77 hours. The dominating bin size was between 5 – 15 µm which increased from 3300 - 6200 particles and confirmed damage propagation. In addition, between 77 – 78 hours, rapid increases in the sub 100 µm particle count were observed, which provided further corroborating evidence of increased damage. Progressive wear was also identified by an increasing severity index value to 0.1 at 76 hours. Between 77 – 78 hours, a fluctuating severity index trend was observed which rapidly increased to a peak value of 1.32, which was further support of further damage. Additional evidence of propagating damage was identified between 77 – 78 hours by increasing iron levels to a maximum value of 0.2 ppm using the SOAP.

Therefore, the off-line wear particle analysis provided further evidence of progressive failure, by an increasing sub 50 µm particle count and severity index. In addition, a rapidly increasing sub 100 µm particle count, severity index and iron levels provided further confirmation of increased damage.

E.5 Electron microscopy images of debris

Images of debris using the electron microscope are shown in Figure E.6. This analysis was carried out to monitor the evolution of wear debris, as well as identifying the mechanisms of failure. In Figure E.6 (a) at 74 hours, a rugged particle morphology generated in an adhesive mechanism confirmed oil-film breakdown and boundary conditions, postulated by the rapid increases in wear site charge, vibration and temperature in section 5.2.1. This was followed at 77 hours by the identification of abnormal 40 µm flakes, indicating damage during a fatigue mechanism, as shown in Figure E.6 (b). At 77 hours 15 minutes further adhesive mechanisms were confirmed by the formation of spheres, which were again consistent with increased wear site charge, vibration and temperature during boundary conditions, as shown in Figure E.6 (c). In the final sample at 78 hours, further abnormal 30 µm flakes confirmed fatigue failure, as shown in Figure E.6 (d – e). However, this particle had features of striation marks which are induced during debris entrainment between the elements.

Furthermore, it can be seen that these particles range between 5 – 50 µm which was consistent with the debris detection by the PODS.

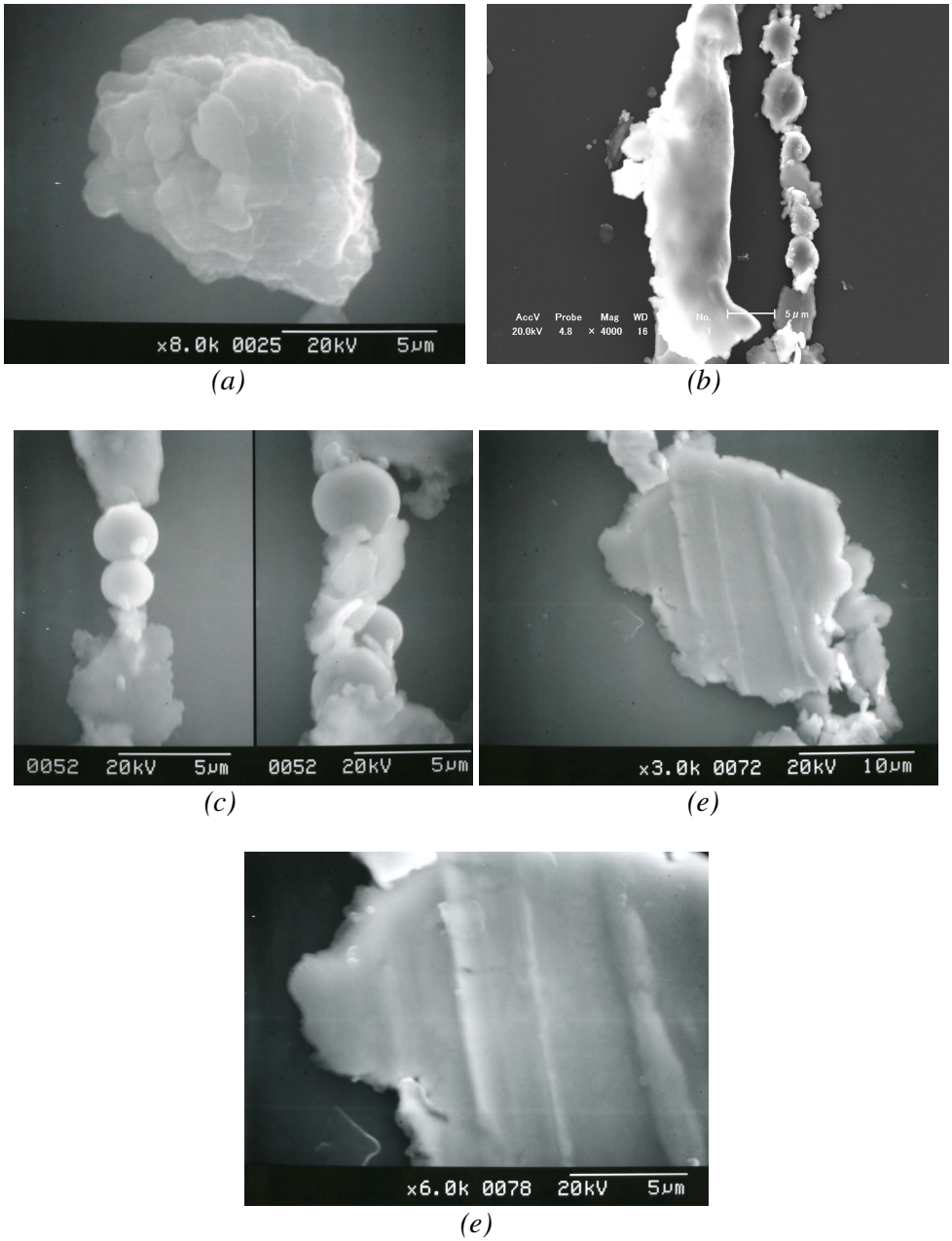

(a) *(b)*

(c) *(e)*

(e)

Figure E.6 Electron microscope images of the debris at (a) 74 hours (b) 77 hours (c) 77 hours 15 minutes (d) and (e) at 78 hours.

E.6 Photographic and gravimetric analysis

Figure E.7 shows photographic evidence of damage to bearing 2, which was the pre-indented bearing element.

Figure E.7 Photographic evidence of inner race spallation to bearing 2.

It is clear that the damage was on the inner raceway of bearing 2, where spallation propagated to approximately 50 % of the element. Damage to the remainder of the bearings included indentations and striations, caused by abrasion during debris entrainment between the elements. Damage was further confirmed on bearing 2 by gravimetric analysis, as shown in Table E.1. In addition, the cup assembly of bearing 4 has increased in weight, which may be an indication of oil flow within the test chamber, with debris entrainment around this bearing.

Gravimetric analysis						
	Pre-gravimetric (g)		Post test gravimetric (g)		Δ (mg)	Δ (mg)
	Cup	Cone	Cup	Cone	Cup	Cone
Bearing 1	61.2977	116.73273	61.1322	116.727	165.5	5.73
Bearing 2	61.04	116.44562	61.0194	115.986	20.6	459.62
Bearing 3	61.2773	116.6689	61.0961	116.669	181.2	0.1
Bearing 4	61.21	116.65419	61.0525	116.741	157.5	86.81

Table E.1 Gravimetric analysis.

E.7 Summary of test 1

For the first time, a combination of in-line and off-line techniques provided corroborating evidence to the initiation, locality, severity and mechanism of bearing failure. During running-in, the in-line sensors indicated increased wear site charge, vibration acceleration, temperature and inductive particle count. Sources of wear site charge related to contact loading, asperity deformation mechanisms, debris liberation and interaction between the elements as well as increased charge mobility during increased temperature. Increased vibration and temperature related to contact loading and impacts between surface protuberances and debris entrainment between the elements, with impulse shocks transmitted to the accelerometer and frictional heating within the contact. Confirmation of debris was obtained by inductive particle counting. Following running-in, the in-line sensors attained steady-state levels which indicated benign wear, with an established lubricating film between the element surfaces. Fluctuations from the in-line techniques related to oil viscosity changes during temperature variation in the transition from day to night.

During the wear out phase, the in-line sensors identified the initiation of failure by increased wear site charge, vibration, temperature and inductive particle count. In addition, rapid increases in wear site charge, vibration, temperature, inductive particle

count and the identification of adhesive debris provided corroborating evidence of boundary conditions. Progressive wear was shown by increasing vibration and inductive particle count. Corroborating evidence of propagating damage was shown off-line by an increasing sub 50 µm particle count and severity index. The identification of 40 µm flakes verified fatigue wear. Further rapid increases in wear site charge, vibration, temperature, inductive and ferromagnetic particle count, sub 100 µm particle count by the PODS, severity index and iron particle levels detected by SOAP provided further support of boundary conditions and increased damage.

Appendix F

F.1 Bearing testing using AE

In this test, the experimental set-up of test 3 was used which also incorporated a Pancom broadband AE sensor, which was located into the bearing test housing, as shown in section 4.4.3. A further change included the removal of the Macom TA 10 and TA 20 particle counters as Macom saw the electrostatic OLS as a competitor to their products. Therefore, Macom recalled their units and were unwilling to sell the sensors for use in any further tests.

F.2 Distress in the bearing test chamber

Figure F.1 shows the WSS's, accelerometer and thermocouple trends. During running-in, there was increasing wear site charge, vibration and temperature, of levels which were consistent with those observed in the preceding tests. The sensor activity was likely to be associated with the mechanisms that were described in the previous sections, which related to contact loading and surface deformation. Following running-in, benign wear prevailed as the WSS, vibration and thermocouples remained relatively stable with fluctuations that were consistent with the room temperature variation. This again shows the affects of temperature which modifies the oil viscosity, and results in minor changes in wear site charge and vibration.

The first sign of anomalous behaviour was at around 100 hours by an increasing vibration trend that persisted until 115 hours. From 115 hours there was a relatively stable acceleration signal that preceded further increases at 138 hours. The increasing acceleration trends at 115 hours and 138 hours were likely to be related to periods of damage, and provided an indication of the wear out phase. However, throughout the wear out phase there was no support of increased wear site charge to highlight the locality of distress or temperature variation for corroborative purposes. At this stage of the test, there was no evidence as to why there was no increased wear site charge or temperature activity. However, a possible reason may be minor damage levels, which may be explained by the slowly increasing acceleration signal over a prolonged period, when compared to the previous tests.

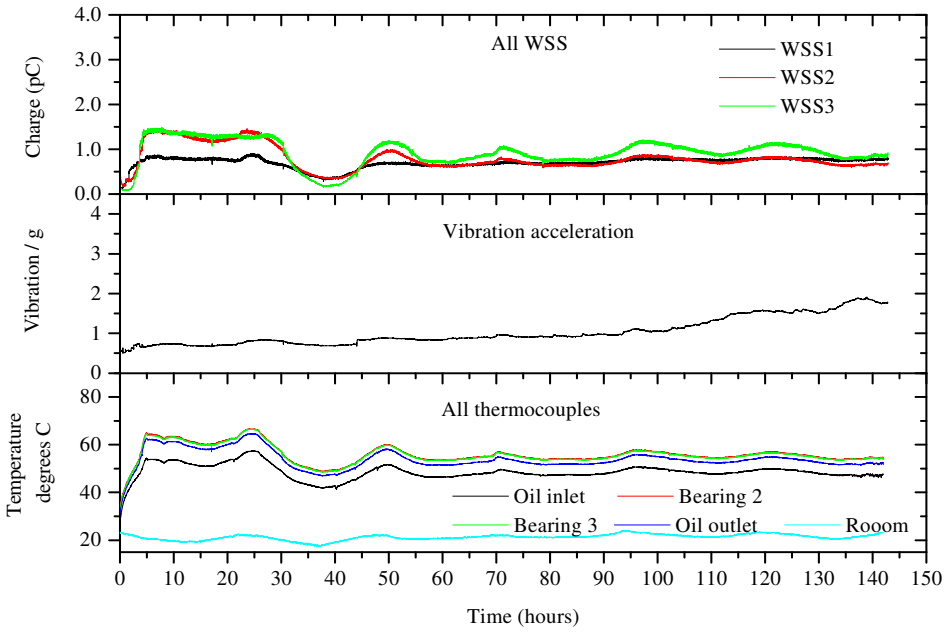

Figure F.1 Electrostatic WSS, vibration acceleration and thermocouples.

Figure F.2 shows the AE peak amplitude activity which needed to be broken down into separate files, due to the amount of data that was collected in a single directory. This shows the importance of selecting the optimum threshold and data sampling rate, otherwise a large data set can be produced. The running-in period is shown in Figure F.2 (a) which identified an increasing peak amplitude of around 75 dB, was likely to be related to contact loading. However, there was also minor peak amplitude activity which was greater than 80 dB, and probably relates to asperity deformation mechanisms that would be expected at this time. There was a small break in the AE signal after 7 hours as the data collection switch was accidently switched off. This was noted after 30 minutes and immediately turned back on. However, from the trend of the AE profile it was anticipated that there was no anomalous behaviour missed during this period. As the test progressed there was fluctuating AE activity that was consistent with temperature variation. In (b) a relatively stable AE response was observed which remained below 80 dB, and provided further evidence of the benign wear. In (c) the first indication of distress was identified after 77 hours with a single hit above 80 dB and was followed at 93 hours by further peak amplitude activity in excess of 80 dB that persisted until the end of the test. This result shows that the increased AE peak amplitude activity was in advance of the increasing acceleration trend and may be the first indications of distress. In (d) at 133 hours there was major AE activity, again with a peak amplitude in excess of 80 dB that provided further support of damage, which again preceded the increased acceleration at 138 hours.

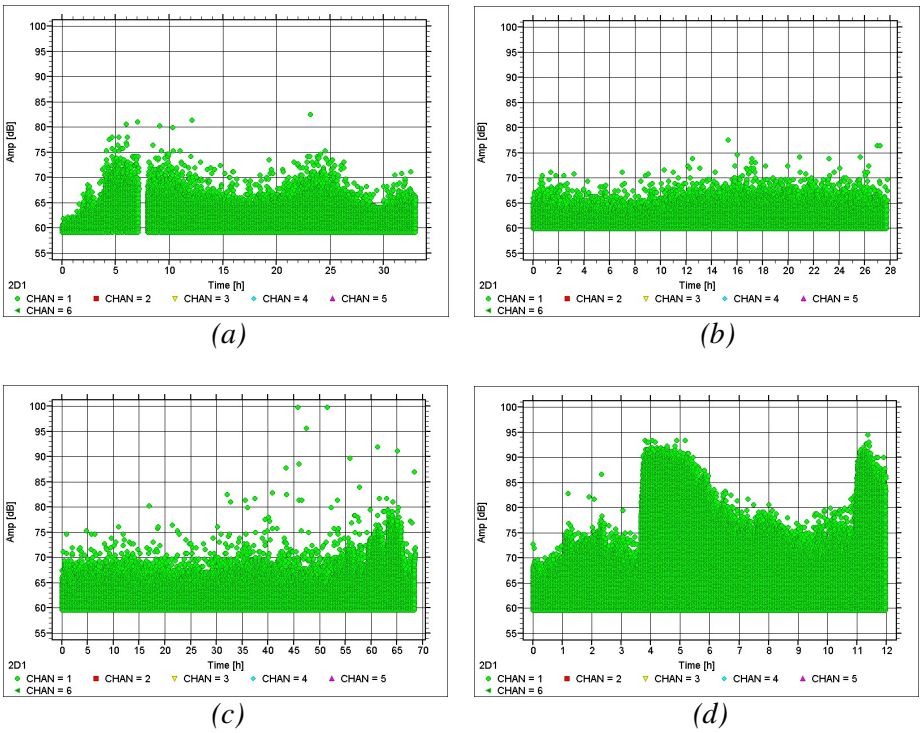

Figure F.2 AE peak amplitude between (a) 0 – 33 hours, (b) 33 – 61 (c) 61 – 129 and (d) 129 – 141.

F.3 Oil-line debris detection

Figure F.3 shows the OLS and indicator value. During the initial stages of the test there was minor activity that was likely to be related to the running-in process. During the steady-state there was a relatively consistent charge and indicator value with minor fluctuations that again correlated with variations in room temperature, and provided corroborating evidence of benign wear. The first signs of distress were around 100 hours by an increasing OLS and indicator value. From this time, the OLS and indicator value showed a very good correlation with the accelerometer, with increasing trends that persisted until around 115 hours and was then followed by further increases at 138 hours. The periods on increased charge and indicator value were likely to be related to periods of double layer stripping during surface damage.

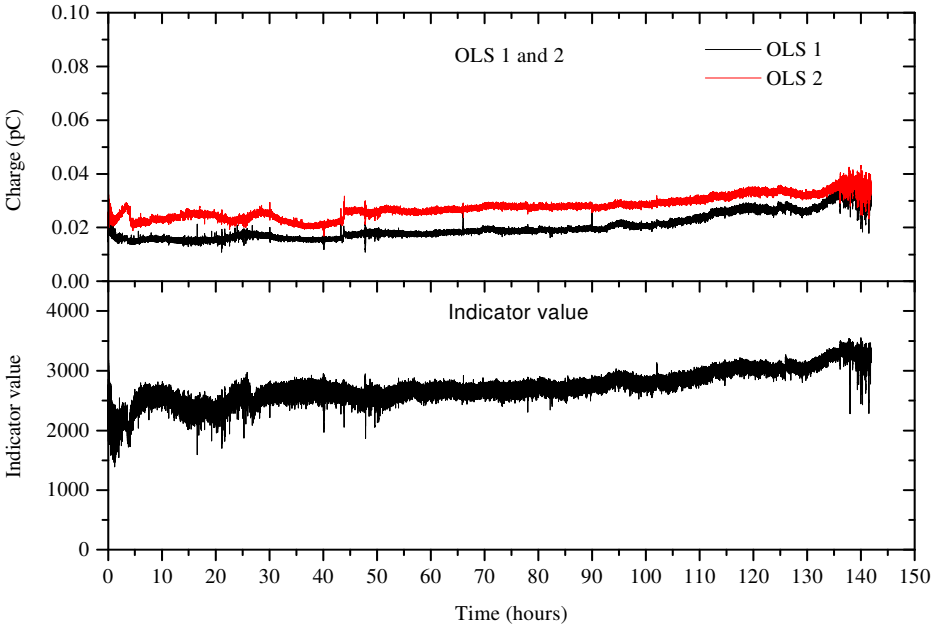

Figure F.3 Electrostatic OLS and indicator value.

F.4 Off-line wear debris detection

Figure F.4 shows the off-line debris analysis. During running-in, there was a 5 – 15 µm debris count that was greater than 4000 particles, which was consistent with the earlier test results that identified abnormal wear. Benign wear was then identified by a reduction in the 5 – 15 µm particle count to below 4000 particles. The earliest sign of distress was observed at 66 hours by a 5 – 15 µm debris count greater than 4000 particles, again confirming abnormal wear and a precursor to the impending wear out phase. Following the increased PODS activity at 66 hours, there was a reduction in debris count to below 4000 particles until 114 hours, a time which was consistent with the increase in acceleration, oil-line charge and indicator value which identified damage and the wear out phase. In addition, there was a further increase in debris count which was greater than 4000 particles at 138 hours, which was consistent with the increased acceleration, oil-line charge and indicator value that identified further damage. Running-in was also identified by a severity index greater than 0.1 which provided further support of abnormal wear. A reduction in severity index then confirmed the steady state. At 66 hours, the severity again index increased to greater than 0.1 and correlated with iron levels of 0.1 ppm, which from the previous tests was further confirmation of abnormal wear. Therefore, corroborating evidence of damage was observed at 66 hours by the PODS, severity index and SOAP and provided an early indicator (precursor) of impending failure.

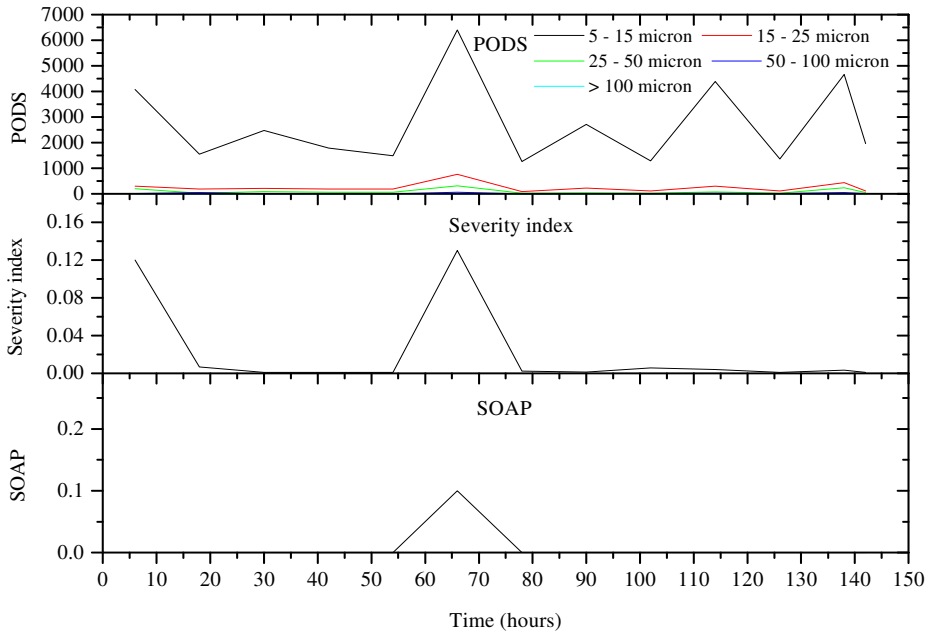

Figure F.4 Off-line PODS, severity index and SOAP.

F.5 The evolution of debris

The particles observed during running-in consisted of 5 µm plate-like debris, which were consistent with those observed during running-in during the previous tests, as shown in Figure F.5 (a). The 5 µm plate-like debris were also observed during the steady state, as shown in (b). However, in (c) at 66 hours, there was evidence of abnormal 20 µm flakes and sub 5 µm spheres indicating a fatigue and adhesive mechanism during oil-film breakdown. These debris types provided further confirmation of abnormal wear that was corroborated by the PODS, severity index and SOAP. There was further evidence of boundary conditions at 114 hours by the identification of further abnormal 20 µm flakes and sub 5 µm spheres, as shown in (d) and was again consistent with increased acceleration, oil-line charge and indicator value at this time.

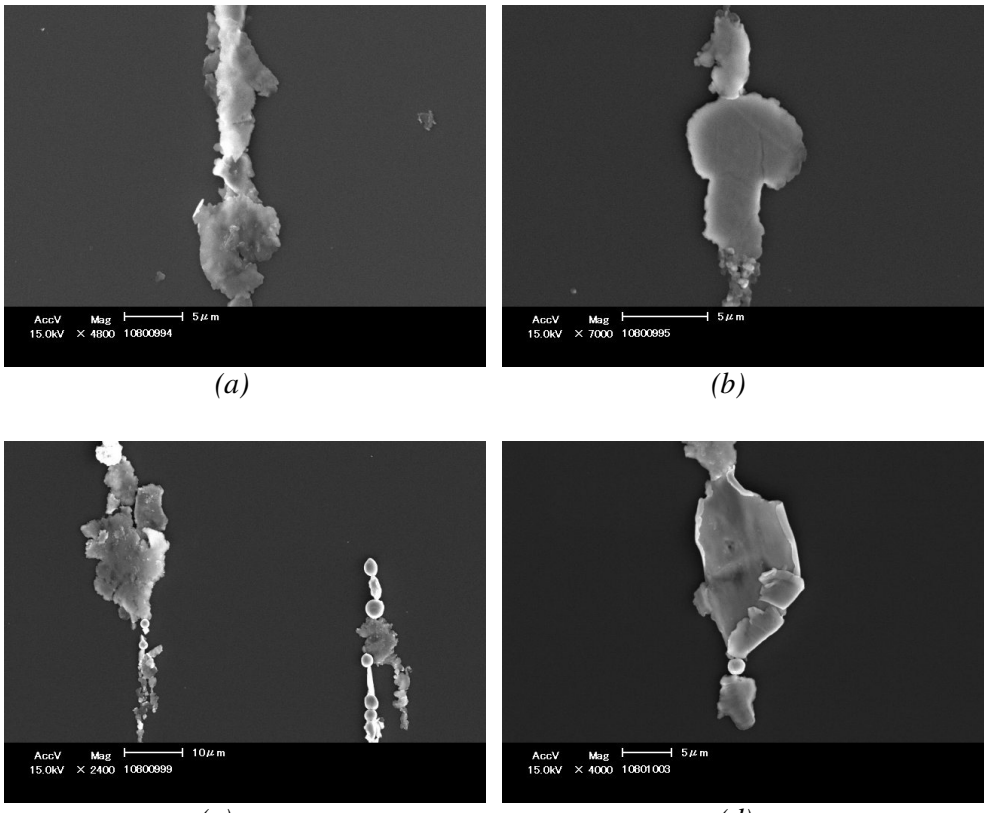

(a) *(b)*

(c) *(d)*

Figure F.5 Off-line debris analysis at (a) 6 hours (b) 18 hours (c) 66 hours and (d) 114 hours.

F.6 Gravimetric analysis

Gravimetric analysis confirmed that the highest mass loss was observed on bearing 2, as shown in Table F.1.

Gravimetric Analysis						
	Pre gravimetric (g)		Post gravimetric (g)		Δ (mg)	Δ (mg)
	Cup	Cone	Cup	Cone	Cup	Cone
Bearing 1	61.14753	116.68499	61.13813	116.67809	0.94	0.69
Bearing 2	61.05145	116.63897	61.01305	116.63521	38.4	3.76
Bearing 3	61.13258	116.70185	61.13048	116.69995	2.1	1.9
Bearing 4	61.14958	116.59376	61.14588	116.59266	3.7	1.1

Table F.1 Gravimetric analysis.

F.7 Summary of test 4

During the initial stages of the test, increased WSS, vibration and thermocouple trends were consistent with the previous tests which identified running-in wear. Running-in was corroborated by an increased OLS and indicator value. Further support of running-in was observed by a 5 – 15 μm debris count greater than 4000 particles by the PODS and a severity index greater than 0.1. Further corroboration of running-in was shown for the first time by an AE peak amplitude greater than 80 dB. The

mechanisms of sensor activity were likely to be consistent with previous tests and relate to contact loading and surface deformation.

Benign wear was identified by steady-state trends from the WSS, vibration, thermocouples, OLS and indicator value. Further corroboration of the transition into benign wear was shown with a reduction in 5 – 15 µm debris count by the PODS to below 4000 particle and a severity index below 0.05.

The first indications of distress were identified at 66 hours by a rapid increase in 5 – 15 µm debris to more than 4000 particles by the PODS, an increase in severity index which was greater than 0.1 and iron levels detected by SOAP of 0.1 ppm. Further corroboration of abnormal wear was identified by 20 µm flakes and sub 5 µm spheres which confirmed fatigue and adhesive mechanisms. Therefore, from tests 3 and 4, the evolution of wear debris provided the most convincing evidence to the earliest signs of bearing distress that provided a precursor of impending failure. The precursor debris activity preceded AE peak amplitude activity of 80 dB at 77 hours and was likely to be related to the interaction of defective elements.

Wear out was identified at 93 hours by an AE peak amplitude greater than 80 dB and was followed by increasing vibration, OLS and indicator value trends at 100 hours. The vibration, OLS and indicator value increased to a time of 115 hours and correlated with a 5 – 15 µm debris count by the PODS that was greater than 4000 particles. The combined sensor activity at this time was likely to be an indication of propagating damage. At 133 hours rapid increases in AE peak amplitude which was greater than 80 dB was followed at 138 hours by further increases in vibration, OLS, indicator value and a 5 – 15 µm debris count greater than 4000 particles by the PODS. The combined sensor data was again likely to be indicative of further damage.

Appendix G

G.1 Distress in the bearing test chamber

In this test a reduced contact pressure of 2 GPa was applied to monitor the effect of loading on failure. In Figure G.1, from the start of the test there were increasing WSS trends and thermocouple trends and heightened vibration activity. This was followed by steady state signatures from the WSS and thermocouples, with fluctuations very consistent with room temperature variation. At 62 hours the software crashed, therefore there was no data collection for the next 5 hours, at which time the software was restarted. There was indications of damage around 135 hours by an increasing vibration trend which attained a peak value around 145 hours, which then remained relatively stable until the end of the test. There was no evidence of failure at any stage of the test by the WSS and thermocouples.

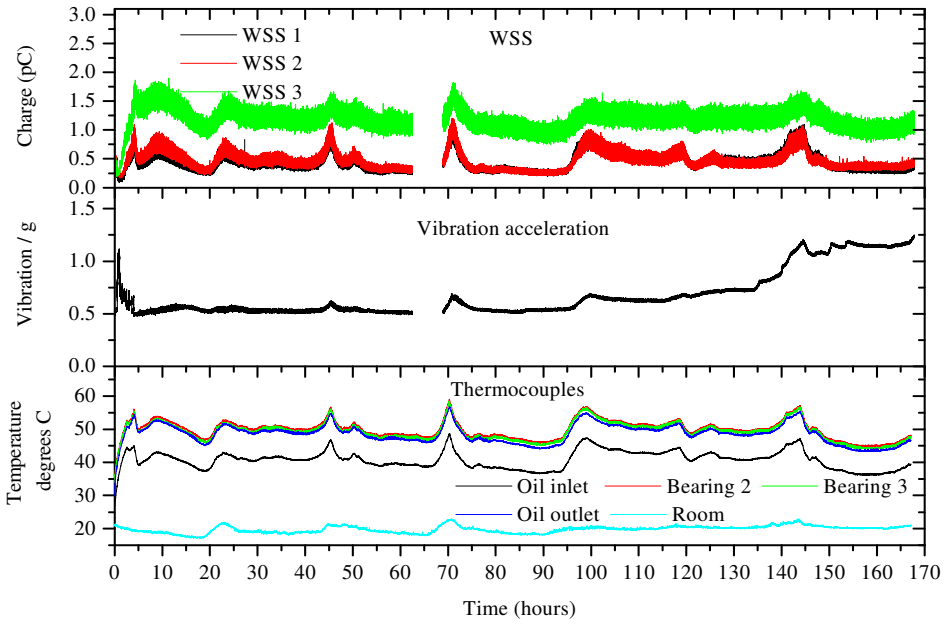

Figure G.1 WSS, accelerometer and thermocouples.

The AE activity is shown in Figure G.2. During the running-in period the peak amplitude was around 75 dB which was consistent with previous tests. This was followed by steady state activity which also remained around 75 dB. At 115 hours there was a single peak amplitude hit of 81 dB. From previous tests, peak amplitude activity greater than 80 dB was indicative of the early signs of distress. There was further peak amplitude activity greater than 80 dB at 137 hours, which was consistent with the increasing vibration trend, and at 150 hours when maximum vibration levels were observed.

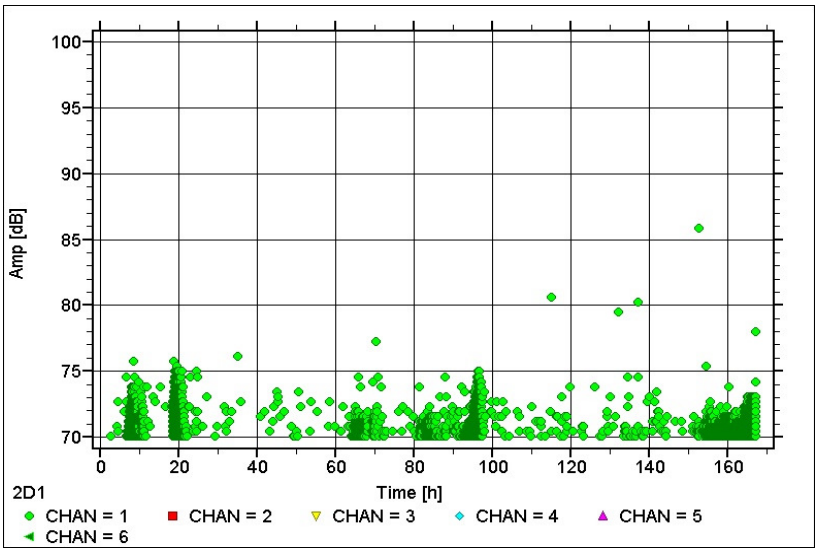

Figure G.2 The AE peak amplitude activity.

G.2 Oil-line debris detection

The OLS and indicator value is shown in Figure G.3. During testing there was no conclusive evidence of debris at any stages of the test. This may be due to insignificant levels of debris entrainment in the scavenge line.

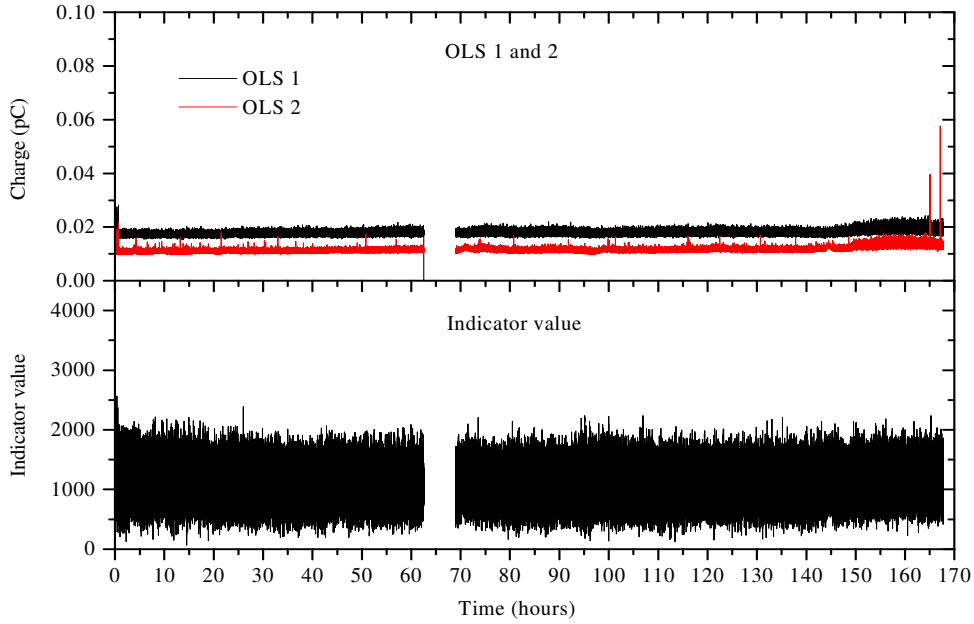

Figure G.3 OLS and indicator value.

G.3 Off-line debris analysis

The off-line debris analysis is shown in Figure G.4. The PODS analysis shows that the dominating 5 – 15 µm bin count was below 4000, which was indicative of normal debris levels throughout the test. The maximum severity index levels were 0.065 which was observed at 30 hours, however for the remainder of the test, values around 0.01 were identified which were indicative of a normal operation. There was no

detection of iron by SOAP at any stage of the test as the debris levels were below the sensitivity of the technique.

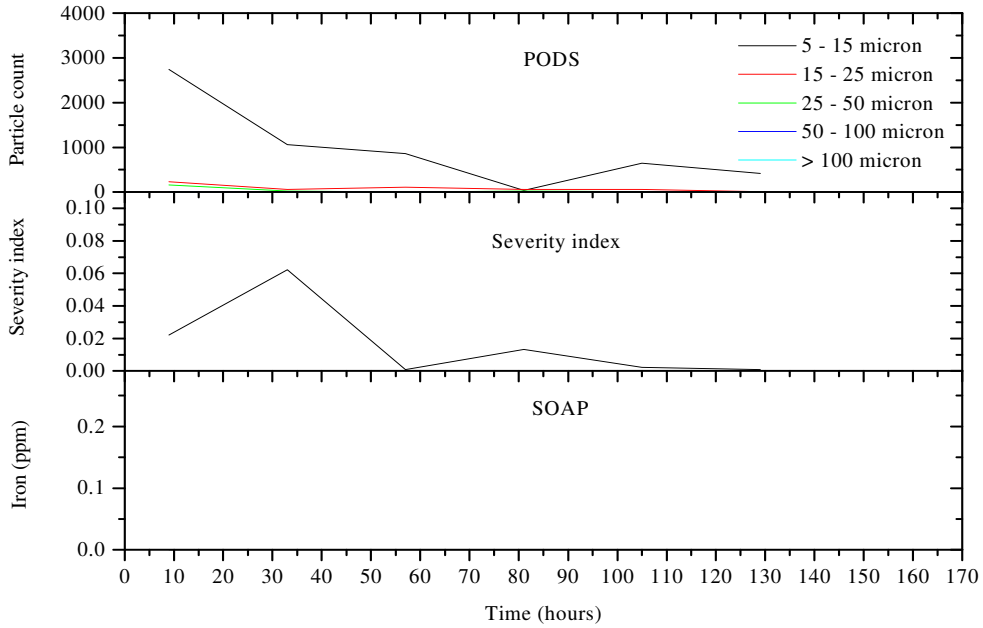

Figure G.4 PODS, severity index and SOAP.

G.4 The evolution of debris

The off-line debris analysis is shown in Figure G.5. During the running-in stages 5 µm plate-like particles dominated, as shown in Figure G.5 (a – b). During the benign wear period the oil samples were still dominated by 5 µm plate-like debris, as shown in Figure G.5 (c). However, Figure G.5 (d) shows that following the increased AE peak amplitude at 115 hours and vibration at 135 hours, there was an increase in the size of the plate-like debris, which were 15 µm.

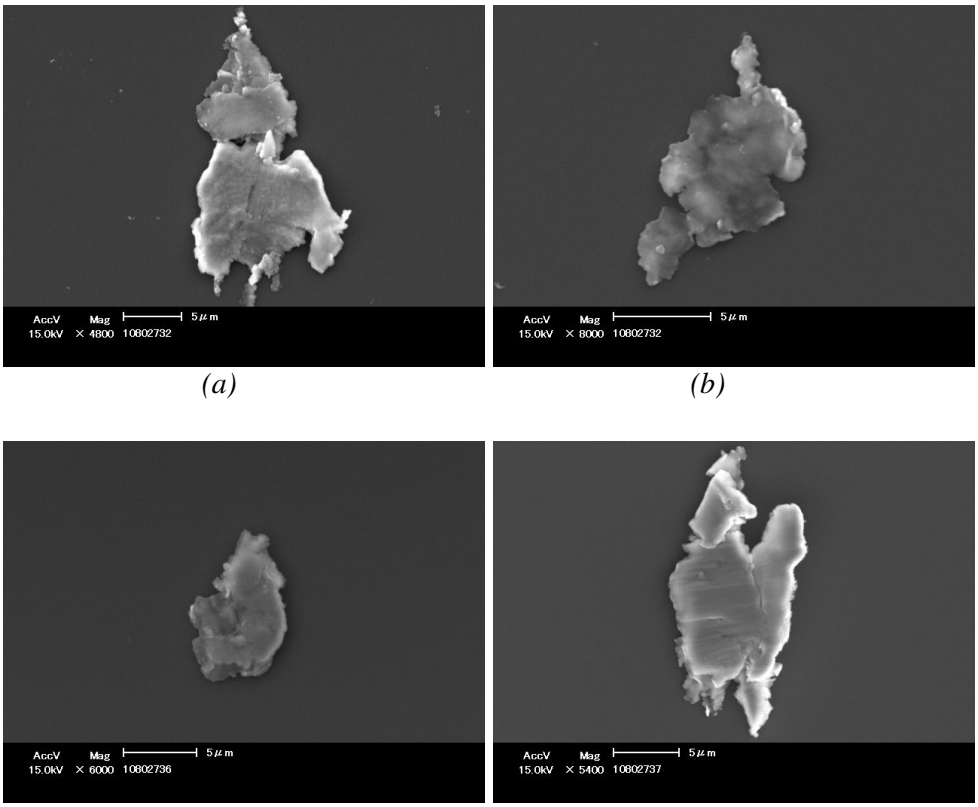

(a) *(b)*

(c) *(d)*

Figure G.5 Wear particle analysis at (a-b) 9 hours, (c) 105 hours and (d) 129 hours.

G.5 Photographic and gravimetric analysis

Figure G.6 shows the failure to bearing number 2. The damage was initiated at the indent and propagated in the direction of the rolling elements.

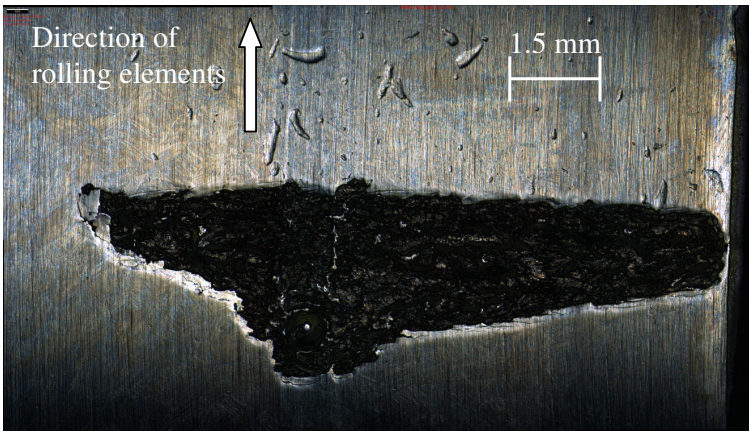

Figure G.6 Inner race failure at the pre-indented bearing number 2.

Further confirmation of damage was observed during gravimetric analysis, shown in Table G.1 which identified the greatest mass loss to the cone assembly of bearing 2.

Gravimetric Analysis						
	Pre-gravimetric (g)		Post gravimetric (g)		Δ (mg)	Δ (mg)
	Cup	Cone	Cup	Cone	Cup	Cone
Bearing 1	61.33856	116.76418	61.3352	116.7616	3.36	2.58
Bearing 2	61.38479	116.69253	61.38004	116.67722	4.75	15.31
Bearing 3	61.36454	116.71359	61.36111	116.7102	3.43	3.39
Bearing 4	61.37994	116.70726	61.37775	116.70548	2.19	1.78

Table G.1 Gravimetric analysis.

G.6 Summary of test

Running-in was identified by increasing wear site charge and thermocouple trends as well as dynamic vibration activity. At this time the AE peak amplitude was around 75 dB. Also during this period 5 µm plate-like particles dominated. Benign wear was identified by steady state sensor trends from all techniques. The first sign of distress was identified by an AE peak amplitude greater than 80 dB which was followed by the identification of 15 µm plate-like particles. The AE and debris activity preceded an increasing vibration trend. Continuation of the test showed that there was further AE peak amplitude activity greater than 80 dB that persisted with an increasing vibration trend.

Appendix H

H.1 Distress in the bearing test chamber

In this test a Hertzian contact pressure of 1.6 GPa was applied. However, the test was stopped as the brushes on the motor were worn which caused a fluctuating motor speed.

Figure H.1 shows that the running-in period was identified by an increasing wear site charge and thermocouple trends whilst vibration levels remained relatively stable. Following running-in, all sensor activity attained steady state levels which indicated benign wear. Wear site charge levels at the test bearings remained around 1.5 pC and vibration was around 1 g. The oil inlet temperature was 40°C, bearing outer race temperatures were 45°C and the oil outlet temperature was around 42°C. These temperatures were lower than test 1 due to the reduced load.

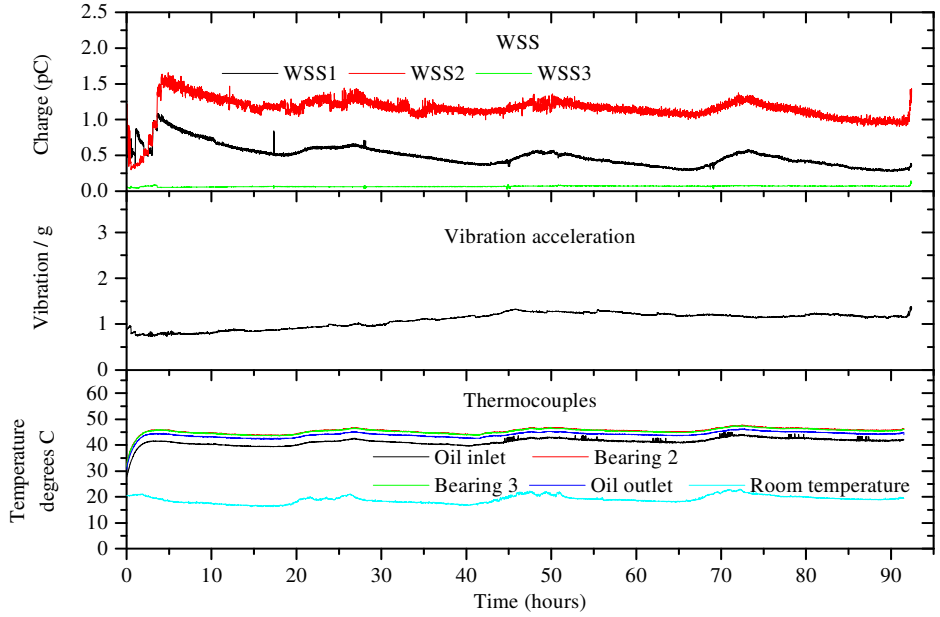

Figure H.1 WSS, vibration and thermocouples.

Figure H.2 shows that during the initial stage of testing there was no significant charge and indicator value that confidently identified running-in. This was because for the duration of the test, steady-state sensor activity was observed. This may be because of insignificant debris levels due to the reduced load when compared to test 1.

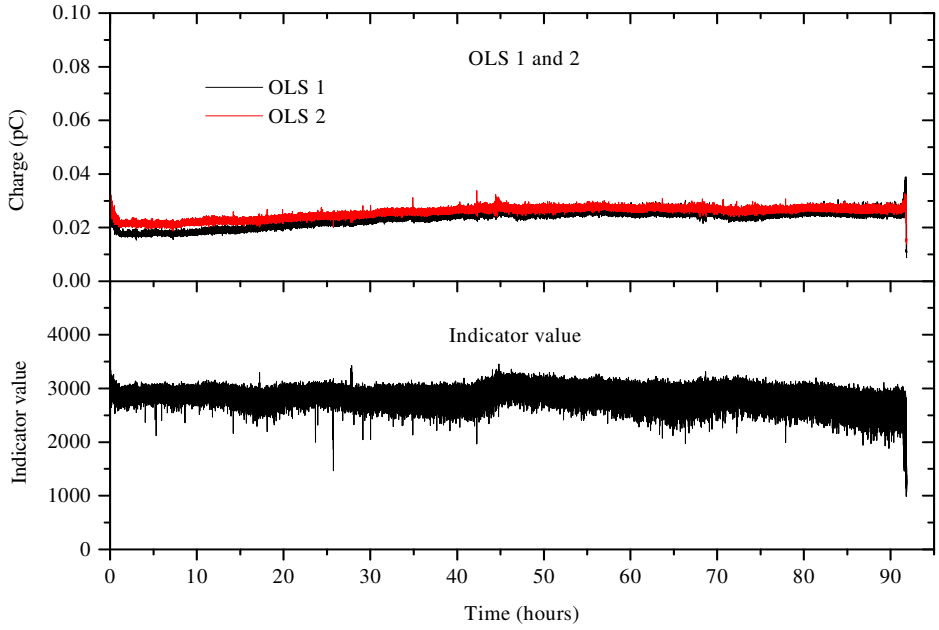

Figure H.2 OLS and indicator value.

There was no off-line debris analysis performed in this test, as the failure was attributed to motor failure. However, the author does appreciate that there may have been some interesting observations during the motor failure, but in order to save time the debris analysis was not performed.

[1] Morhain, A., Mba, D., *Bearing defect diagnosis and acoustic emission.* Journal of Engineering Tribology, 2003. **217**(4): p. 257-273.
[2] Williams, T., Ribadeneira, X., Billington, S., Kurfess, T., *Rolling element bearing diagnostics in run to failure lifetime testing.* Mechanical Systems and Signal Processing, 2001. **15**(5): p. 979-993.
[3] Ebersbach, S., Peng, Z., Kessissoglou, N.J., *The investigation of the condition and faults of a spur gearbox using vibration and wear debris analysis techniques.* Wear, 2006. **260**: p. 16-24.
[4] Heng, R.B.W., Nor, M.J., *Statistical analysis of sound and vibration signals for monitoring rolling element bearing condition.* Applied Acoustics, 1998. **53**(1-3): p. 211-226.
[5] Brotherton, T., Grabill, P., Wroblewski, D., Friend, R., Sotomayer, B., Berry, J., *A testbed for data fusion for engine diagnostics and prognostics.* IEEE Aerospace Conference Proceedings (Cat. No.02TH8593), 2002: p. 3029-3042.
[6] Leger, J.B., Iung, B., Morel, G., *Integrated design of prognosis, diagnosis and monitoring processes for proactive maintenance of manufacturing systems.* IEEE International Conference on Systems, Man, and Cybernetics (Cat. No.99CH37028), 1999: p. 492-498.
[7] Jost, H.P., *Lubrication (Tribology) Education and Research.* 1966.
[8] Jost, H.P. *The tasks of tribology societies in a changing world.* in *2nd World Tribology Conference*. 2001. Vienna.
[9] Bloch, H.P., *Practical Lubrication for Industrial Facilities*. 2000: The Fairmont Press. 345.
[10] White, G., *Introduction to machine vibration.* DLI Engineering corp, 1997.
[11] Maintenace, J.I.o.P., *Lubrication technology.* Japan Management Association Publications, 1991: p. 101.
[12] Zwerlein, O., Schlicht, H., *Rolling contact fatigue testing of bearing steels, ASTM STP 771*, ed. J.J.C. Hoo. 1982, Philidelphia: ASTM.
[13] Ilincic, S., Vorlaufer, G., Fotiu, P.A., Franek, F., *Finite element method - boundary element method modelling of elastic multi-asperity contacts.* Proceedings of the IMechE Part J Journal of Engineering Tribology, 2009. **223**: p. 1-9.
[14] Dwyer-Joyce, R.S., *Tribological Design Data, Part 3: Contact Mechanics*. 1997. p. 1-17.
[15] Williams, J.A., *Engineering Tribology*. 1994, Oxford: Oxford University Press. Appendix 8.
[16] Huthchings, I.M., *Tribology: Friction and Wear of Engineering Materials*. Vol. 1. 1992: Edward Arnold. 245.
[17] Bhushan, B., *Modern Tribology Handbook*. Vol. 2. 2001: CRC Press. 1288.
[18] Johnson, K.L., *Contact mechanics*. 1985: Cambridge University Press.
[19] Roylance, B.J., *Wear and Wear Debris in a Changing World.* Hydraulic Failure Analysis: Fluids, Components and System Effects, ed. G.E. Totten, Wills, D.K., Feldmann, D. 2001, West Conshohocken: American Society for Testing and Materials. 200 - 213.
[20] Booser, R.E., *CRC Handbook of Lubrication.* 1984: CRC Press. 156.
[21] Bhushan, B., *Introduction to Tribology*. 2002: John Wiley and Sons. 513.
[22] Hamrock, B.J., Schmid, S.R., Jacobson, B.O., *Fundamentals of fluid film lubrication*. 2004: CRC Press. 92.
[23] Eschmann, P., Hasbargen, L., Weigand, K., *Ball and Roller Bearings*. 1985: John Wiley and Sons. 217-218.

[24] Cheng, H.S., *Elastohydrodynamics and failure prediction.* Lurication Science, 2006. **2**(2): p. 133-156.
[25] Harris, T.A., Kotzalas, M.N., *Rolling bearing analysis*. 2006: CRC Press. 201.
[26] Dowson, D., Higginson, G. R., *Elasto-hydrodynamic Lubrication*. 1977, Oxford: Permagon Press. 96.
[27] Wang, L., Wood, R.J.K., *The influence of contact conditions on surface reaction layers formed between steel surfaces lubricated by an aviation oil.* Tribology International, 2007. **40**: p. 1655-1666.
[28] Meheux, M., Minfray, C., Ville, F., Mogne, T. Le, Lubrecht, A. A., Martin, J. M., lierade, H. P., *Influence of slide to roll ratio on tribofim generation.* Proceedings of the IMechE Part J Journal of Engineering Tribology, 2007. **222**: p. 325-334.
[29] Olofsson, J., Lindberg, F., Johansson, S., Jacobson, S., *On the role of tribofilm formation on the alumina drive components of an untrsonic motor.* Wear, 2009. **267**(5-8): p. 1295-1300.
[30] Morina, A., Neville, A., *Understanding the composition and low friction tribofilm formation/removal in boundary lubrication.* Tribology International, 2006. **40**(10-12): p. 1696-1704.
[31] Ito, K., Martin, J.M., Minfray, C., Kato, K., *Formation mechanism of low friction ZDDP tribofilm on iron oxide.* Tribology Transactions, 2007. **50**(2): p. 211-216.
[32] Dwyer-Joyce, R.S., *Predicting the abrasive wear of ball bearings by lubricant debris.* Wear, 1999. **233-235**: p. 692-701.
[33] Nilsson, R., Olofsson, U., Sundvall, K., *Filtration and coating effects on self-generated particle wear in boundary lubricated roller bearings.* Tribology International, 2005. **38**(2): p. 145-150.
[34] Gates, J.D., *Two body and three body abrasion: A critical decision.* Wear, 1998. **214**(139-146).
[35] Trezona, R.I., Allsopp, D.N., Hitchings, I.M., *Transitions between two-body and three-body abrasive wear: influence of test conditions in the microscale abrasive wear test.* Wear, 1999. **225-229**: p. 205-214.
[36] Kayaba, T., Hokkirigawa, K., Kato, K., *Analysis of the abrasive wear mechanism by successive wear processes in a scanning electron microscope.* Wear, 1986. **110**: p. 419-430.
[37] Williams, J.A., Hyncica, A.M., *Mechanisms of abrasive wear in lubricated contacts.* Wear, 1991. **152**: p. 57-74.
[38] Booser, R.E., *Tribology Data Handbook*. 1997: CRC Press. 323.
[39] Olver, A.V., *The mechanism of rolling contact fatigue: An update.* Proceedings of the IMechE, Part J: Journal of Engineering Tribology, 2005. **219**(5): p. 313 - 330.
[40] Changsen, W., *Analysis of rolling element bearings*. 1987, London: Mechanical Engineering Publications Ltd. 184.
[41] Harnoy, A., *Bearing design in machinery: Engineering tribology and machinery*. 2002: CRC Press. 484.
[42] Nelias, D., Ville, F., *Detrimental effects of debris dents on rolling contact fatigue.* ASME Journal of Tribology, 2000. **122**(1): p. 55-64.
[43] Ai, X., *Effect of debris contamination on the fatigue life of roller bearings.* Proceedings of the IMechE, Part J: Journal of Engineering Tribology, 2001. **215**(6): p. 563-575.

[44] Benham, P.P., Crawford, R.J., Armstrong, C.G., *Mechanics of Engineering Materials*. 1996: Prentice Hall. 518-555.
[45] Ren, Z., Glodez, S., Fajdiga, G., Ulbin, M., *Surface initiated crack growth simulation in moving lubricated contact.* Theoretical and Applied Fracture Mechanics, 2002. **38**(2): p. 141-149.
[46] Fajdiga, G., Glodez, S., Kramar, J., *Pitting formation due to surface and subsurface initiated fatigue crack growth in contacting mechanical elements.* Wear, 2007. **262**: p. 1217-1224.
[47] Hoeprich, M.R., *Rolling element bearing fatigue damage propagation.* Transactions of the ASME, 1992. **114**: p. 328-333.
[48] Fernandes, P.J.L., *Contact fatigue in rolling element bearings.* Engineering Failure Analysis, 1997. **4**(2): p. 155-160.
[49] Alfredsson, B., *A Study on Contact Fatigue Mechanics*, in *Department of Solid Mechanics*. 2000, Royal Institue of Technology: Stockholm.
[50] Kotzalas, M.N., Harris, P.A., *Fatigue failure progression in ball bearings.* Tribology, 2001. **123**(2): p. 238-242.
[51] Weibull, W. *A statistical theory of the strength of materials*. in *Royal Swedish Institute Engineering Research*. 1939.
[52] Kotzalas, M.N., *Statistical distribution of tapered roller bearing fatigue lives at high levels of reliability.* Journal of Tribology, 2005. **127**: p. 865-870.
[53] Lundberg, G., Palmgren, A., *Dynamic capacity of rolling bearings.* Acta Polytech, 1947. **3**.
[54] Raje, N., Sadeghi, F., Rateick, R.G., Hoeprich, M.R., *A numerical model for life scatter in rolling element bearings.* Journal of Tribology, 2008. **130**: p. 1-10.
[55] Zaretsky, E.V., Poplawski, J.V., Miller, C.R., *Rolling Bearing Life Prediction-Past, Present, and Future*. 2000, NASA TM-2000-210529.
[56] Harris, T.A., Bansby, R.M., *Life ratings for ball and roller bearings.* Part J: Journal of Engineering Tribology, 2001. **215**: p. 577-595.
[57] Zaretsky, E.V., Bamberger, E., Harris, T., Kacmarsky, W., Parker, R., Sherlock, J., *Life adjustment factors for ball and roller bearings, ASME Engineering Guide*. 1971, New York: ASME.
[58] Zaretsky, E.V., *Life factors for rolling bearings.* STLE Publication SP-34, 1992.
[59] Parker, R.J., Pinel, S.I., Signer, R. *Lubrication of optimised design tapered roller bearings to 2.4 million dn*. in *NASA Technical Paper 1714*. 1980.
[60] Orvos, P.S., Dressler, G.J., *Deveopment of 3.5 million dn taper roller bearing cage.* ASLE Transactions, 1980. **23**(2): p. 109-120.
[61] Pope, E., *Rules of Thumb for Mechanical Engineers*. 1997: Gulf Professional Publishing. 159.
[62] Suh, N.P., Sin, H.C., *The Genesis of Friction.* Wear, 1981. **69**(1): p. 91-114.
[63] Stachowiack, G.P., Podsiadlo, P., Stachowiack, S.W., *Shape and features in the automated classification of adhesive and abrasive wear particles.* Tribology Letters, 2006. **24**(1): p. 15-26.
[64] Turley, D.M., Doyle, E.D., Samuels, L.E. *The structure of damaged layers on metals*. in *International Conference on Production Engineering*. 1974. Tokyo.
[65] Newcombe, S.B., Stobbs, W.M., *Transmission electron microscopy study of the white etching layer on a rail head.* Material Science and Engineering, 1984. **66**: p. 195-204.

[66] Archard, J.F., *The temperature of rubbing surfaces.* Wear, 1959. **2**: p. 438-455.
[67] Williams, J.A., *Wear and wear particles-some fundamentals.* Tribology International, 2005. **38**: p. 863-870.
[68] Ajayi, O.O., Hersberger, J.G., Zhang, J., Fenske, G.R., *Microstructural evolution during scuffing of hardened 4340 steel - implication for scuffing mechanism.* Tribology International, 2005. **38**: p. 277-282.
[69] Roylance, B.J., *Machine failure and its avoidance-what is tribilogy's contribution to effective maintenance of critical machinery?* Proceedings of the IMechE, Part J: Journal of Engineering Tribology, 2003. **217**: p. 349-364.
[70] Akagaki, T., Kato, K., *Plastic flow process of surface layers in flow wear under boundary lubricated conditions.* Wear, 1987. **117**: p. 179-196.
[71] Anderson, D.P., *Wear Particle Atlas.* 1982, Naval Air Engineering Centre, NAEC-92-163.
[72] Roylance, B.J., Hunt, T.M., *Wear debris analysis.* 1999: Coxmoore Publishing Company First Edition. 14.
[73] Lockwood, F.E., Dalley, R., *Friction, Lubrication and Wear technology.* ASM Handbook. Vol. 18. 1992. 299 - 312.
[74] Hunt, T.M., *Handbook of wear debris analysis and particle detection in liquids.* 1993, London and New York: Elsevier Applied Science. 51.
[75] Ahn, S.H., *Practical contaminant analysis of lubricating oil in a steam turbine generator.* Tribology International, 1996. **29**(2): p. 161-168.
[76] Flanagan, I.M., Jordan, J.R., Whittington, H.W., *Wear debris detection and analysis techniques for lubricant based condition monitoring.* Journal of Physics E: Scientific Instruments, 1988. **21**(11): p. 1011-1016.
[77] Lloyd, O., Fox, A.F., *Monitoring debris in turbine generator oil.* Wear, 1981. **71**(1): p. 79-91.
[78] Centers, P.W., Price, F.D., *Real time simultaneous in-line wear and lubricant condition monitoring.* Wear, 1988. **123**(3): p. 301-312.
[79] Ozogan, M.S., Khalil, A.I., Katsoulakos, P.S., *Tribological failure detection and condition monitoring for diesel engines.* Wear, 1989. **130**(1): p. 189-201.
[80] Ruff, A.W., *Characterisation of wear debris particles recovered from wearing systems.* Wear, 1977. **42**(1): p. 49-62.
[81] Roylance, B.J., Williams, J.A., Dwyer-Joyce, R., *Wear debris and associated phenomena.* Proc IMechE 214 part J, 2004: p. 79-105.
[82] Ahn, A.H., Yoon, E.S., Sohn, D.G., Kwon, O.K., Shin, K.S., Nam, C.H., *Practical contaminant analysis of lubricating oil in a steam turbine generator.* Tribology International, 1996. **29**(2): p. 161-168.
[83] Laghari, M.S., *Recognition of texture types of wear particles.* Neural Computation and Application, 2003. **12**: p. 18-25.
[84] Kleis, I., Muiste, U., Pilvre, U., Uuemois, H., *The physical mechanism of the formation of metal microspheres in the wear process.* Wear, 1979. **53**: p. 79-85.
[85] Kato, K., *Classification of wear mechanisms/models.* Journal of Engineering Tribology, 2002. **216**: p. 349-355.
[86] Lim, S.C., Ashby, M.F., *Wear mechanism maps.* Acta Metal, 1987. **35**: p. 1-24.
[87] Edwards, D.J., Holt, G.D., Harris, F.C., *Predictive maintenance techniques and their relevance to construction plant.* Quality in Maintenance, 1998. **4**(1): p. 25-37.

[88] Collacott, R.A., *Vibration monitoring and diagnostics*. 1979, London: George Goodwin Limited. 131-135.
[89] Wowk, V., *Machinery Vibration: Measurement and analsysis*. 1991: Mc Graw - Hill Professional. 65.
[90] Donnellan, P., *Condition Monitoring - Engineering the practice*. 2002, Bury St Edmonds and London, UK: Professional Engineering Publishing. 55.
[91] Orhan, S., Akturk, N., Celik, V., *Vibration monitoring for defect diagnosis of rolling element bearings as a predictive maintenance tool: Comprehensive case studies.* NDT&E International, 2006. **39**: p. 293-298.
[92] Li, Y., Billington, C., Zhang, T., Kurfess, T., Danyluk, S., Liang, S., *Dynamic prognostic prediction of defect propagation on rolling element bearings.* Tribology Transactions, 1999. **42**(2): p. 385-392.
[93] Tandon, N., Choudhury, A., *A review of vibration and acoustic measurement methods for the detection of defects in rolling element bearings.* Tribology International, 1999. **32**(8): p. 469-480.
[94] Williams, R.V., *Monitoring the condition of machinery.* Physics in Technology, 1976: p. 166-171.
[95] Amarnath, M., Shrinidhi, R., Ramachandra, A., Kandagal, S.B., *Predictions of defects in antifriction bearings using vibration signal analysis.* Journal of the Institution of Engineers (India), 2004. **85**(2): p. 88-92.
[96] Choy, F.K., Zhou, J., Braun, M.J., Wang, L., *Vibration monitoring and damage quantification of faulty ball bearings.* Transactions of the ASME, 2005. **127**: p. 776-783.
[97] Prabhakar, S., Mohatny, A.R., Sekhar, A.S., *Application of discrete wavelet transform for detection of ball bearing race faults.* Tribology International, 2002. **35**: p. 793-800.
[98] Martin, K.F., Thorpe, P., *Normalised spectra in monitoring of rolling bearing elements.* Wear, 1992. **159**: p. 153-160.
[99] Mathew, J., Alfredson, R.J., *The condition monitoring of rolling element bearings using vibration analysis.* Journal of Vibration, Acoustics, Stress Reliability and Design, 1984. **106**: p. 447-453.
[100] Alfredson, R.J., Mathew, J., *Time domain methods for monitoring the condition of rolling element bearings.* Mech. Eng. Transactions, 1985. **10**(2): p. 102-107.
[101] Villwock, S., Zoubeck, H., Pacas, M. *Rolling bearing condition monitoring based on frequency responce analysis*. in *IEEE International Symposium on Diagnostics for Electric Machines, Power Electronics and Drives, SDEMPED*. 2007.
[102] Tandon, N., Choudhury, A., *A review of vibration and acoustic measurement methods for the detection of defects in rolling element bearings.* Tribology International, 1999. **32**: p. 469-480.
[103] Tandon, N., Kumar, K.S., *Detection of defects at different locations in ball bearings by vibration and shock pulse monitoring.* Noise and Vibration worldwide, 2003. **34**(3): p. 9-16.
[104] Pao, Y.H., Gajewski, R.R., Ceranoglu, A.N., *Acoustic emission and transient waves in an elastic plate.* Journal of the Acoustical Society of America, 1979. **65**(1): p. 96-102.
[105] Williams, J.H., Delonga, D.M., Lee, S.S., *Correlations of acoustic emissions with fracture mechanics parameters in structural bridge steels during fatigue.* Mater. Eval., 1982. **40**(11): p. 1184-1189.

[106] van Bohemen, S.M.C., Sietsma, J., Hermans, M.J.M., Ricahrdson, I.M., *Kinetics of the martensitic transformation in low-alloy steel studied by means of acoustic emission.* Acta. Matter., 2003. **51**(14): p. 4183-4196.
[107] Sayles, R.S., Poon, S.Y., *Surface topography and rolling element vibration.* Precision Eng., 1981. **3**: p. 137-164.
[108] Price., E.D., *High frequency techniques for condition monitoring*. 2002, University of Wales: Swansea.
[109] Holroyd, T., *Using acoustic emissions to ease the task of condition monitoring*. 1999, Oxford: Coxmoore Publishing. 3-10.
[110] Price, E.D., Lees, A.W., Friswell. M.I., *Detection of severe sliding and pitting fatigue wear regimes through the use of broadband acoustic emission.* Engineering Tribology, 2005(219): p. 85-98.
[111] Hong, K.J., Jeong, H.D., Lee, C.S., *Acoustic emission behaviour during plastic deformation of 8090 Al-Li alloy.* Journal of acoustic emissions, 1995. **13**(3-4): p. 61-67.
[112] Mba, D., Hall, L.D., *The transmission of acoustic emission across large scale turbine motors.* NDT&E International, 2002. **35**: p. 529-539.
[113] Olma, B.J., *Experience of identification of loose parts by acoustic monitoring of primary system.* Progress of Nuclear Energy, 2003. **43**(1-4): p. 225-232.
[114] Zuluaga-Gilardo, C., Mba, D., Smart, M., *Acoustic emission during run up and run down of a power generation turbine.* Tribology International, 2004. **37**: p. 415-422.
[115] Toutountzakis, T., Mba, D., *Observations of acoustic emission activity during gear defect diagnosis.* NDT&E International, 2003. **36**: p. 471-477.
[116] Toutountzakis, T., Tan, C.K., Mba, D., *Application of acoustic emission to seeded gear fault detection.* NDT&E International, 2005. **38**: p. 27-36.
[117] Mba, D.H., L.D., *The transmission of acoustic emission across large scale turbine rotors.* NDT&E International, 2002. **35**(8): p. 529-539.
[118] Mechefski, C.K., Sun, G., Sheasby, J., *Using acoustic emissions to monitor sliding wear.* Insight, 2002. **44**(8): p. 490-497.
[119] Beattie, A.G., *Acoustic emission, principles and instrumentation.* Journal of Acoustic Emissions, 1983. **2**(1-2): p. 95-128.
[120] Yoshioka, T., Fujiwara, T., *The crack growth rate in rolling contact fatigue is very fast.* Wear, 1986. **113**: p. 291-293.
[121] Wang, L., Wood, R.J.K., *The influence of contact conditions on surface reactive layers formed between steel surfaces lubricated by an aviation oil.* Tribology International, 2007. **40**(10-12): p. 1655-1666.
[122] Wang, L., Wood, R.J.K., Sun, J., *Acoustic emissions form oil lubricated metal on metal sliding contacts.* Insight: Non destructive testing and condition monitoring, 2008. **50**(9): p. 506-511.
[123] Choudbury, A., Tandon, N., *Application of acoustic emission technique for the detection of defects in rolling element bearings.* Tribology International, 2000. **33**: p. 39-45.
[124] Al-Gamdt, A.M., Mba, D., *A comparative experimental study on the use of acoustic emission and vibration analysis for bearing defect identification and estimation of size.* Mechanical Systems and Signal Processing, 2006. **20**: p. 1537-1571.
[125] Mba, D., Rao, R. B. K. N., *Development of acoustic emission technology for condition monitoring and diagnosis of rotating machines: Bearings, pumps,*

gearboxes, engines and rotating structures. The shock and vibration digest, 2006. **38**(1): p. 3 - 16.
[126] Neale, M.J., *The Tribology Handbook*. 1995: Butterworth-Heinemann.
[127] Murray, R.J., Mitchell, B.F. *Cost savings from a practical predictive-maintenance program*. in *Annual reliability and maintanability symposium (Cat. No. 94CH3391-0)*. 1994.
[128] Leflar, J.A., *Practical TPM*. 2001: Productivity Press. 237.
[129] Peters, R.W., *Maintenace Benchmarking and Best practices*. 2006: Mc Graw-Hill Professional. 256.
[130] Miller, J.L., Kitaljevich, D., *In line oil debris monitor for aircraft engine condition assessment.* Aerospace conference proceedings, 2000. **6**: p. 49-56.
[131] Greenfield, S. *Advanced rotorcraft oil debris monitoring for the 21st century*. in *The Fifth International Conference on Condition Monitoring & Machinery Prevention Technologies*. 2008. Edinburgh.
[132] Toms, A. *On-line diagnostic sensors for tribological and lubrication monitoring - Past, present and future*. in *STLE*. 2008. Ohio, USA.
[133] Morris, S., Wood, R.J.K., Harvey, T.J., Powrie, H.E.G., *Use of electrostatic charge monitoring for early detection of adhesive wear in oil lubricated contacts.* Tribology: Transactions of the ASME, 2002. **124**(2): p. 288-296.
[134] Whittington, H.W., *An on-line wear debris monitor.* Meas.Sci.Technol, 1991. **3**: p. 656-661.
[135] Edmonds, J., *Detection of precursor wear debris in lubrication systems.* IEEE Aerospace Conference Proceedings, 2000. **6**: p. 73-78.
[136] Chambers, K.W., Arneson, M.C., *An on-line ferromagnetic wear debris sensor for machinery condition monitoring and failure detection.* Wear, 1988. **128**(3): p. 325-337.
[137] Rao, B.K.N., *Handbook of Condition Monitoring*. 1996: Elsevier. 87.
[138] Dempsey, P.J., Certo, J.M., Morales, W., *Current status of hybrid bearing damage detection.* Tribology Transactions, 2005. **48**: p. 370-376.
[139] Seifert, W.W., Westcott, V.C., *A method for the study of wear particles in lubricating oil.* Wear, 1972. **21**: p. 27-42.
[140] Belmondo, A., Guiggioli, F., Giorgi, B., *Optimization of ferrographic oil analysis for diesel engine wear monitoring.* 1983. **90**(1): p. 46-91.
[141] Roylance, B.J., Hunt, T.M., *Wear debris analysis*. 1999: Coxmoore Publishing Company First Edition. 14-41.
[142] Hunt, T.M., *Handbook of wear debris analysis and particle detection in liquids*. 1993, London and New York: Elsevier Applied Science. 277.
[143] Scott, D., Westcott, V.C., *Predictive maintenance by ferrography.* Wear, 1977. **44**: p. 173-182.
[144] Hofman, M.V., Hohnson, J.H., *The development of ferrography as a laboratory wear measurement method for the study of engine operating conditions on diesel engine wear.* Wear, 1977. **44**: p. 183-199.
[145] Centers, P.W., *Laboratory evaluation of the on-line ferrograph.* Wear, 1983. **90**: p. 1-9.
[146] Mills, G.H., Davis, F.A., *A ferrographic case study applied to hydraulic systems.* Wear, 1982. **90**(1): p. 101-106.
[147] Scott, D., *The application of ferrography to the condition monitoring of gas turbines.* Wear, 1983. **90**(2): p. 21-29.

[148] Lukas, M., Yurko, R.J. *Current technology in oil analysis spectrometers and what we may expect in the future*. in *Machinery Failure prevention Technology 50th*. 1996. Virginia Beach, VA, USA.
[149] Macian, V., Tormos, B., Olmeda, P., Montoro, L., *Analytical approach to wear rate determination for internal combustion engine condition monitoring based oil analysis.* Tribology International, 2003. **36**: p. 771-776.
[150] Berg, S., *A study of sample withdrawl for lubricated systems. Part 2: Practical sample withdrawl and selection of proper sampling methods.* Industrial Lubrication and Tribology, 2001. **53**(3): p. 97-108.
[151] Roylance, B.J., Hunt, T.M., *Wear debris analysis*. 1994: Coxmoore Publishing Company First Edition. 21-22.
[152] Akagaki, T., Kato, K., *Ferrographic analysis of failure process in full scale journal bearing.* Wear, 1992. **152**(2): p. 241-252.
[153] Jones, W.R., Nagaraj, H.S., Winer, W.O., *Ferrographic analysis of wear particles from sliding elastohydrodynamic experiments.* NASA Technical Paper 1230, 1978.
[154] Odahara, H., Sasaki, Y., Kawabata, M., Taguchi, T. *Practical Application of Lubricant Oil Analysis for Electric Power Plant*. in *World Tribology Conference 2*. 2002. Vienna.
[155] Ghosh, S., Sarkar, B., Saha, J., *Wear characterisation by fractal mathmatics for quality improvement of machine.* Journal of Quality in Maintenance Engineering, 2005. **11**(4): p. 318-322.
[156] Peng, Z., *An integrated intelligence system for wear debris.* Wear, 2002. **252**: p. 730-743.
[157] Peng, Z., Kirk, T.B., *Computer image analysis of wear particles in three-dimensions for machine condition monitoring.* Wear, 1998. **223**: p. 157-166.
[158] Sperring, T.P., Novell, T.J., *SYCLOPS - A qualatative debris classification system developed for RAF early failure detection centres.* Tribology International, 2005. **38**: p. 898-903.
[159] Xu, K., Luxmoore, A.R., Jones, L.M., Deravi, F., *Integration of neural networks and expert systems for microscopic wear particle analysis.* Knowledge-Based Systems, 1998. **11**: p. 213-227.
[160] Reintjes, J., Tucker, J.E., Thomas, S.E., Schultz, A., Tankersley, L.L., Lu, C., Howard, P.L., Sebok, T., Holloway, C. *LaserNet Fines wear debris analysis technology: Application to mechanical fault detection*. in *AIP Conference Proceedings*. 2003.
[161] Roylance, B.J., Albidewi, I.A.A., Price, A.L., Luxmoore, A.R., *The deveopment of a computer aided systematic particle analysis procedure.* Lubrication Engineering, 1992. **48**(12): p. 940-946.
[162] Roylance, B.J., Albidewi, I.A.A., Laghari, M.S., Luxmoore, A.R., Devari, F., *Computer aided vision engineering (CAVE): Quantification of wear particle morphology.* Lubrication Engineering, 1994. **50**(2): p. 111-116.
[163] Samanta, B., Balushi, K.R.A., Arami, S.A.A., *Bearing fault detection using artificial neural networks and genetic algorithm.* Journal on Applied SIgnal Processing, 2004(1): p. 366-377.
[164] Yang, D.M., Stronach, A.F., Mc Connell, P., *The application of advanced signal processing techniques to induction monitor bearing condition diagnosis.* Meccanica, 2003. **38**: p. 297-308.
[165] Shao, Y., Nezu, K., *Prognosis of remaining bearing life using neural networks.* Part I: Systems and Control Engineering, 2000. **214**(3): p. 217-230.

[166] Li, B., Goddu, G., Chow, M.Y. *Detection of common motor bearing faults using frequency domain vibration signals and a neural network approach*. in *Proceedings of the American Control Conference*. 1998. Philidelphia.
[167] Li, B., Chow, M.Y., Tipsuwan, Y., Hung, J.C., *Neural network based motor rolling bearing fault diagnosis.* Transactions of Industrial Electronics, 2000. **47**(5): p. 1060-1069.
[168] Tsang, A.H.C., *Condition based maintenance: Tools and decision making.* Journal of Quality and Maintenance Engineering, 1995. **1**(3): p. 3-17.
[169] Cassanelli, G., Mura, G., Fantini, F., Vanzi, M., Plano, B., *Failure analysis-assissted FMEA.* Microelectronics Reliability, 2006. **46**: p. 1795-1799.
[170] August, J., *RCM Guidebook*. 2003: Penn Well Books. 33.
[171] Williams, J.H., Davies, A., Drake, P.R., *Condition based maintenance and machine diagnostics*. 1994: Springer. 130.
[172] Hess, R.A. *From health and usage monitoring to integrated fleet management - Evolving directions for rotorcraft*. in *IEEE Aerospace conference (No 05TH8788)*. 2005.
[173] Salzano, I.C. *Accelerometers for health and usage monitoring systems (HUMS)*. in *2nd SAIAS Symposium*. 2008. Stellenbosch, South Africa.
[174] Land, J.E. *HUMS - The benefits, past present and future*. in *IEEE Aerospace (Cat No 01TH8542)*. 2001.
[175] Nurse, J., Petch, C., Fisher, C.E., *Engine gas path integrity monitoring.* Aerotech paper C470/6/052, 1994.
[176] Powrie, H.E.G., Mc Nicholas, K., *Gas path condition monitoring during accelerated mission testing of a demonstrator engine.* AIAA Paper 97-2904, 1997.
[177] Powrie, H.E.G., Fisher, C.E., *Monitoring of foreign objects ingested into the intake of gas turbine aero-engine.* International Conference on Condition Monitoring Proceedings, University of Swansea, 1999: p. 175-190.
[178] Cartwright, R.A., Fisher, C., *Marine gas turbine condition monitoring by gas path electrostatic techniques.* International Gas Turbine and Aero Engine Congress and Exposition, ASME paper 91-GT-376, 1991.
[179] Taylor, D.M., Secker, P.E., *Industrial Electrostatics*. 1994: Research Studies Press Ltd. 16-37.
[180] Parsons, R., *Electrical double layer: recent experimental and theoretical developments.* Chemical Reviews, 1990. **90**(5): p. 813-826.
[181] Harvey, T.J., Wood, R.J.K., Denault, D., Powrie, H.E.G., *Effect of oil quality on electrostatic charge generation and transport.* Journal of Electrostatics, 2002. **55**: p. 1-23.
[182] Powrie, H.E.G., Wood, R.J.K., Harvey, T.J., Wang, L., Morris, S. *Electrostatic charge generation associated with machinery component deterioration*. in *IEEE Aerospace Conference Proceedings (Cat. No.02TH8593)*. 2002.
[183] Harvey, T.J., Wood, R.J.K., Denault, D., Powrie, H.E.G., *Investigations of electrostatic charging mechanisms in oil lubricated tribo-contacts.* Tribology International, 2002. **35**(9): p. 605-614.
[184] Ireland, P.M., *The role of changing contact in sliding triboelectrification.* Journal of Physics: Part D: Applied Physics, 2008. **41**.
[185] Zharin, A.L., Rigney, D.A., *Application of the contact potential difference technique for on-line rubbing surface.* Tribology Letters, 1998. **4**(205-213).

[186] Nevshupa, R.A. *Triboemission: An attempt of developing a generalised classsification*. in *Tribology Science and Application*. 2004. Warsaw: CUN PAN.
[187] Kajdas, C., Furey, M.J., Ritter, A.L., Molina, G.J., *Triboemission as a basic part of the boundary friction regime.* Lubrication Science, 2002. **14**(2): p. 223-254.
[188] Molina, G.J., Furey, M.J., Ritter, A.L., Kajdas, C., *Triboemission from alumina, single crystal sapphire and aluminium.* Wear, 2001. **249**: p. 214-219.
[189] Nakayama, K., Suzuki, N., Hashimoto, H., *Triboemission of charged particles and photons from solid surfaces during frictional damage.* Journal of Physics: Applied Physics, 1992. **25**: p. 303-308.
[190] Nakayama, K., *Triboemission of charged particles from various solids under boundary lubrication conditions.* Wear, 1994. **178**: p. 61-67.
[191] Morris, S., Wood, R.J.K., Harvey, T.J., Powrie, H.E.G., *Electrostatic charge monitoring of unlubricated sliding wear of a bearing steel.* Wear, 2003. **255**: p. 430-443.
[192] Kasai, T., Rigney, D.A., Zharin, A., *Changes detected by a non contacting probe during sliding.* Scripta Materialia, 1998. **39**(4-5): p. 561-567.
[193] Sun, J., Wood, R.J.K., Wang, L., Care, I., Powrie, H.E.G., *Wear monitoring of bearing steel using electrostatic and acoustic emission techniques.* Wear, 2005. **259**: p. 1482-1490.
[194] Tasbaz, O.D., Wood, R.J.K., Browne, M., Powrie, H.E.G., Denault, D., *Electrostatic monitoring of oil lubricated sliding point contact for early detection of scuffing.* Wear, 1999. **230**: p. 86-97.
[195] Harvey, T.J., Morris, S., Wang, L., Wood, R.J.K., Powrie, H.E.G., *Real time monitoring of wear debris using electrostatic sensing techniques.* Part J: Journal of Engineering Tribology, 2007. **221**(1): p. 27-40.
[196] Powrie, H.E.G., Tasbaz, O.D., Wood, R.J.K., Fisher, C.E., *Performance of an electrostatic oil monitoring system during FZG scuffing test.* Proceedings of the International Conference of Condiiton Monitoring, Swansea, 1999: p. 155-174.
[197] Harvey, T.J., Wood, R.J.K., Powrie, H.E.G., *Electrostatic wear monitoring of rolling element bearings.* Wear, 2007. **263**: p. 1492-1501.
[198] Chen, S.L., Craig, M., Wood, R.J.K., Wang, L., Callan, R., Powrie, H.E.G., *Use of Artificial Intelligence Methods for Advanced Bearing Health Diagnostics and Prognostics.* IEEE Aerospace Conference, Montana, 2007.
[199] Chen, S.L., Craig, M., Wood, R.J.K., Wang, L., Callan, R., Powrie, H.E.G., *Advanced Condition Monitoring of Tapered Roller Bearings Part 2, with Integrated Data Fusion Techniques.* Submitted to Tribology International, 2008.
[200] Chen, S.L., Craig, M., Wood, R.J.K., Wang, L., Callan, R., Powrie, H.E.G. *Bearing Condition Monitoring Using Multiple Sensors and Integrated Data Fusion Techniques*. in *9th International Conference on Vibration in Rotating Machinery*. 2008. Exeter.
[201] Heng, A., Zhang, S., Tan, A.C.C., Mathew, J., *Rotating machinery prognostics: State of the art, challenges and opportunities.* Mechanical Systems and Signal Processing, 2009. **23**(3): p. 724-739.
[202] Chen, S.L., *Development of Automated Bearing Condition Monitoring using Artificial Intelligence Techniques*, in *nCATS*. 2009, University of Southampton: Hampshire, U.K.

[203] Harvey, T.J., Morris, S., Wang, L., Wood, R.J.K., Powrie, H.E.G., *Real time monitoring of wear debris using electrostatic sensing techniques.* Proceedings of the IMechE, Part J: Journal of Engineering Tribology, 2007. **221**(1): p. 27-40.

[204] Powrie, H.E.G., Wood, R.J.K., Harvey, T.J., Wang, L., Morris, S., *Electrostatic charge generation associated with machinery component deterioration.* IEEE Aerospace Conference Proceedings (Cat. No.02TH8593), 2002.

[205] Jia -Jun, L., Yu, C., Yin-Qian, C., *The generation of wear debris of different morphology in the running in process of iron and steels.* Wear, 1992. **154**(2): p. 259-267.

[206] Ueda, T., Mitamura, N., *Mechanism of dent initiated flaking and bearing life enhancement technology under contaminated lubrication condition Part 1: Effect of tangential force on dent initiated flaking.* Tribology International, 2008. **41**: p. 965 - 974.

[207] Khan, M., A., Starr, A, G., *Wear debris, basic features and machine diagnostics.* Insight, 2006. **48**(8): p. 470-476.

[208] Reda, A.A., Bowen, R., Westcott, V.C., *Characteristics of wear particles generated at the interface between sliding steel surfaces.* Wear, 1975. **34**: p. 261-273.

[209] Stachowiack, G., Batchelor, A.W., *Experimental Methods in Tribology*. 2004: Elsevier Science. 50 - 51.

[210] Wang, L., Wood, R.J.K., Streit, E., Powrie, H. E. G., Care, I. *Performance of hybrid (ceramic on steel) bearings with advanced aircraft engine oils for lubrication*. in *ASME: Turbo Power for Land Sea and Air*. 2004. Austria, Vienna.

[211] Davies, A., *Handbook of Condition Monitoring*. 1997: Chapman and Hall. 446.

[212] Rao, B.K.N., *Handbook of Condition Monitoring*. 1996: Elsevier. 91.

[213] Boyce, M.P., *Gas turbine engineering handbook*. 2002: Gulf Professional Publishing. 682.

[214] Mahaney, J.K., *Advances in the production and use of steel with improved internal cleanliness*. 1999: ASTM International. 22.